On Forecasting the Rur River

Sebastian Hartgring (4362063)

ON FORECASTING THE RUR RIVER

USING HINDCASTS AND FORECASTS OF THE 2021 FLOOD EVENT TO IMPROVE UNDERSTANDING OF FLOOD FORECASTING IN THE RUR CATCHMENT

by

Sebastian HARTGRING

4362063

to obtain the degree of Master of Science
at the Delft University of Technology,
to be defended publicly on 19 December 2023 at 3:30 PM.

Department of Hydraulic Engineering,
Faculty of Civil Engineering and Geosciences,
Delft University of Technology, the Netherlands.

Thesis committee:

Supervisors:

Ir. M. Hegnauer	Deltares
Prof. Dr.-Ing. D. Bachmann	Hochschule Magdeburg-Stendal

Chair:

Dr. E. Ragno	Delft University of Technology

Independent members:

Prof. dr. ir. R. Uijlenhoet	Delft University of Technology
Dr. ir. E. Mosselman	Delft University of Technology and Deltares

Keywords: [flood forecasting], [Rur river], [Rur reservoir], [2021 flood event], [ProMaIDes,] [Wflow], [lignite mining]

Front: Flooding of the Rur River near the Wurm confluence during the 2019 highwater event.

Image source: Rheinische Post (2019). *Hochwasser im Kreis Heinsberg: Rur und Wurm treten über die Ufer - Überschwemmung in Kempen.* https://rp-online.de/.https://rp-online.de/nrw/staedte/kreis-heinsberg/hochwasser-im-kreis-heinsberg-rur-und-wurm-treten-ueber-die-ufer-ueberschwemmung-in-kempen_bid-37505371

An electronic version of this thesis is available at http://repository.tudelft.nl/.

SAMENVATTING

Nederland, Duitsland en België werden in juli 2021 getroffen door hevige en langdurige regenval. Naarmate de tijd vorderde, werden de weerswaarschuwingen opgeschaald en werden evacuaties ingezet vanwege voorspelde overstromingen, zo ook voor het stroomgebied van de Roer. Overstromingen in het stroomgebied van de Roer bleken moeilijk te voorspellen, wat de vraag opriep welke elementen bepalend zijn in een overstromingsvoorspellingsmodel voor de Roer rivier. Deze vraag wordt beantwoord door zowel de overstromingsgebeurtenis van 2021 te bootsen, als de overstromingevoorspellingen aangedreven door de weersverwachting van 13 juli 2021 te gebruiken.

Het stroomgebied van de Roer wordt gekenmerkt door de topografische en geologische verdeling, waarbij de steile Eifel anders reageert dan het vlakke laagland, en door menselijke interventie in de vorm van de aanwezigheid van stuwmeren en bruinkoolmijnen. Er is een hydrologisch *Wflow_SBM* model opgezet voor het stroomgebied van de Roer dat deze kenmerken bevat, en een hydrodynamisch *ProMaIDes* model voor het gedeelte van de Roer dat benedenstrooms van de reservoirs loopt. Deze modellen zijn vergeleken om verschillende aspecten te onderzoeken: de schematisatie van de rivierstroom, stromingen in de uiterwaarden, interacties met de zijbeken, de invloed van de reservoirs en het effect van een verlaagd grondwaterpeil.

De resultaten van de overstromingen in 2021 tonen aan dat het modelleren van stromingen in de uiterwaarden bepalend is voor de vorm van de afvoergolf, zowel in de zijbeken als in de Roer. Daarnaast heeft het reservoir een belangrijke rol gespeeld om de hoogwatergolf te dempen. Het verlaagde grondwaterpeil is gesimuleerd door een lekterm in de verzadigde zone van de ondergrond toe te voegen, wiens indirecte effect significant groter is dan de lekterm zelf. Verder blijkt met name de zijbeken Worm en Inde bepalend in de afvoer van de Roer. Deze kenmerken komen ook terug in de nagebootste voorspellingen, ook al is de resolutie in ruimte en tijd significant lager voor de meteorologische invoer van het model.

Ten slotte toont de karakteristieke respons van de Roer aan dat niet elk type model even praktisch is voor overstromingsvoorspellingen. De dominante afvoer uit de stuwmeren is sterk gereguleerd en zal benedenstrooms niet snel tot inundaties leiden. Complexe inundatiepatronen in de uiterwaarden worden pas relevant in de Nederlandse Roer, waardoor twee-dimensionaal modelleren vooral hier een meerwaarde heeft. Daarom wordt aangeraden voornamelijk gebruik te maken van een één-dimensionaal afvoermodel, waarbij vertragingseffecten door winterbedstromingen versimpeld meegenomen worden. Wanneer voorspelde afvoeren in Stah worden overschreden, kunnen twee-dimensionale simulaties een uitkomst bieden, waarbij het modelgebied gereduceerd is tot de Nederlandse Roer en enkel voorspellingen worden uitgewerkt waar een kritische waarde gerelateerd aan de capaciteit van de uiterwaarden ($Q_{limiet} = 300 \mathrm{m}^3/\mathrm{s}$) wordt overschreden.

SUMMARY

The Netherlands, Germany, and Belgium were hit by heavy and prolonged precipitation in July 2021. As time passed, weather warnings escalated, leading to evacuations due to predicted floods, including in the Rur catchment. It was difficult to forecast the flooding of the Rur, raising the question of which elements are crucial in a flood prediction model for the Rur river. This question is addressed by addressing both a hindcast of the 2021 flood event and creating forecasts based on the weather forecast of July 13, 2021.

The Rur river basin is characterised by topographic and geological variations, with the steep Eifel responding differently than the flat lowlands, and human intervention in the form of reservoirs and lignite mines. A hydrological *Wflow_SBM* model has been derived for the Rur river basin, encompassing these characteristics, along with a hydrodynamic *ProMalDes* model for the downstream reach of the Rur. These models were compared to investigate various aspects: river routing, floodplain flow, tirbutary interactions, the influence of reservoirs, and the impact of reduced groundwater levels.

The results of the 2021 floods indicate that modelling flows in floodplains is crucial to shaping the flood wave, both in tributaries and the Rur itself. Additionally, the reservoir played a significant role in attenuating the flood wave, with the increase in the outflow of the reservoir primarily affecting the tail of the wave. The reduced groundwater level was simulated by adding a leakage term to the saturated subsurface zone, whose indirect effect is significantly greater than the leakage term itself. Moreover, the tributaries Worm and Inde, particularly, are influential in the Rur's discharge. These characteristics are also evident in the simulated forecasts, although the spatial and temporal resolution is significantly lower for these meteorological predictions.

Finally, the characteristic response of the Rur demonstrates that not every model type is equally practical for flood forecasting. The dominant flow from the reservoirs is highly regulated and is unlikely to induce inundations downstream. Complex flow patterns in floodplains only become relevant in the Dutch Rur, which makes two-dimensional modelling particularly valuable here. Therefore, it is recommended to use a one-dimensional discharge model, incorporating delay effects from winter bed flows. When predicted discharges at the Stah station are exceeded, two-dimensional simulations may provide a solution, the model area reduced to the Dutch Rur, focussing on predictions where a critical value related to floodplain capacity ($Q_{\text{limit}} = 300$ m/s) is exceeded.

Eric Dale: Do you know I built a bridge once?

Will Emerson: Sorry?

E: A bridge.

W: No, I didn't know that.

E: I was an engineer by trade.

W: Hmmm... hmmm

E: It went from Dilles Bottom, Ohio to Moundsville, West Virginia. It spanned nine hundred and twelve feet above the Ohio River. Twelve thousand people used this thing a day. And it cut out thirty-five miles of driving each way between Wheeling and New Martinsville. That's a combined 847,000 miles of driving a day. Or 25,410,000 miles a month. And 304,920,000 miles a year. Saved. Now I completed that project in 1986, that's twenty-two years ago. So over the life of that one bridge, that's 6,708,240,000 miles that haven't had to be driven. At, what, let's say fifty miles an hour. So that's, what, 134,165,800 hours, or 559,020 days. So that one little bridge has saved the people of those communities a combined 1,531 years of their lives not wasted in a [*bleep*] car. One thousand five hundred and thirty-one years.

- Quote from the film *Margin Call* (2011)

PREFACE

This thesis is primarily the result of a year of investigating the Rur River in the context of the 2021 floods, but also the culmination of a long and fruitful student career. I started civil engineering with a future in structural design in mind, or more specifically, I wanted to design bridges inspired by a quote from a movie I saw while travelling to Peru to visit my family (you can find the specific quote on the previous page). This moment became the start of a long journey which we call studying and, thankfully, did not consist of pure studying.

Many years later, I finished my bachelor's studies in Civil Engineering at TU Delft and Latin-American studies at Leiden University. Both studies nicely reflect that epiphanic moment in the plane, but I deviated a bit by pursuing a master's degree in Hydraulic Engineering. Let us just say that I became more interested in what was flowing under the bridge than the bridge itself. Now, I look forward to the coming years when I will put my engineering knowledge to work, helping people save time or live a safer life.

I want to specifically thank three groups of people who helped me a lot during my thesis project and who raised the results of this investigation. First and foremost, I want to thank the people at Deltares who helped me with practical dilemmas, but also by inspiring me with their critical thinking and sincere interest. This also includes the other master's students working at HYD that I met during my thesis.

Second, I want to thank my friends and family who supported me during this year. I think this list will become too long when I mention everyone specifically who came with practical suggestions to improve the 'thesis life' or, even better, distractions from this same 'thesis life'.

Finally, I want to thank my thesis committee for its advice and patience over the last year, especially after the setbacks in the summer of 2022. I want to specifically thank my supervisors Mark and Daniel for the very interesting thesis subject, the supervision from Germany and Singapore, and also for being supportive of opportunities such as visiting the Meuse symposium in Liège, the Rur reservoirs in the Eifel, and IPRUM in Magdeburg. I think these examples highlight the international aspect of the 2021 flood event, but also hydraulics and hydrology in general.

- Sebastian Hartgring

NOMENCLATURE

symbol	unit	description
A	[m^2]	river cross-section
$A_{bankfull}$	[m^2]	area of bankfull cross-sections
A_{basin}	[m^2]	basin area
B	[m]	river width
c	[m/s]	wave celerity
c_{DW}	[m/s]	diffusive wave celerity
c_{KW}	[m/s]	kinematic wave celerity
D	[-]	drainage density
d	[m]	water depth
$d_{bankfull}$	[m]	depth of bankfull cross-section
E	[m^3] or [mm]	evapotranspiration per unit of area during a period Δt
f	[-]	scaling factor
g	[m/s^2]	gravitational constant
h	[m]	water head
I	[m^3]	reservoir inflow during a period Δt
K_0	[mm/day]	vertical saturated conductivity
$L_{max,1}$	[mm/day]	maximum leakage parameter for area 1
$L_{max,2}$	[mm/day]	maximum leakage parameter for area 2
L_{stream}	[m]	length of stream
N_i	[-]	number of stream segments of order i
n_x	[-]	number of grid cells in x-direction
n_y	[-]	number of grid cells in y-direction
O	[m^3]	reservoir outflow during a period Δt
P	[m^3] or [mm]	precipitation per unit of area during a period Δt
Q	[m^3/s]	discharge
Q_1	[m^3/s]	calibrated reservoir outflow (lower band)
Q_2	[m^3/s]	calibrated reservoir outflow (upper band)

symbol	unit	description
Q_{bankfull}	[m^3/s]	bankfull discharge
Q_{high}	[m^3/s]	reservoir outflow in high flow regime
Q_{low}	[m^3/s]	reservoir outflow during low flow regime
Q_{max}	[m^3/s]	maximum discharge, maximum discharge
Q_N	[m^3/s]	discharge with return period N in years
$Q_{N\%}$	[m^3/s]	N % percentile of discharge record
Q_{Stah}	[m^3/s]	discharge at Stah
Q_{u}	[m^3/s]	uniform discharge
q	[m2/s]	specific discharge
R_b	[-]	bifurcation ratio
S	[m^3]	reservoir storage
S_0	[-]	river bed slope
S_f	[-]	river friction slope
T	[y]	return period
T_{peak}	[date]	arrival time of flood wave peak
t	[s]	time
t_{wet}	[date]	inundation arrival time
U	[m/s]	depth-averaged flow velocity
w	[-]	unit width
x	[m]	x-coordinate
y	[m]	y-coordinate
z_i	[m]	depth of water table
β	[-]	cell slope
Δ_x	[m]	grid cell width in x-direction
Δ_y	[m]	grid cell width in y-direction
θ_r	[mm]	saturated soil water content
θ_s	[mm]	residual soil water content
ϕ_{global}	[°]	floodplain orientation

ACRONYMS

AMICE Adaptation of the Meuse to the Impacts of Climate Evolutions

DEM Digital Elevation Model

EFAS European Flood Alert System

EPS Ensemble Prediction System

FEWS Flood Early Warning System

HydroMT Hydro Model Tools

IBF Impact Based Forecasting

KNMI Royal Netherlands Meteorological Institute

LANUV Landesamt für Natur Umwelt und Verbraucherschutz

NAP Nieuw Amsterdams Peil

NDWI Normalized Difference Water Index

NRW North Rhine-Westphalia

NSE Nash–Sutcliffe model efficiency coefficient

NWP Numerical Weather Prediction

ProMaIDes Protection Measures against Inundation Decision Support

PTF (Pedo) Transfer Functions

REA Representative Elementary Area

RMI Royal Meteorological Institute of Belgium

RWS Rijkswaterstaat

UPA Upstream Area

WL Waterschap Limburg

WMO World Meteorological Organization

WVER Wasserverband Eifel-Rur

List of Figures

LIST OF TABLES

CONTENTS

1

INTRODUCTION

THE summer of July 2021 left a strong impression on many people. It was a summer of extremes, with severe wildfires in the American continent, heatwaves in Australia, and record-breaking floods in Europe (Munich RE, 2022). Floods are the main cause of water-related natural disasters (WMO, 2011), resulting in an estimated annual death toll of 25,000, affecting 500 million people, and causing an estimated annual damage of 60 billion euros (UNESCO, 2023). The European floods in July 2021 were no exception, with more than 220 deaths and estimated damage of 46 billion euros (NEW, 2021; Munich RE, 2022). Within the context of flood risks increasing globally as a result of climate change (Booij, 2002; Jongman et al., 2012; Kundzewicz et al., 2014; Winsemius et al., 2016; Alfieri et al., 2017; Blöschl et al., 2019), this investigation aims to improve the knowledge on flood forecasting using the 2021 floods in Europe as a relevant case study.

1.1. LIMBURG DURING THE 2021 FLOOD EVENT

July 2021 was already a wet month for the Netherlands, with localised heavy rainfall, leading to disruptions in train services in Limburg, for example, due to flooding (COT, 2022b). A few days later, on the 12th of July, weather forecasts indicated a worrying situation, prompting the Royal Netherlands Meteorological Institute (KNMI) to issue a yellow weather warning around 10:00. The new meteorological forecasts on the 13th of July led to an increase in the warning level to orange, and preparations were made in the background regarding communication and crisis organisation. When heavy precipitation started in Germany and Belgium on the 14th of July, the severity of the event became apparent. The KNMI escalated the warning to red, and in the following days, the crisis organisation expanded and thousands of people were evacuated until the situation was downgraded to normal on the 21nd of July 2021 (COT, 2022a).

Subsequently, there was a (very deserved) sense of pride among the organisation of Waterschap Limburg (WL), and no fatalities were registered in the Netherlands. Still, evaluations of the Limburg flood revealed several challenges. For example, it was challenging

to accurately estimate precipitation volumes from real-time radar measurements (Saadi et al., 2023), underestimating them by a factor of approximately three (R. Imhoff et al., 2021), and not all flow models were able to accurately simulate floods with the extremity of the 2021 flood (NEW, 2021). Regional prediction models also faced problems with malfunctioning measuring stations in Germany (COT, 2022b), and there were challenges in information provision, as it was difficult to determine which water levels shared by WL and Rijkswaterstaat (RWS) were most current (COT, 2022b).

1.2. THE IMPORTANCE OF FLOOD FORECASTING

Reducing the loss of life during floods is linked to timely warnings and evacuation (Jonkman & Vrijling, 2008), which underlines the importance of robust and accurate flood forecasting, used to design flood protection and alert people. In practice, this raises the question of which modelling approach is favourable, often resulting in a trade-off between model complexity and computational effiency. A review of flood forecasting practices shows that different types of models are in use (Jain et al., 2018), and comparisons between flood models highlight how the type of output (Hoch et al., 2019) and the characteristics of the basin (Afshari et al., 2018) may determine the complexity of the model required. In simpler terms: What type of model should we use for flood forecasting?

1.3. RESEARCH ON THE LIMBURG FLOODS AND THE RUR RIVER

The elements mentioned in the previous section demonstrate that there is room for improvement in water prediction systems in Limburg and more generally in northern Europe, where this urgency is increasing due to the warmer summers predicted with longer droughts and more intense rainfall (IPCC, 2021; KNMI, 2021; Kreienkamp et al., 2021). Several reports have already been published that analyse the event itself from a Dutch perspective (NEW, 2021), the crisis organisation (COT, 2022b, 2022a), damages and risks (Slager, 2023), and analysis of tributaries such as Rur, Geul, and Geleenbeek (T. Geertsema & Asselman, 2022; Asselman & van Heeringen, 2022). A large number of master's students from the Netherlands have already researched the flooding events in Limburg (see Table 1.1), focussing mainly on the Geul River and less on the Rur River (Deen, 2022). However, there is still much information to learn to understand the Rur River during the 2021 floods (T. Geertsema & Asselman, 2022), making the Rur River a suitable case study within the context of flood forecasting during the 2021 floods.

Apart from the 2021 flood event, the Rur is an interesting and relevant subject for investigation. It is an international river that originates in Belgium and mainly flows through Germany and enters the Meuse in the Netherlands. Hydrodynamic modelling of the Rur focusses on the Dutch Rur (T. Geertsema & Asselman, 2022; Horn & Hurkmans, 2022), and operational hydrological models of the Rur are cross-border but either showed difficulties with forecasting during the flood event in the case of the linear regression model by WL or are outdated, such as the RWS HBV model. Furthermore, the river basin has a strong anthropogenic character due to the presence of lignite mining pits and artificial reservoirs, which strongly influence the basin's water balance, making it an interesting subject of investigation. These same reservoirs played an essential role during the flood

Author	River	Subject
Deen (2022)	Rur	Measuring equipment
van Dijk (2022)	Geul	Impact of protection measures
Godlewski (2022)	Geul	Improvement of flood early warning system
Klein (2022)	Geul	Understanding hydrological response
Middendorp (2022)	Geul	Design flood bypass tunnel
Muishout (2023)	Geul	Nature-based solutions
Thewissen (2022)	Geul	Event extremity
Tsiokanos (2022)	Geul	Extreme value analysis
Current study	Rur	**Comparing flood forecasting models**

Table 1.1: Studies by TU Delft students with subjects related to tributaries of the Meuse river and the Limburg floods.

event (T. Geertsema & Asselman, 2022), but also offer opportunities to adapt water management to growing flood risks, as was done in the international Adaptation of the Meuse to the Impacts of Climate Evolutions (AMICE) project in 2010 (Pyka et al., 2016).

1.4. STUDY OBJECTIVE AND RESEARCH QUESTION

These reasons demonstrate that there is room for a deeper system analysis of the Rur River during the 2021 floods, that this knowledge can be applied to develop a flood prediction system, and that the Rur River is an interesting case study in flood forecasting.

> **Therefore, the objective of this master's thesis is to identify the determining factors for a flood forecasting model for the Rur catchment based on the flood event of July 2021.**

To fulfil this objective, five research questions are formulated addressing this subject:

> RQ1. What are the characteristics that determine the Rur catchment in the context of hydrological and hydrodynamic models?
>
> RQ2. How can these characteristics be captured in a flood forecasting model?
>
> RQ3. Which factors observed in the hindcast determined the outcome of the flood event in July 2021?
>
> RQ4. What are the sensitivities of this model observed using ensemble forecasts of the July 2021 event?
>
> RQ5. What are the key factors for the prediction of floods in the Rur catchment based on the lessons learnt from the event in July 2021?

RQ1 regards the characteristics of the Rur basin within the context relevant to flood forecasting. Or, in other words: How is the catchment expected to react to flooding based on its characteristic features? Then, RQ2 asks how these typical responses can be captured in the hydrological and hydrodynamic models used in this thesis (*Wflow_SBM*

and *ProMaIDes*, respectively). When these questions are answered, the hindcast and forecast can be evaluated as indicated in RQ3 and RQ4. RQ3 is used to better understand what happened during the flood event of July 2021 and qualitatively validate whether the models are able to capture such an event. Then, the ensemble forecasts are used to discover model sensitivities using a quantitative approach and assess the usability of the models with the forecasts available before the flood event. Finally, RQ5 presents the synthesis of this research by answering the question or giving recommendations when further research is needed.

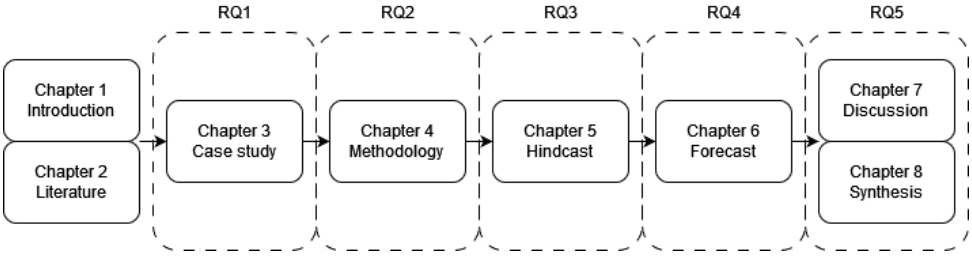

Figure 1.1: Link between the chapters in this thesis and the 5 research questions.

1.5. READING GUIDE

Each research question is related to a chapter in this thesis, as illustrated in Figure 1.1. First, the state-of-the-art on flood forecasting is explored in the literature study in Chapter 2. A division is made between the details of modelling floods, focussing on translating the physical processes behind floods into numerical models, and the use of such models in flood forecasting. This chapter provides general background information on the subject of this thesis. It is followed by the contextualisation of the subject in Chapter 3, which describes the Rur catchment and the 2021 flood event, which together form the case study of this thesis.

The specific research conducted by the author becomes concrete in the chapters describing the methodology and the results. First, the methodology chapter describes how the hydrological model (*Wflow_SBM*) and the hydrodynamic model (*ProMaIDes*) are used in this research, focussing primarily on processes relevant to the Rur basin, such as reservoir modelling, subsurface flow, and different options to set up a forecasting model. Furthermore, Section 4.5 describes the two types of forcing data used in this research, namely detailed gauge-corrected radar measurement used for a qualitative analysis of catchment response during the flood event and ensemble predictions of the flood event, which are used to highlight sensitivities of the possible model configurations. These descriptions are followed by the results in chapters 5 and 6, which focus on five topics: 1) inundation/floodplain flow, 2) flood wave routing, 3) tributary interactions, 4) reservoir modelling, and 5) groundwater effects. These results are then interpreted and evaluated in the discussion in chapter 7.

Finally, the synthesis of this thesis is shared in the conclusion and recommendations in chapter **??**. The answers to the research questions given in previous chapters are sum-

marised and form the conclusion of this thesis in Section 8.1. Finally, some recommendations for future research are shared in Section 8.2, divided into three separate themes: 1) modelling flood processes focused on technical recommendations, 2) recommendations for flood forecasting in general, and 3) some final thoughts on operational water management in an international catchment such as Rur.

2

LITERATURE

In this literature review, flood modelling and flood forecasting topics will be explored, as illustrated by figure 2.1. First, the types and approaches to flood modelling are treated, and their dominant processes are described with the objective of providing an overview of flood modelling. Second, flood forecasting is defined and described as it builds upon flood modelling, paying particular attention to two extensions of flood forecasting: ensemble prediction systems and impact-based forecasting. In the third to fifth sections, three in-depth topics are explored which are relevant for the modelling of floods (and therefore also flood forecasting): model discretization focussing on how physical processes are translated into a mathematical model, diffusive effects describing how flood wave propagation can change throughout the catchment, and influences on catchments by anthropogenic activities such as mining and reservoir management.

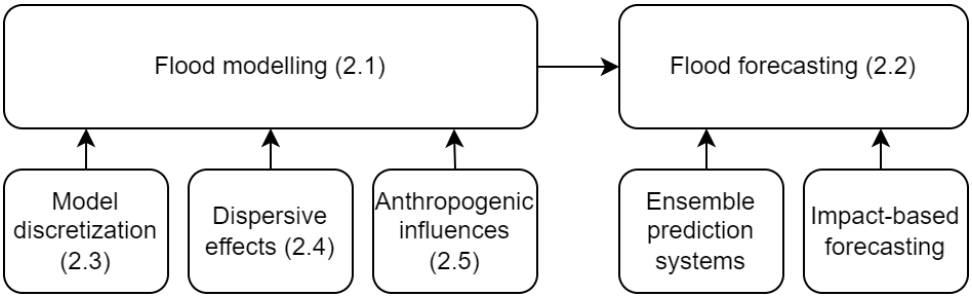

Figure 2.1: Outline of the literature review in this thesis.

2.1. MODELLING OF FLOODING PROCESSES

Before exploring the subject of flood forecasting, the mechanisms behind flooding must be understood. In this section, several types of flood are defined, and the main processes that generate floods are analysed.

2.1.1. FLOOD TYPES

There are many options to define "flooding" and several types of flooding. Good guidance is to follow the definition of World Meteorological Organization (WMO), which defines flooding as follows: "Overflowing by the water of the normal confines of a stream or other body of water, or accumulation of water by drainage over areas that are not normally submerged." (WMO, 2011, p.1-4). Following these WMO guidelines, three types of flooding are identified and briefly described that are relevant to the topic of flood forecasting.

- **Pluvial flooding** is rain-related flooding driven by intense or prolonged rainfall exceeding the capacity of the existing drainage system (van Riel, 2011; Ochoa-Rodríguez et al., 2015). It can occur in both rural and urban areas, but its effects are more pronounced in urban areas, where rainwater ponds on streets and cannot enter a drain point. Pluvial flooding is influenced not only by the magnitude of rainfall, but also by the moisture content of the soil, soil profiles and catchment characteristics such as basin geometry and stream connectivity. As the intensity of the rainfall exceeds the infiltration capacity of the soil, runoff occurs when excess rainfall drains overland to reach the river following the underlying topography. **Flash floods** are a special case of pluvial flooding and regarded as the most lethal form of natural hazards (GWP, 2007; COMET, 2010; WMO, 2012). They are typically the result of high-intensity rainfall events within a few hours (less than six) and often occur in ares with steep slopes, resulting in runoff accumulating rapidly at low lying downstream points.
- **Fluvial flooding** (or riverine flooding) is caused by exceedance of its stream capacity and occurs mostly over a wide range of river and catchment systems, spilling into floodplains (WMO, 2011; Zevenbergen et al., 2010). In this case, the water level in the river channel exceeds the bank height and water leaks into the surrounding land resulting in flooding (Tanaka et al., 2020). Fluvial flooding can result from the same event as flash flooding, typically further downstream and at longer time and length scales.
- **Coastal floods** occur when sea levels rise is induced by storm surges and high winds, often coinciding with high tides (WMO, 2011). Coastal flooding can coincide with pluvial and fluvial flooding, resulting in compound flooding, and wave attack can damage dikes resulting from floods of the hinterland.

These types of flooding emerging from the WMO guidelines can be applied within the Dutch context with some additional explanation. Almost all of the Netherlands is affected by the risk of flooding, either through coastal flooding, as the region lies below sea level, or river flooding through the Meuse and Rhine rivers and its tributaries. As a result, the Netherlands are protected by a system of dikes surrounding the coasts and rivers. Most Dutch rivers are surrounded by two layers of dikes: the summer dikes and winter dikes (Silva et al., 2004).

Summer dikes primarily manage water during regular conditions, while winter dikes or band dikes are specifically constructed to prevent flooding during high river flows, especially in winter. Unlike summer dikes, winter dikes need to withstand the highest water

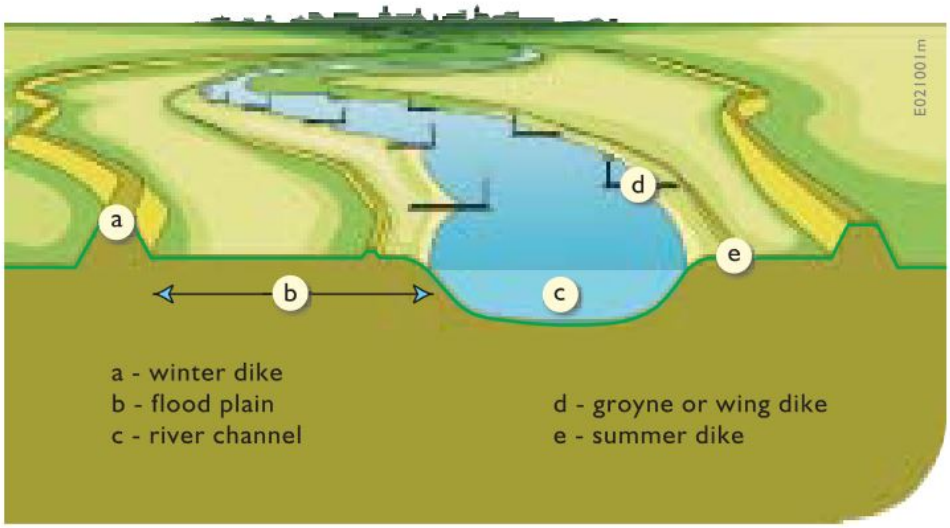

Figure 2.2: Two-tier dike structures and groynes for flood protection along the rivers in The Netherlands. Obtained from Silva et al. (2004).

levels and are only activated during periods of elevated river discharge. The floodplains between the summer and winter dikes ("uiterwaarden" in Dutch) are often inundated and add to the conveyance capacity of the river. In other words, flooding of the summer dikes is part of the functioning of the flood protection systems of the Dutch rivers. Subsequently, in Dutch river management, a distinction is made between 'flooding' and 'inundation.' The first term refers to unintended flooding of the winter dikes, while inundation refers to intended flooding of the summer dikes and the floodplains.

2.1.2. PROCESSES IN FLOODING

Similarly to types of flooding, several processes can be identified that play a role in fluvial and pluvial flooding. These processes are identified as follows:

- **Infiltration excess runoff**, or Hortonian overland flow, after Horton (1933), occurs when rainfall comes at a rate higher than the absorption rate of the unsaturated soil, thus resulting in a runoff of excess water (Smith & Goodrich, 2005).

- **Saturation excess runoff**, or Dunne overland flow, after Dunne and Black (1970a, 1970b), describes the runoff process when the soil has reached saturation. This process often occurs in humid areas, but can also result from upland flows reaching and saturating the soil. When saturation occurs, the groundwater table reaches the surface and surface runoff is generated (Smith & Goodrich, 2005).

- **Channel flow** is the flow of water in rivers and channels. Generally, the length scale of the flow is much larger than the depth, which enables the flow to be described using the shallow water equations (also called Saint-Venant equations), in which

inertial forces, pressure forces, gravitational forces, and frictional forces describe the flow. Depending on the situation, it is possible to simplify the flow equations by neglecting specific terms of the shallow water equations.

- **Groundwater flow** is water flow in confined and unconfined aquifers. Descriptions of groundwater flow are often based on Darcy's law and are defined in terms of the hydraulic head. In aquifers, recharge and discharge occur on long timescales, making them a storage component of the water cycle (Heath, 2004; Holzbecher & Sorek, 2005).
- **Subsurface stormflow** occurs when water moves down a slope through permeable soils, contributing to the storm hydrograph in the river. It is considered a (near) saturated flow mechanism and, in steep terrains with conductive soils, subsurface storm flow may be the primary mechanism for runoff generation. It can consist of two types of different flows, namely homogeneous matrix flow, where water already stored in the subsoil flows homogeneously, and preferential flow, where water flows through distinct structures in the subsoil, such as macropores or areas with higher permeability at rates faster than typical groundwater flow (Weiler et al., 2005; Chifflard et al., 2019).

These processes occur at different lengths and time scales, as illustrated in image 2.3 by Blöschl and Sivapalan (1995). As a result, excess infiltration runoff, excess saturation runoff, and subsurface storm flow are linked processes that can coincide and influence each other (Mirus & Loague, 2013). Similarly, the duration of the rainfall plays a role in addition to intensity, and its variability in space and time will be translated into variability in runoff processes (Woods & Sivapalan, 1999). Taking into account the length scales, the measured characteristics of the soil, such as saturation, must be scaled to the model scales, which introduces biases (Western & Blöschl, 1999). Even if a mechanism such as subsurface storm flow is measured, it can only be measured locally, and effects such as preferential flow are difficult to capture in both observations and models (Chifflard et al., 2019).

Additionally, Dooge (1986) describes how finding 'hydrological laws' for such processes and capturing them accurately in a model is challenging, as they can be derived from two seemingly opposite principles: microscale continuum mechanics and macroscale statistical approaches. Understanding the differences between the two principles is essential for accurate modelling, as models depend on the suitability of using microscale equations to describe macroscale behaviour and, if possible, aggregation rules to obtain macroscale model parameters with the correct distribution for correct modelling (Blöschl & Sivapalan, 1995). Due to this aggregating process, it is generally impossible to derive the model parameters directly from field measurements, resulting in the dependency on calibration (Booij, 2005).

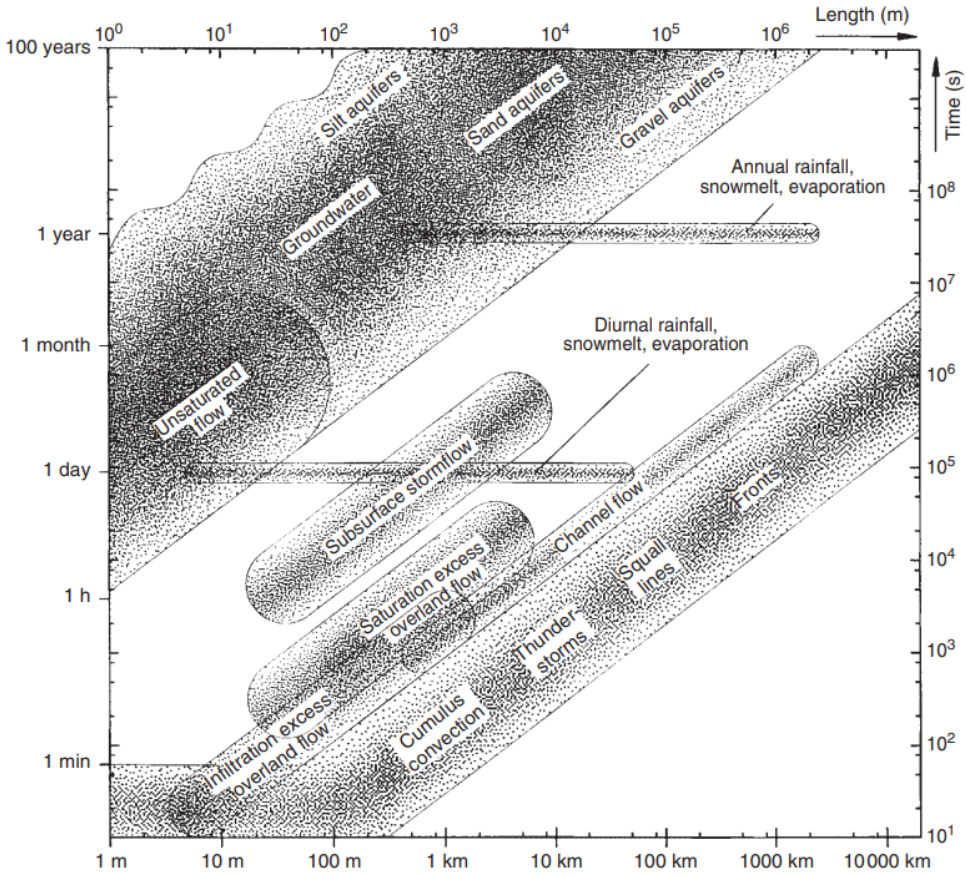

Figure 2.3: Processes in flood modelling and their length scales. Obtained from: Blöschl and Sivapalan (1995)

2.2. FLOOD FORECASTING

The subject of flood forecasting systems is explored in this section. First, three main types of forecasting systems are distinguished. These systems are then extended regarding their meteorological input, going from deterministic forecasting to ensemble prediction systems, and their output as hazard forecasts are extended to impact-based forecasts.

2.2.1. TYPES OF FLOOD FORECASTING SYSTEMS

The WMO defines a flood forecasting system as a system 1) providing forecasts relating to rainfall (both quantity and timing), 2) consisting of flood modelling software that is linked to an observation network, and 3) operating in real-time; a flood warning system is an extension of a flood forecasting system as it has the objective of mobilising people (WMO, 2011). There are different types of flood warning and forecasting systems, ranging from basic to state-of-the-art (WMO, 2011):

- **Threshold-based flood alert**: This service can be based on real-time data measurements along rivers, where measurement trends are extrapolated, resulting in a qualitative estimate of river flow or water level. The extrapolated prediction can be used to find relevant flood extent maps for comparable water levels or discharges. For example, when a discharge of $Q \approx 175$ m^3/s is predicted, it can be compared to existing inundation maps for $Q = 100$ m^3/s and $Q = 250$ m^3/s to estimate flood extent.
- **Flood forecasting**: This system is based on simulation tools and modelling, including simple methods such as statistical curves, level-to-level correlations or time-of-travel relationships, or a simulation of catchment response. Unlike threshold-based flood alerts, the information is not confined to station locations, as in the flood alert, but can be focused on specified locations at risk. For example, a lumped hydrological or one-dimensional hydrodynamic river model can evaluate the response of the catchment, although the flooding itself is not modelled. Again, model results can be compared to existing inundation maps or historical data to evaluate the forecast.
- **Inundation forecasting**: This service requires a hydrological model, hydrodynamic model, or both, and models the inundated areas of the flood extent. It is the most sophisticated system and, in practice, requires the most computational effort.

Flood forecasting and inundation forecasting systems are based on models forced by meteorological predictions. As a result, their temporal modelling range (lead time) is extended to the length of the meteorological prediction. On the contrary, for threshold-based flood alerts, the lead time is only a couple of hours, namely the travel time of the flood wave. All three systems depend on the accuracy of the (meteorological) prediction and observations to validate the prediction. Additionally, the dominant process and its characteristic time and length scale should be considered when addressing the lead time of the forecast. At smaller time and length scales, infiltration and saturation excess overland flow become dominant, which depend on high-resolution meteorological forecasts. When the spatial and temporal scales increase, channel flow may become dom-

inant which is more dependent on accurate hydraulic boundary conditions and relies less on the resolution of the meteorological forecast.

2.2.2. WEATHER FORECASTING TECHNIQUES

Typically, meteorological predictions in flood forecasting systems are generated using either Numerical Weather Prediction (NWP) systems or real-time nowcasting techniques (Jain et al., 2018). NWP systems produce weather forecasts by dividing the atmosphere into grid cells in horizontal and vertical direction, and solving non-linear transport equations and atmospheric processes between these cells (Coiffier, 2011). Nowcasting works differently as it is based on extrapolation of remotely-sensed precipitation estimates, thus taking advantage of high-resolution real-time radar measurements (Pierce, Seed, Ballard, Simonin, & Li, 2012).

As a result, nowcasting forecasts are typically associated with higher spatial and temporal resolutions and a high initial skill score, but their skill reduces with increasing lead-time as they are driven by statistical and extrapolation-based methods. On the other hand, NWP systems are used with lower resolutions and a low update-frequency (forecasts are typically updated every 3 to 6 hours), but perform better for larger lead-times as they are driven by a physics-based approach (R. O. Imhoff, 2022). Blended rainfall forecasts, combining both nowcasting and NWP systems, may be able to combine the "best of both worlds" (R. O. Imhoff, 2022, p.10) and are therefore a promising development in terms of weather forecasting techniques. Figure 2.4 demonstrates the typical skill scores for NWP and nowcasting systems, and blended rainfall forecasts bridging both systems.

2.2.3. ENSEMBLE PREDICTION SYSTEMS

Recently, forecast users are increasingly aware of the limitations of single-value deterministic hydrometeorological forecasts, especially under severe or extreme hydrometeorological conditions (Roundy et al., 2019). An Ensemble Prediction System (EPS) may provide an alternative, differing from deterministic forecasts by offering multiple outcomes ('ensemble members'), therefore addressing uncertainties implicitly in contrast to a single deterministic outcome. Analysis of ensemble members, for example, through quantile regression analysis, may provide information on the probability distribution of weather forecast or river streamflow, which may serve as an estimate of predictive hydrological uncertainty (Weerts et al., 2011). Despite significant improvements in meteorological ensemble forecasting (Froude et al., 2013), it remains challenging to model meteorological conditions, typically described as a chaotic process (Lorenz, 1963; Shen et al., 2021).

EPS outcomes can be used and presented in several ways. Pegram et al. (2019) list several flash flood early warning systems for Europe which work with hydrological simulations, hydrological warnings, meteorological warnings, or a combination of these, with lead times varying from nowcasting to 132 hours. Similarly, Boucher et al. (2019) provides an example of an EPS used as a support tool for the management of short-term and long-term hydroelectric reservoirs, where the ensemble streamflow forecasts are fed into a decision model. Alternatively, Hartman (2019) describes how the preprocessed and

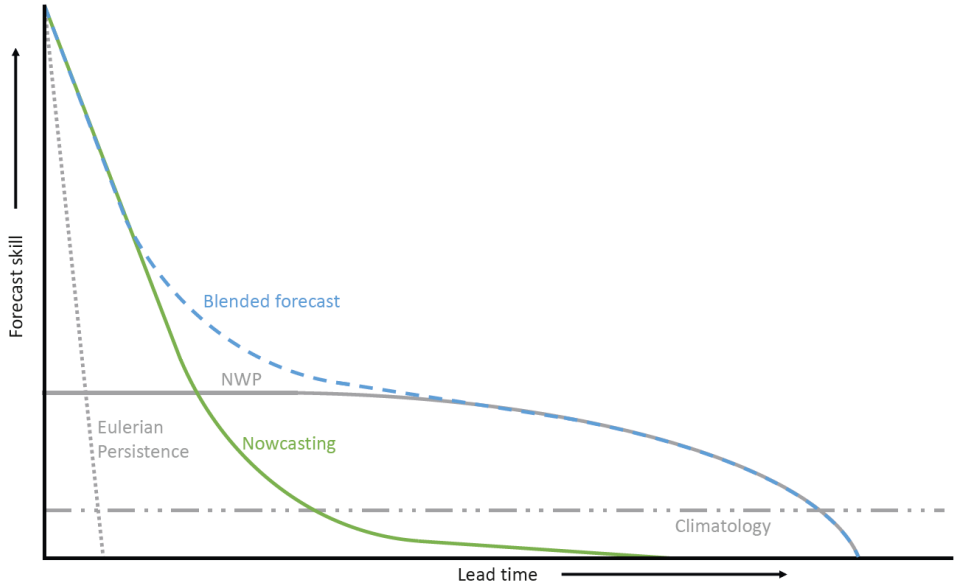

Figure 2.4: Schematic overview of the rainfall forecast skill as a function of lead time for different forecasting systems: Eulerian Persistence (the method of using the last observation as forecast; dotted grey), the climatology (dash-dotted grey), NWP (grey), nowcasting (green) and blended forecasting (dashed blue). Obtained from R. O. Imhoff (2022).

post-processed ensemble stream flows are presented, the first as a 'spaghetti plot' and the latter using confidence intervals.

ENSEMBLE POST-PROCESSING

Processing of the ensemble can occur either before the hydrological model as meteorological ensembles or after modelling as streamflow ensembles. Typically, post-processing streamflow ensembles is easier than pre-processing meteorological ensembles, and the post-processing addresses both meteorological and hydrological biases in the hydrological model output. However, uncertainties remain or may even be introduced (Verkade et al., 2013). Within the exhaustive number of choices for streamflow postprocessing (see also Troin et al. (2021)), Boucher et al. (2019) identifies four categories which are briefly summarised as follows:

- **Analogs**: This method uses the raw ensemble forecasts and streamflows and finds similar forecasts ('analogue') with the corresponding observations.
- **Regression-based methods**: The modelled streamflow forecast is treated as a univariate quantity through multiple linear regression between the streamflow ensemble members. A good example is quantile regression analysis that addresses the quantiles of exceedance of predictions (Koenker & Bassett, 1978; Weerts et al., 2011).

- **Ensemble dressing**: A probability distribution function is arranged around each member of the streamflow ensemble. Next, a mixture distribution is formed by summing these functions to obtain the post-processed probability density function (pdf) from which realisations can be drawn.
- **Bayesian Model Averaging**: This technique merges multiple modelled outputs into a probabilistic streamflow forecast that considers the skill, bias, and uncertainty of each member of the ensemble. It relies on the hypothesis that among a (finite) set of model outputs, one of them would be sufficient for each valid timestep.

All methods demonstrate the necessity for historical observation data when evaluating ensembles and their probabilities. It is possible to treat ensemble members as independent realisations from an EPS, for example, when bias is removed or not present but needs proper post-processing to be able to quantify the probabilistic values for the EPS outcomes correctly. Additionally, extra steps are important when using the EPS results to avoid misinterpretations. The information should be presented clearly and only if relevant (Jutta Thielen-del Pozo et al., 2019), and it is important to quantify the uncertainties post-processed in a readable and usable way (Hopson et al., 2019).

Furthermore, meteorological ensembles are not the only uncertain model parameters that need to be addressed. Initial hydrological conditions are also important for rainfall-runoff models, often obtained using a 'cold state' model with a discrete meteorological product based on radar measurements, satellite data or gauge station observations (Hopson et al., 2019).

2.2.4. IMPACT-BASED FORECASTING

To illustrate the differences between the prediction of hazards and impacts, the WMO defines risk as the union of the probability of occurrence of the hazards, the degree of vulnerability and the level of exposure (WMO, 2015). Following this approach, three forecasting paradigms address these elements, as shown in table 2.1. Regular weather forecasts fall within the first paradigm, as do fixed threshold weather warnings when these thresholds are based only on weather-based factors. When information is added that expresses the consequences of these forecasts with vulnerability and exposure data, the forecast is considered impact-based. (Merz et al., 2020) describe in their extensive literature study on Impact Based Forecasting (IBF) how it is expected to offer new possibilities for emergency management and disaster risk reduction, as it provides richer information to manage crises.

EUROPEAN FLOOD ALERT SYSTEM

On a European level, IBF is implemented in flood modelling through European Flood Alert System (EFAS). EFAS is an EPS (see also Section 2.2.3) based on the distributed hydrological LISFLOOD model (van der Knijff et al., 2008) using ensembles from a numerical weather model as input (Thielen et al., 2009). EFAS uses threshold-exceeding levels to issue warnings. Furthermore, EFAS contains a rapid impact assessment product where flood forecast results are translated into event-based flood hazard maps using pre-made high-resolution hydrodynamic simulations, which are then combined with exposure and vulnerability information, as illustrated in Figure 2.5 (Dottori et al., 2017).

	Description	H	V	E
	Hazard forecasting			
1	Contains only information related to atmospheric variables	✓	✗	✗
	Impact forecasting			
2	Designed to express the expected impacts as a result of the expected weather	✓	✓	✗
3	Designed to provide detailed information down to the individual, activity, or community level;	✓	✓	✓

Table 2.1: Three paradigms of forecasting as defined by WMO guidelines addressing occurrence of the hazard (H), degree of vulnerability (V) and the level of exposure (E) (WMO, 2015).

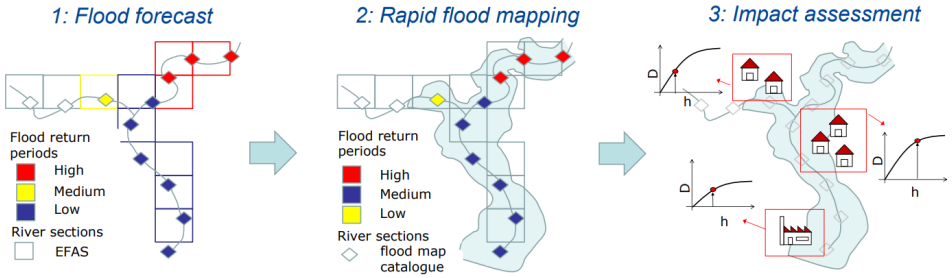

Figure 2.5: Conceptual scheme of the rapid risk assessment procedure in EFAS. Obtained from Dottori et al. (2017).

However, interviews with EFAS users in a study by Demeritt et al. (2013, p.156) show that although its existence is appreciated, "... Forecasters were often conservative and prefer to wait and see rather than act on early warnings from EPS". Warnings issued by this early version of EFAS were useful in raising general awareness of a possible risk, but missed practical applicability, partly due to the low resolution of the model and relatively long lead times and high uncertainties (Demeritt et al., 2013).

REGIONAL IMPACT-BASED FORECASTING

Impact-based flood prediction has also been applied on local and regional scales. Examples of IBF models include combining inundation maps with information related to population housing and insurance data (Le Bihan et al., 2016, 2017), and using forecasts and fragility curves to estimate the probability of dike-breaches and modelling the impact of high-probability failure scenarios on infrastructure (Bachmann et al., 2016; Brown et al., 2016). It can also be used to combine an EPS with a cost-benefit framework to support policy decisions in flood-prone areas (Dale et al., 2014). At the same time, IBF on a local scale is associated with challenges such as addressing the uncertainties of the forecasts and implementing these while also considering the social systems and the structures which support them (Merz et al., 2020), as well as convincing local actors to translate 'early warning' into 'early action' (De Perez et al., 2016) using communication with the proper context, interpretation and presentation (Merz et al., 2007; De Groeve,

2020).

As a result, IBF models and their operational use can differ widely between regions and applications due to such local unique characteristics and as a result of the available data. Furthermore, these models may depend on very high-resolution data and, therefore, very fine model resolution in the order of meters. However, breakthroughs in advanced technologies may drastically reduce computation times, such as the neural network-driven impact-based inundation model by (Rözer et al., 2021).

2.3. DISCRETISATION IN FLOOD MODELS

The flooding processes described in 2.1 are conceptual descriptions of the physical processes that cause flooding. In order to translate these concepts into a model, they must be described discretely; hence, the "discretisation" of the flood model. Numerous options (e.g. Singh (2017)) can be found for the discretisation of these processes, as well as for how they are implemented in the spatial and temporal domain. This can be on a fundamental level, where a distinction can be made between two approaches for discretising these processes. As described by Bouaziz (2021), these can deviate between a bottom-up approach and a top-down approach (Savenije & Hrachowitz, 2017):

1. **Bottom-up approach** where high-resolution descriptions of small-scale processes are numerically integrated into a larger-scale gridded model with many parameters. Models following this approach are called physically-based models.

2. **Top-down approach** consisting of a schematisation of the dominant processes of the water balance, which typically describes the storage, transmission, and release of water with limited parameters. These models are called conceptual models.

In this thesis, the software used is limited to the *Wflow_SBM* and *ProMaIDes* software available to the author, *ProMaIDes* is considered a physically-based model, as it is fully described by hydraulic flow equations. *Wflow_SBM* on the contrary is considered a conceptual model, consisting of a water balance for each cell, although the model itself is spatially distributed and makes use of flow equations for flow routing.

Both types of models depend on the discretization of processes, especially the discretization of flow. Choosing certain types of discretisation by selecting a particular model option can have varying effects on model processes, which may propagate throughout the whole model or even the forecast set-up when multiple models are linked. Therefore, the theoretical background related to the discretisation of flood models is explored in this section, focussing on routing schemes, floodplain modelling, and the effects of spatial resolution.

2.3.1. DIFFERENCES IN ROUTING SCHEMES

Flood routing is a procedure to determine the time and magnitude of flow at a point in the catchment during a flood (Chow et al., 1988). Two approaches are possible as the flood can be modelled either as a lumped system, as a function of time alone based on the relationship between outflow and storage, or as a distributed system based on partial differential equations with variables in time and space (Chow et al., 1988; Singh,

2017). As this thesis focusses on distributed modelling, variations in modelling distributed flood routing are considered.

Distributed flood routing schemes are based on the classical Saint-Venant equations, which describe one-dimensional unsteady flow in open channels. They consist of two equations: the continuity equation (Equation 2.1) and the momentum equation (2.2). Different formulations of these equations exist, such as the conservation and non-conservation forms, and are extended in two dimensions. The equations below are written in one-dimensional conservation form and are based on the derivation in Chow et al. (1988), where Q denotes the discharge, A the average cross-sectional of the flow, d the depth of the water, S_0 the slope of the bed and S_f the frictional slope. The continuity equation for the overland flow should be extended to include a lateral inflow q such as precipitation ($q > 0$), infiltration into groundwater ($q < 0$), or receiving the overland flow ($q > 0$) (Chow et al., 1988). However, these derivations are less illustrative and, therefore, are not presented in this thesis.

$$\frac{\partial Q}{\partial x} + \frac{\partial A}{\partial t} = 0 \tag{2.1}$$

$$\underbrace{\frac{1}{A}\frac{\partial Q}{\partial t}}_{(1)} + \underbrace{\frac{1}{A}\frac{\partial}{\partial x}\left(\frac{Q^2}{A}\right)}_{(2)} + \underbrace{g\frac{\partial d}{\partial x}}_{(3)} - g(\underbrace{S_0}_{(4)} - \underbrace{S_f}_{(5)}) = 0 \tag{2.2}$$

The momentum equation consists of different terms, each with a contribution to the flow of momentum. These terms are divided into five categories, following Chow et al. (1988)[p.280-281] and Bachmann (2016)[p.5]:

1. The acceleration term, which describes the change in momentum due to the change in velocity over time;
2. The convective acceleration term, which describes the change in momentum due to the change in velocity along the channel;
3. The pressure force term, proportional to the change in water depth along the channel;
4. The gravity force term, proportional to the bed slope S_0;
5. The friction force term, proportional to the friction slope S_f.

It should be noted that the above categorisation applies to channel flow and that the pressure term is not strictly related to the change in water pressure but to the change in water depth. This is different from the derivation of the Navier-Stokes equations, where the 'pressure term' means the pressure gradient (Δp).

In its complete form, Equation 2.2 is called the dynamic wave equation. The relative importance of the terms in the momentum equation can be estimated, giving insight into the possibility of simplifying the equation by neglecting specific terms. As a result,

Wave equation	**Local acceleration** (1)	**Convective acceleration** (2)	**Pressure** (3)	**Gravity** (4)	**Friction** (5)
Dynamic	✓	✓	✓	✓	✓
Diffusive	✗	✗	✓	✓	✓
Kinematic	✗	✗	✗	✓	✓

Table 2.2: Different types of flood wave equations based on the terms in equation 2.2.

equation 2.2 can be simplified for different types of flood wave propagation, resulting in the classification described in table 2.2. (Chow et al., 1988; Perumal & Price, 2017)

For the movement of a large flood wave in a large river, inertial and pressure forces become important in describing the wave motion (Chow et al., 1988). Miller (1983) and Perumal and Price (2017) list several studies that evaluate simplifications in momentum equations, where the consensus is that in many cases gravity and friction forces are dominant, making the kinematic wave equation especially applicable for steep slopes and overland flow. Furthermore, river flood waves commonly travel at a lower celerity than dynamic wave celerity. This celerity is governed by the frictional resistance of the river bed and is described by diffusive or kinematic wave equations, where the diffusive model also has the advantage of including hysteresis of the flood wave and backwater effects (Ferrick, 1985; Chow et al., 1988; Battjes & Labeur, 2017; Perumal & Price, 2017). As kinematic and diffusive wave approximations are often incorporated into flood modelling (Moussa & Cheviron, 2015), their description and differences are explored further.

KINEMATIC WAVE EQUATION

For the kinematic wave method in one dimension, the gravity force term balances the friction force term ($S_0 = S_f$), which results in the equation of momentum (equation 2.2) to be rewritten in explicit form using a general power relationship of the form $A = \alpha Q^{\beta}$ (Chow et al., 1988). Inserting this into the continuity equation (equation 2.1) yields equation 2.3.

$$\frac{\partial Q}{\partial t} + \frac{1}{\alpha\beta Q^{\beta-1}}\frac{\partial Q}{\partial x} = \frac{\partial Q}{\partial t} + c_{KW}\frac{\partial Q}{\partial x} = 0 \tag{2.3}$$

For the kinematic wave approach, it can be shown that the celerity of the flood wave depends solely on the depth of the water and the geometry of the channel. Thus, for a nonvarying channel or river, the maximum velocity of the flood wave does not change as the peak stays at the same maximum water depth, assuming it travels without distortions (Chow et al., 1988; Battjes & Labeur, 2017). As a result, the kinematic wave approach cannot capture the attenuation of the flood wave peak. Depending on the formulation of the friction term, one can derive the flood wave celerity $c_{KW} = (5/3)U$ for Strickler or Manning type resistance laws (as in equation 2.3) or $c_{KW} = (3/2)U$ for constant friction, where U denotes the flow velocity averaged in depth (Miller, 1983; Battjes & Labeur, 2017).

It is important to note that the flow velocity, and thus the celerity of the flood wave, increases for larger flow depths, meaning that the peak of the flood wave travels faster than its trailing and leading edges. As a result, the wave steepens, and assumptions made in deriving the Saint-Venant equations become unviable and can finally result in a 'kinematic shock' (Miller, 1983). It is theoretically possible to observe such a kinematic shock (for example, in flash floods). However, it is an uncommon phenomenon in practise, as small flow and catchment irregularities usually produce enough diffusion-like effects (Ponce, 1991). Similarly, in models, such shocks are often prevented by numerical diffusion inside kinematic wave models. Such artificial numerical diffusion results from the truncation error of the applied finite difference scheme (Ponce, 1991). The kinematic wave equation is especially applicable for larger bed slopes and longer wave periods, which is found for steep overland flow or slow rising flood waves (Ponce, 1991).

DIFFUSIVE WAVE EQUATION

As mentioned, flood wave characteristics such as peak attenuation, backwater effects, and hysteresis cannot be captured by the kinematic wave equation in its differential equation form (Moussa, 1996). However, such effects can be captured by including the pressure term in the momentum equation, resulting in the diffusive wave equation 2.4, assuming no lateral inflow.

$$\frac{\partial Q}{\partial t} + c_{DW}\frac{\partial Q}{\partial x} - D\frac{\partial^2 Q}{\partial x^2} = 0, \text{ where } c_{DW} = \left(\frac{5}{3} - \frac{4}{3}\frac{d}{2d+B}\right)U \tag{2.4}$$

This equation is similar to the kinematic wave equation 2.3, and setting the diffusive coefficient D to zero will result in the diffusive wave equation collapsing into the kinematic wave equation. The diffusive wave, again assuming a constant friction coefficient, has a wave celerity c_{DW} and the addition of a diffusive term $D = Q_u/(2S_0B)$ where the discharge Q is related to the uniform discharge Q_u through the approximation in Equation 2.5 (Moussa, 1996; Moussa & Bocquiuon, 1996; Battjes & Labeur, 2017). The celerity c_{DW} is similar to c_{KW} and can be considered as such, being only dependent on depth, multiplied by a correction factor (Cappelaere, 1997).

$$Q = Q_u\left(1 - \frac{1}{2S_0}\frac{\partial d}{\partial x}\right) \tag{2.5}$$

The mathematical formulation addresses dispersive and diffusive effects by applying the diffusive wave equation. The diffusive term is represented in the differential equation itself, and the dispersive effects are illustrated in c_{DW} as a function of the depth of the water d. The kinematic wave approach does not produce these effects, which introduces the need to address them in the analysis of model results, or it does produce diffusive and dispersive effects through numerical artefacts, which may be misinterpreted (Ponce, 1991). These dispersive and diffusive effects emerge in channel and river flow, making the diffusive wave equation a more suitable approach, although it is computationally more demanding. Only in situations with solid dissipative tendencies with accelerating and decelerating flows, such as flows into large reservoirs, strong overbank flows, and flow reversals, would the diffusive wave equation still fall short, as the acceleration terms

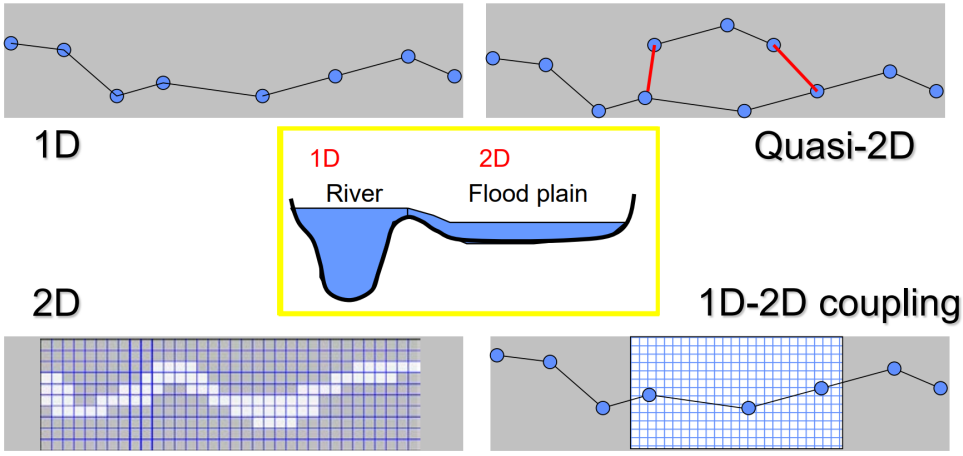

Figure 2.6: Four types of river-floodplain discretisation. Obtained from de Bruijn et al. (2018).

are neglected. In these cases, the dynamic wave approach would produce favourable results (Ponce, 1991; Moussa, 2004).

2.3.2. RIVER AND FLOODPLAIN DISCRETISATION

The routing mechanisms in the previous section are described in one dimension. A one-dimensional approach may be sufficient to model long rivers and is computationally efficient, which may be helpful for modelling large river networks (Morales-Hernández et al., 2016). It is possible to model floodplain flow in one-dimensional models by including floodplain topography and bed roughness in the river cross-sections (1D in Figure 2.6), but also by more advanced quasi-two-dimensional techniques such as modelling floodplain flow as a separate one-dimensional river parallel to the main river channel as in Figure 2.6 (de Bruijn et al., 2018) or using a subgrid approach to distinguish floodplain flow from channel flow (Neal et al., 2012). The drawbacks of one-dimensional models are the dependence of accurate model results on the locations of the cross-sections (Samuels, 1990) and the fact that the extent of inundation must be determined indirectly between cross-sections using, for example, interpolation methods (Bates & De Roo, 2000).

The one-dimensional model can be extended to a fully two-dimensional model (2D in Figure 2.6). In this case, the (reduced) shallow-water equations are derived for two dimensions and solved for each cell of the grid. The location of the river and floodplains is determined by providing the correct elevation and roughness values. However, there is no fundamental distinction between land and river cells as they are all contained in the same grid, which can be formed by rectangular grid cells (rectilinear), curved grid cells with orthogonal faces (curvilinear), or by cells with non-orthogonal faces (flexible mesh). The disadvantages of two-dimensional models are very long computation times compared to one-dimensional or quasi-two-dimensional models, especially for finer resolutions (Bates & De Roo, 2000; Morales-Hernández et al., 2016; de Bruijn et al.,

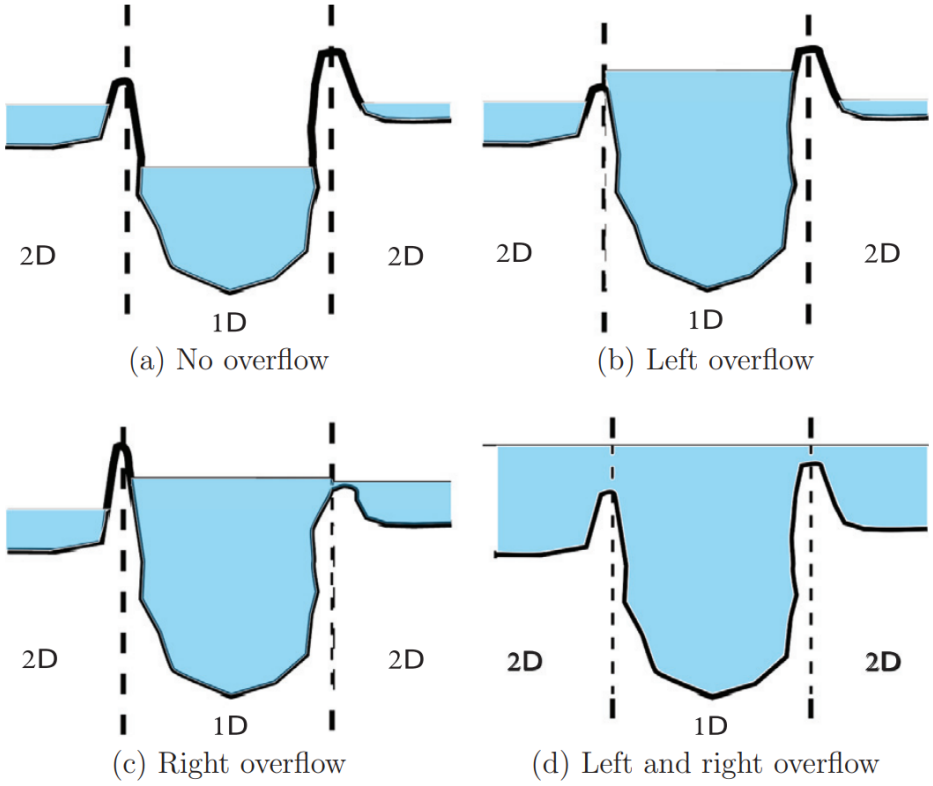

Figure 2.7: Overflow from the one-dimensional river segment into the two-dimensional floodplain. Obtained from Morales-Hernández et al. (2016).

2018), and these types of models are less well suited to parameterisation with traditional cross-sectional surveys (Bates & De Roo, 2000).

An alternative method is to couple one-dimensional and two-dimensional models (1D2D in Figure 2.6), providing a trade-off between computational efficiency and accurate floodplain modelling. In this case, the model consists of one-dimensional river segments that make up the one-dimensional model and two-dimensional grids that describe floodplains and surrounding land. The overflow from the river to the floodplain occurs when a particular water level is reached (illustrated in Figure 2.7), often modelled using a lateral weir equation (Morales-Hernández et al., 2016) or a uniform flow equation (Bates & De Roo, 2000).

2.3.3. EFFECTS OF SPATIAL RESOLUTION

Conceptually, different options have been derived for discretising a river-floodplain model with varying flood routing mechanisms. However, not only is the type of discretisation important, but also the resolution at which it is performed. Equations describing

flood processes are typically based on large-scale volume-based approaches and experiments for which small-scale heterogeneities are numerically integrated throughout space (Dooge, 1986; Clark et al., 2017). For example, consider the runoff coefficient of a catchment, which can be determined by observing the bulk difference between precipitation and downstream river flow instead of observing the actual runoff at each location where rain falls to determine the amount of runoff. As a result, a minimum length scale can be derived for which these closure relations are still valid (Peters-Lidard et al., 2017). For example, Woods and Sivapalan (1999) consider the Representative Elementary Area (REA): runoff processes at scales smaller than REA should be modelled discretely, and for processes larger than REA, a lump approach may suffice (Wood et al., 1990). Effectively, this means that the minimum grid size of a model (maximum resolution) is defined by the REA corresponding to the internal processes of the model.

Similarly, the necessity for a maximum grid size (minimum resolution) can be derived. In principle, using a finer spatial resolution reduces truncation errors in the model, thus improving accuracy (Peters-Lidard et al., 2017). Additionally, decreasing the resolution of a model or increasing the size of the model can result in the average of heterogeneities in the basin, although these local characteristics can be important for runoff observed at the basin scale (Woods & Sivapalan, 1999). For example, topographic features are strongly affected by model resolution, as floodplain features, such as embankments and elevated roads, have a substantial impact on the extent of flooding (M. G. Werner, 2001), and preferential flow paths of high conductivity in the subsoil can dominate the subsurface stormflow response observed at the catchment scale (Clark et al., 2017). The resolution of the grid also affects the extent to which the spatial variability of precipitation is restricted and smoothed, where a large smoothening will result in an underestimate of the flood peaks (Skøien et al., 2003; Bruni et al., 2015), and similarly, the resolution of the model may be restricted to the resolution at which precipitation measurements are considered accurate enough (Terink et al., 2018).

As a result, the spatial resolution for accurate flood modelling is bounded by a minimum and maximum at which the dominant processes still have physical meaning and remain verifiable (Blöschl, 2001). Therefore, a lack of observations at the subcatchment scale can limit the applicability of models in ungauged basins (Hrachowitz et al., 2013), and the chosen grid size should describe important deterministic variability (Seyfried & Wilcox, 1995).

2.4. DISPERSIVE EFFECTS AND FLOOD WAVE PROPAGATION

The shape, size and characteristics of the watershed influence the interactions between the tributaries and the main river. As a result, the watershed may respond differently locally due to dispersive behaviour, meaning that flows originating from the same pluvial source may experience different travel times in the system. It is possible to distinguish three types of dispersion (Saco & Kumar, 2002; Olivera & Koka, 2004; Pattison et al., 2014):

- **Hydrodynamic dispersion** resulting from friction and storage differences within a single reach.

- **Geomorphological dispersion** describing differences within the network structure such as flow lengths (Rinaldo et al., 1991).
- **Kinematic dispersion** assessing a system's nonhomogeneous flood wave celerity due to nonlinear interactions in the wave.

The catchments may experience all three types of dispersion, and the dominant type depends on the characteristics of the catchment and how heterogeneous these are. In the first place, these types of dispersion have been quantified to describe the response of the catchment using a travel-time distribution for the network, such as an instantaneous response function (Saco & Kumar, 2002), and spatially invariant hydrodynamic parameters. However, the distinction of dispersive effects is also useful when addressing and categorising dispersive effects using distributed modelling (Pattison et al., 2014). Two dispersive effects are described in the following sections: floodplain storage resulting in hydrodynamic dispersion and the shape of the catchment drainage network affecting geomorphological dispersion. The attenuation of the flood wave peak related to kinematic dispersion is described to some extent in Section 2.3.

2.4.1. FLOODPLAIN FLOW

Flood wave propagation is strongly affected by the presence of floodplains when the depth of the water is high enough to allow floodplain flow. This water depth is called the 'bankfull depth' of the river cross-section. In general, the floodplain bed has a more significant roughness than the river bed, which reduces the flow velocity and, therefore, the intensity of the flood wave (see, for example, Section 2.3.1). As a result, the flood wave profile becomes more expansive with a lower peak discharge, as illustrated in Figure 2.8. Comparisons of hydrographs before and after inundation zones in the study by Rak et al. (2016) demonstrate the attenuation effects on the peak of the flood wave.

Floodplain beds consist of rougher material that increases flow depth and decreases flood wave celerity, and the most substantial effects were found for shorter flood waves with a strong peak. Different land use cases influence the magnitude of this effect, where forestation model results (higher roughness) show a stronger attenuation effect and longer travel times for the flood wave, but also an increase of total inundated areas than situations with an increase in agricultural land use (lower roughness). However, it is important to note that floodplain changes affect river flow velocities and vice versa, and the effects of river-floodplain interactions on flood waves do not only depend on the width of the floodplain, but also the width-weighted flow velocity of the cross-section (Van de Lee et al., 2001).

2.4.2. RIVER NETWORK

Catchments of similar size and steepness can respond differently to a storm event, as they may have varying types of river networks draining the watershed. There are several methods to describe and characterise a river network, such as the bifurcation ratio R_b (equation 2.6), defined as the ratio of the number of stream segments N_i of any order i to the number of stream segments N_{i+1} of an order $i+1$, and the drainage density D (equation 2.7) which is described by the quotient of cumulative length of streams L_{stream}

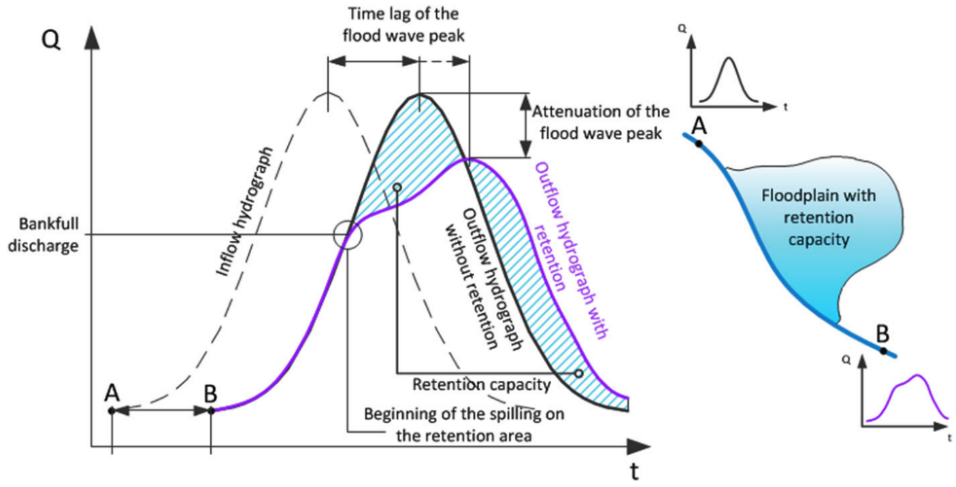

Figure 2.8: Illustration of dispersive effects resulting from floodplain flow. Obtained from Rak et al. (2016).

and total drainage area A_{basin} (Horton, 1945; Strahler, 1957; Fitzpatrick, 2017; Yand et al., 2017). The general bifurcation ratio can also be obtained by averaging the bifurcation ratios of different orders (Yand et al., 2017). Two basins may be similar in size but have a different bifurcation ratio, resulting in the basin with the lower ratio having a faster response, as illustrated in Figure 2.9. Minor variations in discharge timing or size in several tributaries can have an equal or greater significant impact on results than one significant change or variation in a single tributary (Pattison et al., 2014; T. J. Geertsema et al., 2018).

$$R_b = N_i / N_{i+1} \tag{2.6}$$

$$D = \sum \frac{L_{stream}}{A_{basin}} \tag{2.7}$$

The structure of the drainage network controls the response of the watershed in combination with more localised factors, such as the duration of the discharge wave and the time interval between the discharge peaks at confluences. When observing such network interactions, it is necessary to take into account multiple events. The inhomogeneous precipitation pattern for a single event may not adequately represent the behaviour of the system (T. J. Geertsema et al., 2018) and complex physical flood generation processes cannot be fully explained by the morphology of the drainage network alone (Perez et al., 2018).

Furthermore, a study by Olivera and Koka (2004) compares and scales the Nile and Niger watersheds to investigate how the size of the watershed influences the effects of dispersion. When uniform hydrodynamic parameters are applied, it can be shown that the

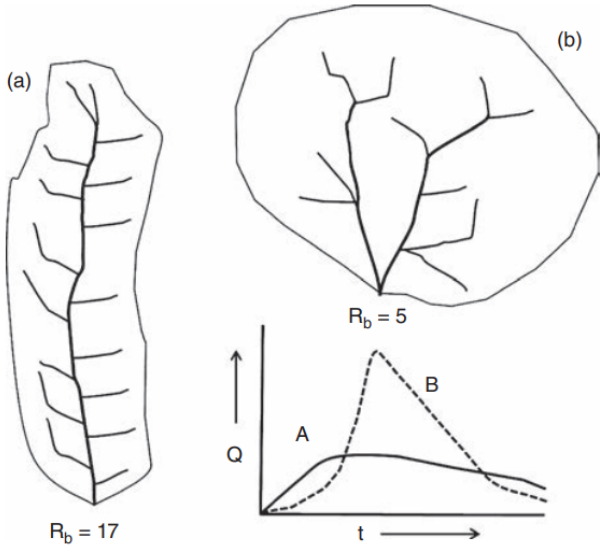

Figure 2.9: Two stream networks with a high (a) and low (b) bifurcation ratio showing different responses to a storm event. Catchment (a) contains 17 streams of order 1 ($N_i = N_1$) and 1 stream of order 2 ($N_{i+1} = N_2$) resulting in $R_b = 17/1 = 17$. Similarly, $N_1 = 10$ and $N_2 = 2$ for catchment (b) resulting in $R_b = 10/2 = 5$. Obtained from Fitzpatrick (2017).

effects of geomorphological dispersion increase compared to hydrodynamic dispersion as the watershed size increases, and vice versa. For non-uniformly distributed parameters, the spatial variability of the parameters still plays a fundamental role in determining which dispersive effect dominates. A similar study by Di Lazzaro et al. (2016) using generalised watersheds found that geomorphological dispersion dominates for very large basins, suggesting that the drainage network determines the response of the catchment under asymptotic conditions. However, the range for which these conditions are not met is extensive. Furthermore, Brauer et al. (2011) highlighted the importance of drainage networks, which may also occur for subsurface flow, and showed their relationship with rainfall intensity, meaning that their dispersive effect can vary for varying rainfall intensities.

2.5. ANTHROPOGENIC CHANGES TO CATCHMENTS

Currently, people live in an environment shaped by the effect of humans on the global scale (Crutzen, 2002). Landscapes are transformed as a result of, among other causes, agricultural and industrial activities (Vitousek et al., 1997), and anthropogenic influences must be taken into account when addressing water balance in terms of water use and storage (e.g. in reservoirs) (Oki & Kanae, 2006). This topic of anthropogenic effects on the water cycle is examined in more detail in this section, focussing on the effects of the presence of reservoirs and mining activities on catchment hydrology.

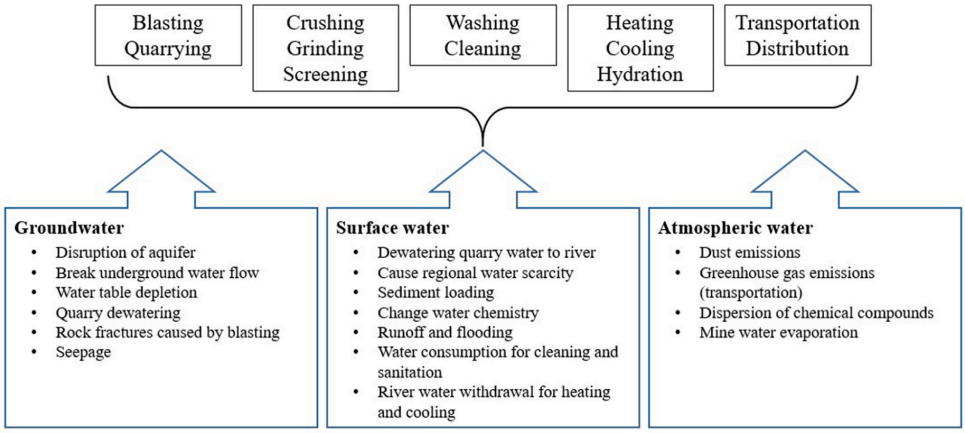

Figure 2.10: Typical nonmetal mineral production lifecycle and its impact on water resources, Obtained from (Mardonova & Han, 2023).

2.5.1. EFFECTS OF MINING ACTIVITIES ON THE WATER BALANCE

Mine site hydrology tries to address the effects of mining activities on the water balance, for example, by examining the availability of nearby water sources, the effects of dewatering on the head of groundwater and determining where extracted water can be discharged to the receiving water bodies (Wolkersdorfer et al., 2020). Numerous examples exist where analytical equations (Marinelli & Niccoli, 2000), numerical models (Mengistu et al., 2019), or both (Zhao et al., 2017) can be used to estimate the effects of mining pits such as recharge and hydraulic head decline, supported with in situ measurements such as groundwater sampling and isotope tracking (Dhakate et al., 2019; Sethi & Di Molfetta, 2019). These methods focus not only on the effects on the preparation of mining planning (Panilas et al., 2008) during the operation (Wang et al., 2017), but also on the post-mining era when the mine becomes part of the landscape (Pusch & Hoffmann, 2000; Hancock et al., 2003).

The examples in these articles show how mining activities affect the water balance. For example: groundwater is extracted to wash minerals or dewater mines and tunnels, resulting in a lower groundwater table. The impact of such groundwater effects on the near-surface depends on whether the affected aquifer is confined or unconfined, as the groundwater table can rise and fall for unconfined aquifers. Other water flows, such as post-mining pit filling and discharge of pumped water into rivers, should be considered in the hydrological assessment of the catchment where mining occurs. Figure 2.10 shows the typical impact of non-metal mineral productions on water resources. However, addressing the widespread impact of mining activities on watersheds remains difficult, as each mine is unique in its size, processes, and locations; the absence of access to data; the long timescales associated with the impacts of mining on water balance; and the cumulative impacts of mining operations in regions (Northey et al., 2016; Mardonova & Han, 2023). Additionally, no articles were found directly linking the effects of the presence of mining pits to flood safety.

2.5.2. FLOOD WAVE DAMPENING BY RESERVOIRS

Similarly to mining sites, reservoirs are large structures that affect their respective watersheds. Even on a global scale, reservoirs affect the water balance through their storage magnitude, as they are estimated to have 'delayed' global sea level rise by 30 mm in the last 50 years (Chao et al., 2008), and their variability in storage, showing significant seasonal variations in storage on a global scale (Zhou et al., 2016). The reservoir operation rules for water supply and flood control are generally operated on longer timescales of multiple days or weeks (Restrepo et al., 2017). At the same time, rainfall observations and forecasts are used to simulate reservoir storage and adjust and test operations rules to ensure short-term flood safety (Wannasin, 2023; Cheng & Chau, 2004). In a network of reservoirs, optimally, the highest reservoirs are filled first and the lowest last to minimise the spilt water, and the lower reservoirs are emptied first to maximise downstream control (Lund et al., 2017).

Reservoirs can reduce an approaching flood wave by retaining water in the reservoir and separating flows downstream from upstream peak flows (Volpi et al., 2018). Larger reservoirs have a larger retention capacity, allowing for a more substantial reduction in peak flow. This reduction also depends on the locations of the reservoirs in the basin and their configuration (Ayalew et al., 2015; Antolini & Tate, 2021), and on the type of operation plan for the reservoir, although for low-frequency flood events the results appear to converge for both controlled and uncontrolled dams (Ayalew et al., 2013). As a result, reservoirs must be addressed in flood modelling and included in a model when the reduction in flood peak is estimated to be significant. The characteristics of the reservoir, such as its location, size, and operation plan, are essential for accurate model results.

3

CASE STUDY

THE previous chapter described the current state of literature, focussing on different aspects of flood forecasting and providing the theoretical background for this study. This chapter has a different goal, as it aims to provide a description of the case study, specifically focussing on the Rur catchment during the 2021 flood event. First, attention is paid to characterising the relevant hydrological and hydrodynamic characteristics of the Rur basin. Second, the meteorological event of 2021 July, which was the driving factor behind the flood event, is described.

3.1. DESCRIPTION OF THE RUR CATCHMENT

The Rur river is a rainfed river that flows into the Meus river. It is one of its larger tributaries with an average annual contribution of 5.5%, which can rise during the summer to 17% in some years (Van der Ploeg et al., 2021; van der Krogt et al., 2022). The Rur catchment is 2353 km^2 in size and covers three countries, as the river originates in the Eifel in Belgium, continues its flow through Germany, crossing the Rur reservoir system and the dam at Obermaubach, and enters the Meuse river in the city of Roermond located in the Netherlands. An overview of Rur and its tributaries is shown in Figure 3.1. The Wurm and Inde tributaries are the most relevant tributaries considered in this thesis with watershed sizes of, respectively, 472 and 366 km^2. Furthermore, the catchment area upstream of the Obermaubach dam is 805 km^2.

The discharge in the Rur is driven by precipitation and therefore shows strong variability and a fast response, similar to the Meuse river (De Boer, 2017; Bouaziz, 2021). The average yearly water budget is 800 mm precipitation, of which 550 mm evaporates and 250 mm results in runoff (using the measurements at the downstream station Stah).

Precipitation is evenly distributed in the northern part of the catchment, ranging from 700 to 900 mm per year (Figure 3.2a). In the southern part, a shadowing effect is caused by the Eifel and Ardennes mountain ranges, leading to varying precipitation patterns.

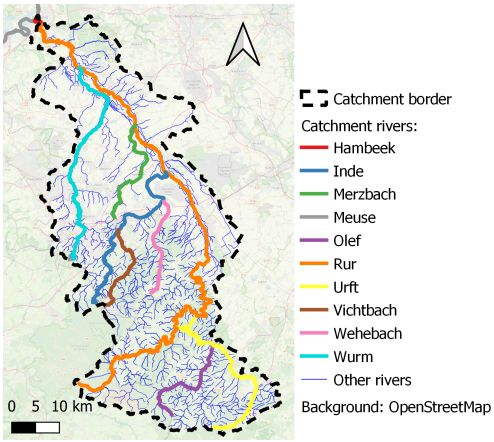

Figure 3.1: Overview of the Rur and its tributaries. Map created using *QGIS* and data from *Gewässerstationierungskarte des Landes Nordrhein-Westfalen* (n.d.).

The western regions receive higher amounts of precipitation, reaching around 1200 mm/year, while the eastern regions experience lower amounts, ranging from 700 to 900 mm/year (Bogena, Pütz, et al., 2005; Montzka, 2008; Kufeld et al., 2010).

Furthermore, the timing of precipitation events differs between the north and the south (Figure 3.2b). In the south, precipitation tends to occur more in winter when evapotranspiration is low. This results in high soil moisture content and rapid runoff. In contrast, the north experiences concentrated precipitation during summer, when evapotranspiration is high. As a result, the north shows effective buffering of precipitation events, leading to smoother hydrographs (Bogena, Pütz, et al., 2005; Montzka, 2008).

Three characteristic aspects of the Rur catchment have proven to be relevant for the hydrological and hydrodynamic study of the Rur river: geology, land use and the reservoir system. These characteristics are explored in more detail in the following sections. Runoff coefficients of the gauge stations related to these aspects can be found in Appendix F.3, highlighting the differences in runoff for each of the affected regions.

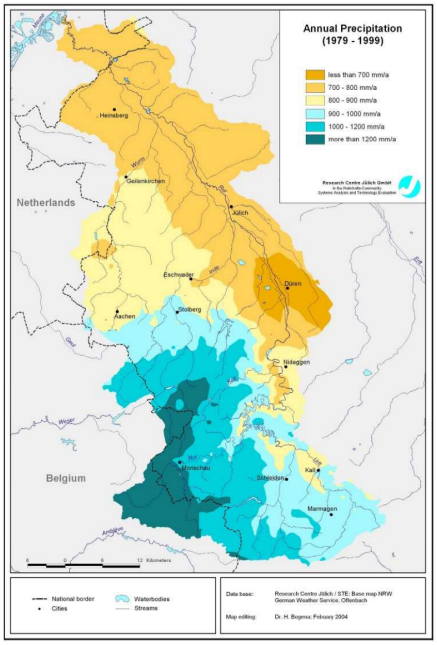

(a) Annual precipitation in the catchment of the Rur River (1979-1999).

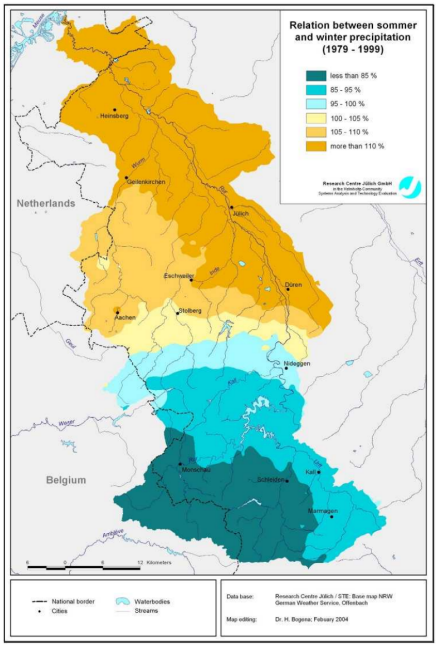

(b) Relation between summer and winter precipitation in the catchment of the Rur River (1979-1999).

Figure 3.2: Climatologial description of the Rur catchment. Obtained from Bogena, Pütz, et al. (2005).

3.1.1. TOPOGRAPHY AND GEOLOGY

The catchment can be divided into a steep and rocky highland area and broad, flat lowlands where industrial and urban areas are concentrated (Bogena, Pütz, et al., 2005). Figure 3.3 shows a Digital Elevation Model (DEM) of the Rur basin, where elevation differences highlight these two regions. The topographical characteristics of the region influence drainage patterns, with surface runoff occurring primarily through well-established river channels that have gradually carved their way through the mountains in the Eifel region (Kufeld et al., 2010).

A geological map of the Rur catchment (Appendix F.1) indicates a clear distinction between the lowland and highland areas (Bogena, Pütz, et al., 2005; Montzka, 2008; Kufeld et al., 2010). In the northern part of the catchment are deposits of unconsolidated sediments from the Quaternary period (2.58 million years ago to the present). Additionally, thick deposits of unconsolidated rock from the Tertiary period (2.58 - 66.0 million years ago) are covered mainly by terrace deposits and aeolian deposits from the Quaternary period. The southern part of the catchment contains much older geological formations from the Predevonian periods (up to 540 million years ago).

These variations result in significant differences in hydraulic conductivity, with a higher conductivity observed in the younger unconsolidated layers of the lowlands compared to the old consolidated layers of the highlands, visible in Figure 3.4a. Exceptions to this

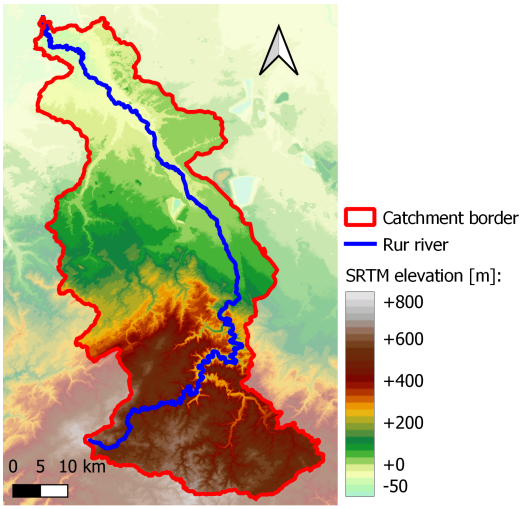

Figure 3.3: DEM of the Rur catchment. Map created using *QGIS* and data from NASA (2013).

pattern are carbonate rocks from the Middle to Upper Devonian near Stolberg and Marmagen, which contribute to higher groundwater storage volumes.

Furthermore, the upper layers of the soil also show variations between the high and lowlands, as described by Kufeld et al. (2010). In the northern part, the major soils are Cumulic Anthrosols near the drainage lines and Haplic Luvisols, both with silt loam textures. These soils are more productive, resulting in high field capacity. In contrast, the soil in the Eifel area consists mainly of Fluvisols, Gleysols (found along the Rur River and its tributaries), Eutric Cambisols, and Stagnic Gleysols, all characterised by a silt loam texture. Such soils have a lower field capacity, visible in Figure 3.4b.

3.1.2. RESERVOIR SYSTEM

The Rur basin contains an elaborate reservoir system consisting of nine reservoirs, of which six reservoirs are managed by Wasserverband Eifel-Rur (WVER) and three reservoirs by water supply companies. The six WVER reservoirs are included in this investigation, as they perform a function on flood safety and information and data from the reservoirs are publicly available (e.g. (Marth, 2021)). On the contrary, the other three reservoirs are only used for drinking water supply and are less described in the literature. From this chapter on, the term 'reservoir' will refer to one of the WVER reservoirs. The operation plan of the Rur reservoir system will be explained in the following paragraph. Additional information on the six reservoirs and the Rur reservoir system can be found in the appendix D.2.

Their operation rules describe the discharge behaviour of the reservoirs. The distinctive feature of the Rur reservoirs is that a volume section release plan (in German: 'Lamellenplan') is used for the discharge at Heimbach, described by the total volume of the Rur, Urft, and Olef reservoirs. This plan (Appendix E.1) can be divided into three regions:

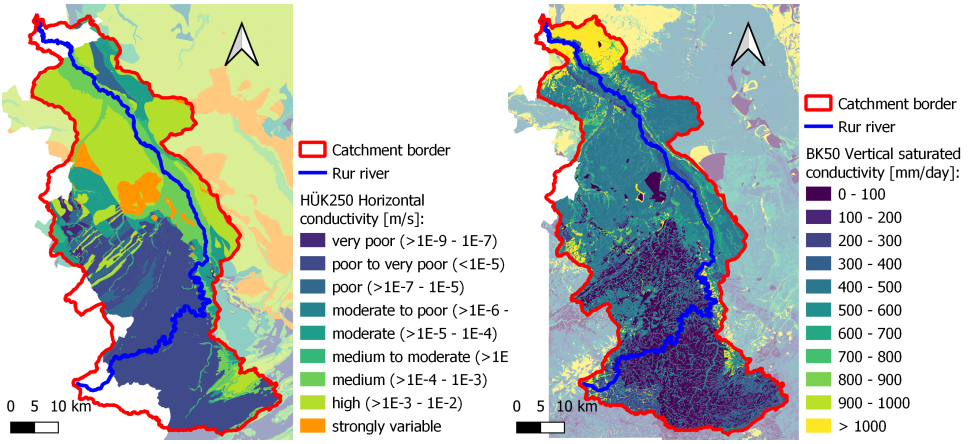

(a) Geohydrological horizontal conductivity of the Rur catchment. Map created using *QGIS* and data from Geodienst NRW (2023b).

(b) Vertical conductivity of the upper soil layer in the Rur catchment. Map created using *QGIS* and data from Geodienst NRW (2023a).

Figure 3.4: Maps describing soil conductivity in the Rur catchment.

1) the flood response that describes distinct discharges for volume levels with a maximum of 60 m^3/s, 2) the low-water response that relies on a minimum discharge of 5 m^3/s for industrial purposes, and 3) a dynamic discharge during normal flow situations (Kufeld, 2013). To account for the minimum flows during dry seasons, the volume of the reservoirs varies as they fill up to prepare for dry summers and drain for wet winters. This variation affects their flood retention capacity, which varies accordingly per season, with a minimum during summer (May - September) and a maximum during the winter months (December - January), ranging from 11.0 million $m^3$to 68.5 million $m^3$for all combined reservoirs. Importantly, the Rur-Urft-Olef reservoir system has been shown to be less robust against flood conditions than dry climate conditions during climate change studies (Demny et al., 2013).

3.1.3. LAND-USE AND LIGNITE MINING

Land use also varies significantly between the two regions, affecting the water balance and the response to precipitation. Industrial activities, such as lignite extraction, affect the level of groundwater and the recharge of soil layers. The withdrawal of groundwater from these activities affects the overall hydrological system of the basin (Bogena, Pütz, et al., 2005). Furthermore, variations in land use affect how runoff is routed to rivers and the infiltration capacity of the soil. Figure 3.5a shows how the upstream Rur basin is mainly covered by forests, while the lowlands contain agriculture, industry, mining and settlements.

As described in Section 2.5.1, mining activities affect the water balance in a catchment. Such effects are also present in the Rur basin, where lignite mines can be found (vom Kothen, 2005; Bogena, Pütz, et al., 2005; Bogena et al., 2018). Lignite mines are open pit mines that affect the catchment by reducing the groundwater table, landscape changes,

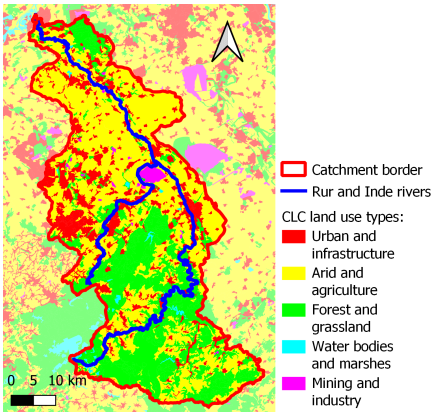

(a) CORINE Land Cover map of the Rur catchment, with the lignite mines visible in purple. Map created using *QGIS* and data from European Environment Agency (2019).

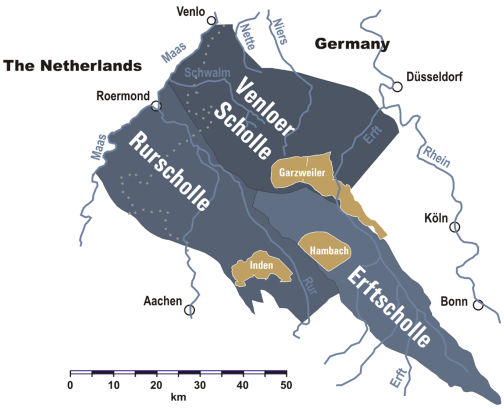

(b) The Rurscholle, Venloer Scholle and Erftscholle with the nearby lignite mines. Image from Becker (2011).

Figure 3.5: Maps describing land use in the Rur catchment and the locations of the lignite mines.

and the release of mining waters in nearby rivers (Dorgarten, 1988; Pusch & Hoffmann, 2000; Hangen-Brodersen et al., 2005; Panilas et al., 2008; Gädeke et al., 2014). Lipton seams are generally found 40 to 100 metres below the surface in Germany, with maximum depths of 350 metres (Grünewald, 2001; Becker et al., 2008, 2009). When mining activities have ended, restoration of the water balance may still take several decades (Pusch & Hoffmann, 2000).

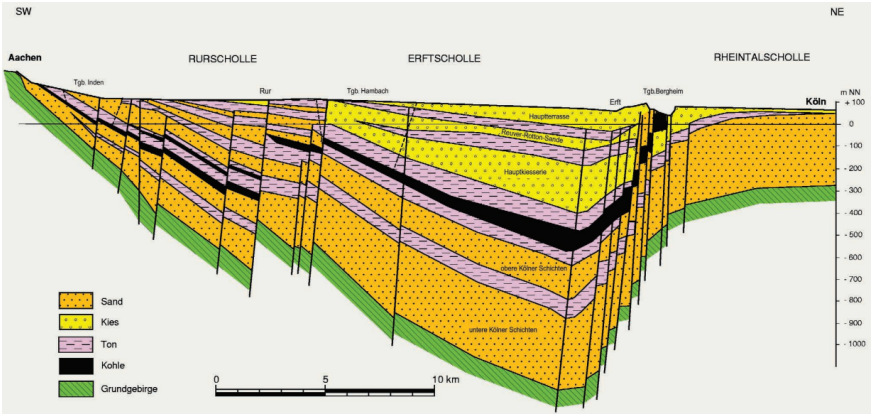

Figure 3.6: A view of deeper ground layers for the Rurscholle, Venloer Scholle and Elftscholle. Lignite (in German: Braunkohle) is located 200+ meters below the land surface. Image from vom Kothen (2005).

Mining activities in the heavily industrialised region of Nordrhein-Westfalen surround the Rur and Inde rivers, as shown in Figure 3.5a (Bogena, Kunkel, et al., 2005). Based on the geological characteristics of the region and the effects of open pit mining, this tec-

tonic region has been identified as the 'Rurscholle' area (vom Kothen, 2005; Becker, 2011) (shown in Figure 3.5b), with a similar name for the multiaquifer groundwater model of this region (Dorgarten, 1988). The Rurscholle is enclosed by fault lines and the Maas River, consisting of several layers of lignite with a permeable soil near the surface. As a result, the effects of groundwater pumping spread through the entire of Rurscholle. Consequently, this region is considered to be the region most affected by mining activities.

Several consequences of mining activities can be identified in the Rur catchment. For example, the Inde River was partially relocated in 2005 to create space for open pit lignite mining, and is affected by groundwater being pumped and released in the river near Lamersdorf and Kirchberg (on average 1.0 m^3/s and 0.5 m^3/s) (LANUV, 2001; Maaß et al., 2018). Furthermore, the Inde mine is reported to pump up more than 200 million m^3 per year, and the influence on the groundwater table is evident with local drops up to 100 metres below ground level (see Figure 3.6) (Bachmann et al., 2007). Other lignite mines, such as the Hambach mine, show similar low levels of the water table with a pumping volume of 310 million m^3 per year (RWE, 2015a, 2015b), which is released in the Erft River next to the rur (Tu, 2006). Although these mines are located outside of Rurscholle, groundwater interchange between neighbouring regions occurs through the permeable upper aquifer (Becker et al., 2008) and is therefore important.

3.2. METEOROLOGICAL DESCRIPTION OF THE 2021 FLOOD EVENT

The intensity and duration of the three-day precipitation were one of the causes of the severity of the flood event in July 2021. Therefore, it is necessary to understand the meteorological conditions that led to this event and investigate the extreme of the precipitation.

The heavy precipitation occurred mainly due to a slowly moving low pressure system named 'Bernd', shown in Figure 3.7. It travelled from France towards Germany and supplied moist air to this region. At the same time, warm and humid air masses travelled from the Mediterranean towards central Europe, rotating around the low-pressure system and feeding it with moist air, especially from the Baltics. Then, the pressure system was lifted with force, partly as a result of underlying orography, and heavy, almost stationary rain began, first locally and then over larger areas (Junghänel et al., 2021; CEDIM Forensic Disaster Analysis (FDA) Group et al., 2021; NEW, 2021; Kreienkamp et al., 2021; Dietze et al., 2022).

As a result, a severe and long-duration precipitation event occurred, breaking several local measurement records. The 24-hour and 48-hour sums of the precipitation event are shown in Figure 3.8.

3.2.1. ESTIMATED RETURN PERIODS

Rain gauge stations in Limburg and Germany provide insight into the extreme magnitude of the rainfall event and the differences between locations. For the 24-hour sums at the gauge stations (Figure 3.9), the results do not pass return periods of 100 years. The mean 48-hour precipitation for South Limburg still indicates a return period of T

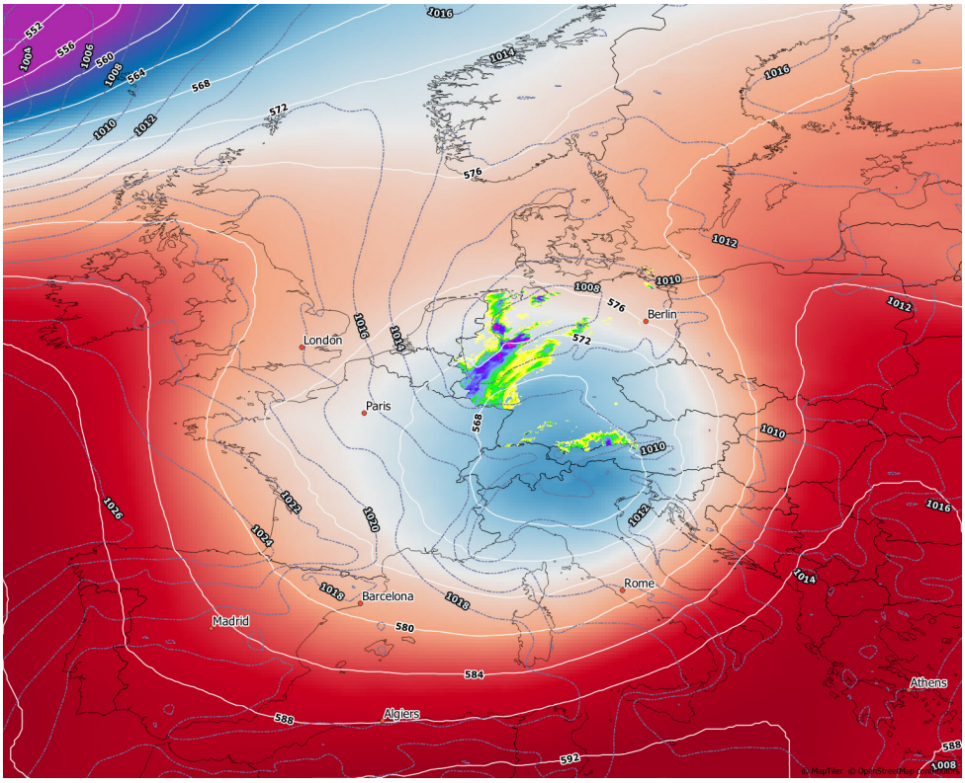

Figure 3.7: The low-pressure system “Bernd”. Color shading indicates the 500-hPa geopotential lines from the 14th of July, 2021, 12UTC. Additionally, the location of the highest precipitation intensities is shown according to RADOLAN (DWD). Obtained from CEDIM Forensic Disaster Analysis (FDA) Group et al. (2021).

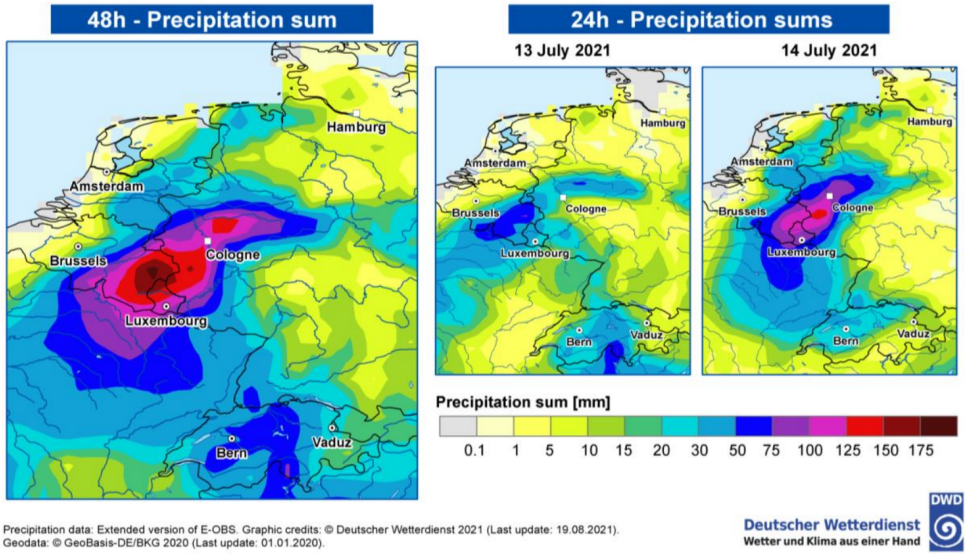

Figure 3.8: Accumulated precipitation over two days (13 - 15 July) and accumulated over 24 hours for each day of the extreme precipitation event. Obtained from Kreienkamp et al. (2021).

25 years. However, individual stations south of Limburg show much longer return periods for the observed precipitation for 48 hours (Figure 3.10). Comparing station observations with the STOWA statistical product (STOWA, 2019) indicates return periods of the order T 100 – 1000 years for several stations, as shown in Figure 3.11. However, it should be noted that local measurements exceeded historical extremes and therefore may be outside the range of the applied statistical models (NEW, 2021; Kreienkamp et al., 2021).

Higher precipitation measurements were observed for gauge stations in the German part of the Rur catchment with similar estimated 100-1000-year return periods (Schüttrumpf, 2022; Homann, 2021b; Junghänel et al., 2021; NEW, 2021). Figure 3.11 indicates the order of magnitude of the event, showing the maximum precipitation measured in the Ubachsberg (South Limburg) and Roetgen (German Rur catchment) and the mean of the gauge measurements in these areas compared to the statistical product of STOWA (STOWA, 2018, 2019). Similarly, an analysis of precipitation in Belgium measurement stations indicates an extreme long duration of high intensity rainfall, greatly exceeding the quantity-duration-frequency curve of 200 years for stations in the Vesdre catchment, located next to the Rur watershed (Dewals et al., 2021).

These observations underline the extreme of the rainfall event that led to the 2021 floods, and observations at gauge stations confirm these high return periods. Inflow from the Urft and Olef rivers was especially extreme, with water levels exceeding the 1.000-year return period threshold and an estimated discharge of $Q > 500$ m^3/s at Gemünd, which corresponds to an estimated return period of over 10.000 years (Homann, 2021b). Preliminary return periods for the lower Rur and Inde and Wurm tributaries are lower but

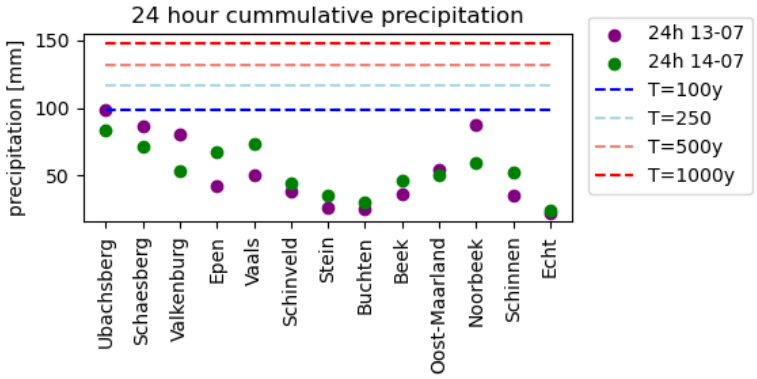

Figure 3.9: Accumulated precipitation accumulated over 24 hours each day for Dutch gauge stations in South Limburg. A comparison is made with the STOWA statistics product (STOWA, 2018, 2019).

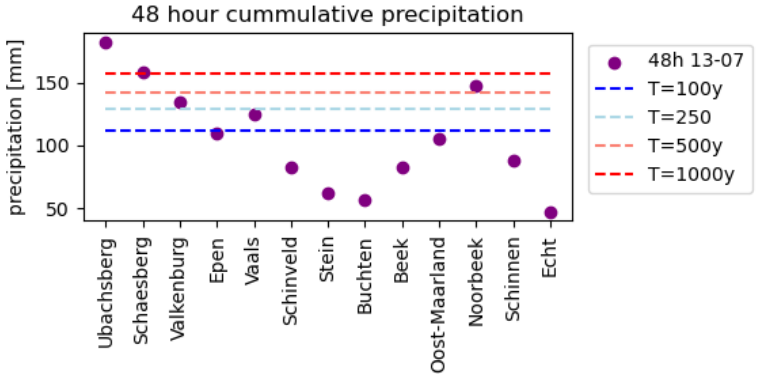

Figure 3.10: Accumulated precipitation accumulated over 48 hours each day for Dutch gauge stations in South Limburg. A comparison is made with the STOWA statistics product (STOWA, 2018, 2019).

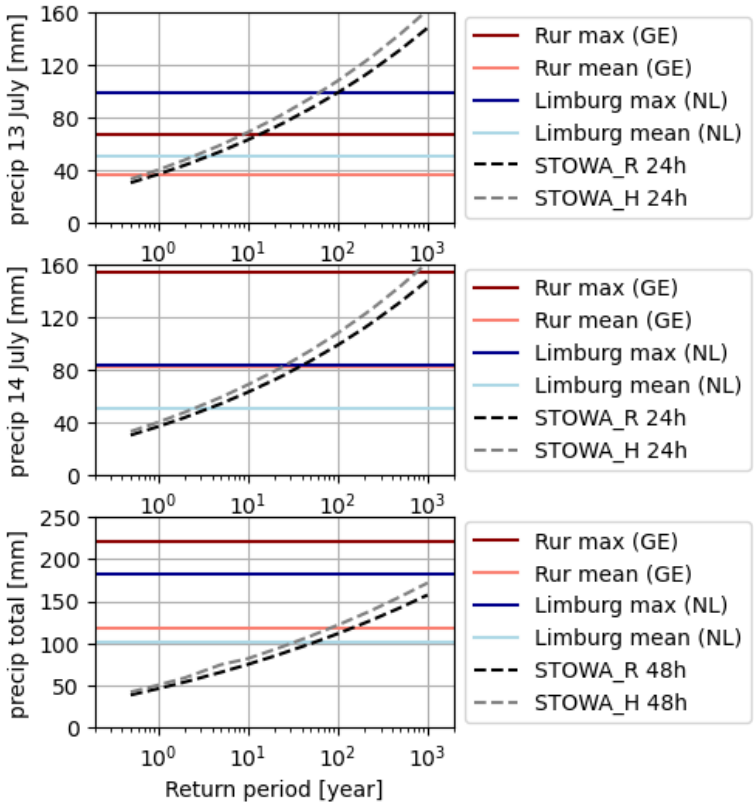

Figure 3.11: Accumulated precipitation over two days (13 - 15 July) and accumulated over 24 hours for each of the individual days for Dutch and German gauge stations. A comparison is made with the STOWA statistics product (STOWA, 2018, 2019).

still exceed the 100-year threshold value. Again, similar observations are made for the Vesdre catchment located next to the Rur watershed where the 100-year threshold value was exceeded multiple times (Dewals et al., 2021). Therefore, it is necessary that the precipitation products applied in this thesis reflect both the extremity of the event and the spatial distribution that varies across the Rur catchment.

4

METHODOLOGY

THIS chapter describes the methods that support the investigation of determining factors for a flood forecasting model for the Rur basin. Two models are used: the hydrological *Wflow_SBM* model and the hydrodynamic *ProMaIDes* model. Therefore, background information is given on both models and details on how the Rur catchment is discretised in both models. In sections 4.3 and 4.4, the most important datasets used in this thesis are described and the equations used to assess the validation of the models. Special attention is paid to the precipitation datasets used to create the hindcast and the forecasts. After these sections, the qualitative and quantitative approaches to the investigation are described in section 4.5; these approaches describe how the models and the data are used to generate the results presented in chapters 5 and 6, respectively.

4.1. HYDROLOGIC MODELLING

A hydrological model is needed to simulate how precipitation can result in flooding of the Rur River. The typical length scale of the Rur catchment is on the order of 100 km, and the time scale of extreme precipitation events is on the order of days, which means that all processes mentioned in Section 2.1 should be taken into account except groundwater modelling. Taking into account these processes, it is possible to use *Wflow_SBM* to model them, as will be explained later in this section. First, the *Wflow_SBM* model will be briefly described, followed by highlights of processes specifically relevant for modelling floods in the Rur catchment.

4.1.1. THE *Wflow_SBM* SOFTWARE PACKAGE

Wflow_SBM (W. J. Van Verseveld et al., 2022) is a specific type of hydrological model within the Wflow.jl framework (W. Van Verseveld et al., 2022), which in itself is a continuation of the wflow framework (Schellekens et al., 2020). The *Wflow_SBM* model distinguishes vertical processes, describing interactions between the saturated zone, the unsaturated zone, and the land for a grid cell, and lateral processes, describing how the

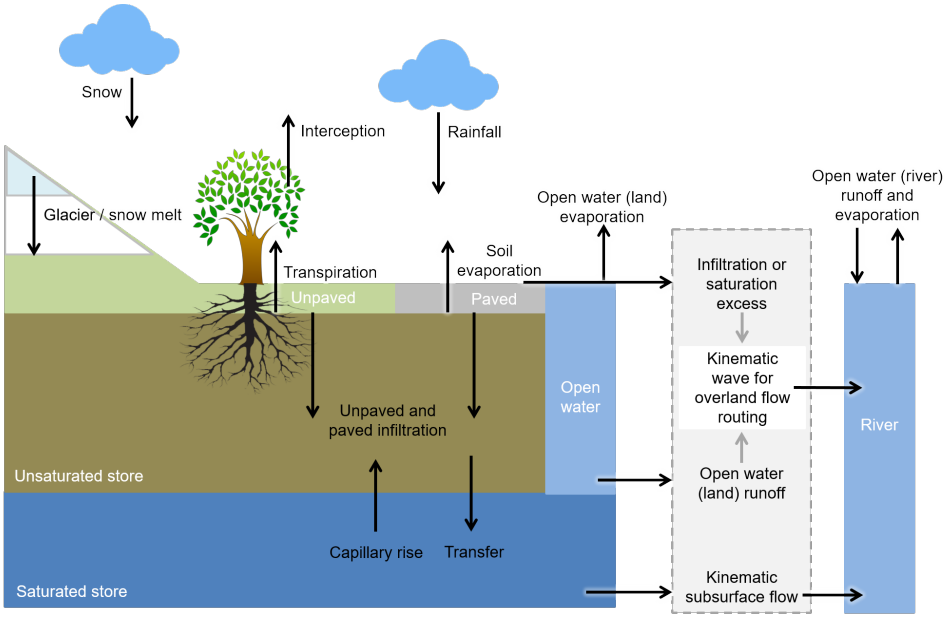

Figure 4.1: Schematization of the lateral and vertical processes inside *Wflow_SBM*. (Deltares, 2022)

river, overland, and subsurface flows are routed. The vertical concepts are based mainly on Topog-SBM (Vertessy & Elsenbeer, 1999), where the soil is split into a saturated and unsaturated zone, and consider the following types of processes (also illustrated in Figure 4.1):

- Precipitation
- Rainfall interception
- Evaporation
- Snow and glacier modelling
- Infiltration
- Capillary rise

Furthermore, *Wflow_SBM* considers the following lateral processes:

- Overland flow
- River flow
- Subsurface flow
- Reservoirs and lakes

The vertical and lateral processes describe the processes within the *Wflow_SBM* model. It should be noted that typical hydrodynamic processes, such as river and overland flow, are also included in the distributed *Wflow_SBM* model. However, it will still be referred to as a hydrological model for practical reasons.

Several processes relevant to flood forecasting were mentioned in the previous chapters, namely overland and river flow, subsurface flow, and reservoir management. Therefore,

the implementation of these processes in *Wflow_SBM* will be elaborated on in the following sections.

OVERLAND AND RIVER FLOW

The *Wflow_SBM* hydrological model differentiates between two approaches for routing surface waters: the kinematic wave approach and the local inertial method (see also 2.3). These can be used in several combinations, as summarised in Table 4.1. When the local innertial method for river flow and the kinematic wave approach for overland flow are combined, then a quasi-two-dimensional approach can be used to model inundation. A sub-grid method is used to derive flow velocities and adjust the water depths in the floodplains to account for storage in the floodplains. This 1-dimensional floodplain flow still occurs in the direction of the river in the river cell and in the resolution of the model, but the updated depth of the water is used in the momentum equation, which accounts for the effects of floodplain flow. An alternative is to use the local inertial approach for both overland and river flow, which results in a coupled 1D2D model using the diffusive wave equation in both models.

Land routing	River routing	Fluvial flooding	Peak attenuation
KW	KW	✗	✗
KW	LI	Quasi-2D	✓
LI	LI	2D	✓
LI	KW	— *combination not possible* —	

Table 4.1: Options for overland and river routing in *Wflow_SBM*.

SUBSURFACE FLOW

Wflow_SBM does not model groundwater flow based on concepts such as hydraulic heads and (un)confined aquifers. Instead, it models only part of the subsurface, differentiating between a saturated and an unsaturated zone. As a result, no flow from or to deeper groundwater layers is included in the model. It is possible to include a leakage term for the saturated zone, resulting in water being removed from the model. The amount of leakage is limited by `MaxLeakage` parameter and by the total water content of the saturated zone of the subsoil.

The subsurface flow, described by 4.1, depends on the element slope angle β, and is modelled using the kinematic wave equation per unit width of the slope w. The purpose of showing this equation is to emphasise that *Wflow_SBM* is not a groundwater model and that the subsurface flow is governed by topography. In this equation, q denotes the magnitude of the subsurface flow, w the width and c the wave celerity, which depends on the saturated vertical conductivity on the surface (K_0), the depth of the water table (z_i), the saturated soil water content (θ_s and residual (θ_r) soil water contents, and a scaling parameter (f).

$$w\frac{\partial q}{\partial t} = cw\frac{\partial q}{\partial x} + cwr \text{ with } c = \frac{K_0 \tan(\beta)}{(\theta_s - \theta_r)} e^{-fz_i} \tag{4.1}$$

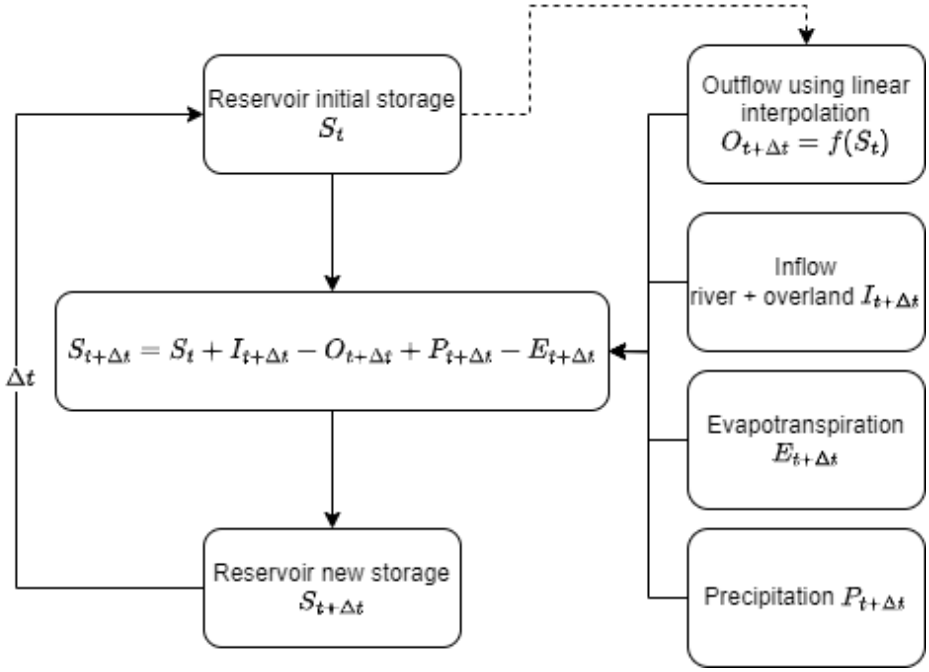

Figure 4.2: A schematization of the volume-based operation rules for the reservoirs applied in *Wflow_SBM*.

The horizontal conductivity K_0 is based on the product between the saturated vertical hydraulic conductivity and the parameter `KsatHorFrac`. The *Wflow_SBM* hydrological model is sensitive to its variations, and it has been shown that the `KastHorFrac` depends on model resolution, as the slope distribution of a catchment changes as the spatial resolution changes, thus requiring a change in `KsatHorFrac` (Aerts et al., 2022).

RESERVOIR OPERATIONS

Reservoirs can be modelled in *Wflow_SBM* using a volume-based approach, where the reservoir outflow depends on the storage and the day of the year [1]. The algorithm applied in *Wflow_SBM* is shown in Figure 4.2 and describes how reservoir storage S varies due to inflow, outflow, precipitation, and evaporation. Alternatively, it is possible to model reservoirs in *Wflow_SBM* using a target storage-and-release-based operation method, see for example Wannasin, Brauer, Uijlenhoet, van Verseveld, and Weerts (2021). However, this method is not used in this thesis.

The volume-based implementation of reservoir modelling has some limitations compared to reality, as the *Wflow_SBM* hydrological model cannot account for 1) a linked reservoir system and 2) free operation rooms. Therefore, some simplifications are re-

[1] The author used a custom version of *Wflow_SBM* v0.6.3 for running the models. Adjustments made to these customisations have been implemented in wflow as a result of this thesis; see also PR#250 on https://github.com/Deltares/*Wflow_SBM*.jl (W. Van Verseveld et al., 2022)

quired to address these limitations when modelling such reservoirs in *Wflow_SBM*. Furthermore, sufficient information on the operation rules should be available in order to implement reservoir modelling in *Wflow_SBM*. As a result, the smaller Obermaubach and Heimbach reservoirs are not included in the *Wflow_SBM* model due to the lack of clearly defined operation rules and their limited size. More information on the implementation of the Wehebach, Olef, Urft and Rur reservoirs can be found in appendix B.1.

4.1.2. SETTING UP A *Wflow_SBM* MODEL

A *Wflow_SBM* model can be created using Hydro Model Tools (HydroMT), a model builder for *Wflow_SBM* developed by Eilander et al. (2023a, 2023b). It contains several global datasets that make model-building efficient. Furthermore, (Pedo) Transfer Functions (PTF) are used to generate parameter maps based on point measurements (R. O. Imhoff et al., 2020). All parameter maps are contained in a single netcdf file called the static maps, and model forcing is provided by a separate netcdf file. Static maps and forcing files can be visualised and manipulated using *Python* using libraries such as *Xarray* and *HydroMT*, or by software packages such as *QGIS*. Output variables (e.g. discharge) can be saved as points in csv format, but also in a gridded form in netcdf format.

4.1.3. *Wflow_SBM* MODEL OF THE RUR CATCHMENT AND CALIBRATION

Appendix A contains detailed information on the sources used to generate these parameter maps and the *HydroMT* configuration settings. This setup can be summarised as follows:

- The model is built in the EPSG:4326 coordinate system at a spatial resolution of 0.00833 degrees, which translates to grid sizes of approximately 1000 meters by 550 meters.
- The hydrologically conditioned MERIT-Hydro dataset (Yamazaki et al., 2019) is used for the DEM and the flow direction maps.
- The river map is derived using an Upstream Area (UPA) threshold of 5 km^2.
- The reservoir system is simplified and applied included in the model.
- The BK50 map (Geodienst NRW, 2023a) is used to describe the vertical conductivity of the catchment, and the horizontal conductivity is derived by calibrating the `ksathorfrac` parameter. No clear PTF exists yet for this parameter, so it is often considered an important calibration parameter of the *Wflow_SBM* model (Aerts et al., 2022).
- A leakage factor `maxleakage` is applied and calibrated to account for the effects of lignite mining on catchment hydrology.
- Profiles from the *ProMaIDes* hydrodynamic model are used to derive the bankful depth and width for the Rur river to improve floodplain flow simulations.

As described above, several steps were taken to calibrate the model. These steps are

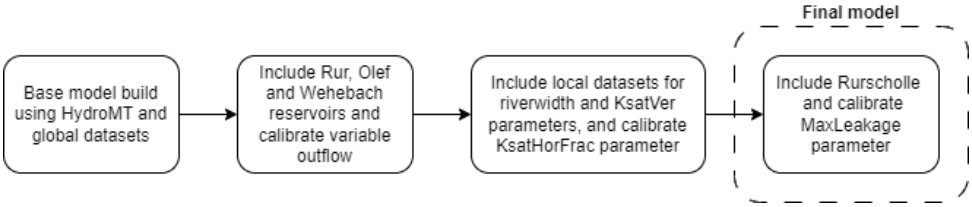

Figure 4.3: Summary of the calibration process of the *Wflow_SBM* model of the Rur.

summarised in Figure 4.3, and a detailed description of model calibration can be found in Appendix B.

4.2. HYDRODYNAMIC MODELLING

The *Wflow_SBM* model described in the previous section is able to model the floodplain inundation and surrounding lands to some extent. However, it is also possible to use the *Wflow_SBM* model to generate boundary conditions for a separate hydrodynamic model. The latter has been performed in this thesis using the hydrodynamic module of the *ProMaIDes*-model, which will be described in this section.

4.2.1. THE *ProMaIDes* SOFTWARE PACKAGE

Protection Measures against Inundation Decision Support (ProMaIDes) is a modular software package designed for flood risk analysis (Bachmann, 2012; Ghomash et al., 2022). It consists mainly of four modules, each describing a facet of flood risk management.

- HYD-module: hydrodynamic module used for the hydraulic analysis of the river system;
- FPL-module: reliability analysis used to quantify the failure probability of flood protection measures along a river;
- DAM-module: damage module used to transform the given hydraulic values of a flood event into consequences for people assets and infrastructure;
- RISK-module: module used for integrating the flood risk analysis.

Only the HYD module is used in this investigation, resulting in a regular forecasting system. However, the *ProMaIDes* software package supports the other modules, which extends the regular forecasting model to an IBF model, as defined in 2.2.4. The HYD module of *ProMaIDes* can be used with two types of discretization, namely, as a one-dimensional model or as a coupled 1D2D model.

4.2.2. SETTING UP A HYDRODYNAMIC *ProMaIDes* MODEL

One-dimensional river models form the basis for the hydrodynamic model in *ProMaIDes*. A *ProMaIDes* model should contain at least one river model, but it is possible to create a network of river models by describing multiple one-dimensional river models. A river

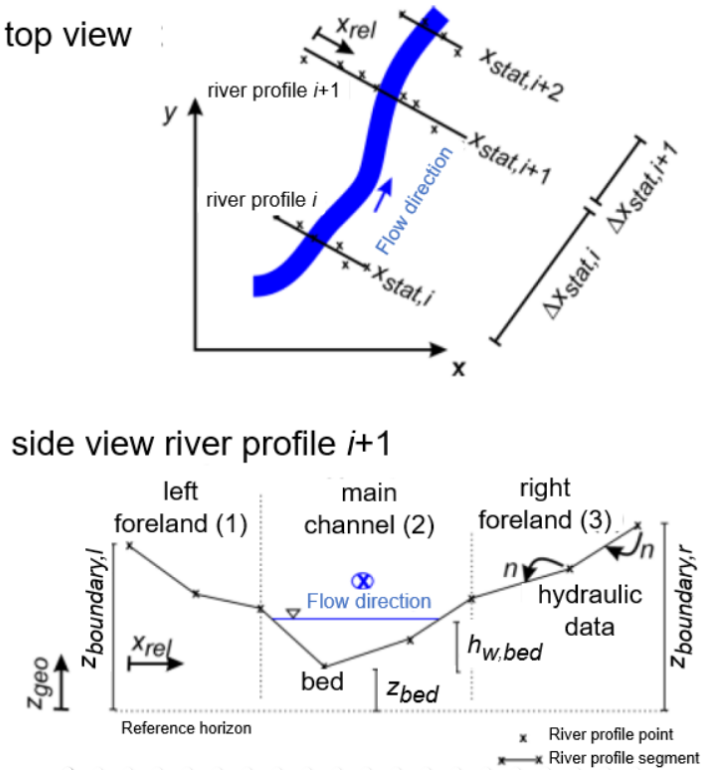

Figure 4.4: Discretization of a one-dimensional *ProMaIDes* river model, showing the placement of cross-sections and separation between left foreland, right foreland and the main channel. Global x and y coordinates are used to define the locations of the river cross-sections. Obtained from HS Magdeburg (2022).

model consists of discretised cross-sectional profiles within the main flow direction. A cross-section is defined as a collection of points in a two-dimensional space (global x and y coordinates, as shown in Figure 4.4), where for each point its geodetic height is described (z-coordinate). In addition, information is provided describing the material property of the point, its flow section (main channel, left foreland, or right foreland), and its local distance on the profile axis to the previous point.

The diffusive wave equation is used to describe the hydrodynamic flow between the river profiles. Additionally, profiles can be assigned to be modelled as weirs and bridges, resulting in additional flow equations being used in the hydrodynamic calculations depending on the local water depth: free and submerged flow for the weirs, and flow open channel flow, pressure flow, and weir overflow for the bridges.

The one-dimensional river model(s) can be extended by including one or more two-dimensional floodplains. These are discretised as rectilinear rasters placed inside the model by defining the sizes of the grid cell and the orientation of the grid (as shown in Figure 4.5). Floodplain flow is solved using the two-dimensional continuity and diffusive

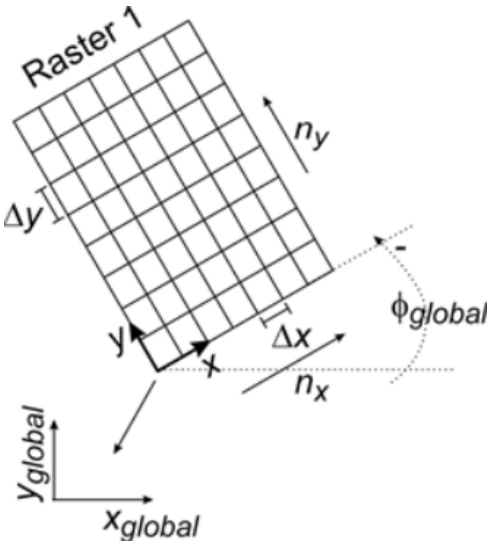

Figure 4.5: Discretization of a one-dimensional *ProMaIDes* floodplain model, consisting of n_x by n_y elements with size Δx and Δy and orientation ϕ. Obtained from HS Magdeburg (2022).

wave equations and can occur when overflow occurs on either side of a river profile. Additionally, dikes can be included in the floodplains, modelled as one-dimensional lines in the two-dimensional floodplain, for which weir overflow can occur, and it is possible to assign 'no flow' elements in which no flow can occur.

Several options exist to link the one-dimensional river models and two-dimensional floodplain models. River models can be coupled to each other through direct inflow, lateral inflow, or by defining a structure coupling the two rivers, such as a weir or gate. Similarly, floodplain models are coupled by overlapping their grids, for which flows are exchanged via the boundary. More important is the coupling between river and floodplain models, which forms the basis for the 1D2D approach used by *ProMaIDes*. The overlap between the floodplain and the river is derived to determine the coupling boundary (as illustrated in Figure 4.6), and the overflow from the river profiles to the floodplain grid is modelled using weir flow equations.

4.2.3. *ProMaIDes* MODEL OF THE RUR RIVER

The basis for the Rur model used in this thesis was provided by Bachmann (2021). It consists of two river models: a model for the Rur, stretching from the dam at Obermaubach to the Meuse near Roermond, and the Hambeek, which is a bifurcation of the Rur in Roermond, connected via a passive weir. The Rur River comprises 763 profiles, including 38 bridges and 37 weirs, and the Hambeek River only has 34 river profiles. An overview of the model is shown in Figure 4.7. Bridges and weirs are distributed along the entire Rur river, and the number of profiles increases as the Rur enters the city of Roermond. Furthermore, the model contains five floodplain grids, each with a ten-by-ten-metre resolution. The elevation of the points of the grid is derived from two DEMs, one for the

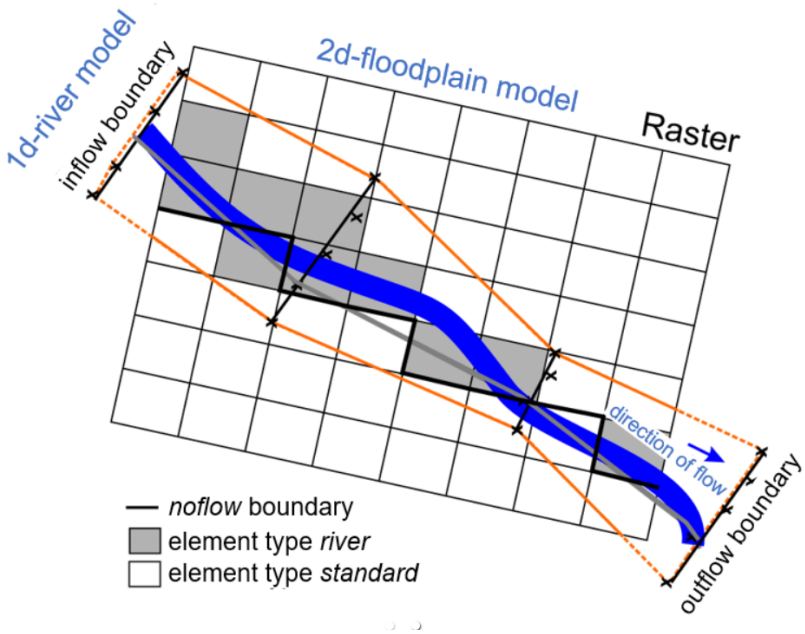

Figure 4.6: Example of a coupled 1D2D *ProMaIDes* model. Obtained from HS Magdeburg (2022).

Netherlands and one for Germany, and constant roughness is assumed for all floodplain cells.

Some features of the Rur model are worth highlighting. First, there are differences between the German and Dutch parts of the Rur. In addition to having to use separate DEM data when generating the floodplains, it is visible that dikes are only included in the German part of the model, and river cross-sections are typically wider in Germany, containing part of the floodplains or even the complete floodplain. Furthermore, no gauge stations in the Dutch Rur were considered in this investigation, and several no-flow elements were used in the floodplain where inundation is expected to reduce computation times.

4.2.4. MODEL ADJUSTMENTS AND BOUNDARY CONDITIONS

Some adjustments were made to the original *ProMaIDes* model. An overview can be found in the Appendix C, but a general description of these adjustments will be given in the following paragraphs.

Firstly, a second *ProMaIDes* model of the Rur has been derived that differs from the model described above. The diversion between the Rur river and the Hambeek is valid during regular flow conditions, but loses validity during periods of high flow. When the water level in Roermond exceeds 19 m + Nieuw Amsterdams Peil (NAP), two flood defence gates are closed to protect the centre of Roermond. As a result, part of the Rur is closed off, and the flow fully concentrates in the Hambeek. Therefore, the two river

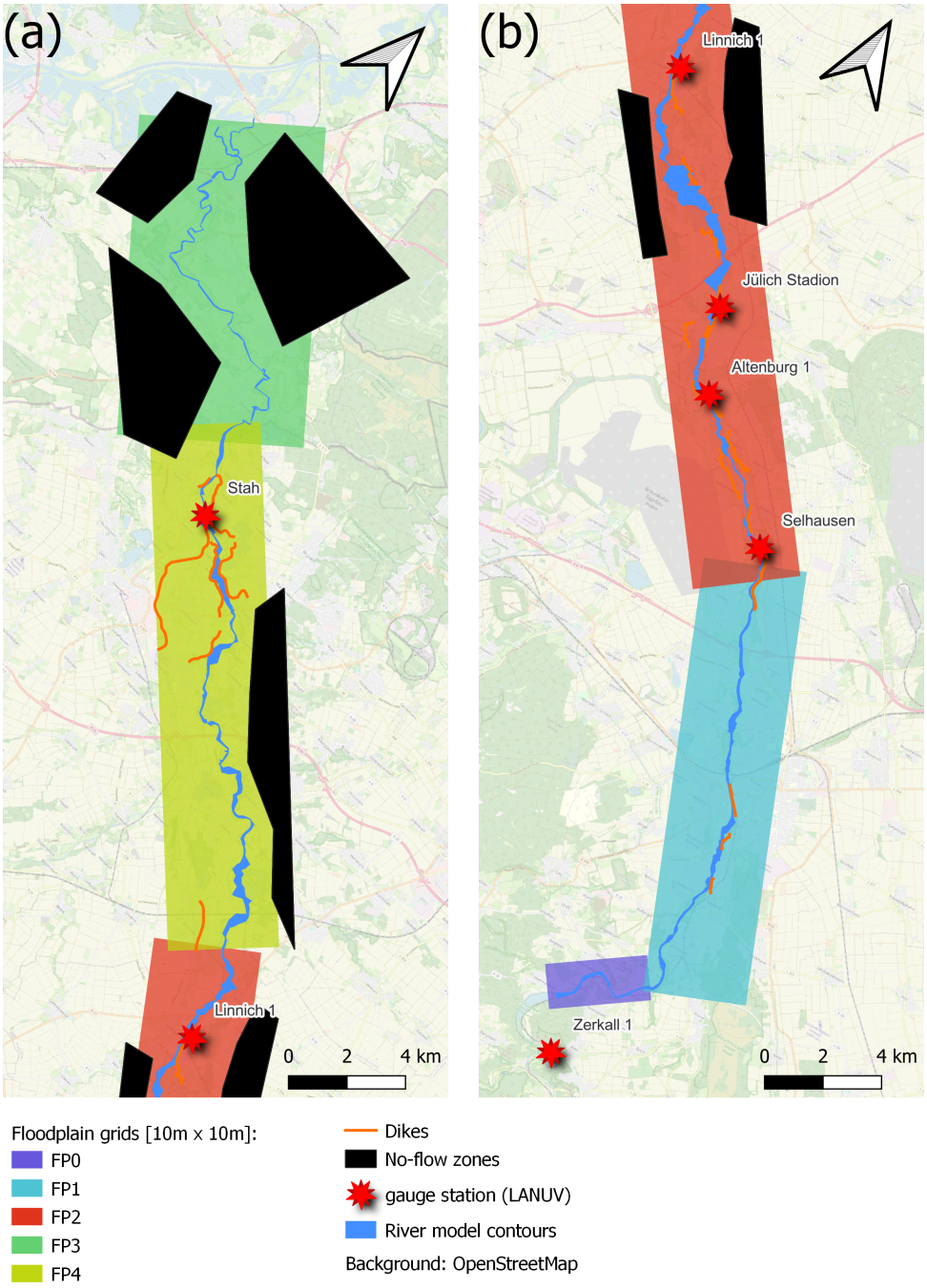

Figure 4.7: Original *ProMaIDes* model of the Rur. It contains two one-dimensional river models and five two-dimensional floodplain grids with ten-by-ten metre resolution. No-flow zones are incorporated to improve computational efficiency, and dikes are included for the German part of the Rur model.

models of Bachmann (2021) are merged into one river model by removing the Rur profiles after bifurcation and adding the Hambeek profiles to the Rur river profiles. More information on this adjustment can be found in Appendix C.

The Rur River model begins at the Obermaubach dam, forming the upstream boundary condition. To this end, the discharge at this point is derived using a hydrological *Wflow_SBM* model. The Obermaubach dam can regulate outflow and is therefore in practise a reservoir. However, the choice was made to simplify the hydrological model by only considering the three largest reservoirs in the catchment (see also Appendix D.2.2). As a result, the flow regulation at the Obermaubach dam is not included in these simulations and the flow of the *ProMaIDes* model will mainly be governed by the outflow of the Rur reservoir upstream of Obermaubach.

The downstream boundary condition is given by the water level of the Meuse River. This is necessary because *ProMaIDes* uses the diffusive wave approach, and the flow in the river is assumed to be subcritical. Therefore, excluding the downstream boundary condition would result in an ill-posed problem. The situation would have been different if a kinematic wave approach had been used. The water level measurements in Roermond Boven were provided by RWS and used to calculate the depth of the downstream water (Rijkswaterstaat, 2022). An additional check was performed by comparing the *ProMaIDes* river profiles at these locations with profiles from a *D-HYDRO* model of the Rur used by Deltares and HKV, which confirmed that their position relative to the Meuse was indeed correct.

In addition, tributaries are included in the model and discretised as point inflows in selected river profiles. These inflows are also computed using a *Wflow_SBM* model. To this end, the *Wflow_SBM* river map is compared with a detailed GSK3E river map of the catchment provided by Landesamt für Natur Umwelt und Verbraucherschutz (LANUV), which enabled the identification of tributaries flowing into the Rur River. The river map generated by *Wflow_SBM* differs from the observed river network for three reasons: 1) it is generated based on a hydrologically conditioned DEM, 2) the *Wflow_SBM* model is limited to $\mathcal{O}$ (1km) resolution, and 3) *Wflow_SBM* does not support bifurcations. In total, 17 tributaries are identified and included as a lateral inflow in the *ProMaIDes* model, as listed in table C.1 in appendix C.3.

4.3. DATASETS

Data sources are used in this thesis to calibrate the hydrological and hydrodynamic models, but also to improve understanding of the response of the Rur catchment during a flood event. This section describes the datasets and how they were acquired.

4.3.1. CALIBRATION: E-OBS

Before the *Wflow_SBM* model of the Rur can be used to create the hindcast and forecasts, it should be calibrated. To this end, a precipitation dataset is required that covers several years. Therefore, several precipitation datasets were considered as listed in Table 4.2.

Dataset	Δx	Δt	Data origin	Coverage
ERA5	~31 km	1 h	Satellite	Global
E-OBS (25.0e)	~10 km	24 h	Gauge stations	Europe, Northern Africa
NL-RDR-DATA-PCP (KNMI-RAD)	~1 km	5 min.	Radar, gauge station	Netherlands
RADOLAN (DWD)	~1 km	5 min.	Radar, gauge stations	Germany

Table 4.2: Overview of the precipitation datasets considered for calibrating the hydrologic model. E-OBS was selected as the most suitable precipitation product to calibrate *Wflow_SBM*.

Different precipitation datasets were considered for model calibration: ERA5 (Hersbach et al., 2020), RADOLAN (Winterrath et al., 2011), KNMI-RAD (KNMI, 2023) and E-OBS (Cornes et al., 2018). Table 4.2 summarises the main differences between the datasets. The ERA5 dataset, released by ECMWF, gives hourly estimates of many atmospheric, land, and oceanic climate variables such as precipitation, temperature, and evapotranspiration and is produced using data assimilation and forecasts by the ECMWF Integrated Forecast System. Thus, it relies both on historical data and modelled forecasts. The E-OBS dataset is different as it is based solely on daily observation data from the stations. It uses interpolation and correction methods to process daily data and estimates uncertainties through 100-member ensembles for each day. Finally, local KNMI and DWD datasets were considered, combining reanalyzed radar measurements with corrections derived from daily gauge station measurements.

The precipitation datasets show that a trade-off can be made between temporal resolution, spatial resolution, and availability. The KNMI dataset did not have sufficient spatial coverage and was thus quickly disregarded. Although the ERA5 dataset seemed to generate well-performing results, the resolution was considered too coarse to confidently model, as one pixel of precipitation data could cover entire or multiple basins, similarly to the study by Klein (2022). Such a coarse resolution may be sufficient when only the discharge at the catchment outlet is considered relevant (e.g. at Stah). However, it is not suitable for modelling interactions between Rur and tributaries such as Inde, Wurm, and Urft and for estimating reservoir inflows. Finally, the RADOLAN dataset seemed to underestimate precipitation volumes in the mountainous Eifel area despite being corrected for by local measurements. This resulted in the E-OBS dataset being the selected precipitation dataset.

4.3.2. HINDCAST: RADFLOOD21

Radar measurements of the flood event severely underestimated precipitation volumes (R. Imhoff et al., 2021; Kreienkamp et al., 2021; Overeem & Leijnse, 2021; Goudenhoofdt et al., 2023). This underestimate was problematic during the flood event and analysis afterwards, as the forecasts depend on accurate forcing data. Therefore, meteorological agencies such as the Dutch KNMI and the Belgium Royal Meteorological Institute

of Belgium (RMI) corrected radar measurements of the flood event, resulting in a more accurate and usable precipitation product. This thesis uses the RADFLOOD21 dataset (Goudenhoofdt et al., 2023), as its coverage is more suitable for use with the location of the Rur catchment.

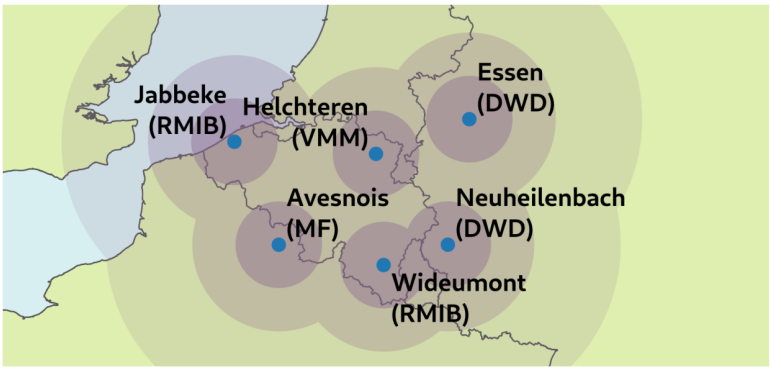

Figure 4.8: Radars used to create the RADFLOOD21 dataset, which provide complete coverage of the Rur catchment. Obtained from Goudenhoofdt et al. (2023)

The creation of the dataset involved several steps to improve precipitation volumes and spatial patterns. The following paragraph is a concise description of the dataset given by Goudenhoofdt et al. (2023). In summary, rain gauge measurements from multiple networks were utilised, with a 5-minute resolution and additional quality control measures. Weather radar measurements were obtained from the following radars (depicted in Figure 4.8):

- Helchteren, Vlaamse Milieumaatschappij (VMM), Belgium
- Jabbeke, Royal Meteorological Institute of Belgium (RMIB), Belgium
- Wideumont, Royal Meteorological Institute of Belgium (RMIB), Belgium
- Neuheilenbach, Deutsche Wetterdienst (DWD), Germany
- Essen, Deutsche Wetterdienst (DWD), Germany
- Avesnois, MeteoFrance (MF), France

Quality control measures were implemented to address errors and uncertainties in the radar data. Convective and non-convective precipitation was identified to estimate ground rainfall rates, and missing data were filled using interpolation techniques. The dataset underwent compositing, accumulation, and radar-gauge merging processes to combine rain rates and incorporate rain gauge measurements.

The resulting RADFLOOD21 dataset offers a spatial resolution of 1 km, covering the entire Rur basin. It provides rainfall accumulations at 5-minute and hourly intervals, which has been transformed into an hourly precipitation product to be used in this thesis. Figure 4.9 shows the precipitation of the RADFLOOD21 dataset over several time intervals.

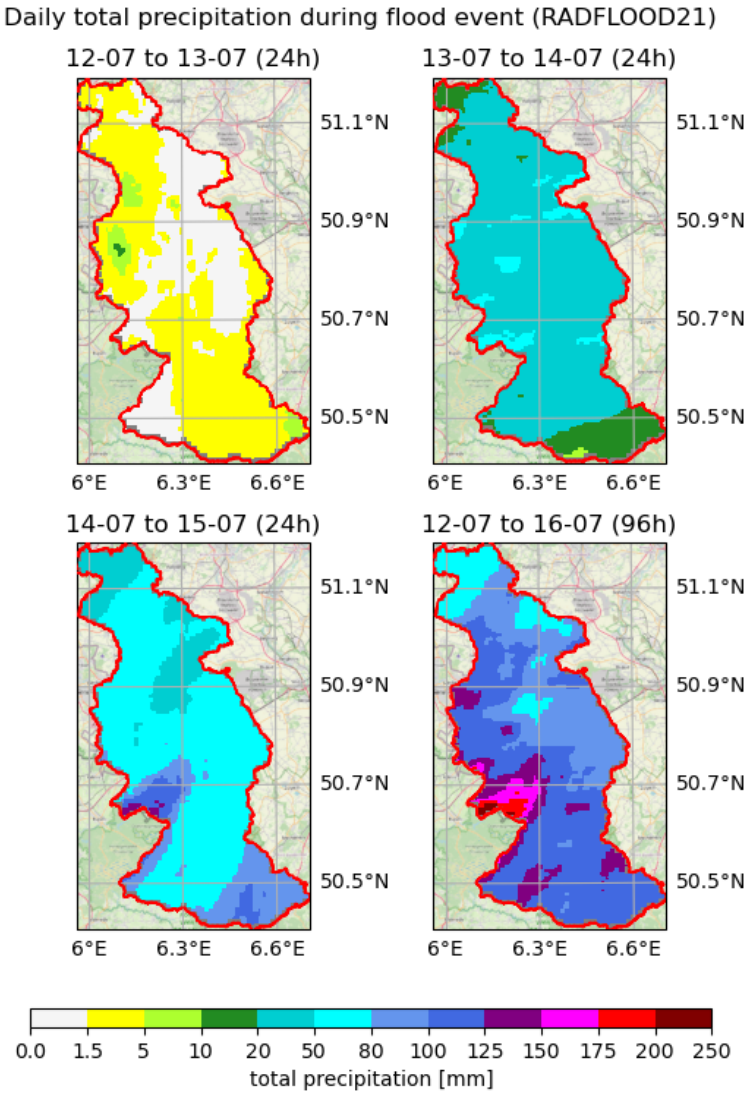

Figure 4.9: RADFLOOD21 precipitation dataset for several time intervals. Heavy precipitation concentrated in the South-West of the Rur catchment during the 2021 flood event.

4.3.3. FORECASTS: ICON-EU-EPS DATASET

There are several numerical weather prediction models for Europe, such as LIST. In this research, the ICOsahedral Non-hydrostratic Model (ICON) developed by the DWD is used (Reinert et al., 2023). The global ICON model has a horizontal resolution of 13.2 km, and its horizontal grid consists of a set of curved triangles projected onto a sphere using the geometric form of the icosahedron. For the vertical dimension, ICON defines

120 vertical levels, which may vary in height as the bottom atmosphere levels may be stretched by underlying topography. The upper boundary consists of the top of the atmosphere at a fixed level of 22.8 km.

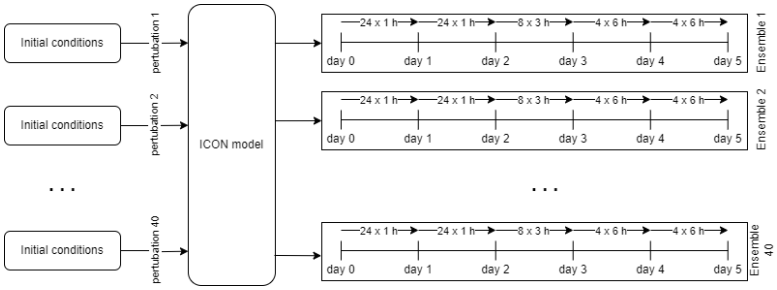

Figure 4.10: A schematic representation of the ICON-EU-EPS dataset. The same initial conditions are used for all 40 ensembles, but each with a unique pertubation. Due to the 'chaotic' nature of non-linear processes in meteorology, 40 unique ensembles are generated from the same initial conditions.

In simple terms, the ICON model solves multiple transport processes such as radiation, turbulence, cloud formation, and precipitation in horizontal and vertical directions. During each forecast, precipitation is given as a model output, which forms the forcing data for the flood forecasting models. Such forecasts are made four times a day, giving a 5-day forecast with varying time steps for the output, as shown in Figure 4.10. For the ensemble predictions, 40 members are gathered by perturbing the initial conditions for each ensemble member of the numerical weather model. The horizontal resolution is decreased for the ensemble version of ICON but also increased for the nested European model inside the global ICON model. As a result, the European ensemble version of ICON (ICON-EU-EPS) has the same average horizontal resolution of 13.2 km (Reinert et al., 2023).

Inspection of the ICON-EU-EPS ensembles shows a wide spread in the mean cumulative precipitation magnitude for the Rur basin for several days in the start days close to the flood event (Figure 4.11). Early predictions (10-07-2021 and 11-07-2021) show an underestimate of the magnitude of the precipitation compared to the RADFLOOD21 dataset and lack temporal resolution to model the flood event in this research. Comparison of the prediction with the general timeline of the flood event (Section 1.1) shows that 12 July coincides with the first meteorological warning for heavy precipitation from the KNMI ('code yellow'), and the 13th of July with a more severe warning ('code orange'). Therefore, the ICON forecasts for July 13 will be applied in this research.

Furthermore, the reanalyzed RADFLOOD21 dataset starts on July 13, which makes running the hydrological model more convenient as both the hindcast and the forecasts can use similar files describing the initial state of the hydrological model. Figure 4.12 demonstrates the resulting precipitation for each of the 40 members of the ensemble, and Figure 4.13 plots the difference between the RADFLOOD21 and ICON-EU-EPS data set.

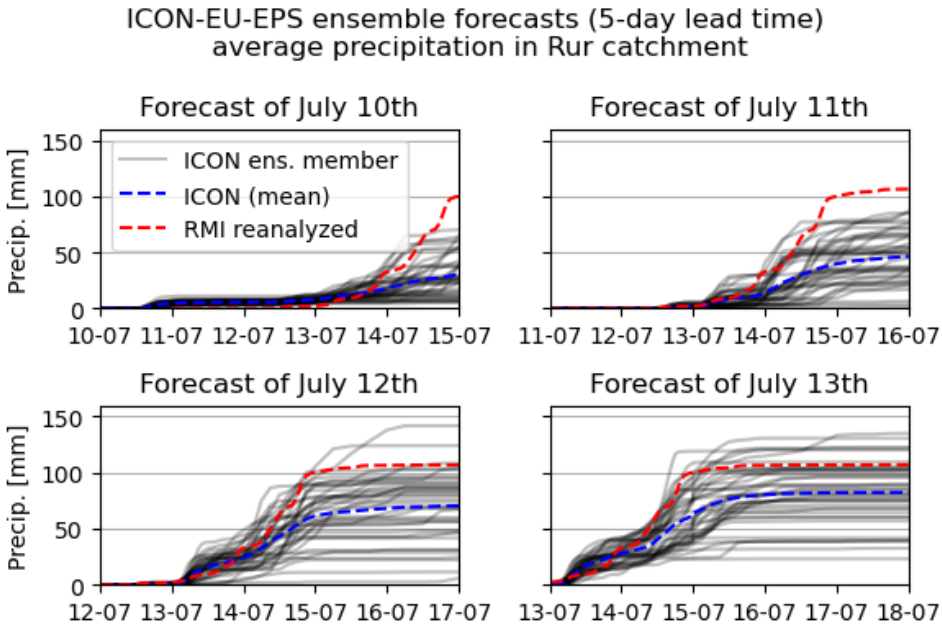

Figure 4.11: Development of the ICON-EU-EPS precipitation forecasts for several starting days. Early forecasts strongly underestimate the amount of precipitation. Forecasts of the 13th of July are selected to create the results in chapter 6.

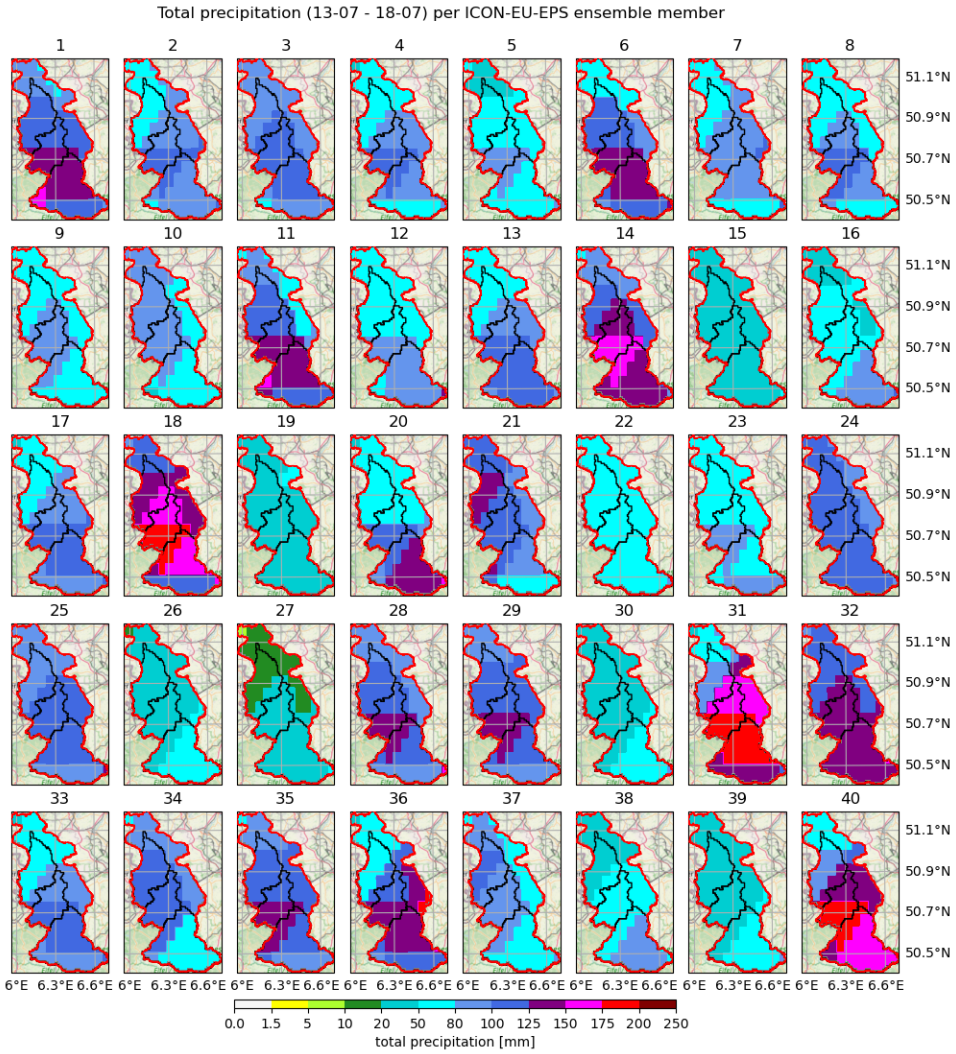

Figure 4.12: ICON-EU-EPS precipitation dataset for the 40 ensemble members. The triangle-shaped pixels are the result of the icosahedral shape of the grid of the weather model. One pixel may cover multiple subcatchment as a result of the coarse resoltution.

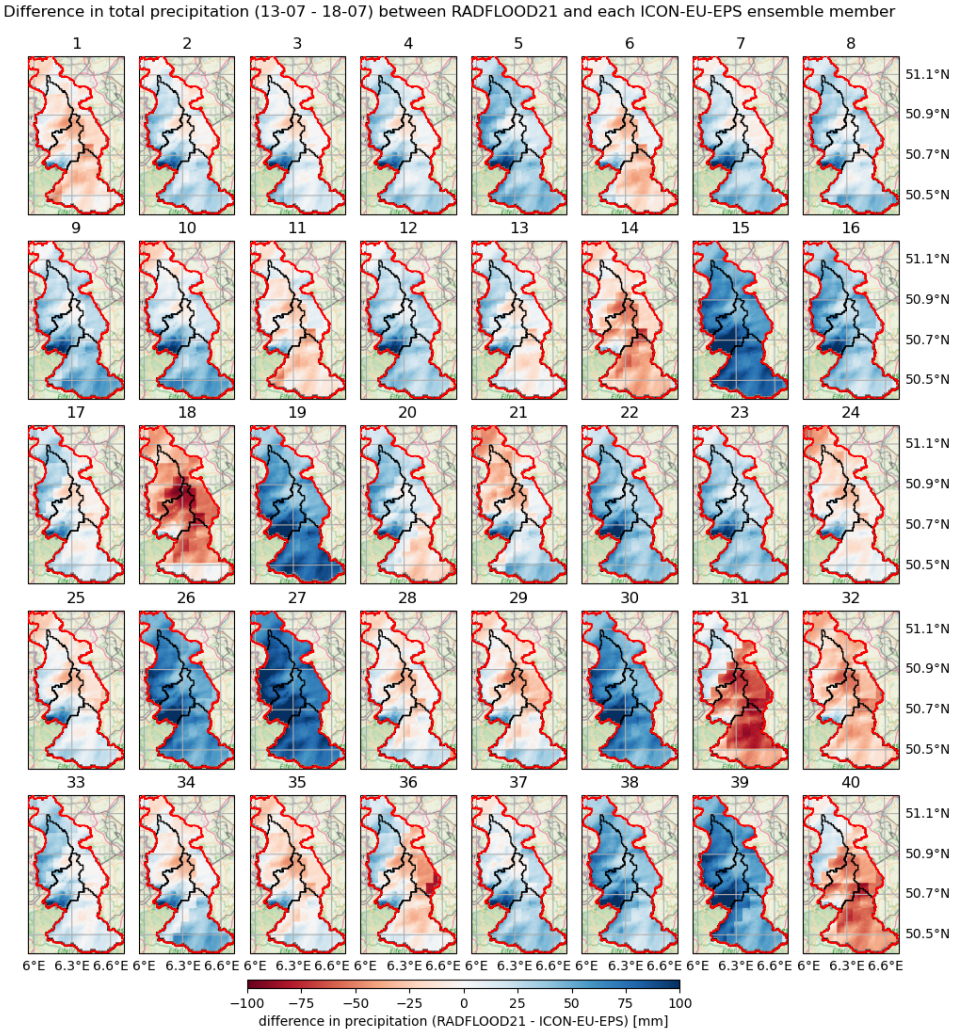

Figure 4.13: Difference between the 40 ICON-EU-EPS ensemble members and the RADFLOOD21 dataset. Most ensemble members underestimate the volume of precipitation, but heavy precipitation tends to concentrate in the Eifel, similar to the RADFLOOD21 dataset.

4.3.4. VALIDATION: FLOW METRICS AND FLOOD EXTENT

The precipitation products described in the previous section are used to generate the results from the hydrological and hydrodynamic models. Additionally, observational data is required to validate the performance of these models. This includes reservoir data, discharge records, observed water depths and satellite imagery of flood extent, and is addressed in Section 5.1.

RESERVOIR DATA

Reservoir data was provided by WVER for the period 2010-2022. The data set contains daily averages for inflow, outflow, and storage data for the Rur, Urft, and Olef reservoirs, and is used to calibrate the reservoirs in the *Wflow_SBM* model. Additionally, preliminary results based on calculations by WVER are used to evaluate the outflow in Heimbach during the flood event (Homann, 2021b).

DISCHARGE

Furthermore, daily discharge records were acquired from LANUV via the ELWAS-WEB data portal (ELWAS-WEB, 2023). These records were obtained for the locations listed in D.1 for the period 2012-2020. These records were used primarily to address the water balance of the catchment and to calibrate the *Wflow_SBM* model. No discharge records are available for the period during the flood event, but estimates of peak flow are gathered from the literature and WL.

WATER DEPTH

Furthermore, hourly water level data is provided directly by LANUV for 2021, which is used to address validation of the depths of the water for the hindcast. Water level records are included for the period of the 2021 flood event. Similarly, water-level observations from RWS were used at the Roermond-boven station, which was used to establish the downstream boundary condition for the *ProMaIDes* models.

FLOOD EXTENT

Observations of flood extent are used to evaluate the results of inundation maps created by *ProMaIDes* models. Data were found for the 2019 flood event (SENTINEL 19-03-2019) and the 2021 flood event (LANDSAT 18-07-2021). In addition, a flood extent map was drawn for the flood event of 2021. This map covers the Dutch Rur and is the result of interpreting aerial photos of inundated areas (Het Waterschapshuis, 2022) and converting these into a vectorised shapefile with the extent of the flood, as illustrated in Figure 4.14.

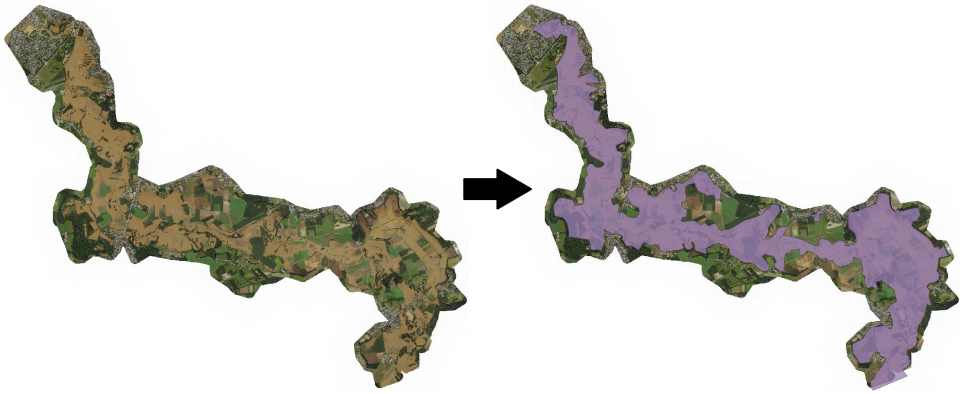

Figure 4.14: Flood extent map of the 2021 flood event created from aereal photos obtained from Het Waterschapshuis (2022). The photos are taken op the 17th of July 2021 in the morning.

4.4. PERFORMANCE METRICS

Several equations will be used to address the performance of the model results. An overview of the definitions of these equations is provided in this section.

4.4.1. NASH-SUTCLIFFE COEFFICIENT

The Nash–Sutcliffe model efficiency coefficient (NSE) score is used to evaluate the performance of the model using observational values. Higher discharges have a stronger effect on the NSE score as a result of squaring the differences and are thus considered a suitable metric in this research focussing on floods. The NSE score is calculated using the following function from the *HydroMT* package (*Python*): `hydromt.stats.skills.nashsutcliffe()`.

$$NSE = 1 - \frac{\sum_{i=1}^{N}(sim_i - obs_i)^2}{\sum_{i=1}^{N}(obs_i - \bar{obs})^2} \tag{4.2}$$

4.4.2. RELATIVE BIAS

The relative bias is used to evaluate the deviation between the modelled and observed storage of the reservoirs. It is preferred over the NSE score as the relative bias does not square the differences, therefore it is less sensitive to higher outliers, and the NSE score is typically used for discharges.

The relative bias is calculated using the following function from the *HydroMT* package (*Python*):`hydromt.stats.skills.percentual_bias()`.

$$rel.bias = \frac{\sum_{i=1}^{N}(sim_i - obs_i)}{\sum_{i=1}^{N}(obs_i)} \tag{4.3}$$

4.4.3. NDWI

The Normalized Difference Water Index (NDWI) (McFeeters, 1996; Sentinel, 2023) is used to identify inundated areas based on the ratio of the intensity of the green and near-infrared bands. It allows the interpretation of satellite imagery (such as SENITNEL and LANDSAT data; see also Section 4.3.4) in terms of coverage by water. A value close to 1 signifies that the area is covered by water and a value close to -1 signifies the opposite. Equation 4.4 describes how the NDWI can be determined.

$$NDWI = \frac{band_{green} - band_{NIR}}{band_{green} + band_{NIR}} \tag{4.4}$$

4.5. RESEARCH SET-UP

Several subjects were identified in chapter 2 that influence the behaviour of a flood wave and thus affect accurate flood forecasting. These effects may be significant for the Rur basin and should therefore be considered in the forecast. At the same time, different types of discretization have varying capabilities of incorporating these processes in the forecasts and pose a trade-off as improved modelling can result in increased computational efforts being necessary.

4.5.1. MODEL CONFIGURATIONS

The following chapters will address these questions by comparing the performance of the model for varying model configurations, addressing several subjects that are expected to be relevant for flood forecasting in the Rur. In general, five types of model will be considered:

- Wflow-KW: a setup consisting of only the hydrological *Wflow_SBM* model using the kinematic-wave approach for land and river routing;
- Wflow-LI: a setup consisting of only the hydrological *Wflow_SBM* model using the kinematic-wave approach for land routing and the local-inertial method (diffusive wave) for river routing;
- Wflow-FP: setup consisting of only the hydrological *Wflow_SBM* model using the kinematic-wave approach for land routing and the local-inertial method (diffusive wave) for river routing, with the additional discretization of floodplain flow using a subgrid approach;
- PM-1D: a coupled hydrological *Wflow_SBM* and hydrodynamic *ProMaIDes* model, for which only river modelling is considered in the *ProMaIDes* model and no two-dimensional floodplain modelling;
- PM-2D: a coupled hydrological *Wflow_SBM* and hydrodynamic *ProMaIDes* model, for which the 1D2D approach is used for modelling river-floodplain interactions in the *ProMaIDes* model.

A coupled PM-1D or PM-2D model uses the *Wflow_SBM* model to determine the boundary conditions for the *ProMaIDes* model. Typically, *ProMaIDes* models will use the

Wflow-FP model to determine the hydrodynamic boundary conditions. However, the applied *Wflow_SBM* model will be mentioned explicitly alongside the PM-1D and PM-2D models to avoid confusion.

Conceptually, the model variants can be illustrated as shown in Figures 4.15 to 4.17. The *Wflow_SBM* models are standalone and the whole catchment is discretised. It therefore includes land cells (green), the Rur river (light blue), and its tributaries (dark blue). The PM-1D model consists of a 1-dimensional *ProMaIDes* river model of the Rur (light blue) with the tributary inflows derived from the *Wflow_SBM* model (dark blue with arrows). Therefore, the *Wflow_SBM* river cells located on the Rur River (grey) are not used for the PM-1D model. Similarly, the PM-2D model consists of a 1-dimensional *ProMaIDes* river model and *Wflow_SBM* tributary inflows with the addition of a high-resolution two-dimensional floodplain model (purple).

4.5.2. RESEARCH SUBJECTS

The following subjects relevant to flood forecasting will be investigated using these models:

- Flood wave routing: differences between routing mechanisms and discretization methods;
- Floodplain flow and inundation: location of flooding in the Rur and the attenuation effects as a result of floodplain flow;
- Tributary interactions: identify tributary contributions and the influence of smaller tributaries;
- Reservoirs: investigate flood wave dampening by the reservoirs and the effects of overflow;
- Groundwater effects: the effects of leakage to deeper groundwater layers on the flood wave peak and on inundation.

To this end, a hindcast will be performed that addresses the flood event with a qualitative approach. For example, this type of investigation will focus on flood maps, comparing hydrographs, and observing the shape of the flood wave peak. Alternatively, the 40 ensemble forecasts will be used in a quantitative approach addressing characteristics such as the peak discharge, total inundation, and peak flow arrival times.

4.5.3. OPERATIONAL SET-UP

As described in Sections 1.2 and 2.2.1, different types of flood forecasting models exist and are being used in an operational settings. Such as setting relies on meteorological predictions beind fed into the forecasting model, and processing of the model results. Such an Flood Early Warning System (FEWS) (e.g. M. Werner et al. (2013)) can couple *Wflow_SBM* to a hydrodynamic model and automate the processes of flood forecasting. An example of such a system using *Wflow_SBM* is an operation flood forecasting system in Australia which combines *Wflow_SBM* with the SFINCS hydrodynamic model from Deltares (De Kleermaeker et al., 2022).

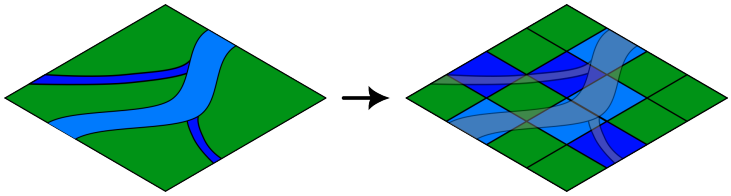

Figure 4.15: Conceptualisation of the stand-alone *Wflow_SBM* models with the Rur river (light), its tributaries (dark blue) and land cells (green).

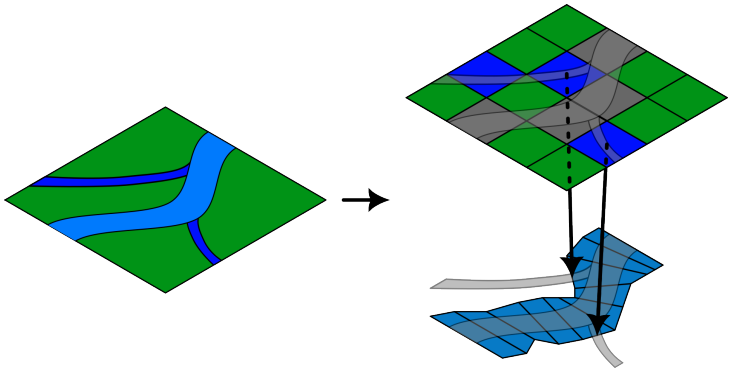

Figure 4.16: Conceptualisation of the PM-1D model with *Wflow_SBM* tributary inflows (light blue) and land cells (green), and a one-dimensional river model of the Rur in *ProMaIDes* (dark blue). *Wflow_SBM* river cells located within the Rur are not considered and therefore marked grey.

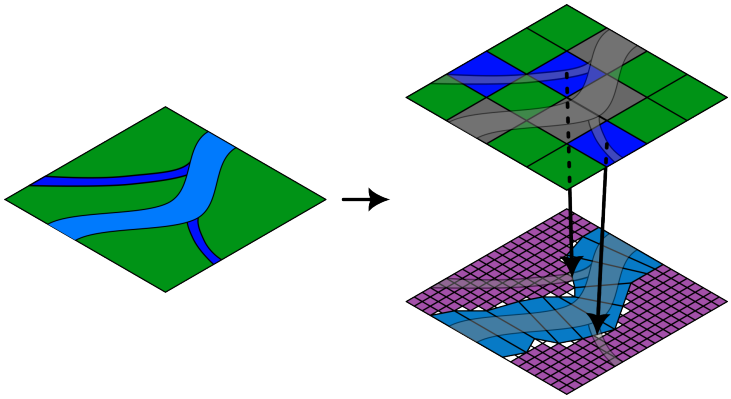

Figure 4.17: Conceptualisation of the PM-2D model with *Wflow_SBM* tributary inflows (light blue) and land cells (green), and a one-dimensional river model of the Rur in *ProMaIDes* (dark blue) with a two-dimensional high resolution floodplain model (purple). *Wflow_SBM* river cells located within the Rur are not considered and therefore marked grey.

The set-up in this thesis has not been implemented in a FEWS, but some processes still required automation through scripting, namely generating the correct intial state of the models. For the *Wflow_SBM* models, the E-OBS dataset is used to warm-up starting on 1 January 2019 to 1 June 2021 with a daily timestep. Additionally, the RADCLIM dataset with hourly timestep is used to bridge the transition from daily timestep of the E-OBS to the hourly timestep of the RADFLOOD21 dataset, which starts on the 13th of July 2021. Furthermore, reservoir storage levels are updated in *Wflow_SBM* based on data from WVER. It is expected that such values would be available in an operational setting and, therefore, can be updated in the model.

The *ProMaIDes* software supports setting an initial depth of water for the river profile, but in practise this proved to be insufficient to start the model in a 'warm' state. Therefore, a spin-up is applied to the *ProMaIDes* model by setting stationary flow conditions for the first 24 hours of the simulation. After these 24 hours, the 'real' simulation starts on the 13th of July 2021. Boundary conditions for the *ProMaIDes* are derived automatically from output generated using a Wflow-FP model.

4.5.4. COMPUTATIONAL TIME

Computational times are based on model runs which were performed on a HP ProBook 650 G2 with an Intel i5-6200U chip and 8gb RAM memory. These results are shown in table 4.3. Alternatively, model runs were executed on a Deltares network computer with an Intel(R) Xeon(R) Gold 6144 CPU chip and 16gb RAM memory, but these run times are not included in the overview of computational times.

run type	**Wflow-KW**	**Wflow-LI**	**Wflow-FP**	**PM-1D**	**PM-2D**
calibration	8 min.	50 min.	75 min.	-	-
hindcast/forecast	3 sec.	10 sec.	11 sec.	7 min.	13 h.

Table 4.3: Average computational times of the models used in this research.

An advantage of the *ProMaIDes* software package is the option for running simulations in parallel on multiple cores. When the river and floodplains profiles are identical, they only need to be initialized once, and each core can afterwards run a simulation with distinct boundary conditions. As the PM-2D models take several hours to run, the overhead of parallel simulations is relatively very small. *Wflow_SBM* supports parallel computing inside a single simulations, but with relatively large overhead as simulations only take a couple of minutes.

5

HINDCASTING THE 2021 FLOOD EVENT

THIS chapter aims to examine the response of the Rur River following the occurrence of the flood in 2021 and to conduct a comparative analysis of various model types in capturing this response. Subsequently, the catchment response is examined with respect to five distinct topics, each accompanied by selected model types. The comparison between the model types serves to address the research objective of identifying the determining factors for a flood forecasting model for the Rur.

5.1. VALIDATION OF THE HINDCAST RESULTS

This section describes the main results of the hindcast and how these relate to observations made during the 2021 flood event. First, the tributary inflows and the reservoir outflow simulated in *Wflow_SBM* are considered as they determine the boundary conditions for the PM-1D and PM-2D models. The Wflow-FP model is used to generate these boundary conditions, but the results are compared to the Wflow-KW and Wflow-LI models to motivate the choice of Wflow-FP. Afterwards, the hindcast results for the Rur itself are compared to observations in terms of waterlevel, discharge and inundation.

5.1.1. FLOOD WAVE DAMPENING BY THE RESERVOIRS

The extraordinary amount of rainfall during the flood event consequently led to large runoff to the Rur tributaries and reservoirs. Figure 5.1 shows the inflows to the reservoirs (full line) and the corresponding response based on the operating rules described in Section 3.1.2 (dashed line). Clearly, the reservoirs dampen the flood wave and create a controlled outflow at the outlet. The Rur reservoir is the most dominant reservoir system, as it is the largest in size, retention capacity, and discharge, and it reduced the inflow from the Eifel from approximately 400-600 m^3/ s to 50 m^3/s, according to the model results. This flow reduction is of the same order of magnitude as the conclusions from WVER,

where a maximum inflow of approximately 760 m^3/s was derived for the Rur reservoir (Homann, 2021b).

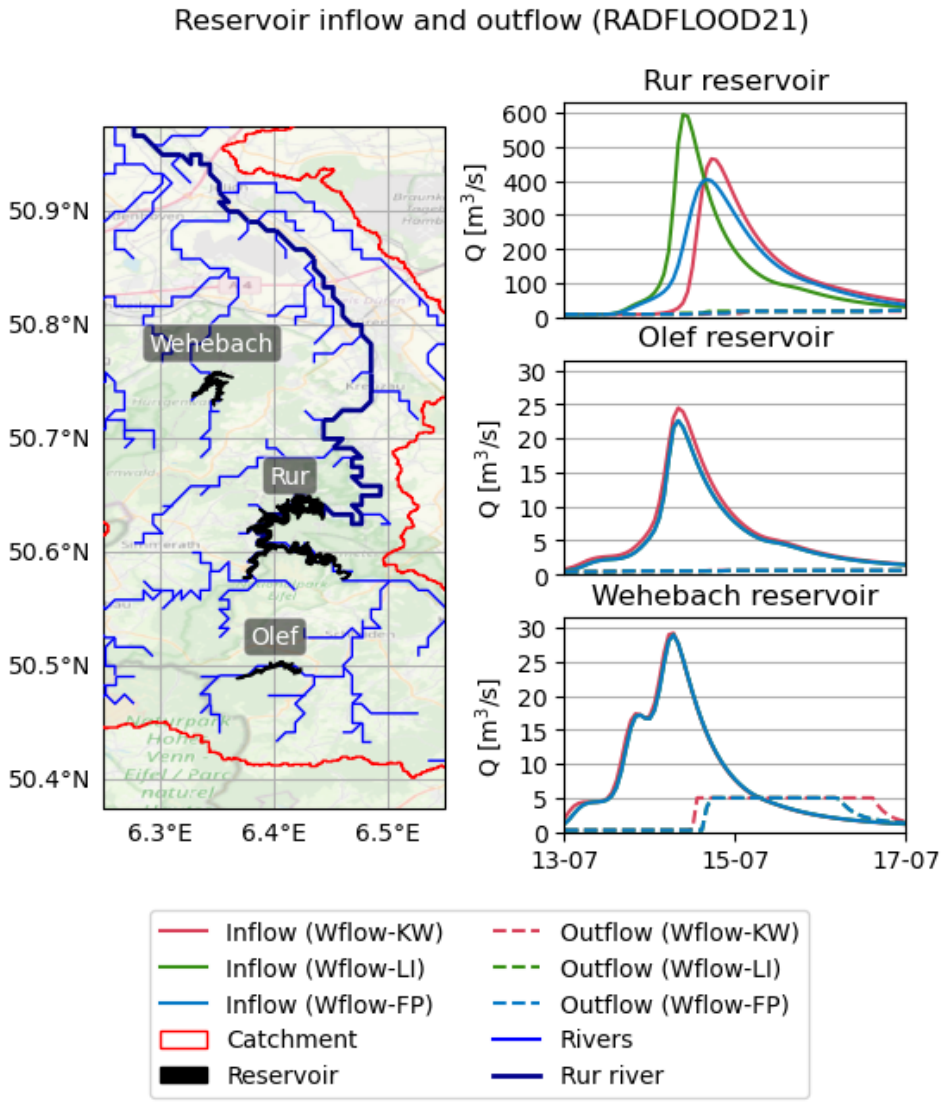

Figure 5.1: Reservoir response to the 2021 flood event using RADFLOOD21. Inflow curves for Wflow-KW and Wflow-LI fully overlap for the Olef and Wehebach reservoirs.

The differences between Wflow-KW, Wflow-LI and Wflow-FP are limited for the Olef and Wehebach reservoirs, with good performance of simulation of the Olef reservoir. The results for the Wehebach reservoir do not align with observations during the flood event, as the flow did not exceed 0.2 m^3/s. The impact of this reservoir on the hydrology of

the catchment is limited and limited data was available for the reservoir. Therefore, the Wehebach reservoir and its impact will not be further considered in this section.

5.1.2. RESERVOIR OUTFLOW TO RUR

Initially, the outflow of the Rur reservoir system is simulated using the implementation of volume-based operations plans in *Wflow_SBM*. Figure 5.2 shows a more detailed overview of the inflow, outflow, and storage compared to data based on WVER observations and calculations (Homann, 2021b). Generally. The inflow to the reservoir is underestimated, and therefore also the storage of the reservoir, which on its turn governs the outflow. The peak inflow of the Wflow-LI model shows the strongest similarities with the observations, as the peak flow coincides around 01:00 on 15-07-2021, but both the rising and falling limbs are narrower and the peak inflow differs by approximately 160 m^3/s.

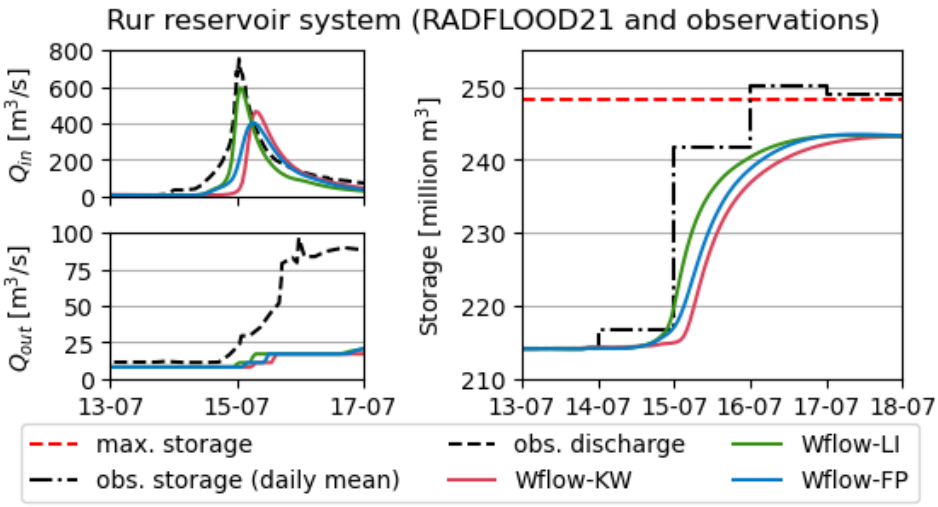

Figure 5.2: Inflow, outflow and storage for the Rur reservoir system during the 2021 flood event, modelled using RADFLOOD21. Inflow from the Wflow-LI model aligns with observed inflow, and reservoir outflow is underestimated for all *Wflow_SBM* models.

Similarly, the reservoir storage is lower for all model results. The *Wflow_SBM* models approach similar storage levels, which is to be expected since they all use the same forcing data for precipitation and only differ in the river routing schematization: the timing of the river runoff varies, but approximates the same volume of total runoff. Finally, the modelled outflow is almost five times lower than the observed outflow. This difference has three main causes: underestimated inflow, the upper levels in the reservoir's operational plan were not reached, a constant volume for the storage volume of the Olef reservoir was assumed (see also Appendix B) which is too low in the case of an extreme flood event, and an additional release was commissioned for the Rur reservoir, which deviates from the operation plans.

To account for these differences, the simulated reservoir outflow is replaced by an artificial outflow derived from preliminary reservoir calculations by WVER. The additional release is included by imposing an approximation of the observed Rur reservoir release on the *Wflow_SBM* models. The outflow of the reservoir can be imposed by changing the file of the operation plan (`res_sq_1.csv`) to impose the approximate outflow for all storage levels, such that it becomes independent of the reservoir volume. As the operation rules are fixed for each day of the year in the model, the daily mean outflow is approximated based on observations, as shown in Figure 5.4. Consequently, *Wflow_SBM* models with forced pre-release are expected to produce better results for the forecast of the flood event.

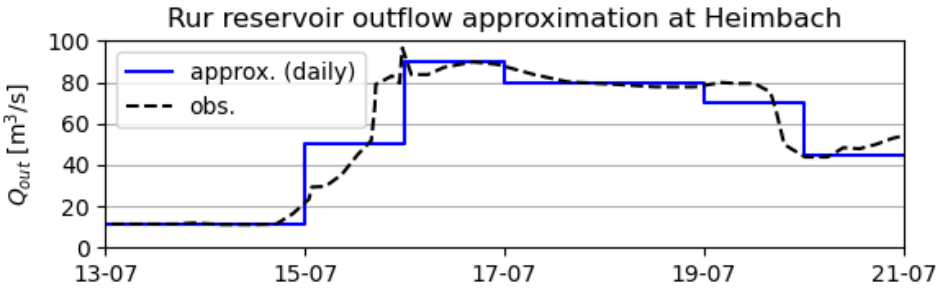

Figure 5.3: Imposed outflow at Heimbach for the *Wflow_SBM* models.

Although these alterations improve the modelled discharge at Obermaubach, a considerable underestimation is observed between 15-07 at 12:00 and 16-07 at 12:00. This underestimate may be caused by an increased release in the Obermaubach reservoir, which is not included in the *Wflow_SBM* models, as these only model the Rur reservoir and its outflow reaching Obermaubach. In practise, an additional prerelease may have been applied at Obermaubach to increase the retention capacity even more, but it is not possible to incorporate these effects into the current *Wflow_SBM* models.

The situation is different for the *ProMaIDes* models, which do not include reservoir modelling but have their upstream boundary at the outlet of the Obermaubach reservoir. Therefore, an hourly approximation of the observed outflow in Obermaubach can be applied as the upstream boundary condition for the PM-1D and PM-2D models (Figure 5.4).

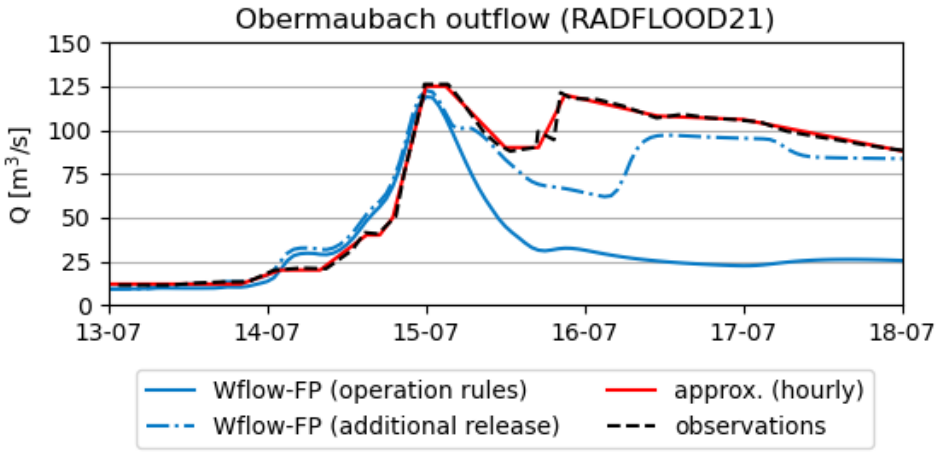

Figure 5.4: Imposed outflow at Obermaubach for the *ProMaIDes* models.

5.1.3. TRIBUTARY INFLOWS TO RUR

Section 5.1.2 demonstrated the implications of varying river routing schemes for the inflow of the Rur reservoir. Similarly, changes in these schematizations may affect tributary inflows to the Rur River. To this end, the schematizations of river routing *Wflow_SBM* are compared with water level observations from the 2021 flood event at LANUV stations located on the Inde and Wurm rivers. The stations that recorded these data are the stations at Eschweiler and Korenlimünster for the Inde and Randerath and Herzogenrath 1 for the Wurm.

It should be considered that it is difficult to compare the observed and simulated flow depths for the *Wflow_SBM* models. The depth of water observed at the gauge station depends on the local geometry of the river section, while the depth of the modelled water represents an average over the entire length of the size of the grid cell (1̃ km). Additionally, data on the river profile must be incorporated into the *Wflow_SBM* model to accurately simulate the local water depth, but only rough estimates of the river width are available for the tributaries. Still, the observations and simulations can be compared qualitatively, focussing on the shape of the hydrograph, showing, for example, the peak arrival times.

Figure 5.5 shows the resulting water depths for these stations. The results for Wflow-KW and Wflow-LI show a spiky hydrograph with peaks that arrive too early compared to the observations, while the hydrograph from the Wflow-FP results shows a stronger resemblance with the observations and wider trailing edges. The downstream stations closest to the Rur (Eschweiler and Randerath) show improved results when floodplain flow is included.

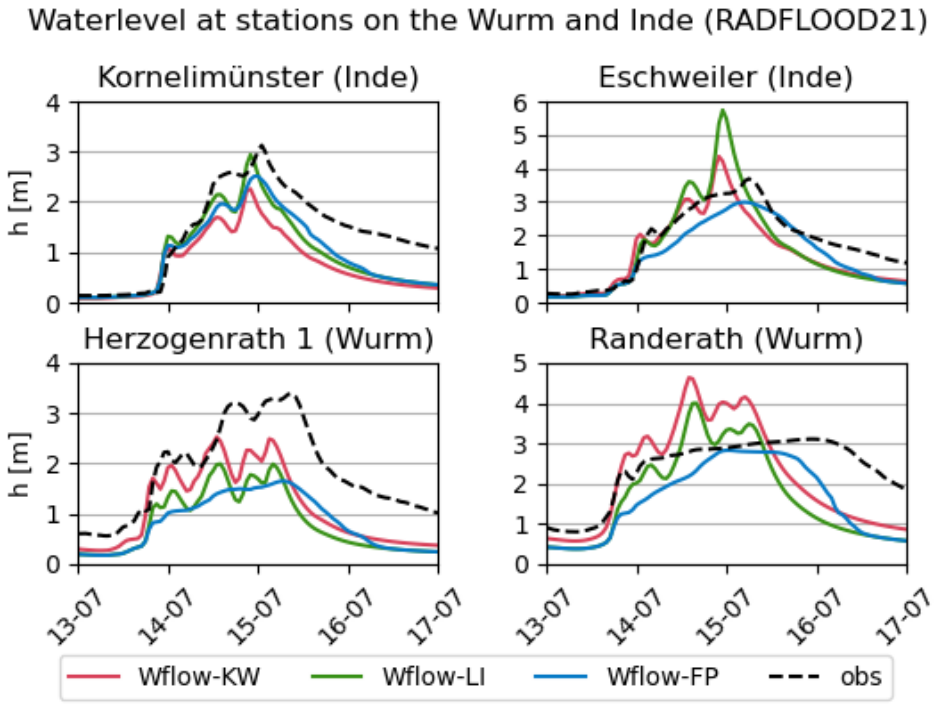

Figure 5.5: Water depths at gauge stations in the Wurm and Inde tributaries using the RADFLOOD21 dataset compared to observed water levels.

5.1.4. RUR WATERLEVEL AND DISCHARGE

The results for the Rur tributaries and the reservoir system show how river routing affects the model results. In this section, the results are addressed for the Rur downstream at Obermaubach for the *Wflow_SBM* models as well as the *ProMaIDes* models, which are driven by the Wflow-FP model. First, simulated water depths are compared to hourly observations made during the 2021 flood event. Only the gauge stations at Selhausen and Stah are included, as information from other gauge stations (Altenburg 1, Jülich Stadion and Linnich 1) did not align with the river cross-sections in the *ProMaIDes* model, and the PM-2D results are used to derive a simple Q-h relationship to convert *Wflow_SBM* discharge results to accurate water depths.

The results at Selhausen agree reasonably well with the observations (Figure 5.6. This can be attributed to the dominance of reservoir flow in this river reach, as it lies upstream of the Inde and Wurm confluences. This is different at gauge station Stah, where large differences are observed between model results, espcially for the Wflow-KW and Wflow-LI models. The results for the tributary inflows (Figure 5.5) already indicated that models without floodplain attenuation overestimate peak flow and large flood wave celerities, and similar differences are observed at Stah in Figure 5.6. The results of Wflow-FP and PM-1D show better alignment with the observations, but the water depth declines be-

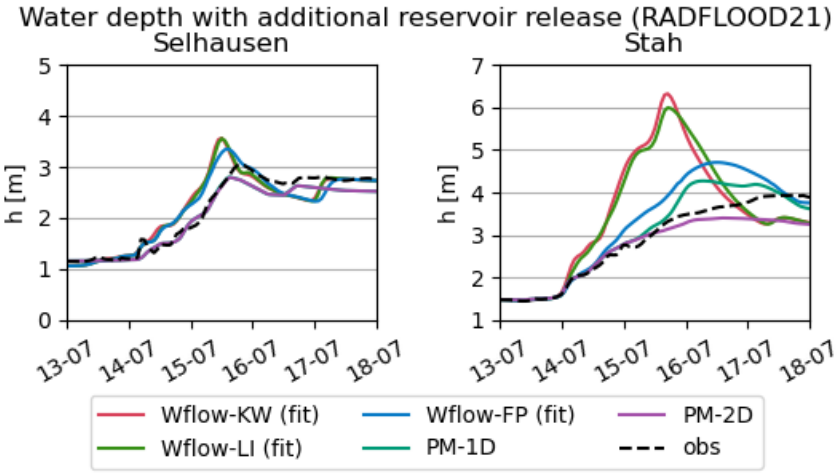

Figure 5.6: Water depths at Selhausen and Stah for the model results with the additional reservoir release included using RADFLOOD21. Water depths for the *Wflow_SBM* models are derived from discharge results using a Q-h relationship derived from the PM-1D model using the RADCLIM dataset.

tween the 16th and 17th of July, which was not observed in practice. Only the PM-2D model is able to capture the wide and attenuated flood wave with a peak discharge on the 17th of July.

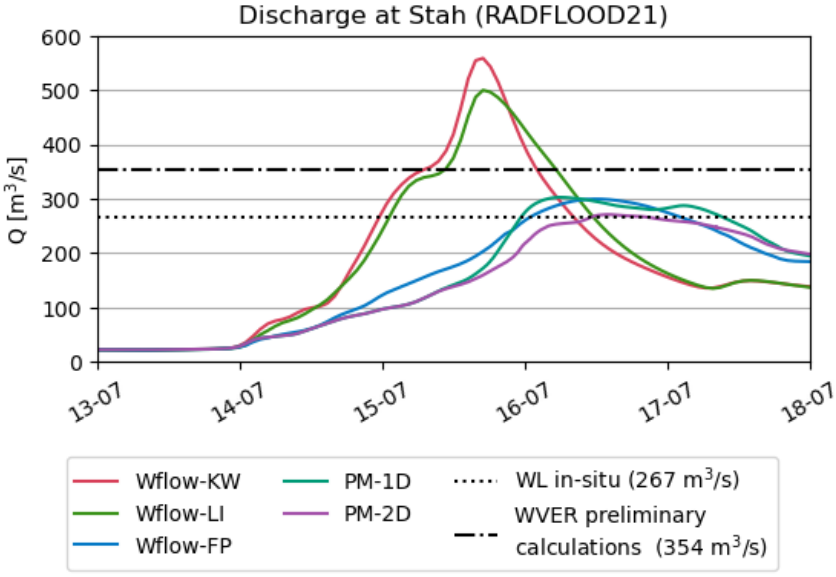

Figure 5.7: Discharge at Stah for models using RADFLOOD21. Simulated discharges are compared to an in-situ measurement by WL and preliminary model simulations performed by WVER.

Similarly, the hindcast results can be compared to the observed in discharge. The gauge stations did not measure the discharge during the flood event, but estimates of the maximum discharge were obtained based on preliminary calculations by WVER and an in situ measurement by WL (Horn & Hurkmans, 2022). In practice, it remains difficult to obtain an accurate estimate of the maximum discharge, as tried, for example, by T. Geertsema and Asselman (2022) for a range of peak discharges ranging between 195 m^3/s to 300 m^3/s.

5.1.5. RUR INUNDATION

The Rur catchment was subject to significant inundation during the 2021 flood event. To simulate the extent of the flooding and compare it to observations, only the PM-2D model suffices, as it is capable of modelling flooding processes with enough detail. The Wflow-FP and PM-1D models do include floodplain modelling but fail to convert these results into high-resolution inundation maps without extensive post-processing. Therefore, all flood maps are the result of only the PM-2D model. The floodplain inundation map of each floodplain grid is included in the Appendix F.2.

Observing the maximum depth of inundation h_{max} for the floodplain grids of the PM-2D model results shows a clear distinction between inundated areas along the Rur River. Inundation is limited directly downstream of the Rur reservoir in floodplain grids 0 and 1 (Figures F.2 and F.3). The flow in these reaches is dominated by the regulated outflow of the Rur reservoir system, which regulates the discharge and prevents flooding. Inundation increases beyond the confluences of the Inde tributary in Jülich and the Wurm tributary in Stah, as observed in floodplain grid 2 (F.4). For this region, inundation concentrates on floodplains between urban regions. Especially the floodplains at the Dutch-German border (Figures F.5 and F.6) act as a buffer, also storing large volumes of water during the 2021 flood event.

The quality of the flood maps produced by the PM-2D model can be assessed by comparing the results with the observations listed in Section 4.3. Hindcast results are compared with an NDWI map of the LANDSAT satellite imagery (Figure 5.8) and a flood extent map for 2021 (Figure 5.9). Both results show flood patterns similar to those of the PM-2D results for the Dutch Rur. Especially the flood extent from the aereal photos shows an almost exact overlap with the simulated inundation, with the exception of areas near Roermond. Some flooding of the city is simulated, which was not observed during the flood event. In Germany, flooding of the dike in Ophoven is simulated, which coincides with observations during the flood event (Bezirksregierung Köln, 2021).

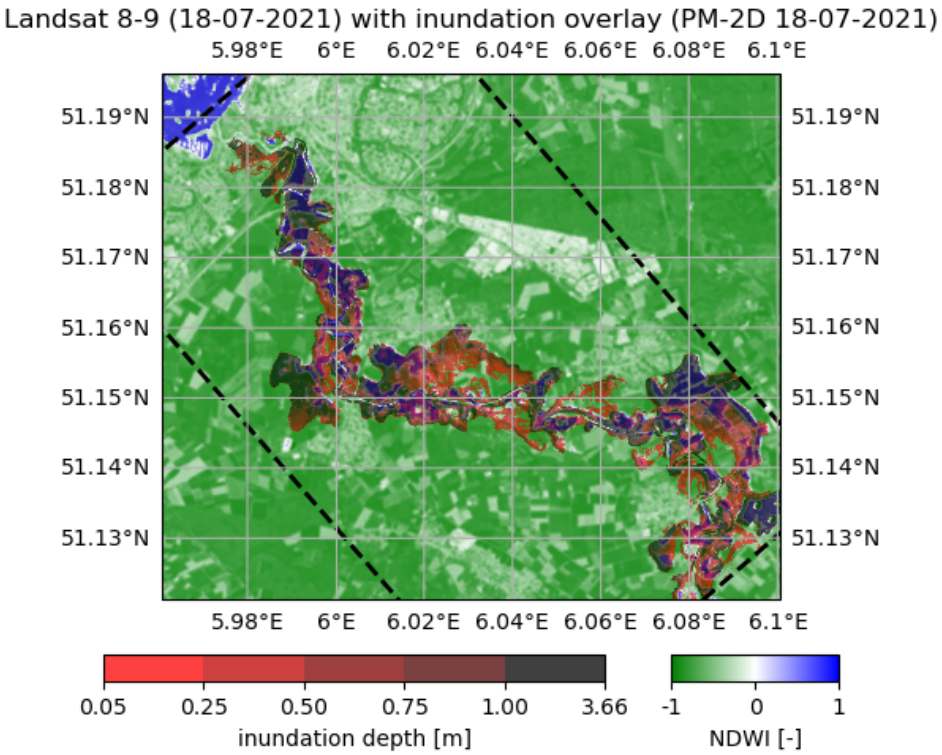

Figure 5.8: NDWI map of the 2021 flood event using LANDSAT satellite imagery compared to the PM-2D hindcast. An overlap of the simulated water depth with the blue zones indicated that simulated inundation overlaps with observed inundation(or with the Rur itself).

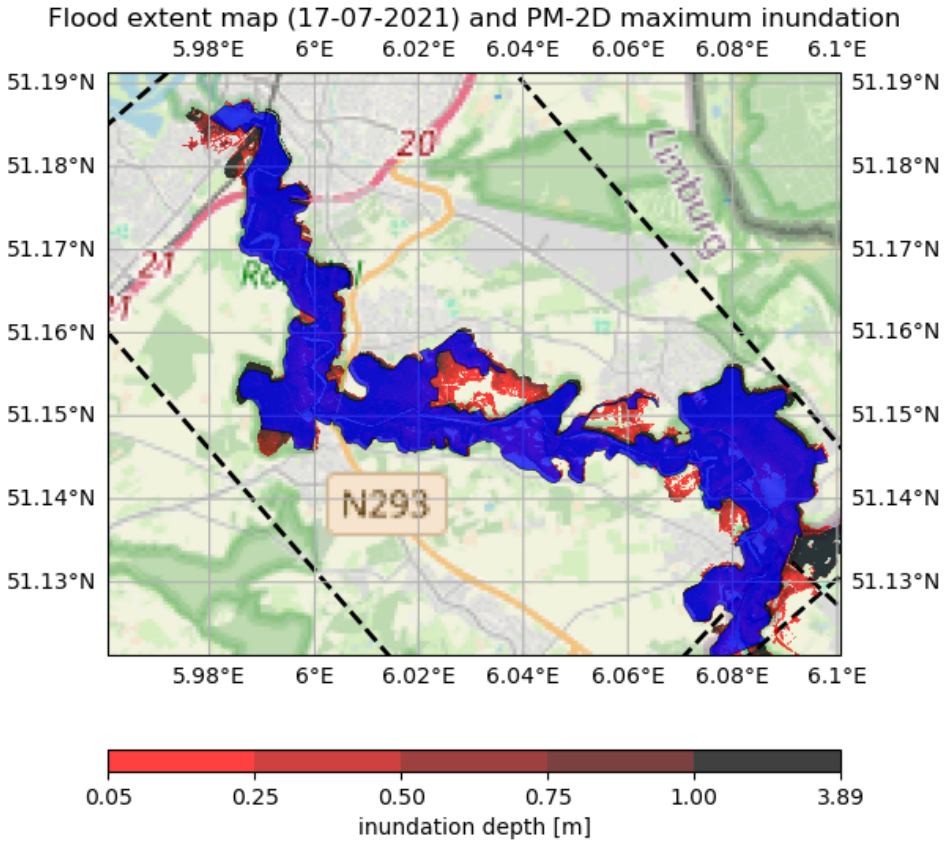

Figure 5.9: Flood extent map of the 2021 flood event (blue) compared to the PM-2D hindcasts (red). The flood extent map fully overlaps the PM-2D results and is taken on the 17th of July, which is approximately the same moment as the peak of the flood wave reached Stah. The flood extent map has been drawn by hand, see also section 4.3.4.

5.1.6. CONCLUDING REMARKS ON THE VALIDATION

The hindcast results for all models have been validated based on available observations of the 2021 flood event. Additionally, inundation maps of the PM-2D model have been validated using aereal photography and satellite imagery. Some uncertainties remain, such as the peak discharge at Stah, and discretization errors still persist, for example in approximating the outflow of the Obermaubach reservoir in the *Wflow_SBM* models. In the current hindcast, flooding occurs in the city of Roermond, which is likely caused by the absence of certain (small) flood retention structures in the DEM of the floodplain grid in the PM-2D model, similarly to the Rur model in Horn and Hurkmans (2022). Despite these errors, the current setup is considered accurate enough to be used as the hindcast of the 2021 flood event, and all models will be used in the following sections.

5.2. FLOOD WAVE ROUTING

This section investigates how the flood wave propagated through the Rur river during the 2021 flood event and how the varying discretization of the river routing affects the propagation of the flood wave. The results describing the reservoir inflow (Section 5.1.1) already illustrated how the variation of the river routing scheme affects the arrival and magnitude of the peak flows. Similarly, the effects of different types of model schematization are considered in this section.

In this analysis, the additional release from the Rur reservoir system is not considered, such that the focus remains on the 'natural' run-off downstream of Obermaubach. All models are included, ranging from the simple Wflow-KW, using the kinematic wave, to the Wflow-LI and Wflow-FP models, using the diffusive wave equation, and the more detailed PM-1D and PM-2D models. Some implicit river bank flow is included for the Wflow-FP and PM-1D models, as certain river cross-sections from the PM-1D model contain part of the floodplain and the widths of the river cells in the *Wflow_SBM* models are derived from these same PM-1D river profiles (see also Appendix B.4).

The Rur River is divided into three reaches by using the confluences of the Inde and Wurm rivers and stretching from Obermaubach to Roermond. The width of the Rur is lowest for the first reach from Obermaubach to Inde, containing profiles with little to no embankment. The second reach from the Inde to the Wurm contains the widest profiles, whereas the third reach from the Wurm to Roermond is more neutral. LANUV gauge stations are used in the analysis, but artificial stations have been added, which are depicted in Figure 5.10. Inflows from smaller tributaries are in the *ProMaIDes* model for practical reasons, as removing tributary inflows in the Wflow model would require large alterations to the hydrological processes performed by the model or result in significant losses in flood water volume.

The model results show a similar flood wave shape for the different types of flood wave routing in the first reach (Figure 5.11). The inflow at Obermaubach determines the shape of the wave as lateral inflows are limited and the reservoir flow is dominant. Differences between Wflow-FP and the Wflow-LI and Wflow-KW models are small as floodplain flow remains limited for this reach due to the limited magnitude of the reservoir outflow. The PM-1D and PM-2D results also show limited floodplain attenuation and lower flow mag-

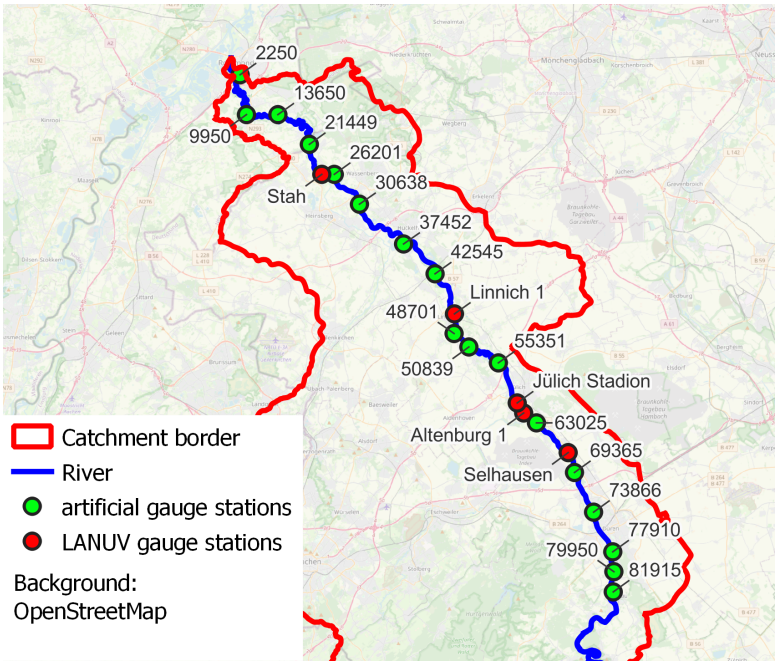

Figure 5.10: Location of the gauge stations (LANUV and artificial) on the Rur river.

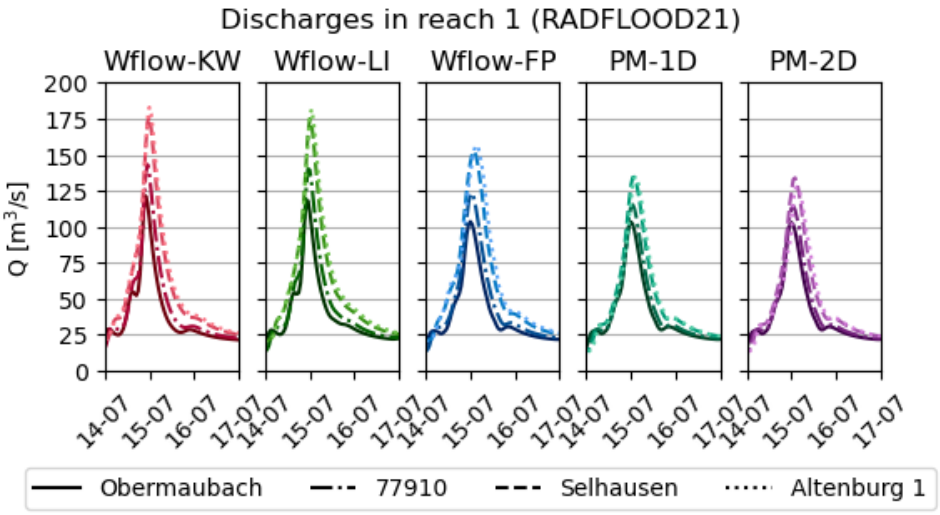

Figure 5.11: Hydrographs for all models in reach 1 using the RADFLOOD21 dataset. The additional reservoir release is not included in these results. Differences are small between model results, with a lower flood wave celerity for the Wflow-FP, PM-1D and PM-2D models, and highest celerity for Wflow-KW.

nitudes are simulated as direct surface run-off is not captured by the *ProMaIDes* models. The differences between the Wflow-KW and Wflow-LI show the effect of varying numerical schematization as the wave celerity is higher for the kinematic wave and attenuation stronger using the diffusive wave, and differences between Wflow-LI and Wflow-FP can be attributed to floodplain flow attenuation.

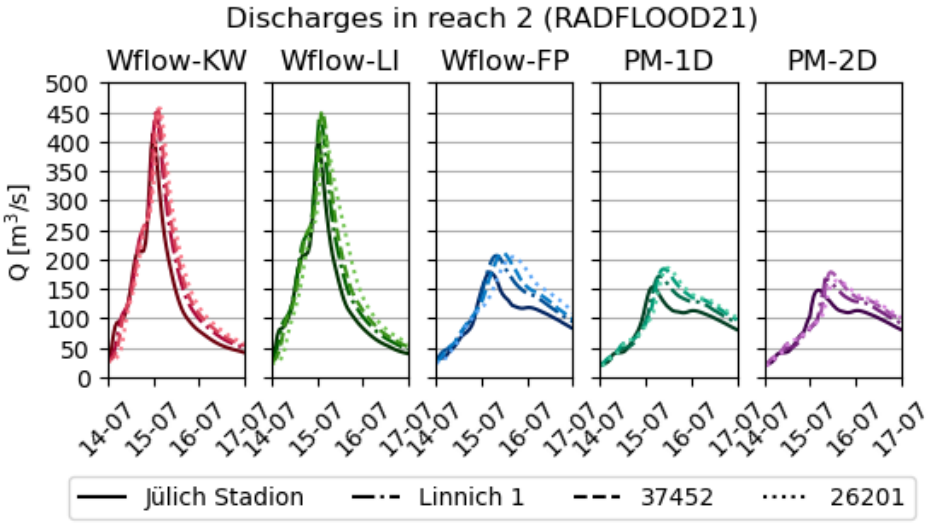

Figure 5.12: Hydrographs for all models in reach 2 using the RADFLOOD21 dataset. The additional reservoir release is not included in these results. Strong attenuation by floodplain flow starts to affect the results of the Wflow-FP, PM-1D and PM-2D models.

The situation is different in the second reach of the Rur River (Figure 5.12), where floodplain flow becomes more important. The one-dimensional river profiles, used in the PM-1D and PM-2D models, are wide for this reach, which contains part of the floodplains. As a result, floodplain flow is captured similarly by the PM-1D model and PM-2D models, as the flow remains inside the one-dimensional river model. The Wflow-FP results show stronger attenuation compared to the Wflow-LI model, which has a similar diffusive wave approach but no floodplain flow. The peach discharges of the Wflow-KW and Wflow-LI models can be considered unrealistic as the bankfull discharge is certainly exceeded at such magnitudes.

For the downstream reach (Figure 5.13), the one-dimensional river profiles are narrow and do not contain much information about the floodplain. As a result, the PM-1D does not capture the floodplain flow for this reach, resulting in fewer differences in peak attenuation compared to the Wflow-FP model. Furthermore, inundation is strongest in this reach, which is evident when observing the discharge for the PM-2D model. It should be noted than part of the flow travels through the floodplains, which is not captured by the observation point placed in the river cross-section. Clearly, the complex dynamic flow in the floodplains is only captured by the PM-2D model for this reach.

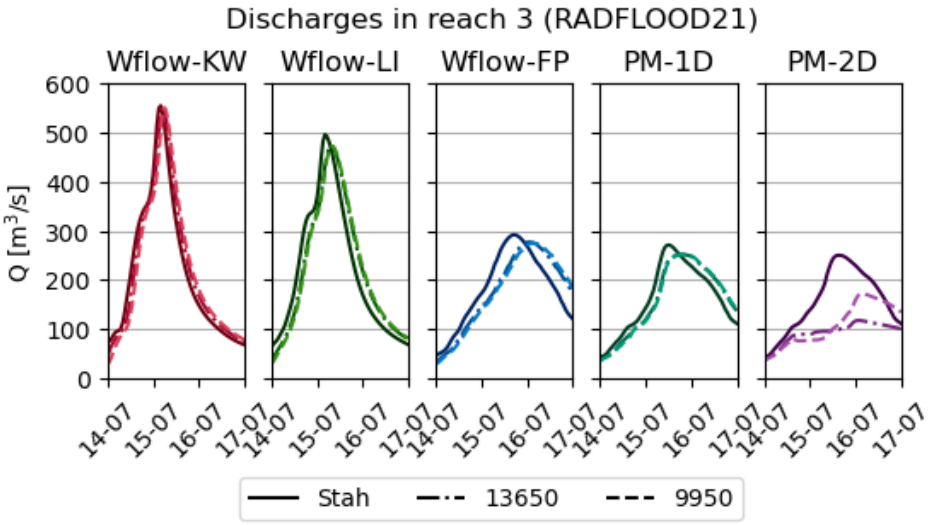

Figure 5.13: Hydrographs for all models in reach 3 using the RADFLOOD21 dataset. The additional reservoir release is not included in these results. Differences between Wflow-FP and PM-1D remain small, and the flood wave flattens out for the PM-2D results when passing the wide floodplains of the Dutch Rur.

5.3. FLOODPLAIN FLOW

The previous section addressed the effects of floodplain attenuation on flood wave routing. Additionally, the different approaches of modelling floodplain flow are compared in this section for the simple Wflow-FP and the advanced PM-2D models. Although the Wflow-FP model does not produce results that can easily be converted to flood maps, it tracks the amount of volume stored in the floodplains of river cells. Therefore, a comparison can be made between the Wflow-FP and PM-2D models to validate whether the quasi-2D Wflow-FP model produces similar results with respect to the volume of water in the floodplains and its temporal and spatial distribution.

Figure 5.14 shows the floodplain storage concentration for the Wflow-FP model. The results show that the largest floodplain storage occurs in the wide floodplains, similar to the results obtained by the PM-2D model and observations for the Dutch Rur. This figure highlights at the same time the coarse resolution of the *Wflow_SBM* models, which makes the floodplain pattern itself not suitable for deriving detailed flood maps.

A comparison in terms of volume with the PM-2D model (Figure 5.16) shows that floodplain storage is larger for the Wflow-FP model than for the PM-2D model, although other observations (Section 5.2) underline that flow damping is stronger for the PM-2D model. Another interesting aspect is floodplain storage that occurs in the Inde tributary near the lignite mine. This mine was filled with significant volumes of water during the 2021 flood event (Schüttrumpf, 2022), which is captured by the Wflow-FP model, and therefore also the PM-1D and PM-2D models which use the Wflow-FP model to generate the boundary conditions.

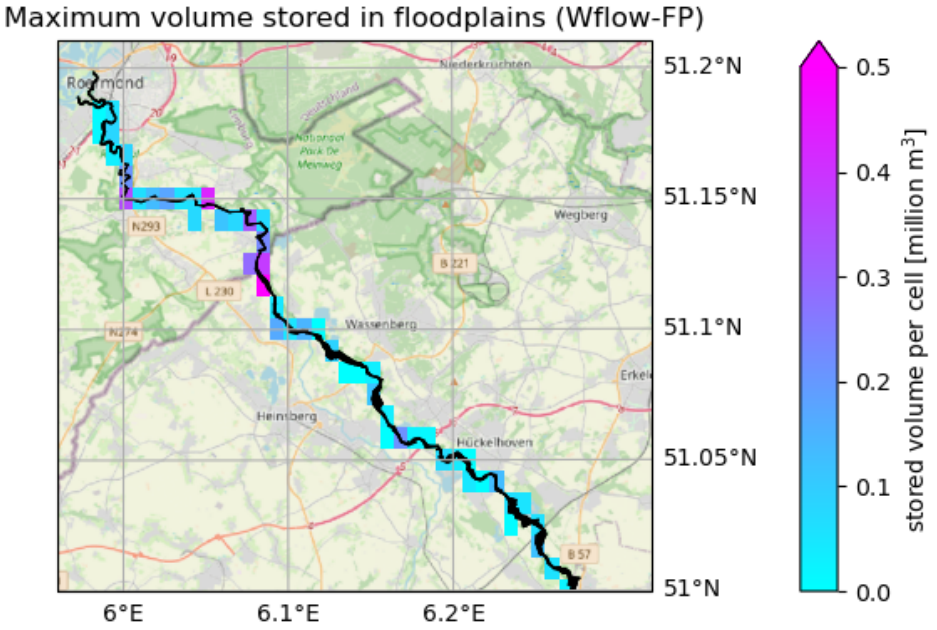

Figure 5.14: Concentration of floodplain storage for the Wflow-FP model in the hindcast (RADFLOOD21). Floodplain storage occurs predominantly in the Dutch Rur, similar to the observations of the flood event and the PM-2D results.

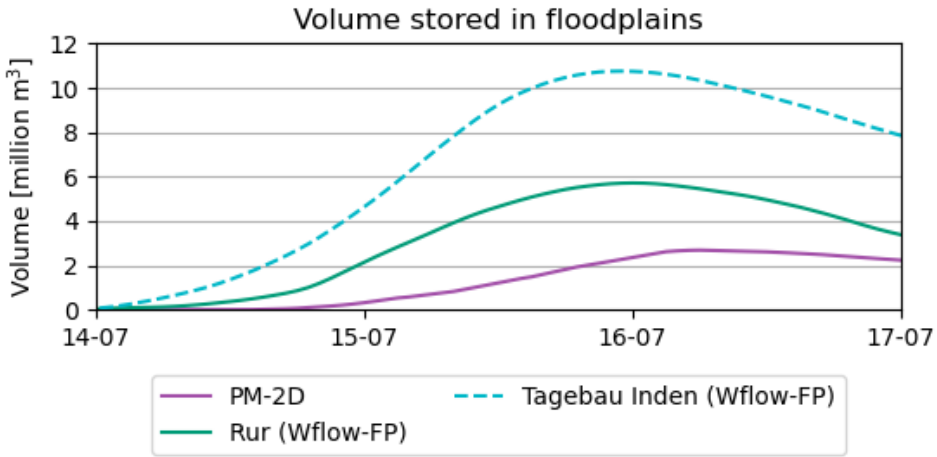

Figure 5.15: Floodplain storage for the Wflow-FP and PM-2D model during the hindcast (RADFLOOD21).

Figure 5.16: Floodplain storage for the Wflow-FP and PM-2D model during the hindcast (RADFLOOD21). The volume of water stored in the floodlpains is significantly higher for the Wflow-FP model, and flooding of the Inden lignite mine is also included and significant.

5.4. TRIBUTARY INTERACTIONS

This section focusses on the interactions between the tributaries and the Rur river during the 2021 flood event. First, the hydrographs of the three main inflows to the Rur are compared. Hereafter, the contributions of the main tributaries are compared with flows from smaller tributaries and direct runoff to the Rur river with respect to the 2021 storm, and the implications of simplifying the Rur river system are investigated.

5.4.1. PRIMARY INFLOW TO THE RUR RIVER

Three river routing schemes were compared to determine the primary inflow contributions to be used in the PM-1D and PM-2D models (Section 5.1.3). In this section, their contributions are compared in terms of volume. Figure 5.17 shows the differences between the contributions from the Obermaubach reservoir and the Inde and Wurm tributaries for the Wflow-KW, Wflow-LI and Wflow-FP models. The inflow from the Obermaubach reservoir is similar for all three models as the reservoir outflow at Heimbach has been imposed, as described in Section 5.1.2. Contributions from the Wurm and Inde are similar for Wflow-KW and Wflow-LI, both showing three peaks with can be related to the precipitation pattern observed during the flood event. The total contribution is maximum on the 15th of July and declines afterwards, and the peak of the flood wave arrives a couple of hours later at Stah.

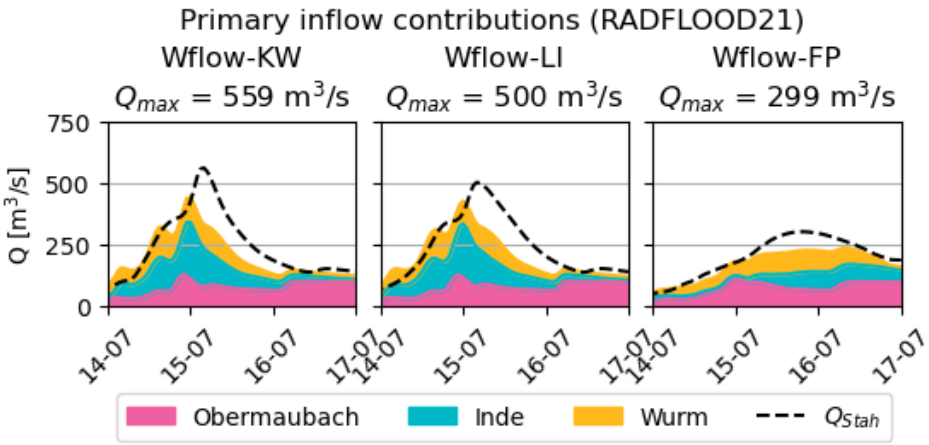

Figure 5.17: Discharge at the inflow points from the Inde and Wurm rivers and the Obermaubach dam using the RADFLOOD21 dataset. The cummulative inflow is largest on the 15th of July for the Wflow-KW and Wflow-LI models, and after the 16th of July for the Wflow-FP model.

The results differ for the Wflow-FP model where the hydrographs of the Inde and Wurm inflows has become smooth, and inflow increases until the 16th of July. Furthermore, the peak of the flood wave arrives at Stah before the summed contributions have reached their maximum.

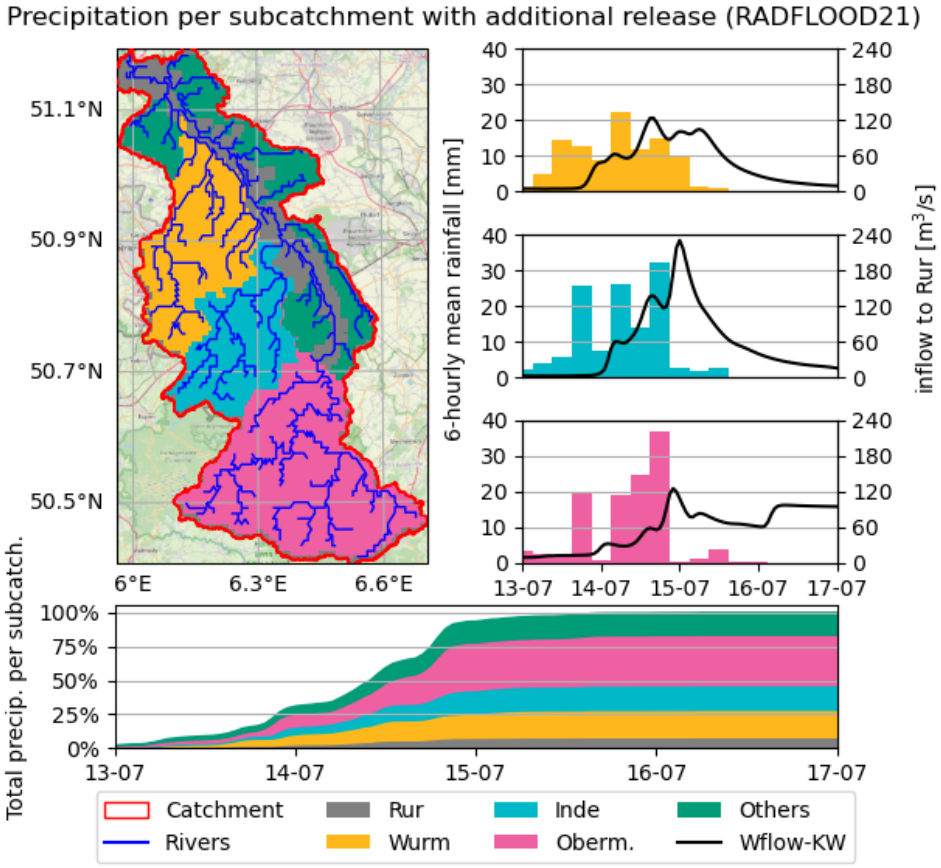

Figure 5.18: Rainfall hyetographs and the Wflow-KW hydrograph at Stah using the RADFLOOD21 dataset.

5.4.2. SUBBASIN CONTRIBUTIONS

The relative contribution of the tributaries is further analysed by investigating the amount of precipitation in each subbasin. To this end, the RADFLOOD21 dataset is analysed using *HydroMT* and *Xarray* by sampling the dataset to the resolution of the *Wflow_SBM* models and determining the average and cumulative precipitation. The result is shown in Figure 5.18 focussing on the primary flows from the Obermaubach reservoir and the Inde and Wurm rivers. Hydrographs are derived at the outlets of each of these subbasins using the Wflow-KW model, including reservoir prerelease. Furthermore, contributions of smaller tributaries flowing towards the Rur are lumped together under 'Others', and direct land runoff into the Rur is assigned the label 'Rur'.

The rain hyetographs in Figure 5.18 highlight some of the characteristics of the storm that led to the 2021 flood event. It shows that heavy precipitation occurred for 48 hours and that three distinct peaks could be observed in the Wurm and Inde hyetographs with similar peaks in the hydrograph. Furthermore, precipitation commenced in the Wurm

	Wurm	Inde	Obermaubach	Rur	Others
Surface area	20.1%	15.6%	34.1%	10.1%	20.1%
RADFLOOD21	20.1%	18.3%	37.1%	8.0 %	16.5%
E-OBS 2011-2021	19.3%	16.8%	37.7%	8.8 %	17.4%

Table 5.1: Distribution of precipitation and area for the Rur catchment.

subbasin, coincidently located most downstream of the tributaries, which generated the initial storm runoff towards the Dutch Rur for the Wflow-KW model, and most intense precipitation occurred in the Inde subcatchment at the end of the 14th of July. These observations coincide with the meteorological description in Section 4.3.2 where the peak in precipitation was observed around Aachen on the 12th of July, and the most intense precipitation on the 14th of July south of Aachen.

The contributions of Wurm, Inde and Obermaubach are significant in terms of cumulative precipitation with 20%, 18% and 37% respectively. The other smaller tributaries have a summed contribution of approximately 17%, while direct runoff towards the Rur only accounts for 8 %. The precipitation distribution during the flood event strongly resembles the 10-year E-OBS distribution of precipitation and the surface area of the subcatchments (Table 5.1), showing that the rainfall was distributed proportionally to the subbasin area in the subcatchments of the Rur river.

5.4.3. SIMPLIFYING THE RIVER SYSTEM

The previous section has shown the relative contributions of the subcatchments and the importance of the Wurm, Inde, and Obermaubach inflows. This raises the question of whether other tributaries must be included to describe the response of the Rur to the flood event, as contributions from smaller tributaries and direct runoff are significant, but spread throughout the river. Therefore, a comparison is made between a simplified PM-1D model, containing only inflows from the Wurm, Inde and Obermaubach, a PM-1D model with the tributaries included and a Wflow-FP model, which also includes overland runoff and subsurface runoff to the Rur. An alternative version of the Wflow-FP model was used for the simplified PM-1D model with an UPA of 100 km^2, which results in the *Wflow_SBM* river map that contains only Wurm and Inde as tributaries. All three models do not include the additional release from the Rur reservoir system.

Figure 5.19 displays the results at the LANUV stations in the Rur for streamflow and cumulative discharge. Differences between model results vary per station, but it is clear that the volume of water passing the station increases as more runoff processes are included, resulting in a larger peak discharge. The maximum discharge is especially reduced for the simplified PM-1D model starting with a reduction of 50 m^3/s at Selhausen increasing to 100 m^3/s at Stah, while the full PM-1D model remains closer to the Wflow-FP quantities.

Reducing the complexity of the river network also has indirect effects. For example, the Wehebach and Olef reservoirs are disconnected from the river network and therefore are no longer included in the *Wflow_SBM* models. In the *ProMaIDes* models, total runoff

to the Rur decreases as several river profiles are no longer coupled to a point inflow, although runoff still occurs at these points as the topography remains unchanged.

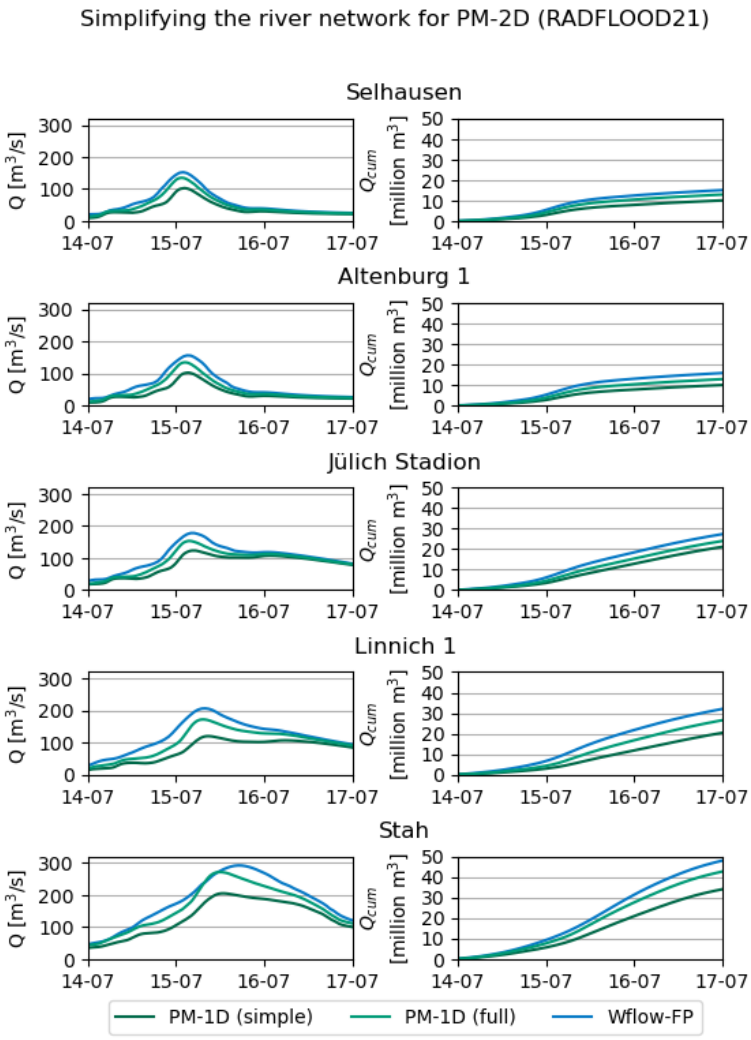

Figure 5.19: Comparison of Wflow-FP and PM-1D results with the full river network and a reduced river network using the RADFLOOD21 dataset. Reducing the river network for the PM-1D results in a decline of one-third for both peak discharge and total volume, compared to Wflow-FP results. No additional reservoir release is imposed on the Wflow-FP and PM-1D models.

5.5. RESERVOIRS

Reservoirs play an important role in flood protection due to their retention capacity and attenuation of the peak of the flood wave. These effects are investigated in this section for the Rur reservoirs during the 2021 flood event. Firstly, the effect of removing the imposed reservoir outflow is examined. Second, the sensitivity of the initial storage of the Rur reservoir system is examined. Finally, the local effects of possible increased flooding are addressed by investigating the results of the PM-2D model.

5.5.1. EXCLUDING THE ADDITIONAL RESERVOIR RELEASE

Figure 5.20 shows the differences between the hindcast results with and without imposed reservoir outflow. Without imposed reservoir outflow, the outflow is determined fully by the operational plans and therefore lower than the imposed outflow where an additional release is included. The additional release of the Rur reservoir was timed such that this release wave would not enhance the maximum flow downstream at, for example, Stah. However, the question can be asked whether this additional release from the reservoir will result in differences downstream with regard to flood depth and flood extent.

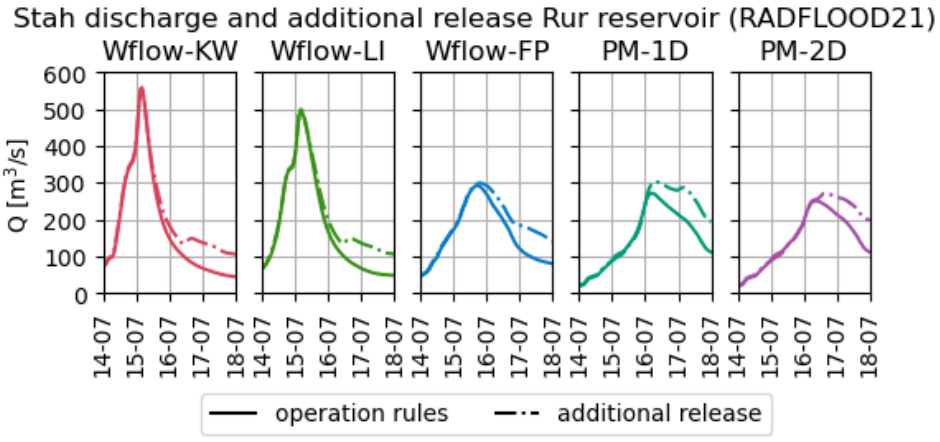

Figure 5.20: Differences in discharge at Stah between models with and without imposed reservoir outflow. The additional release affects predominantly the recession limb of the flood wave.

Including the additional release affects predominantly the recession limb of the flood wave, especially for Wflow-KW and Wflow-LI results. In these cases the additional release arrives after the peak flow has passed Stah. The model results with stronger attenuation (i.e. Wflow-FP, PM-1D and PM-2D) do show an increase of the peak discharge with a later arrival time as a results of this additional release. Still, this increase is lower than the peak of the release wave from the reservoir which arrives a day later on the 18th of July 2021.

5.5.2. INITIAL STORAGE OF RUR RESERVOIR SYSTEM

The flow of the reservoir is determined by the storage level in the reservoir, especially when no deviation is implemented from the operation plans (which occurred during the flood event of 2021). Therefore, a sensitivity analysis of the Rur reservoir system is performed by varying the initial storage level of the combined Rur reservoirs. No additional reservoir release is included in the model, and downstream results at Stah are used to investigate the arrival of the flood wave when the reservoir overflows. Only the faster Wflow-KW and Wflow-LI models are used to perform this analysis.

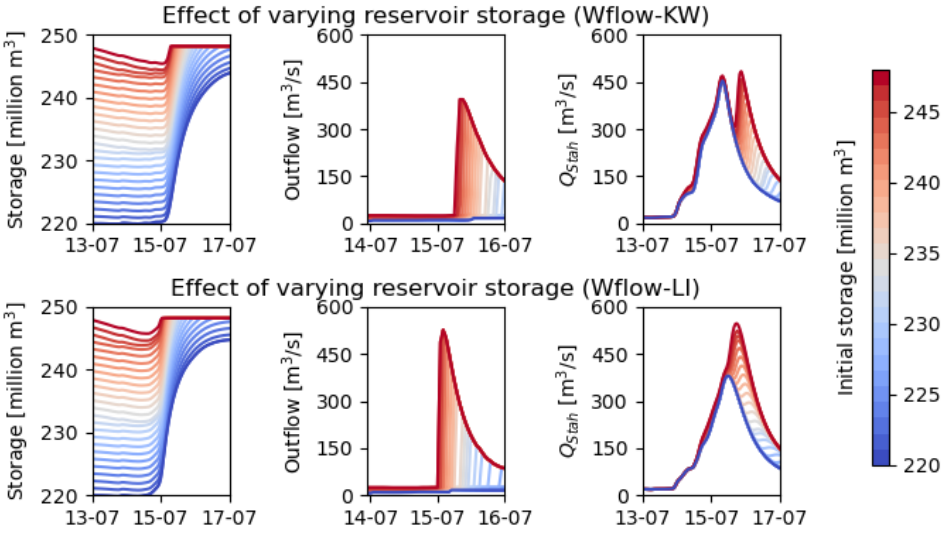

Figure 5.21: Effect of varying initial storage of the Rur reservoir system (RADFLOOD21).

The results in Figure 5.21 show that the increase in the maximum discharge in Stah depends on the type of river routing. The reservoir system is located approximately 12 hours upstream of Stah, resulting in the flood wave of the Wflow-KW model always arriving later than the first peak at Stah. Even if reservoir overflow occurs, the flood wave from the Eifel is slowed enough to ensure no increase in peak discharge. However, results show that the Wflow-KW overestimates the celerity of the flood wave. Even the Wflow-LI results, which do not include floodplain flow, show an enhancement of the peak discharge at Stah when reservoir overflow occurs.

5.5.3. FLOOD PEAK ATTENUATION AND INUNDATION PREVENTION

The reservoirs in the Rur catchment are expected to have protected the lowlands against strong inundation during the 2021 flood event. This effect is further investigated by comparing model results where reservoirs are enabled (without additional reservoir release) and fully disabled. Figure 5.22 shows the discharge at Stah without reservoirs, showing a strong increase in the magnitude of the flood wave. The Wflow-KW and Wflow-LI results are clearly too high as they lack dampening of the flood wave by inundation, but

highlight the large volume of water retained by the reservoir. The model results with floodplain attenuation (Wflow-FP, PM-1D, and PM-2D) also show a high peak discharge exceeding 400 m^3/s. Removing the reservoirs also results in a narrower shape of the flood wave, thus resulting in a lower discharge for the *Wflow_SBM* models between the 17th and 18th of July. This effects is not visible in the *ProMaIDes* results.

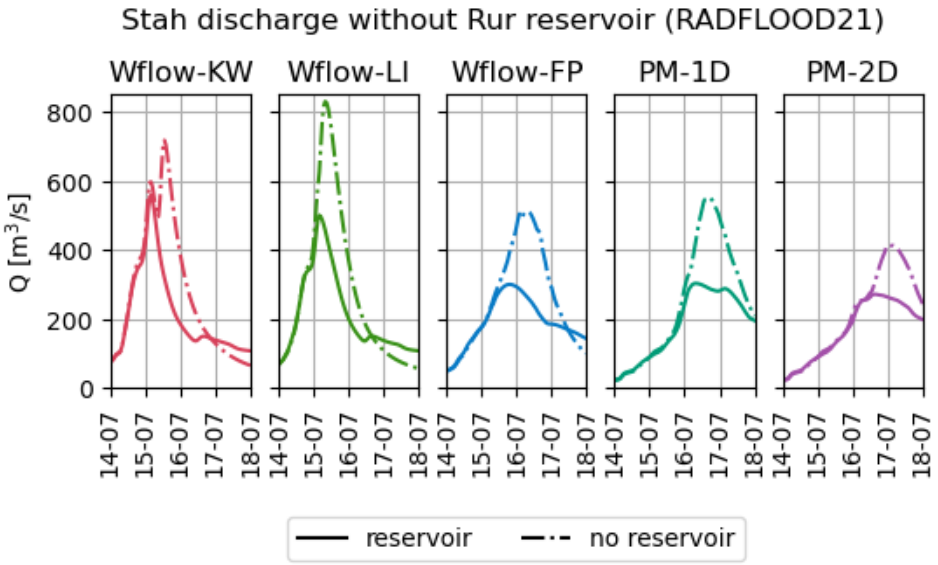

Figure 5.22: Discharge at Stah after removing the reservoirs (RADFLOOD21). The flood wave from the Eifel run-off arrives after the peak at Stah for the Wflow-KW model, resulting in a limited peak discharge. For all the other model results, the peak flow is strongly enhanced by the Eifel run-off.

The effects of such an increased flow magnitude can be visualised by inundation maps. Figures 5.24 and 5.25 show the increase in flooding for the upper and lower Rur, respectively. The flood already occurs downstream of Obermaubach, thus slowing the flood wave and reducing its peak magnitude. Changes in inundation depth remain limited near the Dutch-German border, where the wide floodplains were already inundated. Flooding occurs in Roermond, but remains limited according to the model results.

Figure 5.23 depicts the flood arrival time and clearly highlights that the flood is caused by the late flood wave arriving from Eifel, which would normally be captured by the Rur reservoir system.

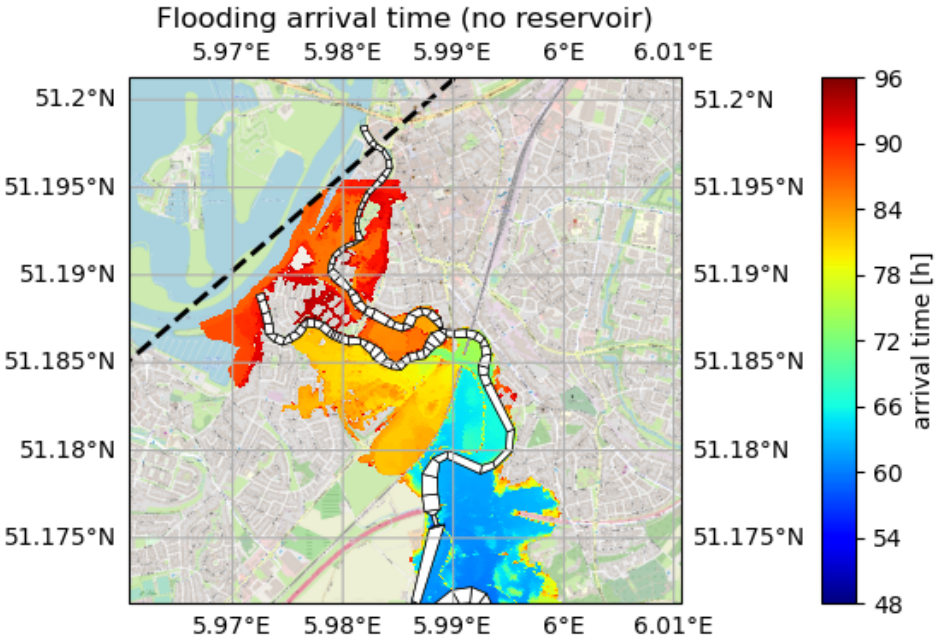

Figure 5.23: Flood arrival time after 00:00 on the 13th of July 2021 in Roermond when reservoirs are removed. Inundation is caused by the run-off from the Eifel which is not dampened by the presence of any reservoirs. Generated using PM-2D and RADFLOOD21.

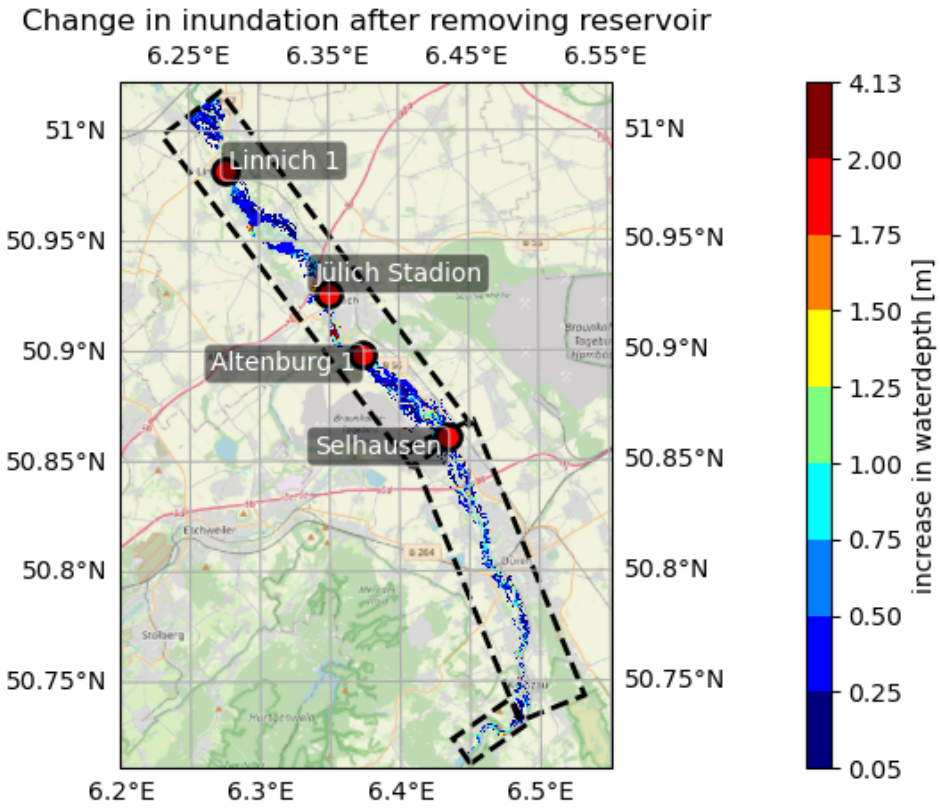

Figure 5.24: Increase in inundation of the upper Rur after removing reservoirs. Generated using PM-2D and RADFLOOD21. Flooding occurs along the whole Rur slowing dampening the flood wave generated by Eifel run-off.

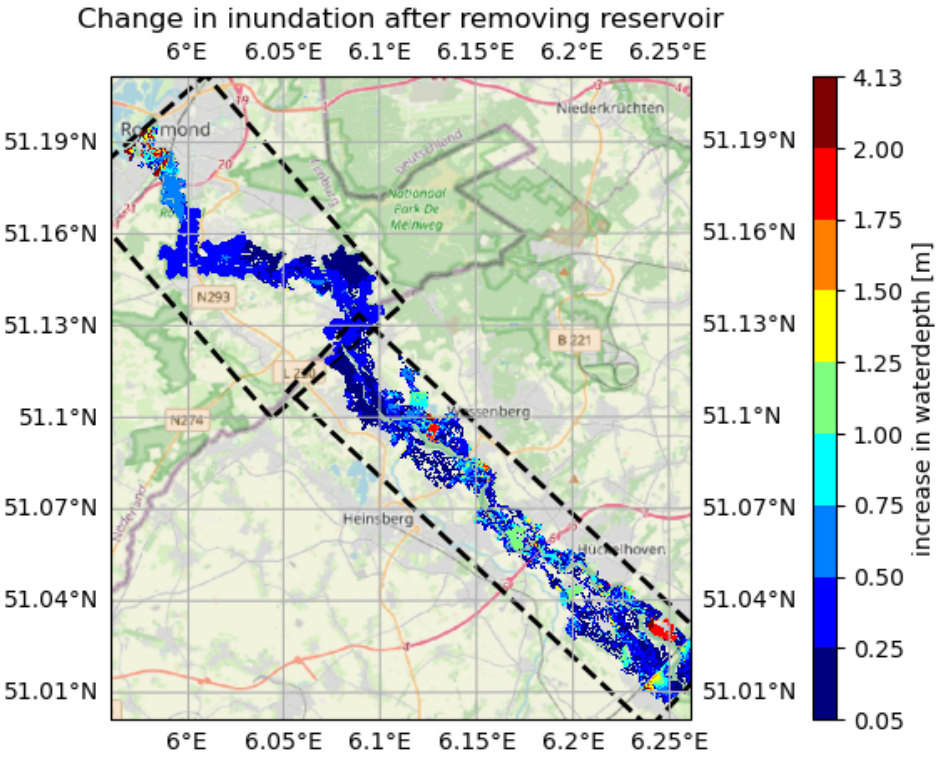

Figure 5.25: Increase in inundation of the lower Rur after removing reservoirs. The increase of the maximum water depth remains limited to several decimeters in the wide floodplains of the Dutch Rur. Additionally, flooding occurs in parts of the city of Roermond. Generated using PM-2D and RADFLOOD21.

5.6. GROUNDWATER EFFECTS

The Stah gauge station is used to investigate the effects of the leakage term on peak flow (Figure 5.26), as it is the station downstream of the Wurm confluence and is therefore affected by leakage in the subbasins of both the Inde and Wurm tributaries. The *Wflow_SBM* models with the leakage term included produce a lower peak flow at Stah. This is observed directly in the Wflow-KW, Wflow-LI, and Wflow-FP results and indirectly in the PM-1D and PM-2D results, as leakage is not explicitly included in the *ProMaIDes* models. The maximum discharge is reduced by approximately 10 to 25 % and the overall hydrograph has a smoother shape, for the PM-1D and PM-2D results.

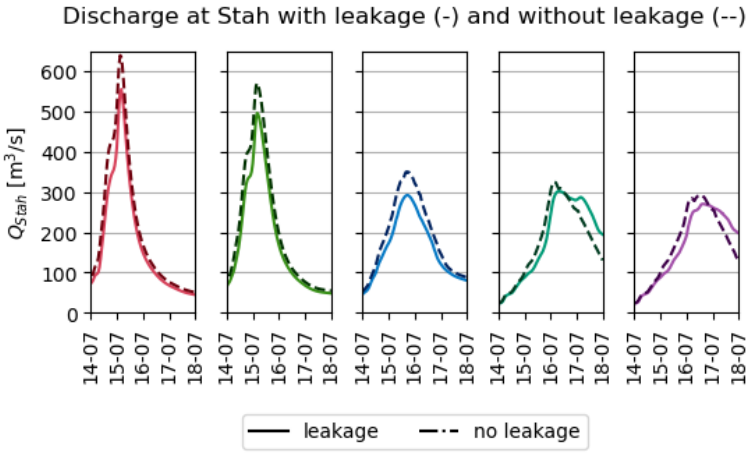

Figure 5.26: Difference in peak discharge at Stah when leakage is removed using RADCLIM21. The peak discharge increases for all model results and the rising limb of the flood wave appears earlier.

The large differences in discharge suggest that a large volume of water is affected by the leakage. Therefore, the total volume of leaked water from the *Wflow_SBM* model results is compared with the difference in cumulative discharge at the gauge station in Stah in Figure 5.27 for all models. The Wflow-FP model results are used for the total leakage, which produced almost identical results as the Wflow-KW and Wflow-LI models.

These results show that in the first 24 hours, the volume difference in Stah is slightly less than the total leakage. This is expected because areas downstream of Stah are also affected by the leakage parameter, and therefore the 'volume loss' observed at Stah should be lower than the leakage volume. However, as precipitation begins, the difference at Stah increases and exceeds the total leakage volume strongly. Therefore, the differences in discharge between models with and without leakage cannot be fully explained by the volume losses of the leakage term.

Further investigation of the hydrological model shows changes in storage between models with and without leakage, as shown in Figure 5.28. Again, the Wflow-FP model is used, but it produced very similar results to the Wflow-KW and Wflow-LI models. Initially, the difference in the average stored water of the catchment remains approximately

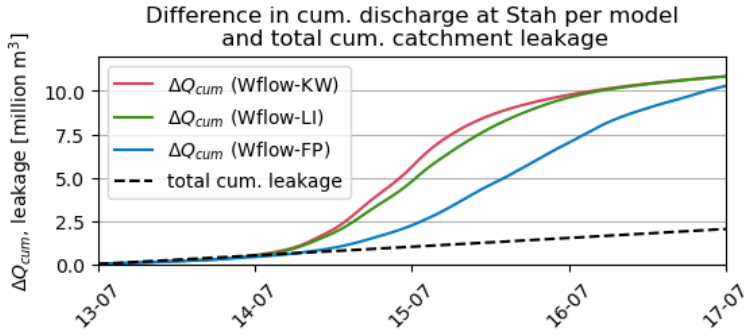

Figure 5.27: Cummulative discharge increase at Stah when leakage is removed using RADCLIM21. Note that the difference in cummulative flow is significantly larger than the volume of total leakage.

constant. The model without leakage stores a larger volume of water than the model with leakage, but the difference between the two remains constant, as indicated by the catchment storage relative to the storage at 00:00:00 on 13-07. When heavy precipitation starts, the storage in the *Wflow_SBM* models with leakage increases faster than Wflow-FP without leakage, and consequently, a relative increase in water storage is observed for the model with leakage and therefore a flow reduction is observed at Stah.

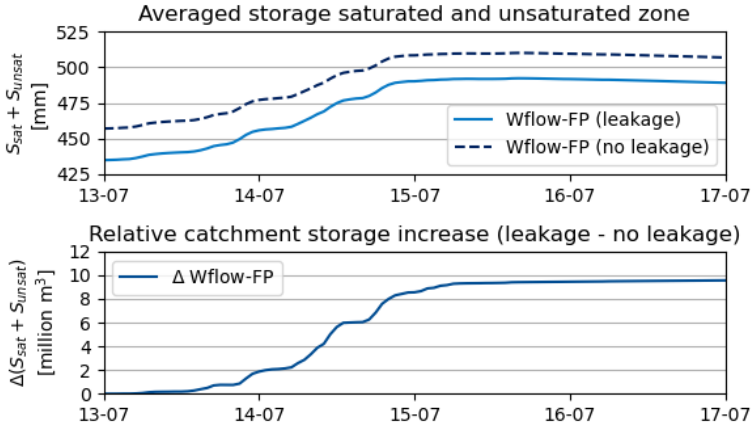

Figure 5.28: Increase in storage for the Rur catchment using RADCLIM21. Including leakage in the *Wflow_SBM* models results in a relative increase of the storage on catchment scale.

Following these observations, the indirect effects of the term of leakage, which determines the additional storage of the subsoil, appear to be more significant than the direct leakage itself during the flood event.

6

UNDERSTANDING CATCHMENT RESPONSE USING FORECASTS

SIMILAR to chapter 5, several topics are explored that are expected to be relevant for flood forecasting in the Rur basin. To this end, precipitation forecasts for the 13th of July and onwards are used obtained from the ICON-EU EPS. This ensemble product consists of 40 independent members, each with its own precipitation pattern and volume. To illustrate these differences between the ensemble members and how they relate to the RADFLOOD21 hindcast, Figure 6.1 shows a comparison of the mean cumulative precipitation for the entire Rur basin, used as forcing data for the *Wflow_SBM* models.

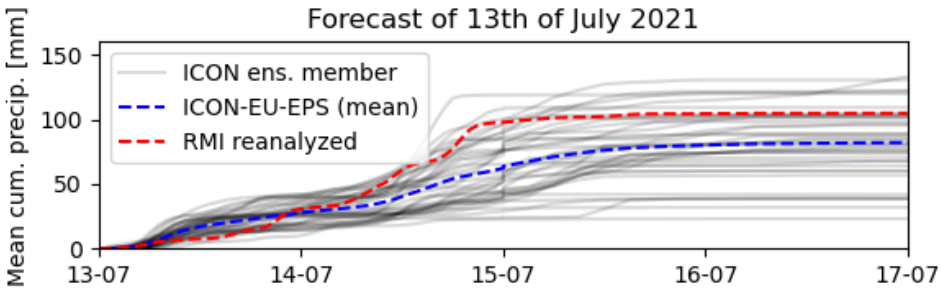

Figure 6.1: Mean cumulative precipitation for the 40 ensemble members of the ICON-EU EPS dataset. The blue line marks the mean of all 40 ensemble members, and the red line is the mean cumulative precipitation of the RADFLOOD21 dataset. The vertical 'jumps' on 15-07 are the result of the timestep change, increasing from $\Delta t = 1$ to $\Delta t = 3$ hours.

It is interesting to note that the ensemble predictions in fact underestimated the total precipitation in the catchment when comparing the mean of the ensemble dataset with the RADFLOOD21 hindcast. Furthermore, the precipitation patterns also vary between

these 40 members of the group (see Figure 4.12), making this dataset suitable for a quantitative analysis of the response of the catchment that highlights its sensitivities.

An important remark is that the PM-2D results in this chapter end on the 16th of July, while the Wflow-KW, Wflow-LI, Wflow-FP and PM-1D results run until the 18th of July. This difference can be attributed to the long computational time of the required simulation, especially for 40 ensemble members with the limited hardware available.

6.1. FLOOD WAVE ROUTING

The results in Section 5.2 demonstrate the challenges in observing flood wave attenuation as a result of lateral inflow, both overland and through tributaries. Furthermore, observing the shape of the flood wave and delineating the baseflow and stormflow for all ensembles proved to be very difficult. As a result, differences in flood wave routing are addressed by observing flood peak arrival times at gauge station locations along the Rur River for ensemble results. The results are compared for the Wflow-KW, Wflow-LI, Wflow-FP, PM-1D, and PM-2D models.

Figure 6.2 shows the spread of arrival times for the three models for the gauge stations located on the Rur River and at Obermaubach. The curves describing the arrival times for the PM-1D model show similar slopes, as they are affected similarly by lateral inflow which takes place at selected river profiles. The Wflow-KW and Wflow-LI models have more variation within the distribution as land runoff and subsurface flows are included in the river cells, thus affecting river flow along the entire Rur reach. Furthermore, peak arrival times at Obermaubach are identical for the PM-1D model and Wflow-FP model, as the boundary condition for the PM-1D model is generated using the Wflow-FP model.

Highlighting the average peak arrival times, as demonstrated in Figure 6.3, shows that on average the flood wave peak travels more slowly in the PM-1D model and that attenuation is stronger past Jülich. This can be attributed to the river profiles containing wide embankments inside the 1D river model, allowing the PM-1D model to simulate the attenuation that occurs when the bankfull depth of the river is exceeded. Parts of these cross-sections are also included in the Wflow-KW and Wflow-LI models, but to a limited extent.

The ensemble envelope for the *Wflow_SBM* results (Figure 6.4) further underlines how the hydrographs of the ensemble members develop as the flood wave propagates downstream of the Rur River. The Wflow-KW and Wflow-LI models look similar with little attenuation occurring for the Wflow-LI results. However, this is much smaller compared to the effect of including floodplain flow in Wflow-FP, resulting in smoother hydrographs and lower peak discharges.

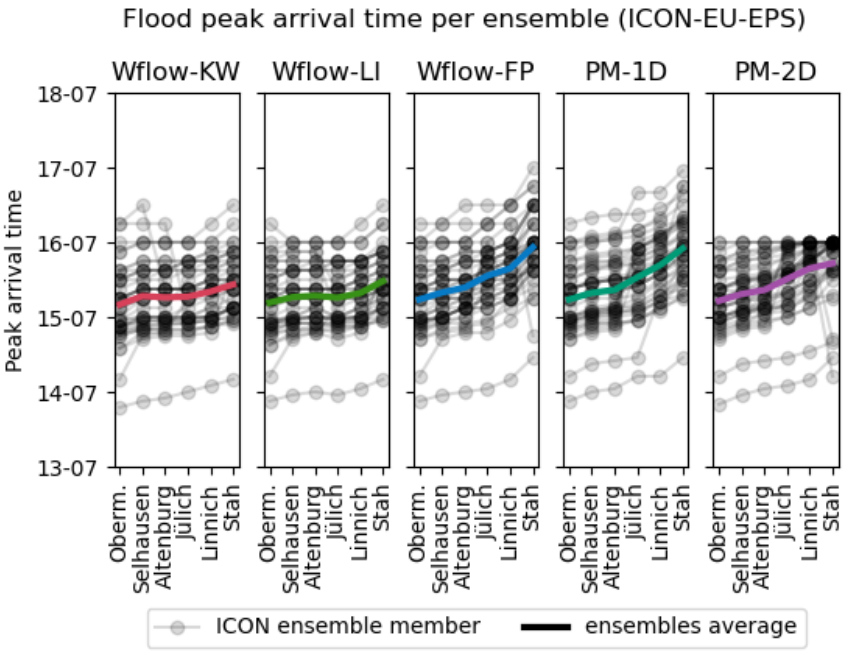

Figure 6.2: Flow peak arrival times for the 40 ensemble members of the ICON-EU EPS dataset. The dotted line indicated the average arrival time of the ensemble members at the corresponding station. On average, the Wflow-KW and Wflow-LI show similar results in terms of flood wave routing, as to Wflow-FP and PM-1D. It should be noted that the PM-2D simulations all ended on the 16th of July instead of the 18th of July.

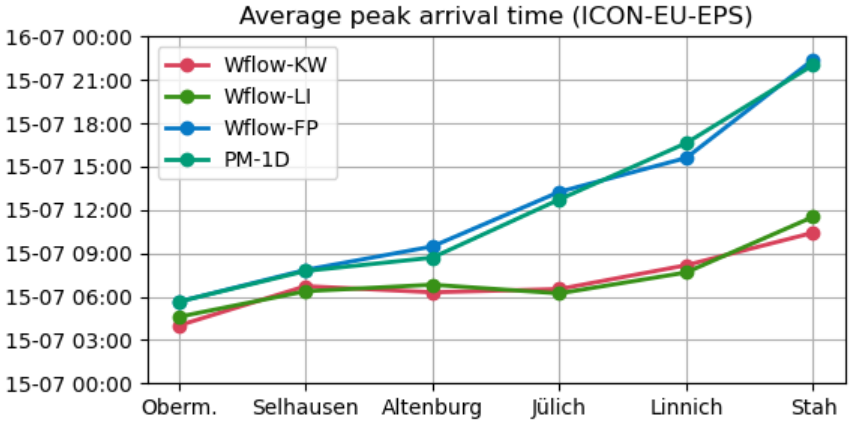

Figure 6.3: The average flow peak arrival times of the 40 ensemble members of the ICON-EU EPS dataset. The dotted line indicated the average arrival time of the ensemble members at the corresponding station. PM-2D results have been left out as their average was strongly affected by the shorter simulation period ending on the 16th of July.

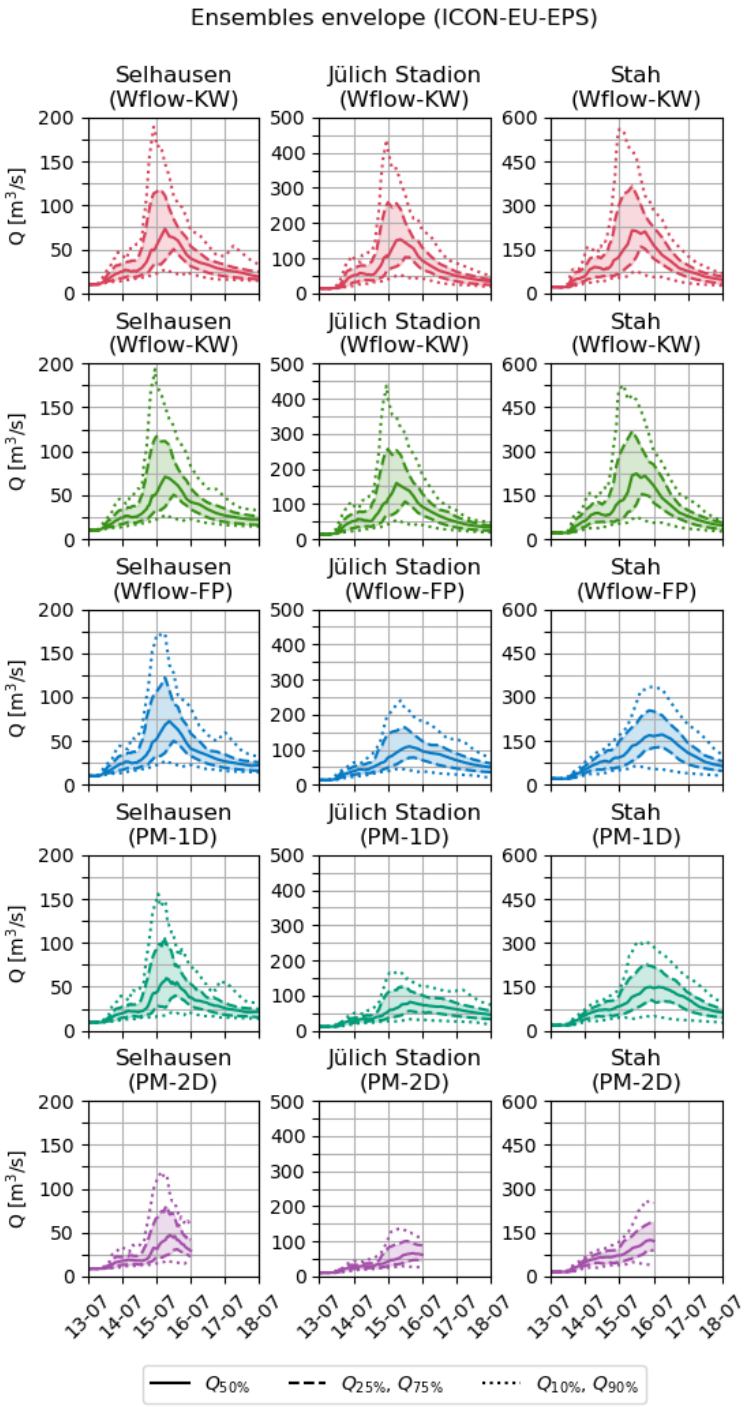

Figure 6.4: Envelope of the hydrographs for the 40 ensemble members of the ICON-EU EPS dataset for the *Wflow_SBM* and *ProMaIDes* models at Selhausen, Jülich Stadion and Stah. All envelopes are similar at Selhausen, but start to show differences at Jülich Stadion and Stah as a result of floodplain attenuation. Note that the PM-2D simulations stopped on the 16th of July.

6.2. FLOODPLAIN INUNDATION

The influence of flooding on the propagation of flood waves is investigated by comparing hydrodynamic results between similar models: Wflow-LI and Wflow-FP, and PM-1D and PM-2D. The Wflow-FP model is an extension of the Wflow-LI model with a 1 dimensional floodplain schematization, and similarly, the PM-2D is an extension of the PM-1D model with 2 dimensional floodplain flow. Therefore, the peak flows of these model results are compared to gain insight into the effect of floodplain flow attenuation. In addition, flood heat maps of the PM-2D results are examined to gain insight into where floodplain flow occurs.

6.2.1. PEAK FLOW

Firstly, the peak discharges of the 40 ensemble members are compared in Figure 6.5. Three stations were chosen, namely Selhausen (downstream of the reservoir), Jülich Stadion (downstream of the Inde confluence), and Stah (downstream of the Wurm confluence). These model results show floodplain attenuation, especially downstream of tributary inflows at Jülich Stadion and Stah. This attenuation effect is stronger in the transition from no floodplain flow to one-dimensional floodplain flow (Wflow-LI to Wflow-FP) and appears at different magnitudes of peak discharge.

The difference in attenuation is less visible for the *ProMaIDes* models, which both contain some form of floodplain discretization. Still, strong attenuation is observed for the outliers of ensemble members 14, 31 and 40 for which the 2 dimensional floodplain flow is expected to be important as the river starts flowing outside of its banks. Furthermore, the spread in peak discharge is reduced for PM-2D models and seems to approach a physical limit (Q_{limit}) at Stah. Only the three outliers exceed 300 m^3/s at Stah for these models, while several Wflow-FP model results do exceed these thresholds.

Comparisons between the arrival of the flood wave peak (Figure 6.6) show similar attenuation effects. Generally, the peak arrival time is extended when floodplain flow is included in the discretization. The expectation for ensemble member 19 can be explained due to the fact that simulated discharges are very low and therefore little attenuation results in a different part of the flood wave becoming the new 'peak'.

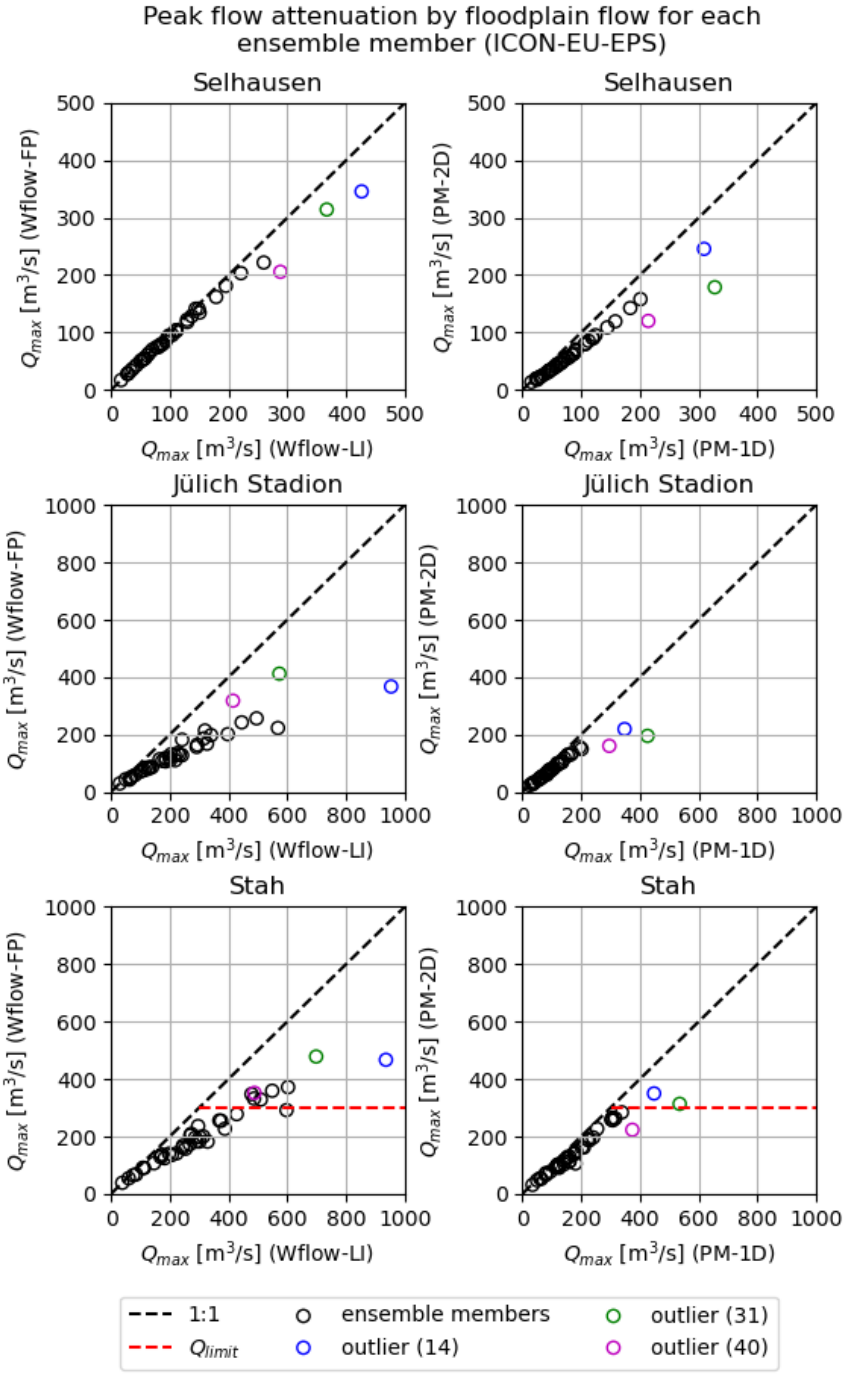

Figure 6.5: A comparison of maximum peak discharge between Wflow-LI and Wflow-FP, and PM-1D and PM-2D. The PM-2D results at Stah seem to approach a limit of Q_{limit} = 300 m^3/s, which may indicate the maximum capacity of the Dutch Rur during extreme flow conditions.

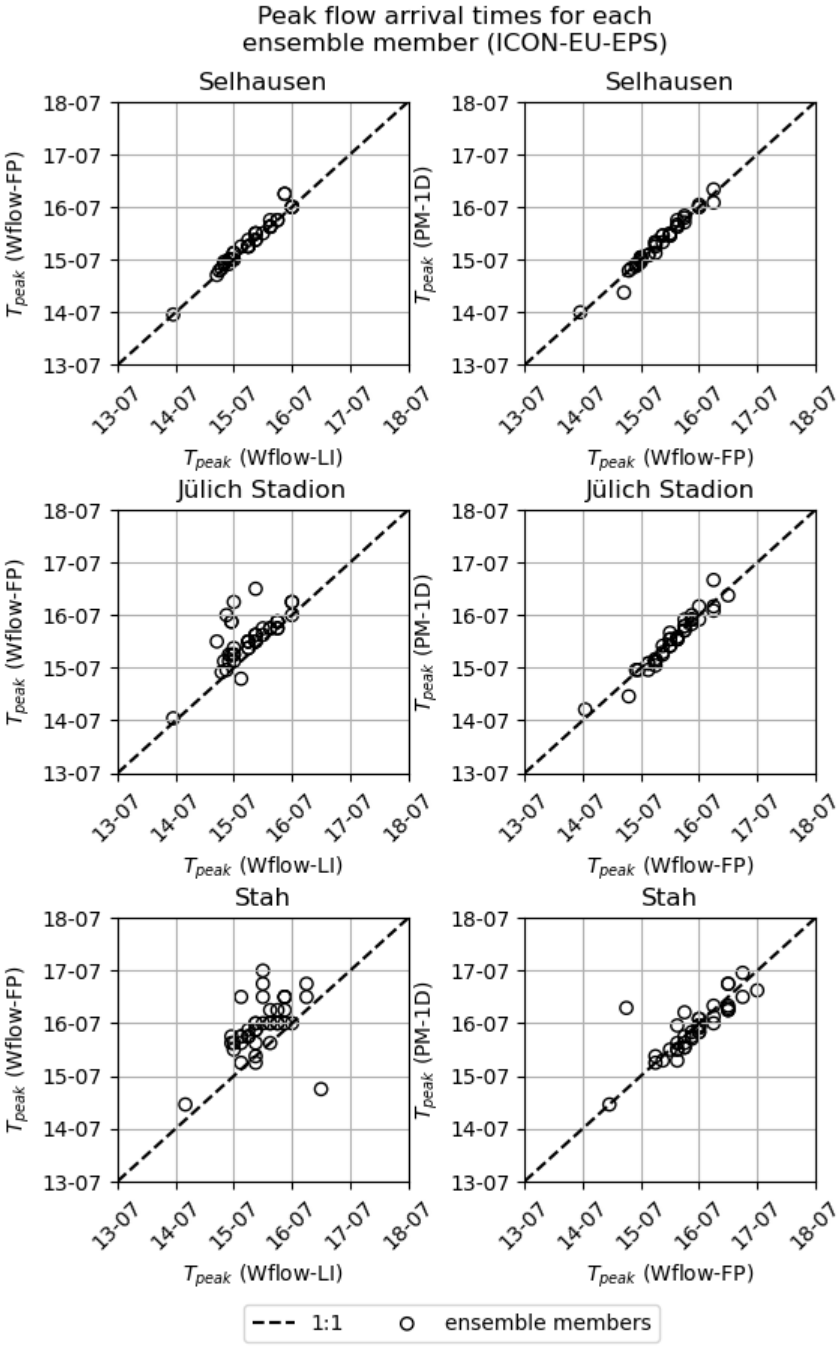

Figure 6.6: A comparison of peak arrival time between Wflow-LI and Wflow-FP, and Wflow-FP and PM-1D. Flood peak arrival times are similar for the Wflow-FP and PM-1D models, both simulating floodplain attenuation, and differ with respect to the Wflow-LI results.

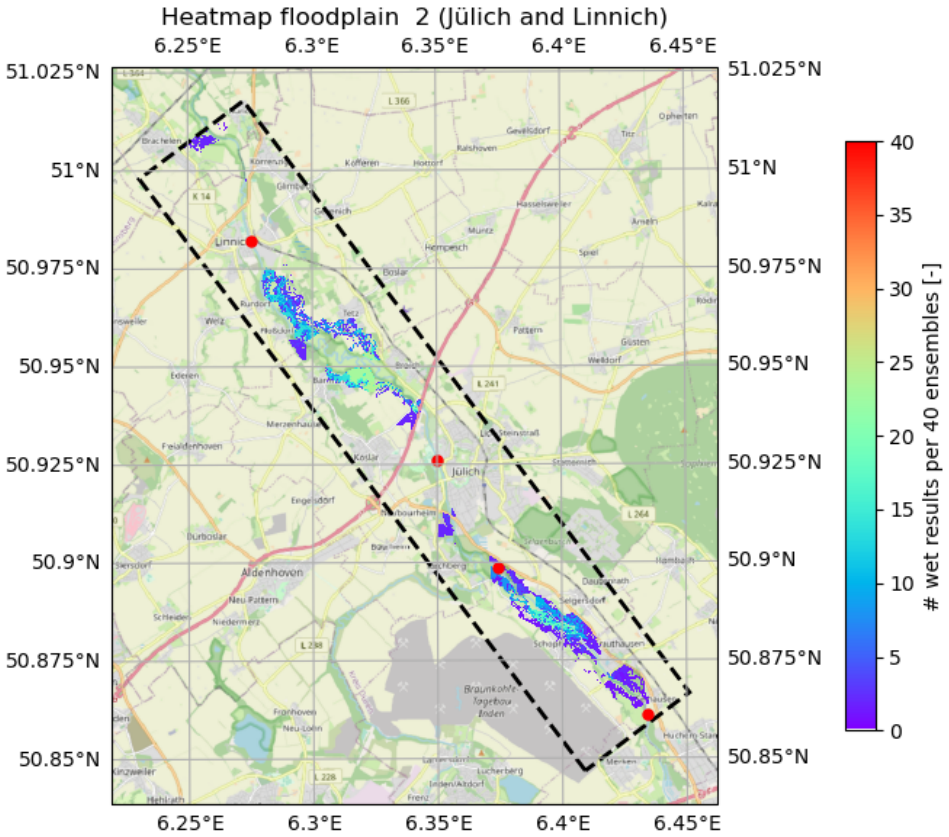

Figure 6.7: PM-2D inundation heatmap (floodplain grid 2) at Jülich and Linnich with, in upstream direction, gauge stations Selhausen, Altenburg 1, Jülich Stadion and Linnich 1. Floodplain flow occurs between Jülich and Linnich, but remains limited to 10-20 ensemble members.

6.2.2. INUNDATION HEATMAP

The PM-2D floodplain results are further investigated to gain insight into the location of floodplain flow by creating a heat map of the wet cells in the floodplain grids. Floodplain grids 0 and 1 show limited flooding, as reservoir flow dominates in these reaches. Therefore, only floodplain grids 2, 3 and 4 are considered. Figure 6.7 shows that floods occur near the cities of Jülich and Linnich in the wide floodplains of the Rur, and the gaps in these inundated areas can be explained by changes in the cross-sectional widths of the 1-dimensional river model inside the PM-2D model. The corresponding gauge stations are located inside the cities of Linnich and Jülich, where the flow concentrates and no inundation occurs.

Inundation increases in the lower Rur, especially around and downstream of the gauge station at Stah (Figure 6.8). The differences in colour of the heat map indicate that the floodplain flow pattern is complex: floodplains with gradually changing colour show that

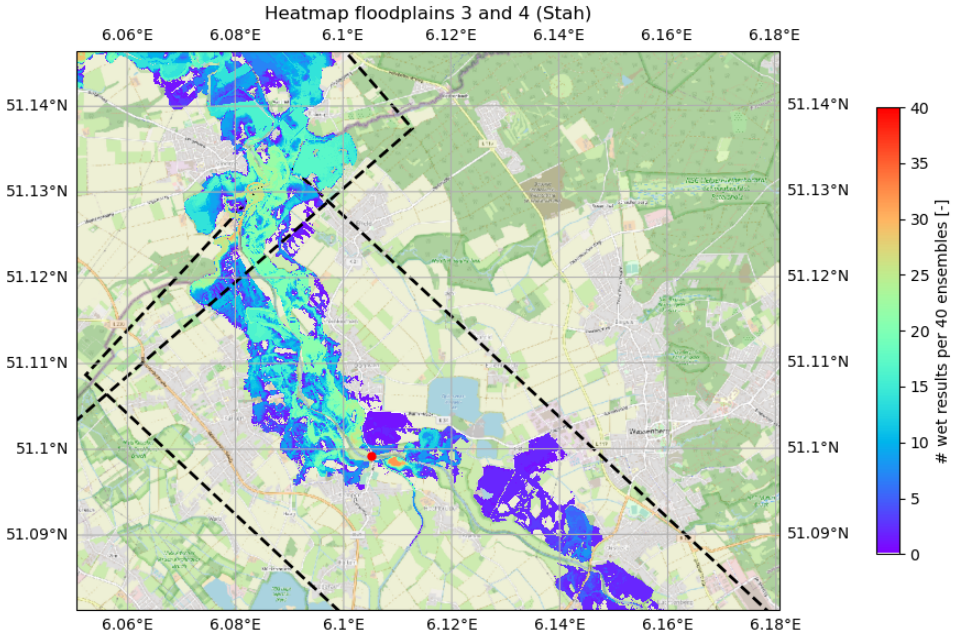

Figure 6.8: PM-2D inundation heatmap (floodplain grids 3 and 4) at gauge station Stah, indicated by the red dot. Inundation is limited to few ensemble members before Stah, and increases in downstream direction.

for some areas the flood extent increases gradually as discharge varies, while other inundated areas are of uniform colour, indicating that inundation is only limited to a fixed number of ensemble members. Such dynamics can be captured by the PM-2D model, but to a lesser extent by the Wflow-FP and PM-1D models. Flooding in urban areas does occur for some ensemble members, for example, at Ophoven, which also experienced a dike breach during the 2021 flood event.

Figure 6.9 highlights the storage capacity of the floodplains for the Dutch Rur, which inundated a large number of members of the ensemble. Floodplains are wide and relatively uniform in depth, so that an increase in discharge generally increases the depth of the water, while the additional extent of the flood remains limited. Additionally, floodplain flow is well contained within wetlands with limited flooding near urban areas. Flooding occurs in Roermond, but it remains limited to very few members of the ensemble, as shown in Figure 6.10.

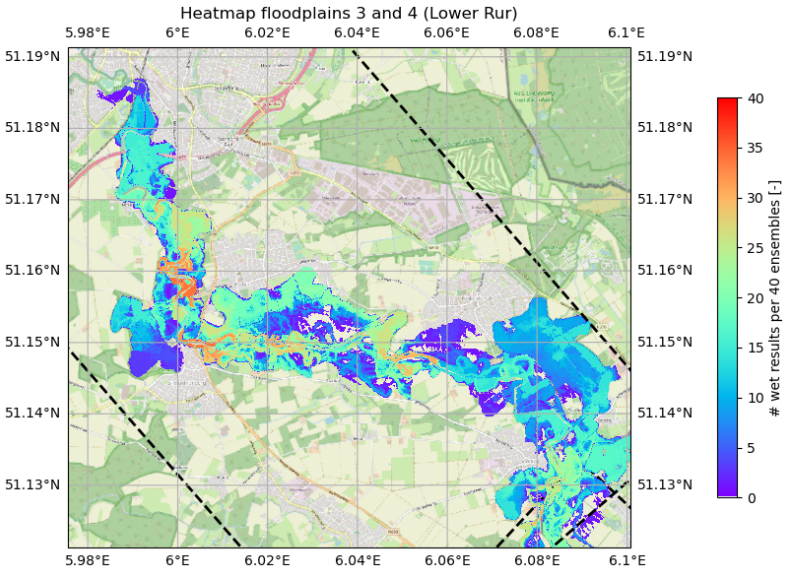

Figure 6.9: PM-2D inundation heatmap at the lower Rur (floodplain grids 3 and 4). Almost all ensemble members show inundation of the floodplains, and inundation patterns are complex with dry areas being fully enclosed by floodplain flow.

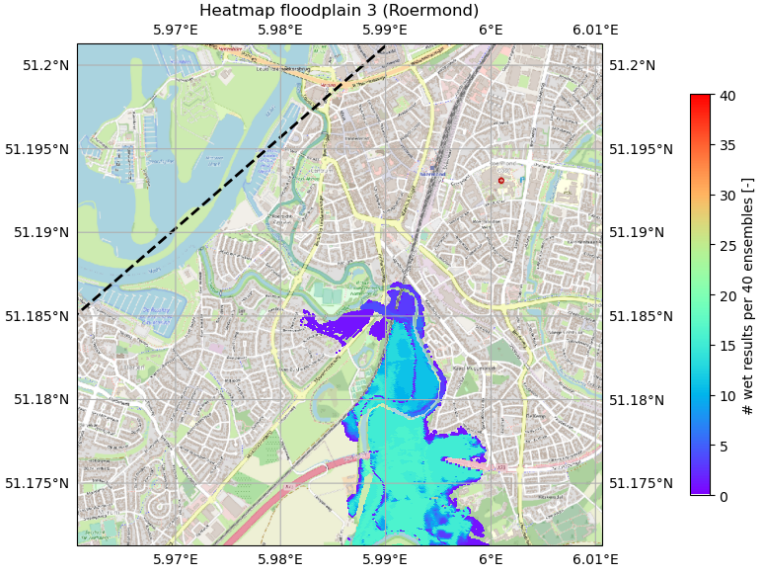

Figure 6.10: PM-2D inundation heatmap at Roermond (floodplain grid 3). Flooding of Roermond, which can be attributed to a discretization error in the DEM of the PM-2D model, is limited to only a couple of ensemble members.

6.3. RESERVOIRS

Previous chapters have shown how reservoirs influence flood safety and flood wave propagation, and how reservoirs affect the magnitude and timing of the flood wave peak. Therefore, the effects of Rur reservoirs on flood wave response are investigated in this section by comparing reservoir performance for the 40 ensemble members and observing how removing the reservoirs affects flood wave propagation. In this section, only the *Wflow_SBM* models are considered, as they describe the reservoir processes and the river and land routing to the reservoirs. Therefore, the effects of floodplain flow and inundation are not included in the analysis in this section.

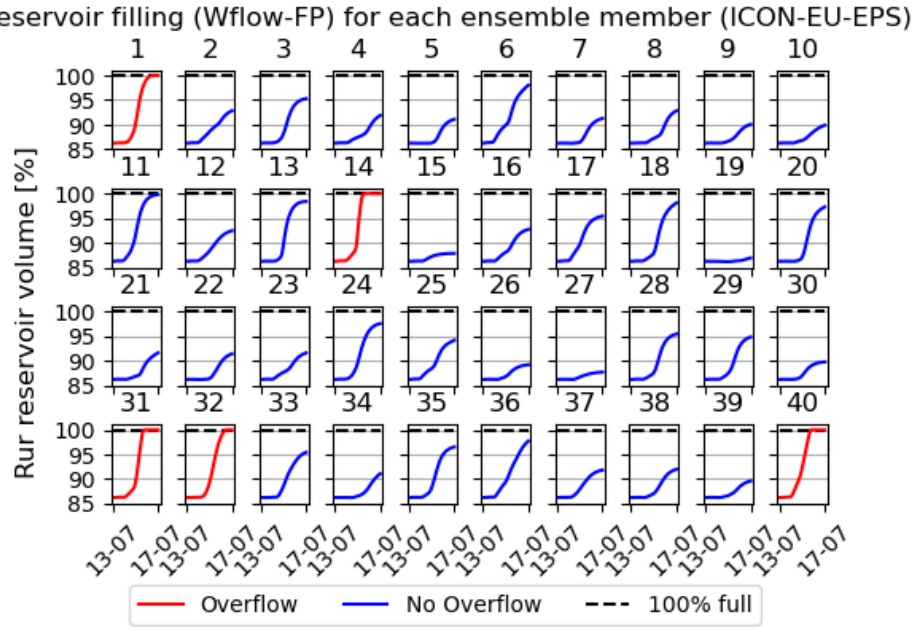

Figure 6.11: Reservoir storage for each of the 40 members of the ICON-EU EPS dataset using the Wflow-FP models. Reservoir overflow was observed for ensemble members 14, 31, and 40.

6.3.1. RESERVOIR OVERFLOW

Figure 6.11 shows how the Rur reservoir storage reacted to the flows generated by each of the members of the group using the Wflow-FP model. Clearly, the storage capacity of the Rur reservoir resulted in a decrease in discharge to the downstream Rur for most of the ensemble members, as the flood wave that came from Eifel was fully stored in the reservoir. However, precipitation and runoff for members 14, 31, and 40 of the ensemble were large enough to cause significant reservoir overflow and little overflow for members 1 and 32. Similar results were obtained when using the Wflow-KW and Wflow-LI models for which the timing of the runoff varied, but a similar volume of inflow was obtained.

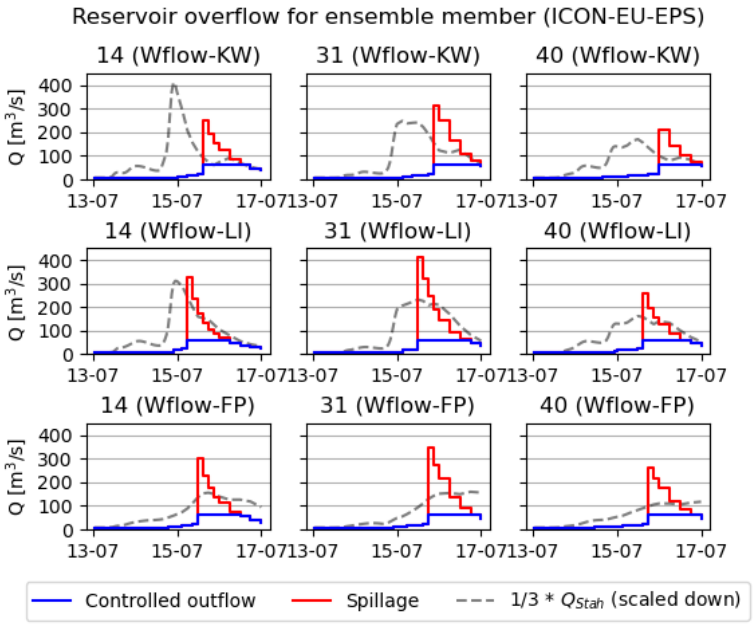

Figure 6.12: Reservoir outflow for members 14, 31, and 40 of the ICON-EU EPS dataset using the Wflow-KW, Wflow-LI and Wflow-FP models. The timing of the overflow is compared to the peak flow at Stah, approximately 12 hours downstream of the Rur reservoir.

The controlled reservoir outflow is modelled to be limited to Q_{max} = 60 m^3/s, which is also the maximum outflow of the reservoir when no overflow occurs. When the reservoir storage capacity reaches zero, overflow occurs in the form of spillage. In this case, the magnitude and duration of the spill depend on the timing and magnitude of the runoff to the reservoir.

This is confirmed by the results in Figure 6.12 which displays the spillage for members 14, 31, and 40 of the ensemble for both the Wflow-KW, Wflow-LI and Wflow-FP models. Using a diffusive routing scheme for river routing results in faster runoff to the reservoir, resulting in earlier reservoir overflow with a higher outflow peak with a maximum of approximately 350 m^3/s for run 31.

Although a high outflow is observed, the reservoir overflow slows down the flood wave because the leading edge of the flood wave is stored in the reservoir. Assessing the exact timing of reservoir overflow is difficult, as it happens in the forecast window for which the time step has increased to Δt = 3 - 6 hours, but the travel time of the flood wave between the reservoir and Stah is known to be approximately 12 hours. The flood wave peak passes through Stah before the reservoir overflow occurs, and since the travel time is equal to 12 hours, the reservoir overflow peak is not expected to enhance the peak of the flood wave in the Rur River.

6.3.2. FLOOD WAVE ATTENUATION

Previous results show how reservoirs fill up when a flood wave arrives, slowing down and decreasing the flood wave peak. These effects can be highlighted by comparing the downstream magnitude and arrival time of the flood wave peak between model runs with reservoirs and without, for which it should be noted that not only the Rur reservoir is removed, but also the Olef and Wehebach reservoirs. This comparison has been made for the Wflow-KW, Wflow-LI and Wflow-FP models, for which the results are displayed in Figure 6.13. These results (table 6.1) show that the peak discharge can increase almost twice when there are no reservoirs. Furthermore, the arrival time of the peak of the flood wave in Stah is delayed for the Wflow-KW and Wflow-LI models when the reservoirs are removed, as the flood wave arriving from Eifel determines T_{peak} (Figure 6.14).

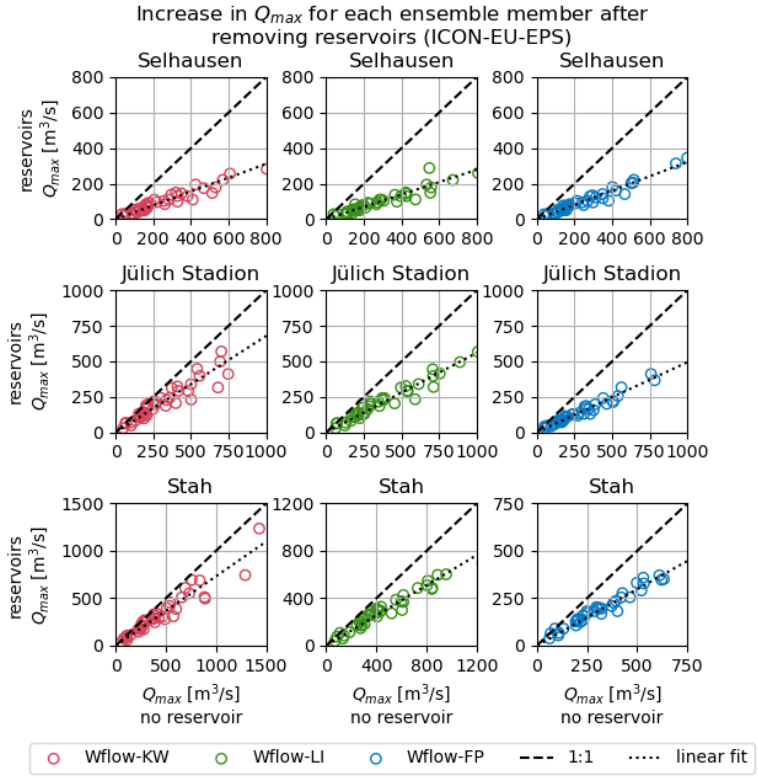

Figure 6.13: Magnitude of the flood wave peak at Selhausen, Jülich Stadion and Stah for each of the 40 members of the ICON-EU EPS dataset using the Wflow-KW, Wflow-LI and Wflow-FP models. The increase in Q_{max} is largest at Selhausen, where flow is dominated by the reservoir outflow. The relative increase becomes smaller at Jülich Stadion and Stah where inflows from respectively the Inde and Wurm rivers enter the Rur.

	Q_{max} reduction factor f_{res}		
station	**Wflow-KW**	**Wflow-LI**	**Wflow-FP**
Selhausen	0.389	0.348	0.403
Jülich Stadion	0.679	0.560	0.494
Stah	0.732	0.637	0.595

Table 6.1: Average reduction of peak flow for the 40 ICON-EU-EPS ensemble members when reservoirs are included in the model.

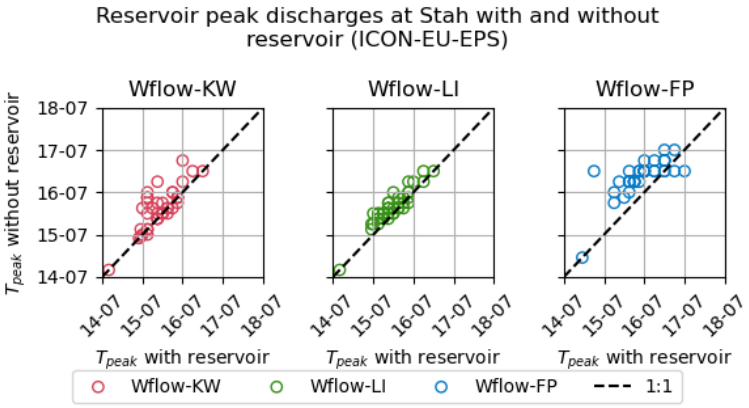

Figure 6.14: Timing of the flood wave peak at Stah for each of the 40 members of the ICON-EU EPS dataset using the Wflow-KW and Wflow-LI models. The outlier observed for ensemble member 19 is the result of the peak with a limited magnitude (around 50 m^3/s) arriving outside of the temporal model domain at Stah for the Wflow-LI model without reservoirs, resulting in another small peak becoming Q_{max}.

6.4. GROUNDWATER EFFECTS

In this section, the effects of the leakage parameter on the *Wflow_SBM* results for the ICON-EU-EPS ensemble members are investigated. To this end, the results of the *Wflow_SBM* models with leakage are compared with the results of the models without leakage. Figure 6.15 shows the decline in peak discharge in Honsdorf, Randerath, and Stah. The reduction is strongest at Honsdorf, which is located entirely on the Rurscholle and therefore fully affected. The reduction is lower in Randerath and Stah, located downstream of the Wurm and Rur rivers, but still significant, as shown in the table 6.2. It is interesting to note that the effect appears to be proportional to the peak discharge at all stations and for all models. As a result, a linear fit is also included in Figure 6.15 for which the slope is proportional to the values in Table 6.2: $Q_{max,leakage} = f_{leak} \cdot Q_{max,noleakage}$

	Q_{max} reduction factor f_{leak}		
station	**Wflow-KW**	**Wflow-LI**	**Wflow-FP**
Honsdorf	0.354	0.357	0.367
Randerath	0.815	0.818	0.797
Stah	0.830	0.841	0.812

Table 6.2: Average reduction of peak flow for the 40 ICON-EU-EPS ensemble members when leakage is added to model results.

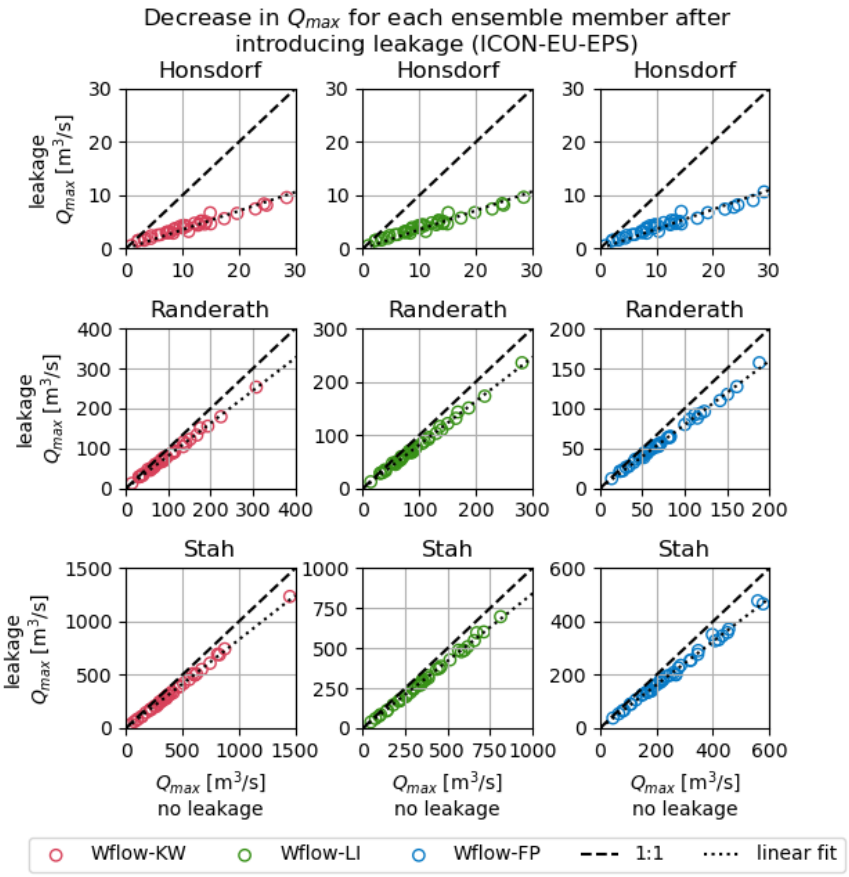

Figure 6.15: Peak discharge at Stah for the *Wflow_SBM* models with and without leakage using the ICON-EU-EPS ensemble members. Including the leakage term results in a decrease of peak discharge across all ensemble members.

7

DISCUSSION

This chapter analyzes and interprets the hindcast results, establishing their significance and relevance in connection to the literature research. Additionally, a comparison is made between the hindcast and forecast outcomes, highlighting challenges in flood forecasting for the Rur catchment.

7.1. INTERPRETING THE HINDCAST RESULTS

The widespread distribution of precipitation across the Rur catchment caused runoff from all areas. This had an effect on the characteristics of the catchment, which in turn impacted the runoff to the Rur river. The findings in Chapter 5 demonstrate the importance of flooding processes and catchment features in forming the hindcast. As described in Section 3.1.1, the upper parts of the Rur catchment had a different reaction than the lower regions. Fast runoff was observed in the Eifel area due to the steep and impermeable slopes, particularly in the Urft and Olef tributaries, leading to flooding in Gemünd and a large influx of water to the Rur reservoir system. The hindcast results in Chapter 5 also show a rapid runoff with sharp hydrographs for the upper tributaries and an extreme inflow of 400 - 600 m^3/s to the Rur reservoir system.

The Rur reservoir system was designed to protect the region from flood waves, and it was successful in dampening the incoming wave, with a peak outflow of 100 m^3/s. The controlled outflow resulted in flooding being concentrated in the designated floodplains of the Rur. However, the effectiveness of the reservoir depends on the initial storage and the operation plans used during the flood event. To increase storage, the outflow at Heimbach was increased from 17 m^3/s to 100 m^3/s. This higher outflow was planned by WVER to arrive after the peak of the flood wave, which is evident in the hindcast results: a comparison of hydrographs with and without additional reservoir release shows that mostly the recession limb is affected.

Downstream of the Eifel area and the reservoir system, the topography becomes flat,

and the Rur increases in width. Similarly, the type of flooding shifts from local pluvial flooding to fluvial flooding affecting wider regions. The floodplain flow became especially apparent in the Dutch Rur, where the flow was stored in wide floodplains with high storage capacity. Comparisons between the hindcast results for all models show that including or excluding floodplain flow has a dramatic impact on the quality of the hindcast. Without floodplain attenuation, peak discharges at Stah would exceed 500 m^3/s and arrive 24 hours earlier than observed. Different models are able to capture these attenuating effects, varying from a one-dimensional approach (PM-1D), quasi-2D approach (Wflow-FP) and fully two-dimensional (PM-2D). However, floodplain flow in the wide floodplains of the Dutch Rur becomes too complex to capture by simpler models, thus relying on time-consuming two-dimensional flow calculations by the PM-2D model.

The flood was dominated by inflows from the Rur reservoir system and the Wurm and Inde tributaries. The discretization of these inflow points is important, as is shown by the effects of floodplain attenuation in the tributaries and the imposing additional reservoir release. However, it is important to also include the smaller tributaries, as their contribution is still significant and a reduced river network imposes practical challenges as the reservoirs are disconnected from the river network. Furthermore, fast runoff in the Eifel area flows through a network of steep rivers, and reducing the river network would result in the loss of these runoff mechanisms. As a result, the complete river system should be included.

Additionally, the presence of lignite mining seems to have had an overall positive impact on flood safety. Groundwater pumping increased the storage capacity of the soil, and flooding of the Inden lignite mine resulted in 10 million $m^3$of water being 'stored', although this amount has not been validated. Excluding the indirect effects of the low groundwater table could result in an overestimation of runoff toward the Rur River, but it does not alter the shape of the flood wave itself. However, it should be noted that the only direct casualty of the flood event occurred in the lignite mine, as a mine worker was taken by the flow escaping the Inde river, breaking through the mine.

7.2. FORECASTING EXTREME FLOODS

The 2021 flood event in the Rur river and its tributaries was particularly severe, as evidenced by the meteorological description in section 3.2. The estimated return periods for both observed precipitation and flow were well above 100 years. Unfortunately, real-time radar measurements underestimated the volume of precipitation, and NWP ensembles only recognized the potential extremity shortly before the start of the extreme rainfall. This highlights the importance of accurate meteorological input for flood forecasting models. The RADFLOOD21 dataset relies on corrections by gathering precipitation data from stations afterwards, which is not a viable option in practice. As such, the RADFLOOD21 dataset is not representative of such a data source during flood forecasting.

Despite the ICON-EU-EPS ensemble forecast from the 13th of July including ensemble members that were close to or even exceeded the observed precipitation in terms of

pattern and volume, the KNMI still increased the weather warning to orange. This allowed for a four-day lead time for the Dutch Rur flood forecast, as the peak arrived on the 17th of July. The advantage of a rainfall-runoff-driven flood forecasting model is that it does not depend on information from gauge stations, which failed during the 2021 flood event, making the WL ML-model ineffective at that time.

A comparison between the hindcasts from Chapter 5 and the forecasts from Chapter 6 reveals that the ensemble members demonstrate a similar response during the flood event as the hindcast itself. The inclusion of floodplain flow has a significant impact on the hydrographs, particularly downstream of the confluences from the Wurm and Inde tributaries. The kinematic wave equation may be sufficient for modelling runoff in the steep Eifel to the reservoir system, but overestimates the celerity of the flood wave in the lowland and lacks the possibility of including floodplain attenuation, which requires the use of the diffusive wave equation. Moreover, the inclusion of the leakage term has an effect that is almost linearly proportional to the peak discharge for all ensemble members. Similarly, the inclusion of the reservoir system is essential for obtaining an accurate estimation of the magnitude and timing of the peak of the flood waves, and its dampening effect is clearly visible, even when overflow occurs.

By examining the lead time of a couple of days and comparing it to the catchment area of 100 kilometers, we can see that runoff processes and channel flow are likely to be the most influential. In the upper regions of the Rur, Wurm and Inde rivers, infiltration excess overland flow and topography are the main factors that determine the flow response. In the lower regions of these rivers, floodplain flow becomes more important, which is related to channel flow, which operates on different timescales. For these downstream locations, the hydrological processes upstream tend to be averaged out and hydrodynamic processes become more prominent, such as the accurate modelling of floodplain flow. The lower resolution of the NWP is not as important for these hydrodynamic processes, as long as the prediction of the amount of precipitation is accurate.

7.3. MODEL COMPLEXITY AND USE IN PRACTICE

Flood forecasting has a variety of applications, as discussed in Section 2.2.1. The models used in this thesis range in complexity and output. Hydrological models *Wflow_SBM* lack sufficient spatial detail resolution to generate precise flood maps, but can be used for threshold-based flood forecasting. The PM-1D model has a higher spatial resolution and can provide information on simulated water depth per river cross-section, which can be useful for assessing the risk of dike failures. The PM-2D model can generate inundation maps and can even be extended to an IBF, using the capabilities of the *ProMaIDes* software package.

These wide range of possibilities can be related to the observed response of the Rur catchment, both in the hindcast and the forecasts. The inundation of the Rur upstream of the Inde confluence is limited due to reservoir management, making it impractical to use a two-dimensional model for this reach. Floodplain flow is complex for the Dutch Rur and hard to capture with one-dimensional models, but the floodplains are wide and

deep, leading to similar inundation patterns for different peak discharges upstream at Stah. Thus, one-dimensional models with floodplain flow (e.g. Wflow-FP and PM-1D) may be sufficient for modelling the majority of the Rur until the Dutch border, and can accurately predict inundation until the floodplains reach their maximum storage capacity. The ensemble forecasts in Section 6.2 suggest that this limit may be at Q_{limit} = 300 m^3/s, and forecasts above this point would require a two-dimensional approach to account for the water depths in the Dutch floodplains

The effects of groundwater leakage and the presence of reservoirs on the peak discharge at Stah can be estimated using a reduction factor. However, the arrival time of the flood wave peak is also affected when reservoirs are not taken into account, and its implementation in a hydrological model has a minimal effect on computation times. The leakage term can be implemented without any additional computational cost, but it has not been tested and there is limited knowledge of the influence of low groundwater levels due to mining on flood safety. Therefore, it is considered to be a safe option to exclude this leakage term.

The ICON-EU-EPS ensemble members were employed to generate forecasts of the 2021 flood event in this thesis. This approach has a low temporal and spatial resolution, which can be a hindrance for precise forecasting of pluvial flooding, particularly in the upper part of the Rur catchment located in the Eifel, such as the city of Gemünd. Nevertheless, these NWP forecasts were found to be useful for fluvial flooding, particularly concerning the Duth Rur and Roermond. These processes occur at longer temporal and spatial timescales, which makes this type of forecasting more suitable than radar-based products with shorter lead times. For instance, at a lead time of 6 hours, the runoff may not even leave the reservoir system and thus not reach the lower part of the Rur river during the forecast.

7.4. OPERATIONAL CHALLENGES FOR FORECASTING THE RUR

The findings of this thesis indicate that there are certain challenges that would be encountered when the models are used in practice. Primarily, the two-dimensional modelling of NWP ensemble members would be a computationally demanding task. A single PM-2D run takes around 12 hours to complete, so running 40 ensemble members would require a lot of resources. Even if these resources were available, faster processing would be necessary to make the 12 hour runs feasible in terms of the updating frequency of the meteorological forecast, which is usually 12 to 24 hours for NWP. This is because new observations or new weather forecasts may render the model results outdated.

The Rur reservoir system is essential for an operational model used for flood forecasting. It can either provide an upstream boundary condition, when operation plans are sent from WVER, or its outflow can be part of the forecast, thus requiring precise initial conditions of the reservoir storage. Additionally, the 2021 flood event showed that the ouflow may even be increased beyond the maximum outflow of the operational plans in the case of extreme flow. In either case, the data from WVER is necessary to set up a flood forecasting model that includes the Rur reservoir system.

8

SYNTHESIS

In this chapter, the synthesis of this thesis will be provided. First, the research questions will be answered in the conclusion. Secondly, recommendations will be made with regards to further research and the implementation of a flood forecasting system for the Rur. Finally, some technical recommendations will be made on how to improve the *Wflow_SBM* and *ProMaIDes* models when used in further research.

8.1. CONCLUSION

RQ1. WHAT ARE THE CHARACTERISTICS THAT DETERMINE THE RUR BASIN IN THE CONTEXT OF HYDROLOGICAL AND HYDRODYNAMIC MODELS?

The Rur catchment can be divided into the Eifel upstream area and the downstream lowlands. The upstream area is characterised by steep slopes and lower soil permeability, resulting in relatively fast runoff. Additionally, more precipitation occurs, and the orography of the Eifel influences its location. As a result, flooding in this area typically occurs in the form of rapid overland runoff, resulting in flash floods that are difficult to predict due to their locality and short time scale, making them rely heavily on accurate weather forecasts. On a more aggregate level, runoff in the Eifel area concentrates toward the Rur reservoir, which connects the upstream Eifel area and the downstream catchment.

Wide floodplains and an anthropogenic presence characterise the downstream lowlands. Weirs control the water levels in the downstream Rur during regular flow, the reservoir system provides the Rur with a minimum inflow, and the groundwater table is significantly lowered to accommodate open pit lignite mining. These effects are visible in the overall water balance of the Rur and may also play an essential role in flood safety.

Flood processes in the lowlands occur on a longer time scale, as the topography is less steep and the soil more permeable, increasing the importance of subsurface flow. Similarly, lignite mining has transformed the catchment, but its effects take place on a long

timescale within the order of days to years. The academic literature concludes that groundwater removal generally affects catchment hydrology, but may be unique for each type of mine. In the case of the Rur catchment, lignite mining may actually have a positive effect on flood safety because groundwater recharge increases the storage capacity of the soil and the mining pit itself can be used to store large amounts of water, in the order of million cubic metres, during an extreme flood.

Reservoir management has a positive effect on damping the flood wave. The Rur reservoir system decelerates runoff from the Eifel, and floodplains allow flood wave attenuation in the case of floods. The system of reservoirs in the Rur basin is complex and has reservoirs both in series and parallel, and the operation rules are based on the reservoir system as a whole. Theoretically, the benefits of a controlled reservoir increase for high-frequency flood events, which is reflected in the example of the 2021 floods. However, reservoir management can govern the response of a catchment during floods as a (late) spillwave will have different downstream implications compared to a (early) pre-release as the wave interacts with tributary inflows.

Inundating floodplains characterise the lowlands of the Rur catchment, both for the Rur river itself and for tributaries such as the Wurm and Inde. Floodplain flow generally slows down a wave due to the higher roughness of the floodplain bed, but the exact effects depend on the width-weighted flow and, therefore, require information about the affected river profiles. For the Rur, both a coarse and a detailed approach are tested and show that the model results lie closer to observations when floodplain attenuation is included. Simultaneously, tributary timing becomes less important as the flood waves in the main river and the inflow points become strongly attenuated with reduced peak-peak interactions. Within the theoretical framework of dispersion, this shows that hydrodynamic dispersion (related to friction and storage differences) dominates over geomorphological dispersion (related to the river network itself) in the case of an extreme flood wave in the lower Rur catchment. This is not valid for the highlands, for which model results without floodplain attenuation produce results closer to observations.

RQ2. HOW CAN THESE CHARACTERISTICS BE CAPTURED IN A FLOOD FORECASTING MODEL?
This research used two types of models: the hydrological *Wflow_SBM* model and the hydrodynamic *ProMaIDes* model. The hydrological model can simulate the rainfall-runoff processes and the subsurface flow, describing the flow to the Rur River and the reservoir. The influence of human intervention on the water balance of the catchment can be captured in the hydrological model by adding a custom code to optimise reservoir modelling and calibarating a leakage term for the saturated zone of the soil to account for the effects of groundwater pumping. The flow of rivers and floodplains can both be modelled using the *Wflow_SBM* and *ProMaIDes* software, with varying options for complexity and river routing schemes. The aimed advantage of such a catchmenst-scale forecasting model was to increase forecasting lead times as the forecast can continue for the duration of the (accurate) precipitation forecast.

Furthermore, both models have been shown to be suitable for flood forecasting in an operational setting with an EPS, using the *Wflow_SBM* model to generate boundary conditions for the *ProMaIDes* model or using the *Wflow_SBM* model as a standalone

model. Additionally, the *ProMaIDes* model can be extended to an impact-based model using the risk and damage modules available for the software. Although this option has not been explicitly explored or tested in this thesis, it is clear that the 1D2D version of the *ProMaIDes* model is the only suitable model for forecasting floods (as defined in Section 2.2.1), since the floodplain flow in *Wflow_SBM* is simulated at a very coarse resolution. The downside of this type of forecasting model is its computational costs, as each model run takes approximately 20 hours to simulate, which is almost a quarter of the total lead time. Without parallel computation, a 40-ensemble prediction can even take 800 hours to simulate. Therefore, a combination of different types of models seems to be the most practical option. A very fast *Wflow_SBM* EPS can be used to produce flood warnings based on threshhold, of which distinct members can be chosen to simulate in 1D2D using *ProMaIDes*.

Several other operational challenges arise for a flood forecasting model of the Rur catchment, both under regular conditions and during an extreme flood. First, accurate forecasts depend on correctly prediciting reservoir outflow, which may vary due to the free room in the operation plan for the Rur reservoir system. An approach was implemented in which two outflow bands (Q_1 and Q_2) were added to the operating plan based on calibration by the WVER data. In practise, the upper bands of the volume-based operation plan for the Rur reservoir system are narrow and therefore sensitive to changes in storage. Underestimations or overestimations of the variable outflow may therefore result in an incorrect estimation of the storage, resulting in an over- or underestimation of the peak outflow corresponding to that storage. Furthermore, large deviations from the plan itself can occur in the case of extreme flows, such as in 2021, as shown by the increase from 60m^3/s to 100 m^3/s at Heimbach.

Deviations from the predicted reservoir outflow can be incorporated in an operational forecasting model but limit the lead time of the forecast to the length of this deviation. Additionally, including the watersheds upstream of the reservoir system may become unnecessary when the reservoir outflow is imposed, therefore effectively turning into an upstream boundary condition.

Using the leakage parameter (`MaxLeakage`) to account for a lowered groundwater table shows significant changes in model outcomes, both at longer and shorter timescales. The results observed during the calibration of the *Wflow_SBM* model show promising results, especially with regard to the water balance at the downstream gauge stations and the order of magnitude of the total recharge. An important observation is that the indirect effect of the leakage parameter on soil moisture capacity is greater than that of the leakage itself, which can result in significant changes in terms of flood extent in the case of an extreme flood.

However, the *Wflow_SBM* model inherently lacks the ability to model groundwater flows, since the soil thickness is limited to two metres and the subsurface flow is driven by topography, not groundwater head differences. A possible solution is to validate the results of *Wflow_SBM* by coupling them to a groundwater model such as MODFLOW, see for example van der Vat et al. (2019), and comparing the location and magnitude of the leak with the modelled recharge in the upper soil layer. At the same time, groundwa-

ter processes take place at a much larger timescale and forecast lead time, which limits the practical use of such an operational coupled *Wflow_SBM*-groundwater model. A more practical application may be to use a coupled *Wflow_SBM* -groundwater model to hindcast the state of soil storage capacity at the start time of the forecast, which is then used in the *Wflow_SBM* forecast.

RQ3. WHICH FACTORS OBSERVED IN THE HINDCAST DETERMINED THE OUTCOME OF THE FLOOD EVENT IN JULY 2021?

The July 2021 flood event in the Rur catchment was determined by a variety of factors. Widespread precipitation throughout the basin, inflows from the Inde and Wurm tributaries, and the Obermaubach reservoir all had a major impact on the flood wave's characteristics. Excluding smaller tributaries would lead to an underestimation of both base flow and peak flow. Hydrographs from gauge stations located in steep areas showed peaks in precipitation intensity, but these were smoothed out near the Rur inflow locations.

Accurate floodplain flow modelling was necessary for precise forecasts, and models lacking floodplain attenuation significantly overestimated peak discharge and peak timing. The Rur reservoir system was instrumental in limiting the extent of the flooding, and its strategic operation, including additional releases and initial storage capacity, had a major influence on flood retention and the timing and magnitude of the spillwave. Lastly, the lignite mines in the catchment area had a positive effect on flood safety, as the leakage towards these mines decreased peak flow and increased storage capacity. In conclusion, precipitation distribution, tributary flows, precipitation intensity, floodplain dynamics, reservoir system operation, and the presence of lignite mines played a crucial role in determining the outcome of the flood event of July 2021 in the Rur catchment. A detailed understanding and accurate modelling of these factors is essential to improve flood forecasts and improve flood safety measures in the region.

RQ4. WHAT ARE THE SENSITIVITIES OF THIS MODEL OBSERVED USING ENSEMBLE FORECASTS OF THE JULY 2021 EVENT?

Human-induced factors, such as reservoirs and lignite mines, had a visible effect on all ensemble runs, with the magnitude of the impact proportional to the maximum discharge at Stah. These results were observed in all types of models and appear to be generalisable as characteristics of the response of the Rur catchment during a flood event.

In addition, variations in floodplain flow and different flood wave routing schemes highlighted the dynamics of the Rur catchment. Models that accounted for floodplain attenuation, such as Wflow-FP, PM-1D, and PM-2D, showed more consistent results compared to those that did not, such as Wflow-KW and Wflow-LI. Inundation patterns were also observed, mainly near Jülich and Linnich in the wide floodplains, and were effectively captured by the models. However, downstream of Stah, the floodplain flow became more complex and difficult to replicate accurately. PM-2D results approached a physical limit, surpassing the Wflow-FP outcomes. Roermond's edge experienced limited inundation, mainly affecting extreme ensemble members, while the majority of inundation was concentrated in the wide floodplains.

RQ5. WHAT ARE THE KEY FACTORS FOR THE PREDICTION OF FLOODS IN THE RUR CATCHMENT BASED ON THE LESSONS LEARNT FROM THE EVENT IN JULY 2021?

The importance of several characteristics of a flood forecasting model is highlighted by the hindcast and forecasts. In particular, accurate modelling of floodplain flow is essential for extreme floods, as the shape of the flood wave is determined by floodplain attenuation in the Rur, Wurm and Inde rivers. Additionally, the Rur reservoir system is a key factor and should be included in the forecasting system, as it sets the upstream boundary condition for this part of the Rur river, and its flood retention capacity is able to store a large amount of runoff from extreme precipitation. It is also possible to take into account the presence of lignite mining through a leakage parameter and by including the mining pit in the floodplain of the Inde river, although this may require further research. All these effects can be captured by the hydrological *Wflow_SBM* model without significant additional computational costs.

The characteristics of the catchment area can restrict the types of models that can be practical. Inundation in the Dutch Rur is usually complex, so two-dimensional modelling is the most suitable approach, although it is computationally intensive. For the upstream reaches of the Dutch Rur, a one-dimensional model such as Wflow-FP or PM-1D can be used to capture other flow characteristics as inundation is limited and the flow is dominated by reservoir outflow. Furthermore, data from WVER is necessary to accurately model the Rur reservoir system, either by setting or forecasting the reservoir outflow. Limiting the two-dimensional model to only the Dutch Rur has the advantage of decreasing the size of the model, and therefore reducing computational times.

The accuracy of flood forecasting using a rainfall-runoff model depends heavily upon the quality of the meteorological input. If the amount of rainfall is underestimated, then the predicted flows will also be too low, which is crucial for flood forecasting. This thesis utilized a NWP product for creating the forecasts of the flood event in the Rur catchment, which was found to be suitable. Although the spatial resolution of this type of meteorological input is lower than radar-based products, it is still adequate to generate responses in the subcatchments of the Rur, and the temporal length of the forecasts is compatible with the spatial and temporal scales of the predominant hydrodynamic processes.

8.2. RECOMMENDATIONS

Suggestions can be made based on the findings of this thesis, such as directions for further research, technical model enhancements, and the establishment of a flood forecasting model. These suggestions are described in further detail in this section.

8.2.1. IMPLEMENTING A FLOOD FORECASTING MODEL

The discussion in Chapter 7 and the conclusion in Section 8.1 mention several elements that should be considered in a flood forecasting model of the Rur, with the focus on the Dutch Rur. In summary, such a flood forecasting setup would consider the following:

- A rainfall-runoff model model of the whole Rur catchment, including the Rur reservoir system, a leakage term addressing the effects of the lowered groundwater table, and the option for modelling floodplain attenuation (such as the Wflow-FP model);
- Meteorological input from a NWP, where sufficient lead time is more important than spatial and temporal resolution;
- This model can be used for a threshold-based forecasting system, where the gauge station at Stah will function as point of interest;
- When sufficient ensemble members show the exceedance of the threshold value (e.g. 300 m^3/s, based on the critical capacity of the Dutch floodplains), the forecasts should be compared to existing inundation maps;
- Additionally, the most extreme ensemble members can be selected and modelled using a high resolution two-dimensional model (such as the PM-2D) model;
- When new weather forecasts are generated, the hydrographs at Stah can be compared. When new extremes are similar to extremes of the previous forecast, then these inundation maps can be re-used.

8.2.2. FUTURE RESEARCH

In addition to the proposed flood forecasting system, several relevant topics warrant further investigation:

Investigating Mining Activities and Flood Safety: Hindast and forecast results indicate that the presence of the lignite mine appeared to be favourable to flood safety conditions. Information on this topic in the academic literature was limited, so a generalisation study linking mining activities and flood safety may pose an interesting subject for future research. Additionally, the case of the Inden lignite mine in the Rur catchment can be further investigated, both in terms of its effect on catchment hydrology as its role during the 2021 flood event.

Investigating Tributary Interactions: The ensemble forecasts highlighted a significant correlation between peak flow at Stah and precipitation in the Inde subbasin. However, the proximity of the Wurm inflow to Stah suggests that it should have a more substantial impact on maximum flow. To improve understanding of the interactions between the

Rur and its tributaries, it is recommended to investigate this topic further. This could involve improving the discretization of bankfull depth and width in the *Wflow_SBM* models of the Wurm and Inde or extending the *ProMaIDes* model of the Rur to incorporate the Wurm and Inde tributaries, both in one dimension and in two dimensions. This exploration will contribute to a more comprehensive understanding of the dynamics of the tributaries.

8.2.3. TECHNICAL IMPROVEMENTS FOR THE RUR MODELS

IMPROVING THE *Wflow_SBM* MODEL

Incorporate Groundwater Dynamics: While the models *Wflow_SBM* addressed the effects of lignite mining through a simplified leakage factor, this approach may oversimplify the intricate interactions between groundwater and surface water. To address this limitation, an extension of the *Wflow_SBM* hydrological model is recommended to encompass a more comprehensive groundwater model such as MODFLOW; see, for example, van der Vat et al. (2019). This expansion will enable for a more accurate representation of groundwater-surface water interactions.

Improve Wurm and Inde bankfull depth and width: To improve the accuracy of floodplain flow predictions, it is advisable to adopt a similar approach to that applied to the Rur cross-sectional data. By incorporating detailed cross-sectional data for the Wurm and Inde tributaries, the *Wflow_SBM* model can better capture floodplain flow dynamics. This improvement will lead to a more accurate depiction of the interactions of the tributaries and the arrival of flood waves from these tributaries.

IMPROVING THE *ProMaIDes* MODEL

Calibrate Roughness Parameters: In particular, limited calibration was performed for the *ProMaIDes* model. To improve the accuracy of the model, calibration of the roughness parameters within the model is recommended (see also Horn and Hurkmans (2022)). As evidenced by its impact on the HKV model, this calibration process can lead to improved model results.

Validate DEM of floodplain grids: The accuracy of the Digital Elevation Model (DEM) used in the *ProMaIDes* model is important. To ensure precise modelling results, it is recommended to consider checking and improving the DEM by verifying the inclusion of structures based on observations or other hydrodynamic models of the Rur. This enhancement will contribute to more accurate flood simulations.

REFERENCES

Aerts, J. P., Hut, R. W., Van De Giesen, N. C., Drost, N., Van Verseveld, W. J., Weerts, A. H., & Hazenberg, P. (2022). Large-sample assessment of varying spatial resolution on the streamflow estimates of the wflow_sbm hydrological model. *Hydrology and Earth System Sciences*, *26*(16), 4407–4430. doi:10.5194/hess-26-4407-2022

Afshari, S., Tavakoly, A. A., Rajib, M. A., Zheng, X., Follum, M. L., Omranian, E., & Fekete, B. M. (2018). Comparison of new generation low-complexity flood inundation mapping tools with a hydrodynamic model. *Journal of Hydrology*, *556*, 539–556. doi:10.1016/j.jhydrol.2017.11.036

Alfieri, L., Bisselink, B., Dottori, F., Naumann, G., de Roo, A., Salamon, P., … Feyen, L. (2017). Global projections of river flood risk in a warmer world. *Earth's Future*, *5*(2), 171–182. doi:10.1002/2016EF000485

Antolini, F., & Tate, E. (2021). Location Matters: A Framework to Investigate the Spatial Characteristics of Distributed Flood Attenuation. *Water*, *13*(19), 2706. doi:10.3390/W13192706

Asselman, N., & van Heeringen, K.-J. (2022). *Een watersysteemanalyse - wat leren we van het hoogwater van juli 2021?* (Tech. Rep.). Deltares.

Ayalew, T. B., Asce, S. M., Krajewski, W. F., & Mantilla, R. (2013). Exploring the Effect of Reservoir Storage on Peak Discharge Frequency. *Journal of Hydrologic Engineering*, *18*(12), 1697–1708. doi:10.1061/(ASCE)HE.1943-5584.0000721

Ayalew, T. B., Krajewski, W. F., & Mantilla, R. (2015). Insights into Expected Changes in Regulated Flood Frequencies due to the Spatial Configuration of Flood Retention Ponds. *Journal of Hydrologic Engineering*, *20*(10), 04015010. doi:10.1061/(asce)he.1943-5584.0001173

Bachmann, D. (2012). *Beitrag zur Entwicklung eines Entscheidungsunterstützungssystems zur Bewertung und Planung von Hochwasserschutzmaßnahmen* (PhD thesis). RWTH Aachen, Aachen.

Bachmann, D. (2016). *ProMaIDes – Benchmark and performance tests of the HYD-module (Hydrodynamic module) (presentation).*

Bachmann, D. (2021, 9 30). *Flood Event 2021 in Germany: More Research Into Practice!* Presentation at the 4th Dutch German French workshop in Magdeburg.

Bachmann, D., Becker, B., & van Linn, A. (2005). *Aufbau und Kalibrierung des Grundwassermodells Rurscholle* (Tech. Rep.). RWTH Aachen.

Bachmann, D., Becker, B., Van Linn, A., & Köngeter, J. (2007). Das Großraum-Grundwassermodell Rurscholle. *Grundwasser*, *12*(1), 26–36. doi:10.1007/s00767-007-0020-2

Bachmann, D., Eilander, D., De Leeuw, A., De Bruijn, K., Diermanse, F., Weerts, A., & Beckers, J. (2016). Prototypes of risk-based flood forecasting systems in the Nether-

lands and Italy. In *FLOODrisk 2016 - 3rd European Conference on Flood Risk Management*. EDP Sciences. doi:10.1051/e3sconf/20160718018

Bates, P. D., & De Roo, A. P. J. (2000). A simple raster-based model for flood inundation simulation. *Journal of Hydrology*, *236*, 54–77.

Battjes, J., & Labeur, R. J. (2017). *Unsteady flow in open channels*. Cambridge University Press.

Becker, B. (2011). *The groundwater model "erftscholle, rurscholle and venloer scholle" (presentation)*.

Becker, B., Homann, C., & Köngeter, J. (2009). Coupling of large scale groundwater models. *Computing and Visualization in Science*, *12*(2), 71–76. doi:10.1007/s00791-007-0079-4

Becker, B., Köngeter, J., Klauder, W. S., & Reuter, C. (2008). Modellierung der Randüberströme zwischen Erftscholle, Rurscholle und Venloer Scholle durch Kopplung von Großraum-Grundwassermodellen. *Grundwasser*, *13*(1), 15–26. doi:10.1007/s00767-007-0056-3

Bezirksregierung Köln. (2021). *Rur-Damm im Kreis Heinsberg gebrochen (twitter)*. Retrieved from https://twitter.com/BezRegKoeln/status/1416137543045746691

Blöschl, G. (2001). Scaling in hydrology. *Hydrological Processes*, *15*(4), 709–711. doi:10.1002/HYP.432

Blöschl, G., Bierkens, M. F., Chambel, A., Cudennec, C., Destouni, G., Fiori, A., … Zhang, Y. (2019). Twenty-three unsolved problems in hydrology (UPH)–a community perspective. *Hydrological Sciences Journal*, *64*(10), 1141–1158. doi:10.1080/02626667.2019.1620507

Blöschl, G., & Sivapalan, M. (1995). Scale issues in hydrological modelling: A review. *Hydrological Processes*, *9*, 251–290. doi:10.1002/HYP.3360090305

Bogena, H., Kunkel, R., Schöbel, T., Schrey, H. P., & Wendland, F. (2005). Distributed modeling of groundwater recharge at the macroscale. *Ecological Modelling*, *187*, 15–26. doi:10.1016/j.ecolmodel.2005.01.023

Bogena, H., Montzka, C., Huisman, J., Graf, A., Schmidt, M., Stockinger, M., … Vereecken, H. (2018). The TERENO-Rur Hydrological Observatory: A Multiscale Multi-Compartment Research Platform for the Advancement of Hydrological Science. *Vadose Zone Journal*, *17*(1), 1–22. doi:10.2136/VZJ2018.03.0055

Bogena, H., Pütz, T., Hake, J., Montzka, C., & Kunkel, R. (2005). *MOSYRUR - Water balance analysis in the Rur basin* (Tech. Rep.).

Booij, M. J. (2002). *Appropriate modelling of climate change impacts on river flooding* (PhD thesis). University of Twente, Enschede.

Booij, M. J. (2005). Impact of climate change on river flooding assessed with different spatial model resolutions. *Journal of Hydrology*, *303*, 176–198. doi:10.1016/j.jhydrol.2004.07.013

Bouaziz, L. J. E. (2021). *Internal processes in hydrological models: A glance at the Meuse basin from space* (PhD thesis, Delft University of Technology, Delft). doi:10.4233/uuid:09d84cc1-27e2-4327-a8c7-207a75952061

Boucher, M., Roulin, E., & Fortin, V. (2019). Short-Range Ensemble Forecast Postprocessing. In Q. Duan, F. Pappenberg, A. Wood, H. Cloke, & J. Schaake (Eds.),

Handbook of hydrometeorological ensemble forecasting (pp. 798–818). Springer. doi:10.1007/978-3-642-39925-1

Brakensiek, D., Rawls, W., & Stephenson, G. (1984). Modifying scs hydrologic soil groups and curve numbers for rangeland soils. *ASAE Paper (PNR-84203)*.

Brauer, C. C., Teuling, A. J., Overeem, A., Van Der Velde, Y., Hazenberg, P., Warmerdam, P. M., & Uijlenhoet, R. (2011). Anatomy of extraordinary rainfall and flash flood in a Dutch lowland catchment. *Hydrology and Earth System Sciences*, *15*(6), 1991–2055. doi:10.5194/HESS-15-1991-2011

Brown, E., Bachmann, D., Cranston, M., De Leeuw, A., Boelee, L., Diermanse, F., … Beckers, J. (2016). Methods and tools to support real time risk-based flood forecasting-a UK pilot application. In *Methods and tools to support real time risk-based flood forecasting-a UK pilot application* (p. 18019). E3S Web of Conferences. doi:10.1051/e3sconf/20160718019

Bruni, G., Reinoso, R., Van De Giesen, N. C., Clemens, F. H. L. R., & Ten Veldhuis, J. A. E. (2015). On the sensitivity of urban hydrodynamic modelling to rainfall spatial and temporal resolution. *Hydrology and Earth System Sciences*, *19*, 691–709. doi:10.5194/hess-19-691-2015

Cappelaere, B. (1997). Accurate Diffusive Wave Routing. *Journal of Hydraulic Engineering*, *123*(3), 174–181.

CEDIM Forensic Disaster Analysis (FDA) Group, Schäfer, A., Mühr, B., Daniell, J., Ehret, U., Ehmele, F., … Kunz, M. (2021). *Hochwasser mitteleuropa, juli 2021 (deutschland): 21. juli 2021 – bericht nr. 1 "nordrhein-westfalen & rheinland-pfalz"* (Tech. Rep.). Karlsruher Institut für Technologie (KIT). doi:10.5445/IR/1000135730

Chao, B. F., Wu, Y. H., & Li, Y. S. (2008). Impact of artificial reservoir water impoundment on global sea level. *Science*, *320*(5873), 212–214. doi:10.1126/science.1154580

Cheng, C. T., & Chau, K. W. (2004). Flood control management system for reservoirs. *Environmental Modelling and Software*, *19*(12), 1141–1150. doi:10.1016/j.envsoft.2003.12.004

Chifflard, P., Blume, T., Maerker, K., Hopp, L., van Meerveld, I., Graef, T., … Achleitner, S. (2019). How can we model subsurface stormflow at the catchment scale if we cannot measure it? *Hydrological Processes*, *33*(9), 1378–1385. doi:10.1002/HYP.13407

Chow, V. T., Maidment, D. R., & Mays, L. W. (1988). *Applied Hydrology*. MacGraw-Hill, Inc.

Clark, M. P., P Bierkens, M. F., Samaniego, L., Woods, R. A., Bennett, K. E., N Pauwels, V. R., … Peters-Lidard, C. D. (2017). The evolution of process-based hydrologic models: Historical challenges and the collective quest for physical realism. *Hydrology and Earth System Sciences*, *21*, 3427–3440. doi:10.5194/hess-2016-693

Coiffier, J. (2011). *Fundamentals of Numerical Weather Prediction*. Cambridge University Press. doi:10.1017/CBO9780511734458

COMET. (2010). *Flash Flood Early Warning System Reference Guide*.

Cornes, R. C., van der Schrier, G., van den Besselaar, E. J., & Jones, P. D. (2018). An Ensemble Version of the E-OBS Temperature and Precipitation Data Sets. *Journal of Geophysical Research: Atmospheres*, *123*(17), 9391–9409. doi:10.1029/2017JD028200

COT. (2022a). *Een crisis van ongekende omvang* (Tech. Rep.). Presentation at Waterschap Limburg.

COT. (2022b). *Rapportage Leerevaluatie Hoogwater Maas en Roer* (Tech. Rep.). Rotterdam.

Crutzen, P. J. (2002). Geology of mankind. *Nature*, *415*, 23. doi:0.1038/415023a

Dale, M., Wicks, J., Mylne, K., Pappenberger, F., Laeger, S., & Taylor, S. (2014). Probabilistic flood forecasting and decision-making: An innovative risk-based approach. *Natural Hazards*, *70*(1), 159–172. doi:10.1007/s11069-012-0483-z

De Boer, T. (2017). *Added value of distribution in rainfall-runoff models for the Meuse basin* (PhD thesis, Delft University of Technology, Delft). doi:10.4233/uuid:89a78ae9-7ffb-4260-b25d-698854210fa8

de Bruijn, K., Slager, K., Piek, R., Riedstra, D., & Slomp, R. (2018). *Leidraad voor het maken van overstromingssimulaties* (Tech. Rep.). Deltares.

De Bruin, H., & Lablans, W. (1998). Reference crop evapotranspiration determined with a modified makkink equation. *Hydrological Processes*, *12*(7), 1053–1062.

Deen, L. (2022). *Het Roer om. Een analyse van de meetapparatuur in de rivier Roer* (BSc thesis). Delft University of Technology.

De Groeve, T. (2020). Knowledge-Based Crisis and Emergency Management. In *Science for policy handbook* (pp. 182–194). Elsevier. doi:10.1016/b978-0-12-822596-7.00016-4

De Kleermaeker, S., Leijnse, T., Morales, Y., Druery, C., & Maguire, S. (2022). Developing a real-time data and modelling framework for operational flood inundation forecasting in australia. In *Hydrology & water resources symposium 2022 (hwrs 2022): The past, the present, the future: The past, the present, the future* (pp. 856–865).

Deltares. (2022). *Wflow.jl online documentation*. https://deltares.github.io/Wflow.jl/stable/. (Accessed: 2022-10-01)

Demeritt, D., Nobert, S., Cloke, H. L., & Pappenberger, F. (2013). The European Flood Alert System and the communication, perception, and use of ensemble predictions for operational flood risk management. *Hydrological Processes*, *27*(1), 147–157. doi:10.1002/hyp.9419

Demny, G., Homann, C., Huasmann, B., & Kufeld, M. (2013). Increasing Risks for the Management of the North-Eifel Reservoir System caused by Climate Change. In *Proceedings of the 1st International Short Conference on Advances in Extreme Value Analysis and Application to Natural Hazards* (pp. 179–184).

De Perez, E. C., Van Den Hurk, B., Van Aalst, M. K., Amuron, I., Bamanya, D., Hauser, T., … Zsoter, E. (2016). Action-based flood forecasting for triggering humanitarian action. *Hydrology and Earth System Sciences*, *20*(9), 3549–3560. doi:10.5194/hess-20-3549-2016

Dewals, B., Erpicum, S., Pirotton, M., & Archambeau, P. (2021). *July 2021 extreme floods in the belgian part of the meuse basin*. University of Liege, Liege, Belgium. Retrieved from https://henry.baw.de/server/api/core/bitstreams/6b2b809e-becd-465e-bd3b-d24e3a9f467a/content

Dhakate, R., Modi, D., & Rao, V. V. S. G. (2019). Impact assessment of coal mining on river water and groundwater and its interaction through hydrological, isotopic characteristics, and simulation flow modeling. *Arabian Journal of Geosciences*, *12*(1). doi:10.1007/s12517-018-4110-5

Dietze, M., Bell, R., Ozturk, U., Cook, K. L., Andermann, C., Beer, A. R., … Thieken, A. H.

(2022). More than heavy rain turning into fast-flowing water-a landscape perspective on the 2021 Eifel floods. *Natural Hazards and Earth System Sciences*, *22*, 1845–1856. doi:10.5194/nhess-22-1845-2022

Di Lazzaro, M., Zarlenga, A., & Volpi, E. (2016). Understanding the relative role of dispersion mechanisms across basin scales. *Advances in Water Resources*, *91*, 23–36. doi:10.1016/J.ADVWATRES.2016.03.003

Dooge, J. C. (1986). Looking for hydrologic laws. *Water Resources Research*, *22*(9), 46S-58S. doi:10.1029/WR022I09SP0046S

Dorgarten, H. W. (1988). Finite Element Modeling of the Rurscholle Multi-Aquifer Groundwater System. *Developments in Water Science*, *35*, 71–76. doi:10.1016/S0167-5648(08)70319-8

Dottori, F., Kalas, M., Salamon, P., Bianchi, A., Alfieri, L., & Feyen, L. (2017). An operational procedure for rapid flood risk assessment in Europe. *Natural Hazards and Earth System Sciences*, *17*(7), 1111–1126. doi:10.5194/nhess-17-1111-2017

Dunne, T., & Black, R. D. (1970a). An Experimental Investigation of Runoff Production in Permeable Soils. *Water Resources Research*, *6*(2), 478–490. doi:10.1029/WR006i002p00478

Dunne, T., & Black, R. D. (1970b). Partial Area Contributions to Storm Runoff in a Small New England Watershed. *Water Resources Research*, *6*(5), 1296–1311. doi:10.1029/WR006i005p01296

Eilander, D., Boisgontier, H., Bouaziz, L. J. e., Buitink, J., Couasnon, A., Dalmijn, B., … Verseveld, W. v. (2023a). HydroMT: Automated and reproducible model building and analysis. *Journal of Open Source Software*, *8*(83), 4897. doi:10.21105/JOSS.04897

Eilander, D., Boisgontier, H., Bouaziz, L. J. E., Buitink, J., Couasnon, A., Dalmijn, B., … van Verseveld, W. (2023b). HydroMT v0.7.1. doi:10.5281/ZENODO.7827521

ELWAS-WEB. (2023). *Elwas-web*. https://www.elwasweb.nrw.de/elwas-web/. (Accessed: 2022-11-27)

European Environment Agency. (2019). *Corine land cover 2018 (raster 100 m) version 2020_20u1*. European Environment Agency. Retrieved from https://sdi.eea.europa.eu/catalogue/copernicus/api/records/960998c1-1870-4e82-8051-6485205ebbac?language=all doi:10.2909/960998C1-1870-4E82-8051-6485205EBBAC

Ferrick, M. G. (1985). Analysis of River Wave Types. *Water Resources Research*, *21*(2), 209–220. doi:10.1029/WR021i002p00209

Fitzpatrick, F. (2017). Watershed Geomorphological Characteristics. In V. Singh (Ed.), *Handbook of applied hydrology* (pp. 4401–4412). McGraw-Hill Education.

Froude, L. S., Bengtsson, L., & Hodges, K. I. (2013). Atmospheric predictability revisited. *Tellus A: Dynamic Meteorology and Oceanography*, *65*(1). doi:10.3402/tellusa.v65i0.19022

Gädeke, A., Hölzel, H., Koch, H., Pohle, I., & Grünewald, U. (2014). Analysis of uncertainties in the hydrological response of a model-based climate change impact assessment in a subcatchment of the Spree River, Germany. *Hydrological Processes*, *28*(12), 3978–3998. doi:10.1002/hyp.9933

Geertsema, T., & Asselman, N. (2022). *Analyse hoogwater Roermonding* (Tech. Rep.). Deltares.

Geertsema, T. J., Teuling, A. J., Uijlenhoet, R., Torfs, P. J., & Hoitink, A. J. (2018). Anatomy of simultaneous flood peaks at a lowland confluence. *Hydrology and Earth System Sciences*, *22*(10), 5599–5613. doi:10.5194/hess-22-5599-2018

Geodienst NRW. (2023a). *BK50*. https://www.gd.nrw.de/pr_kd_bodenkarte-50000.php. (Accessed: 2023-02-15)

Geodienst NRW. (2023b). *HÜK250*. https://www.gd.nrw.de/pr_kd_hydrogeologische-karte-250000.php. (Accessed: 2023-02-15)

Gewässerstationierungskarte des Landes Nordrhein-Westfalen. (n.d.). https://www.lanuv.nrw.de/umwelt/wasser/oberflaechengewaesserfluesse-und-seen/fliessgewaesser/gewaesser-stationierungskarte/. (Accessed: 2022-10-23)

Ghomash, S. K. B., Schotten, R., & Bachmann, D. (2022). ProMaIDes: A State-of-the-Science Flood Risk Management Tool. In *Proceedings of the 39th IAHR World Congress* (pp. 245–256).

Godlewski, G. B. (2022). *Improvement of the Flood Early Warning System for Valkenburg along the Geul River* (MSc thesis). Delft University of Technology.

Goudenhoofdt, E., Journée, M., & Delobbe, L. (2023). *Observational rainfall data of the 2021 mid-July flood event in Belgium – Part 2. Radar product RADFLOOD21*. Zenodo. Retrieved from https://zenodo.org/record/7740059 doi:10.5281/ZENODO.7740059

Grünewald, U. (2001). Water resources management in river catchments influenced by lignite mining. *Ecological Engineering*, *17*, 143–152. doi:10.1016/S0925-8574(00)00154-3

GWP. (2007). *Guidance on Flash Flood Management: Recent Experiences from Central and Eastern Europe* (Tech. Rep.). Global Water Partnership.

Hancock, G. R., Loch, R. J., & Willgoose, G. R. (2003). The design of post-mining landscapes using geomorphic principles. *Earth Surface Processes and Landforms*, *28*(10), 1097–1110. doi:10.1002/esp.518

Hangen-Brodersen, C., Strempel, P., & Grünewald, U. (2005). Characteristics of catchments disturbed by lignite mining - Case study of Schlabendorf/Seese (Germany). *Ecological Engineering*, *24*, 37–48. doi:10.1016/j.ecoleng.2004.12.005

Hartman, R. (2019). Best Practice in Communicating Uncertainties in Flood Management in the USA. In Q. Duan, F. Pappenberg, A. Wood, H. Cloke, & J. Schaake (Eds.), *Handbook of hydrometeorological ensemble forecasting* (pp. 1093–1108). Springer. doi:10.1007/978-3-642-39925-1

Heath, R. C. (2004). *Basic Ground-Water Hydrology*. U.S. Geological Survey.

Hengl, T., De Jesus, J. M., Heuvelink, G. B., Gonzalez, M. R., Kilibarda, M., Blagotić, A., … Kempen, B. (2017). SoilGrids250m: Global gridded soil information based on machine learning. *PLOS ONE*, *12*(2), e0169748. doi:10.1371/JOURNAL.PONE.0169748

Hersbach, H., Bell, B., Berrisford, P., Hirahara, S., Horányi, A., Muñoz-Sabater, J., … Thépaut, J. N. (2020). The ERA5 global reanalysis. *Quarterly Journal of the Royal Meteorological Society*, *146*(730), 1999–2049. doi:10.1002/QJ.3803

Het Waterschapshuis. (2022). *Geodata Hoogwater Limburg*. Retrieved from https://storymaps.arcgis.com/stories/7488a4903f47499a9f765a23619eb2f4

Hoch, J. M., Eilander, D., Ikeuchi, H., Baart, F., & Winsemius, H. C. (2019). Evaluating the impact of model complexity on flood wave propagation and inundation extent with a hydrologic–hydrodynamic model coupling framework. *Natural Hazards and Earth System Sciences*, *19*(8), 1723–1735. doi:10.5194/nhess-19-1723-2019

Holzbecher, E., & Sorek, S. (2005). Numerical Models of Groundwater Flow and Transport. In M. Anderson (Ed.), *Encyclopedia of hydrological sciences* (pp. 2401–2414). John Wiley & Sons, Ltd.

Homann, C. (2021a). *The Northern Eifel Reservoir System - IHE Delft (virtual) visit to the Urft reservoir (presentation)*.

Homann, C. (2021b). *WVER-Mitgliederdialog zur Hochwasser-Katastrophe - EXTREMNIEDERSCHLÄGE UND ABFLÜSSE IM VERBANDSGEBIET (presentation)*.

Hopson, T., Wood, A., & Weerts, A. (2019). Motivation and Overview of Hydrological Ensemble Post-processing. In Q. Duan, F. Pappenberg, A. Wood, H. Cloke, & J. Schaake (Eds.), *Handbook of hydrometeorological ensemble forecasting* (pp. 783–794). Springer. doi:10.1007/978-3-642-39925-1

Horn, G., & Hurkmans, R. (2022). *Analyse en Maatregelen wateroverlast Roer* (Tech. Rep.). HKV Lijn in Water.

Horton, R. E. (1933). The role of infiltration in the hydrological cycle. *Transactions American Geophysical Union*, *14*(1), 446–460.

Horton, R. E. (1945). Erosional Development of Streams and their Drainage Basins; Hydrophysical Approach to Quantitative Morphology. *Bulletin of the Geological Society of America*, *56*, 275–370.

Hrachowitz, M., Savenije, H. H., Blöschl, G., McDonnell, J. J., Sivapalan, M., Pomeroy, J. W., … Cudennec, C. (2013). A decade of Predictions in Ungauged Basins (PUB)—a review. *Hydrological Sciences Journal*, *58*(6), 1198–1255. doi:10.1080/02626667.2013.803183

HS Magdeburg. (2022). *ProMaIDes online documentation*. https://promaides.myjetbrains.com/youtrack/articles/PMID-A-7/General. (Accessed: 2022-10-03)

Imhoff, R., Brauer, C., Van Heeringen, K. J., Leijnse, H., Overeem, A., Weerts, A., & Uijlenhoet, R. (2021). A climatological benchmark for operational radar rainfall bias reduction. *Hydrology and Earth System Sciences*, *25*(7), 4061–4080. doi:10.5194/hess-25-4061-2021

Imhoff, R. O. (2022). *Rainfall nowcasting for flood early warning* (PhD thesis, Wageningen University, Wageningen). doi:10.18174/573867

Imhoff, R. O., van Verseveld, W. J., van Osnabrugge, B., & Weerts, A. H. (2020). Scaling Point-Scale (Pedo)transfer Functions to Seamless Large-Domain Parameter Estimates for High-Resolution Distributed Hydrologic Modeling: An Example for the Rhine River. *Water Resources Research*, *56*(4), e2019WR026807. doi:10.1029/2019WR026807

IPCC. (2021). Summary for Policymakers. *Climate Change 2021: The Physical Science Basis. Contribution of Working Group I to the Sixth Assessment Report of the Intergovernmental Panel on Climate Change*.

Jain, S. K., Mani, P., Jain, S. K., Prakash, P., Singh, V. P., Tullos, D., … Dimri, A. (2018). A brief review of flood forecasting techniques and their applications. *International Journal of River Basin Management*, *16*(3), 329–344. doi:10.1080/15715124.2017.1411920

Jongman, B., Ward, P. J., & Aerts, J. C. (2012). Global exposure to river and coastal flooding: Long term trends and changes. *Global Environmental Change*, *22*(4), 823–835. doi:10.1016/J.GLOENVCHA.2012.07.004

Jonkman, S. N., & Vrijling, J. K. (2008). Loss of life due to floods. *Journal of Flood Risk Management*, *1*(1), 43–56. doi:10.1111/j.1753-318X.2008.00006.x

Junghänel, T., Bissolli, P., Daßler, J., Fleckenstein, R., Imbery, F., Janssen, W., … Weigl, E. (2021). *Geschäftsbereich Klima und Umwelt Hydro-klimatologische Einordnung der Stark-und Dauerniederschläge in Teilen Deutschlands im Zusammenhang mit dem Tiefdruckgebiet "Bernd" vom 12. bis 19. Juli 2021* (Tech. Rep.). Deutscher Wetterdienst.

Jutta Thielen-del Pozo, J., Salamon, P., Peter Burek, P., Pappenberger, F., Eklund, C., Sprokkereef, E., … Garcia-Sanchez, R. (2019). Medium Range Flood Forecasting Example EFAS. In Q. Duan, F. Pappenberg, A. Wood, H. Cloke, & J. Schaake (Eds.), *Handbook of hydrometeorological ensemble forecasting* (pp. 1261–1278). Springer. doi:10.1007/978-3-642-39925-1

Klein, A. C. (2022). *Hydrological Response of the Geul Catchment to the Rainfall in July 2021* (MSc thesis). Delft University of Technology.

KNMI. (2021). *KNMI Klimaatsignaal '21: hoe het klimaat in Nederland snel verandert* (Tech. Rep.). De Bilt.

KNMI. (2023). *Precipitation - radar/gauge 5 minute real-time accumulations over the Netherlands.* Retrieved from https://dataplatform.knmi.nl/dataset/nl-rdr-data-rtcor-5m-1-0 (Accessed: 2023-01-18)

Koenker, R., & Bassett, G. (1978). Regression Quantiles. *Econometrica*, *46*(1), 33–50.

Kreienkamp, F., Y.S., P., Tradowsky, J., Kew, S., Lorenz, P., Arrighi, J., … Wander, N. (2021). Rapid attribution of heavy rainfall events leading to the severe flooding in Western Europe during July 2021. *World Weather Attribution*, *2021*, 1–51.

Kufeld, M. (2013). *Anpassung der Talsperrensteuerung an Klimaänderungen: Bewertung von Leistungsfähigkeit und Robustheit* (PhD thesis). Aachen University of Applied Sciences, Aachen.

Kufeld, M., Lange, J., & Hausmann, B. (2010). *Das Einzugsgebiet der Rur : Ergebnisbericht der im Rahmen des AMICE-Projekts durchgeführten Literaturrecherche* (Tech. Rep.). AMICE.

Kundzewicz, Z. W., Kanae, S., Seneviratne, S. I., Handmer, J., Nicholls, N., Peduzzi, P., … Sherstyukov, B. (2014). Flood risk and climate change: global and regional perspectives. *Hydrological Sciences Journal*, *59*(1), 1–28. doi:10.1080/02626667.2013.857411

LANUV. (2001). *Gewässergütebericht 2001 Nordrhein-Westfalen - Berichtzeitsraum 1995-2000.*

Le Bihan, G., Payrastre, O., Gaume, E., Moncoulon, D., & Pons, F. (2016). Regional models for distributed flash-flood nowcasting: towards an estimation of potential impacts and damages. In *FLOODrisk 2016 - 3rd European Conference on Flood Risk Man-*

agement (p. 18013). E3S Web of Conferences. doi:10.1051/e3sconf/20160718013

Le Bihan, G., Payrastre, O., Gaume, E., Moncoulon, D., & Pons, F. (2017). The challenge of forecasting impacts of flash floods: Test of a simplified hydraulic approach and validation based on insurance claim data. *Hydrology and Earth System Sciences*, *21*(11), 5911–5928. doi:10.5194/hess-21-5911-2017

Lin, P., Pan, M., Allen, G., Frasson, R., Zeng, Z., Yamazaki, D., & Wood, E. (2019). *Global estimates of reach-level bankfull river width leveraging big-data geospatial analysis*. Zenodo. Retrieved from https://zenodo.org/record/3552776 doi:10.5281/ZENODO.3552776

Lorenz, E. (1963). Deterministic nonperiodic flow. *Journal of the Atmospheric Sciences*, *20*(2), 130–141. doi:10.1175/1520-0469(1963)020<0130:DNF>2.0.CO;2

Lund, J. R., Hui, R., Escriva-Bou, A., Porse, E. C., Adams, L., Connaughton, J., … Yi, S. (2017). Reservoir Operation Design. In V. P. Singh (Ed.), *Handbook of applied hydrology* (pp. 1301–1308). McGraw-Hill Education.

Maaß, A. L., Esser, V., Frings, R. M., Lehmkuhl, F., & Schüttrumpf, H. (2018). A decade of fluvial morphodynamics: relocation and restoration of the Inde River (North-Rhine Westphalia, Germany). *Environmental Sciences Europe*, *30*(1). doi:10.1186/s12302-018-0170-0

Mardonova, M., & Han, Y. S. (2023). Environmental, hydrological, and social impacts of coal and nonmetal minerals mining operations. *Journal of Environmental Management*, *332*. doi:10.1016/j.jenvman.2023.117387

Marinelli, F., & Niccoli, W. L. (2000). Simple analytical equations for estimating ground water inflow to a mine pit. *Ground Water*, *38*(2), 311–314. doi:10.1111/j.1745-6584.2000.tb00342.x

Marth, I. F. (2021). *Application of reservoir operation models in hydrological forecasts for regulated catchments* (MSc thesis). RWTH Aachen University.

McFeeters, S. K. (1996). The use of the normalized difference water index (ndwi) in the delineation of open water features. *International journal of remote sensing*, *17*(7), 1425–1432.

Mengistu, H. A., Demlie, M. B., Abiye, T. A., Xu, Y., & Kanyerere, T. (2019). Conceptual hydrogeological and numerical groundwater flow modelling around the Moab Khutsong deep gold mine, South Africa. *Groundwater for Sustainable Development*, *9*. doi:10.1016/j.gsd.2019.100266

Merz, B., Kuhlicke, C., Kunz, M., Pittore, M., Babeyko, A., Bresch, D. N., … Wurpts, A. (2020). Impact Forecasting to Support Emergency Management of Natural Hazards. *Reviews of Geophysics*, *58*(4). doi:10.1029/2020RG000704

Merz, B., Thieken, A., & Gocht, M. (2007). Flood risk mapping at the local scale: concepts and challenges. In S. Begum, M. Stive, & J. Hall (Eds.), *Flood risk management in europe* (pp. 231–251). Dordrecht: Springer Netherlands.

Middendorp, R. M. (2022). *Design of a flood bypass tunnel for Valkenburg aan de Geul Operation and hydraulic design to reduce the risk of flooding* (MSc thesis). Delft University of Technology.

Miller, J. E. (1983). *Basic concepts of kinematic-wave models. U.S. geological survey professional paper 1302* (Tech. Rep.). United States Department of the Interior.

Mirus, B. B., & Loague, K. (2013). How runoff begins (and ends): Characterizing hydro-

logic response at the catchment scale. *Water Resources Research*, *49*(5), 2987–3006. doi:10.1002/wrcr.20218

Montzka, C. (2008). *Einsatz von multispektralen Satellitenbilddaten in der Wasserhaushalts-und Stoffstrommodellierung-dargestellt am Beispiel des Rureinzugsgebietes* (Tech. Rep.). Jülich.

Morales-Hernández, M., Petaccia, G., Brufau, P., & García-Navarro, P. (2016). Conservative 1D-2D coupled numerical strategies applied to river flooding: The Tiber (Rome). *Applied Mathematical Modelling*, *40*(3), 2087–2105. doi:10.1016/j.apm.2015.08.016

Moussa, R. (1996). Analytical Hayami solution for the diffusive wave flood routing problem with lateral inflow. *Hydrological Processes*, *10*(9), 1209–1227. doi:10.1002/(SICI)1099-1085(199609)10:9<1209::AID-HYP380>3.0.CO;2-2

Moussa, R. (2004). Criteria for the choice of flood routing methods for natural channels with overbank flow. In *Proceedings of wetHYDRO Workshop3* (pp. 73–82).

Moussa, R., & Bocquiuon, C. (1996). Criteria for the choice of flood-routing methods in natural channels. *Journal of Hydrology*, *186*(1), 1–30.

Moussa, R., & Cheviron, B. (2015). Modeling of Floods - State of the Art and Research Challenges. In P. Rowiński & A. Radecki-Pawlik (Eds.), *Rivers - physical, fluvial and environmental processes* (pp. 169–192). Springer.

Muishout, C. (2023). *The Hydrological Effect of Urban Nature-based Solutions on Catchment Scale* (MSc thesis). Delft University of Technology.

Munich RE. (2022). *Weather disasters in USA dominate natural disaster losses in 2021* (Tech. Rep.). Munich Reinsurance Company.

Myneni, R., Knyazikhin, Y., & Park, T. (2015). *Mcd15a3h modis/terra+aqua leaf area index/fpar 4-day l4 global 500m sin grid v006*. NASA EOSDIS Land Processes Distributed Active Archive Center. Retrieved from https://lpdaac.usgs.gov/products/mcd15a3hv006/ doi:10.5067/MODIS/MCD15A3H.006

NASA. (2013). *Shuttle Radar Topography Mission (SRTM)*. (Accessed: 2023-02-15) doi:10.5069/G9445JDF

Neal, J., Schumann, G., & Bates, P. (2012). A subgrid channel model for simulating river hydraulics and floodplain inundation over large and data sparse areas. *Water Resources Research*, *48*(11). doi:10.1029/2012WR012514

NEW. (2021). *Hoogwater 2021 Feiten en Duiding* (Tech. Rep.). Expertise Waterveiligheid Nederland.

Northey, S. A., Mudd, G. M., Saarivuori, E., Wessman-Jääskeläinen, H., & Haque, N. (2016). Water footprinting and mining: Where are the limitations and opportunities? *Journal of Cleaner Production*, *135*, 1098–1116. doi:10.1016/j.jclepro.2016.07.024

Ochoa-Rodríguez, S., Onof, C., Maksimovic, C., Wang, L.-P., Willems, P., Van Assel, J., … Ten Veldhuis, M.-C. (2015). *Urban Pluvial Flood Modelling: Current Theory and Practice* (Tech. Rep.). RainGain. Retrieved from http://www.raingain.eu/sites/default/files/wp3_review_document.pdf

Oki, T., & Kanae, S. (2006). Global Hydrological Cycles and World Water Resources. *Science*, *313*(5790), 1068–1072. doi:10.1126/science.1128845

Olivera, F., & Koka, S. (2004). Hydrodynamic Dispersive and Advective Processes

in Watershed Responses. *Journal of Hydrologic Engineering*, *9*(6), 534–543. doi:10.1061/(asce)1084-0699(2004)9:6(534)

Overeem, A., & Leijnse, H. (2021). *Evaluatie & verbetering radarneerslagproducten: Casestudie externe neerslag Zuid-Limburg 13-15 juli 2021* (Tech. Rep.). KNMI.

Panilas, S., Petalas, C. P., & Gemitzi, A. (2008). The possible hydrologic effects of the proposed lignite open-cast mining in Drama lignite field, Greece. *Hydrological Processes*, *22*(11), 1604–1617. doi:10.1002/HYP.6729

Pattison, I., Lane, S. N., Hardy, R. J., & Reaney, S. M. (2014). The role of tributary relative timing and sequencing in controlling large floods. *Water Resources Research*, *50*(7), 5444–5458. doi:10.1002/2013WR014067

Pegram, G., Raynaud, D., Sprokkereef, E., Ebel, M., Rademacher, S., Olsson, J., … Sppångmyr, H. (2019). Present and Future Requirements for Using and Communicating Hydrometeorological Ensemble Prediction Systems for Short-, Medium-, and Long-Term Applications. In Q. Duan, F. Pappenberg, A. Wood, H. Cloke, & J. Schaake (Eds.), *Handbook of hydrometeorological ensemble forecasting* (pp. 1047–1092). Springer. doi:10.1007/978-3-642-39925-1

Perez, G., Mantilla, R., & Krajewski, W. F. (2018). The Influence of Spatial Variability of Width Functions on Regional Peak Flow Regressions. *Water Resources Research*, *54*(10), 7651–7669. doi:10.1029/2018WR023509

Perumal, M., & Price, R. K. (2017). Reservoir and Channel Routing. In V. P. Singh (Ed.), *Handbook of applied hydrology* (pp. 5201–5216). McGraw-Hill Education.

Peters-Lidard, C. D., Clark, M., Samaniego, L., Verhoest, N. E., Van Emmerik, T., Uijlenhoet, R., … Woods, R. (2017). Scaling, similarity, and the fourth paradigm for hydrology. *Hydrology and Earth System Sciences*, *21*(7), 3701–3713. doi:10.5194/HESS-21-3701-2017

Pierce, C., Seed, A., Ballard, S., Simonin, D., & Li, Z. (2012). Nowcasting. In J. Bech & J. L. Chau (Eds.), *Doppler radar observations* (chap. 4). Rijeka: IntechOpen. doi:10.5772/39054

Ponce, V. M. (1991). Kinematic Wave Controversy. *Journal of Hydraulic Engineering*, *117*(4), 511–525.

Pusch, M., & Hoffmann, A. (2000). Conservation concept for a river ecosystem (River Spree, Germany) impacted by flow abstraction in a large post-mining area. *Landscape and Urban Planning*, *51*, 165–176.

Pyka, C., Jacobs, C., Breuer, R., Elbers, J., Nacken, H., Sewilam, H., & Timmerman, J. (2016). Effects of water diversion and climate change on the Rur and Meuse in low-flow situations. *Environmental Earth Sciences*, *75*(16), 1–15. doi:10.1007/S12665-016-5989-3/TABLES/10

Rak, G., Kozelj, D., & Steinman, F. (2016). The impact of floodplain land use on flood wave propagation. *Natural Hazards*, *83*(1), 425–443. doi:10.1007/s11069-016-2322-0

Reinert, D., Prill, F., Frank, H., Denhard, M., Baldauf, M., Schraa, C., … Zängl, G. (2023). *DWD Database Reference for the Global and Regional ICON and ICON-EPS Forecasting System Version 2.2.2* (Tech. Rep.). Deutscher Wetterdienst.

Restrepo, P. J., Deweese, M., Schaake, C., John, & Hartman, R. (2017). Flood Forecasting and Flash Flood Forecasting—Special Considerations in Hydrologic Modeling for the Expressed Purpose of Flood and Flash Flood Forecasting. In V. P. Singh (Ed.),

Handbook of applied hydrology (chap. 129). McGraw-Hill Education.

Rijkswaterstaat. (2022). *Waterinfo*. https://waterinfo.rws.nl/. (Accessed: 2022-10-07)

Rinaldo, A., Marani, A., & Rigon, R. (1991). Geomorphological Dispersion. *Water Resources Research*, *27*(4), 513–525.

Roundy, J. K., Duan, Q., & Schaake, J. C. (2019). Hydrological Predictability, Scales, and Uncertainty Issues. In Q. Duan, F. Pappenberg, A. Wood, H. Cloke, & J. Schaake (Eds.), *Handbook of hydrometeorological ensemble forecasting* (pp. 3–31). Springer. doi:10.1007/978-3-642-39925-1

Rözer, V., Peche, A., Berkhahn, S., Feng, Y., Fuchs, L., Graf, T., … Neuweiler, I. (2021). Impact-Based Forecasting for Pluvial Floods. *Earth's Future*, *9*(2). doi:10.1029/2020EF001851

RWE. (2015a). *Antrag auf Erteilung der wasserrechtlichen Erlaubnis zur Fortsetzung der Entnahme und Ableitung von Grundwasser für die Entwässerung des Tagebaus Hambach im Zeitraum 2020-2030. Erläuterungsbericht* (Tech. Rep.). RWE Power AG. Retrieved from https://fragdenstaat.de/anfrage/rwe-antrag-zum-abpumpen-des-grundwasser-im-tagebau-hambach/

RWE. (2015b). *Antrag auf Erteilung der wasserrechtlichen Erlaubnis zur Fortsetzung der Entnahme und Ableitung von Grundwasser für die Entwässerung des Tagebaus Hambach im Zeitraum 2020 – 2030. Anlage G: Grundwassermodell* (Tech. Rep.). RWE Power AG. Retrieved from https://fragdenstaat.de/anfrage/rwe-antrag-zum-abpumpen-des-grundwasser-im-tagebau-hambach/

Saadi, M., Furusho-Percot, C., Belleflamme, A., Chen, J.-Y., Trömel, S., & Kollet, S. (2023). How uncertain are precipitation and peak flow estimates for the July 2021 flooding event? *Natural Hazards and Earth System Sciences*, *23*, 159–177. doi:10.5194/nhess-23-159-2023

Saco, P. M., & Kumar, P. (2002). Kinematic dispersion in stream networks: 1. Coupling hydraulic and network geometry. *Water Resources Research*, *38*(11), 26–1. doi:10.1029/2001wr000695

Samuels, P. G. (1990). Cross-section location in 1-D models. In *International Conference on River Flood Hydraulics* (pp. 339–350). Wallingford: Hydraulics Research Limited.

Savenije, H. H., & Hrachowitz, M. (2017). HESS Opinions "Catchments as meta-organisms - A new blueprint for hydrological modelling". *Hydrology and Earth System Sciences*, *21*(2), 1107–1116. doi:10.5194/hess-21-1107-2017

Schellekens, J., van Verseveld, W., Visser, M., Winsemius, H., Bouaziz, L., Euser-De Boer, T., … Jansen, M. (2020). openstreams/wflow: Bug fixes and updates for release 2020.1.2. doi:10.5281/ZENODO.4291730

Schüttrumpf, H. (2022). *The July Flood 2021 (presentation)*.

Sentinel. (2023). *Sentinel NDWI script*. https://custom-scripts.sentinel-hub.com/sentinel-2/ndwi/. (Accessed: 2023-06-07)

Sethi, R., & Di Molfetta, A. (2019). *Groundwater Engineering: A Technical Approach to Hydrogeology, Contaminant Transport and Groundwater Remediation*. Cham, Switzerland: Springer.

Seyfried, M. S., & Wilcox, B. P. (1995). Scale and the Nature of Spatial Variability: Field

Examples Having Implications for Hydrologic Modeling. *Water Resources Research*, *31*(1), 173–184. doi:10.1029/94WR02025

Shen, B. W., Pielke, R. A., Zeng, X., Baik, J. J., Faghih-Naini, S., Cui, J., & Atlas, R. (2021). Is weather chaotic? Coexistence of chaos and order within a generalized lorenz model. *Bulletin of the American Meteorological Society*, *102*(1), E148-E158. doi:10.1175/BAMS-D-19-0165.1

Silva, W., Dijkman, J. P., & Loucks, D. P. (2004). Flood management options for the netherlands. *International Journal of River Basin Management*, *2*(2), 101–112.

Singh, V. P. (2017). *Handbook of Applied Hydrology*. McGraw-Hill Education.

Skøien, J. O., Blöschl, G., & Western, A. W. (2003). Characteristic space scales and timescales in hydrology. *Water Resources Research*, *39*(10). doi:10.1029/2002WR001736

Slager, K. (2023). *Gevolgen overstromingen Limburg Inventarisatie en duiding* (Tech. Rep.). Deltares.

Smith, R. E., & Goodrich, D. C. (2005). Rainfall Excess Overland Flow. In M. Anderson (Ed.), *Encyclopedia of hydrological sciences* (pp. 1708–1718). John Wiley & Sons, Ltd.

STOWA. (2018). *Neerslagstatistieken voor korte duren* (Tech. Rep.). Amersfoort: Stichting Toegepast Onderzoek Waterbeheer.

STOWA. (2019). *Neerslagstatistiek en -reeksen voor het waterbeheer 2019* (Tech. Rep.). Stichting Toegepast Onderzoek Waterbeheer.

Strahler, A. N. (1957). Quantitative Analysis of Watershed Geomorphology. *Transactions, American Geophysical Union*, *38*(6), 913–921.

Tanaka, T., Kiyohara, K., & Tachikawa, Y. (2020). Comparison of fluvial and pluvial flood risk curves in urban cities derived from a large ensemble climate simulation dataset: A case study in Nagoya, Japan. *Journal of Hydrology*, *584*, 124706. doi:10.1016/j.jhydrol.2020.124706

Terink, W., Leijnse, H., Van Den Eertwegh, G., & Uijlenhoet, R. (2018). Spatial resolutions in areal rainfall estimation and their impact on hydrological simulations of a lowland catchment. *Journal of Hydrology*, *563*. doi:10.1016/j.jhydrol.2018.05.045

Thewissen, A. (2022). *Flood event of July 2021: How extreme were the floods in the Ahr, Vesdre and Geul?* (MSc thesis). Delft University of Technology.

Thielen, J., Bartholmes, J., Ramos, M.-H., & De Roo, A. (2009). The European Flood Alert System-Part 1: Concept and development. , *13*, 125–140.

Troin, M., Arsenault, R., Wood, A. W., Brissette, F., & Martel, J. L. (2021). Generating Ensemble Streamflow Forecasts: A Review of Methods and Approaches Over the Past 40 Years. *Water Resources Research*, *57*(7). doi:10.1029/2020WR028392

Tsiokanos, A. (2022). *Investigation of the Impacts of Climate Variability and Land Use Changes on the Hydrology of the Geul River Catchment* (MSc thesis). Delft University of Technology.

Tu, M. (2006). *Assessment of the effects of climate variability and land use change on the hydrology of the Meuse river basin* (PhD thesis). UNESCO-IHE, Delft.

UNESCO. (2023). *Floods (IFI)*. Retrieved from https://en.unesco.org/themes/water-security/hydrology/programmes/floods

Van de Lee, W., Udo, J., Barneveld, H., & Duizendstra, H. (2001). *Voortplantingssnelheid*

hoogwatergolven in de Maas (Tech. Rep.). Rijkswaterstaat.

van der Knijff, J. M., Younis, J., & de Roo, A. P. (2008). LISFLOOD: a GIS-based distributed model for river basin scale water balance and flood simulation. *International Journal of Geographical Information Science*, *24*(2), 189–212. doi:10.1080/13658810802549154

van der Krogt, W., Becker, B., & Boisgontier, H. (2022). Low river discharge of the meuse: A meuse river basin water management modelling study using ribasim.

Van der Ploeg, M., Bannink, A., & Oomen, T. (2021). *Jaarrapport 2020: De Maas: Zijn extreme afvoeren het nieuwe normaal?* (Tech. Rep.). RIWA - Vereniging van Rivierwaterbedrijven.

van der Vat, M., Boderie, P., Bons, K. C., Hegnauer, M., Hendriksen, G., van Oorschot, M., … others (2019). Participatory modelling of surface and groundwater to support strategic planning in the Ganga Basin in India. *Water*, *11*(12), 2443. doi:10.3390/w11122443

van Dijk, Y. (2022). *Flooding problems in the catchment area of the River Geul* (MSc thesis). Delft University of Technology.

van Riel, W. (2011). *Exploratory study of pluvial flood impacts in Dutch urban areas* (Tech. Rep.). Deltares. Retrieved from https://https://edepot.wur.nl/287817

Van Verseveld, W., Visser, M., Boisgontier, H., Bootsma, H., Bouaziz, L., Buitink, J., … Hegnauer, M. (2022). *Deltares/Wflow.jl: unstable-master. https://github.com/Deltares/Wflow.jl.*

Van Verseveld, W. J., Weerts, A. H., Visser, M., Buitink, J., Imhoff, R. O., Boisgontier, H., … Russell, B. (2022). Wflow_sbm v0.6.1, a spatially distributed hydrologic model: from global data to local applications. *Geoscientific Model Development Discussion*, *[preprint]*. doi:10.5194/gmd-2022-182

Verkade, J. S., Brown, J. D., Reggiani, P., & Weerts, A. H. (2013). Post-processing ECMWF precipitation and temperature ensemble reforecasts for operational hydrologic forecasting at various spatial scales. *Journal of Hydrology*, *501*, 73–91. doi:10.1016/J.JHYDROL.2013.07.039

Vertessy, R. A., & Elsenbeer, H. (1999). Distributed modeling of storm flow generation in an Amazonian rain forest catchment: Effects of model parameterization. *Water Resources Research*, *35*(7), 2173–2187. doi:10.1029/1999WR900051

Vitousek, P. M., Mooney, H. A., Lubchenco, J., & Melillo, J. M. (1997). Human Domination of Earth's Ecosystems. *Science*, *277*(5325). doi:10.1126/science.277.5325.494

Volpi, E., Di Lazzaro, M., Bertola, M., Viglione, A., & Fiori, A. (2018). Reservoir Effects on Flood Peak Discharge at the Catchment Scale. *Water Resources Research*, *54*(11), 9623–9636. doi:10.1029/2018WR023866

vom Kothen, N., V. andütz. (2005). *Ergebnisbericht Rur und südliche sonstige Maaszuflüsse* (Tech. Rep.).

Wang, J., Lu, C., Sun, Q., Xiao, W., Cao, G., Li, H., … Zhang, B. (2017). Simulating the hydrologic cycle in coal mining subsidence areas with a distributed hydrologic model. *Scientific Reports*, *7*. doi:10.1038/srep39983

Wannasin, C. (2023). *Modelling and forecasting daily streamflow with reservoir operationin the upper chao phraya river basin, thailand* (Doctoral dissertation, Wagenin-

gen University). doi:10.18174/584572

Wannasin, C., Brauer, C. C., Uijlenhoet, R., van Verseveld, W. J., & Weerts, A. H. (2021). Daily flow simulation in Thailand Part I: Testing a distributed hydrological model with seamless parameter maps based on global data. *Journal of Hydrology: Regional Studies*, *34*, 2214–5818. doi:10.1016/J.EJRH.2021.100794

Weerts, A. H., Winsemius, H. C., & Verkade, J. S. (2011). Hydrology and Earth System Sciences Estimation of predictive hydrological uncertainty using quantile regression: examples from the National Flood Forecasting System (England and Wales). *Hydrology and Earth System Sciences*, *15*, 255–265. doi:10.5194/hess-15-255-2011

Weiler, M., McDonnell, J. J., Tromp-van Meerveld, I., & Uchida, T. (2005). Subsurface Stormflow. In M. Anderson (Ed.), *Encyclopedia of hydrological sciences*. John Wiley & Sons, Ltd. doi:10.1002/0470848944.hsa119

Werner, M., Schellekens, J., Gijsbers, P., van Dijk, M., van den Akker, O., & Heynert, K. (2013). The delft-fews flow forecasting system. *Environmental Modelling & Software*, *40*, 65–77. doi:10.1016/j.envsoft.2012.07.010

Werner, M. G. (2001). Impact of grid size in GIS based flood extent mapping using a 1D flow model. *Physics and Chemistry of the Earth, Part B: Hydrology, Oceans and Atmosphere*, *26*(7-8), 517–522. doi:10.1016/S1464-1909(01)00043-0

Western, A. W., & Blöschl, G. (1999). On the spatial scaling of soil moisture. *Journal of Hydrology*, *217*(3-4), 203–224. doi:10.1016/S0022-1694(98)00232-7

Winsemius, H. C., Aerts, J. C. J. H., Van Beek, L. P. H., Bierkens, M. F. P., Bouwman, A., Jongman, B., … Ward, P. J. (2016). Global drivers of future river flood risk. *NATURE CLIMATE CHANGE*, *6*. doi:10.1038/NCLIMATE2893

Winterrath, T., Rosenow, W., & Weigl, E. (2011). On the DWD quantitative precipitation analysis and nowcasting system for real-time application in German flood risk management. , *351*.

WMO. (2011). *Manual on flood forecasting and warning* (Tech. Rep.). World Meteorological Organization.

WMO. (2012). *Integrated Flood Management Tools Series: Management of Flash Floods* (Tech. Rep.). World Meteorological Organization.

WMO. (2015). *WMO Guidelines on Multi-hazard Impact-based Forecast and Warning Services* (Tech. Rep.). Geneva, Switzerland: World Meteorological Organization.

Wolkersdorfer, C., Nordstrom, D. K., Beckie, R. D., Cicerone, D. S., Elliot, T., Edraki, M., … Soler i Gil, A. (2020). *Guidance for the Integrated Use of Hydrological, Geochemical, and Isotopic Tools in Mining Operations* (Vol. 39) (No. 2). Springer. doi:10.1007/s10230-020-00666-x

Wood, E. F., Sivapalan, M., & Beven, K. (1990). Similarity and scale in catchment storm response. *Reviews of Geophysics*, *28*(1), 1–18. doi:10.1029/RG028I001P00001

Woods, R., & Sivapalan, M. (1999). A synthesis of space-time variability in storm response: Rainfall, runoff generation, and routing. *WATER RESOURCES RESEARCH*, *35*(8), 2469–2485. doi:10.1029/1999WR900014

WVER. (2017a). *Die Oleftalsperre (Infoblatt)*. Retrieved from https://wver.de/wp-content/uploads/2019/11/Oleftalsperre.pdf

WVER. (2017b). *Die Rurtalsperre (Infoblatt)*. Retrieved from https://wver.de/wp-content/uploads/2019/11/Rurtalsperre.pdf

WVER. (2017c). *Die Stauanlage Heimbach (Infoblatt)*. Retrieved from https://server.wver.de/images/content/talsperren/datenblaetter/stb_heimbach.pdf

WVER. (2017d). *Die Stauanlage Obermaubach (Infoblatt)*. Retrieved from https://wver.de/wp-content/uploads/2019/11/stb_obermaubach.pdf

WVER. (2017e). *Die Urfttalsperre (Infoblatt)*. Retrieved from https://wver.de/wp-content/uploads/2019/11/urfttalsperre.pdf

WVER. (2017f). *Die Wehebachtalsperre (Infoblatt)*. Retrieved from https://wver.de/wp-content/uploads/2019/11/wehebachtalsperre.pdf

Yamazaki, D., Ikeshima, D., Sosa, J., Bates, P. D., Allen, G. H., & Pavelsky, T. M. (2019). MERIT Hydro: A High-Resolution Global Hydrography Map Based on Latest Topography Dataset. *Water Resources Research*, *55*(6), 5053–5073. doi:10.1029/2019WR024873

Yand, D., Jayawardena, A., & Cong, Z. (2017). Watersheds, River Basins, and Land Use. In V. Singh (Ed.), *Handbook of applied hydrology* (pp. 201–208). McGraw-Hill Education.

Zevenbergen, C., Cashman, A., Evelpidou, N., Pasche, E., Garvin, S., & Ashley, R. (2010). *Urban flood management*. CRC Press. doi:10.1201/9781439894330

Zhao, L., Ren, T., & Wang, N. (2017). Groundwater impact of open cut coal mine and an assessment methodology: A case study in NSW. *International Journal of Mining Science and Technology*, *27*(5), 861–866. doi:10.1016/j.ijmst.2017.07.008

Zhou, T., Nijssen, B., Gao, H., & Lettenmaier, D. P. (2016). The Contribution of Reservoirs to Global Land Surface Water Storage Variations. *Journal of Hydrometeorology*, *17*(1), 309–325. doi:10.1175/JHM-D-15-0002.1

A

MODEL CONFIGURATIONS

A.1. *HydroMT*

The *Wflow_SBM* models are built using the *HydroMT* framework consisting of the `hydromt` (core) and `hydromt_wflow` Python packages. First, the model (named `model_a`) is generated using the following command:

```
hydromt build wflow "./models/model_a"
    -r"{'subbasin': [5.988550,51.185190],
         bounds': [5.9650, 50.4017, 6.7042, 51.1983],
        'strord': 8}"
    -i "./configs/model_base.ini"
```

The model build depends on the region settings (`-r`). A subbasin is generated for the given outlet coordinates `[5.988550,51.185190]` (in the WGS84 coordinate system), a bounding box is defined to reduce computation times and a threshold Strahler order of 8. Furthermore, a configuration file (`*.ini`) is parsed after `-i`, which contains the source files and settings for the several methods used to build the model. An overview and description of these methods and source files are provided in table A.1, and additional settings are listed in table A.2.

A

`hydromt_wflow` method	Generated maps	Source
`setup_basemaps`	Catchment boundary, elevation map, flow direction map, slope, stream order	Yamazaki et al. (2019)
`setup_rivers`	River map, river width, river depth, river slope, hydrologically conditioned elevation map	Lin et al. (2019) and *Gewässerstationierungskarte des Landes Nordrhein-Westfalen* (n.d.)
`setup_floodplains`	Floodplain volume map for multiple water depths	Yamazaki et al. (2019)
`setup_reservoirs`	Reservoir maps	WVER (2017a, 2017b, 2017e, 2017f)
`setup_lulcmaps`	Land use maps, vegetation maps	European Environment Agency (2019)
`setup_laimaps`	Leaf area index climatology per month	Myneni et al. (2015)
`setup_soilmaps`	Soil maps including, among others, soil thickness, vertical saturated conductivity, average saturated soil water content, and average residual water content	Hengl et al. (2017) and Geodienst NRW (2023a)

Table A.1: An overview of the methods used by the *HydroMT* model builder, the related *Wflow_SBM* maps and the sources used to create these maps.

setup_basemaps		
upscale_method	ihu	Iterative Hydrography Upscaling method to upscale flow direction map
res	0.00833	model resolution in degrees
setup_rivers		
river_upa	5.0 (**full**) 100 (**reduced**)	minimum upstream area threshold for a river cell
rivdph_method	powlaw	power law function used to compute river depth from bankfull discharge
min_rivdph	2.5	threshold value for river depth
min_rivwth	3.0	threshold value for river width
slope_len	2000.0	slope length used to derive river slope from subgrid elevation difference
smooth_len	5000.0	length used for averaging missing values for the river depth
river_routing	local-inertial / kinematic-wave	used to enable/disable conditioning of the bankfull elevation map
setup_floodplains		
floodplain_type	1d	derive a floodplain profile for every river cell
flood_depths	[0.5, 1.0, 1.5, 2.0, 2.5, 3.0, 4.0, 5.0]	flood depths at which a volume is derived
setup_soilmaps		
ptf_ksatver	brakensiek	Use PTF for calculating vertical saturated conductivity from Brakensiek et al. (1984)
setup_temp_pet_forcing		
press_correction	True	Correct using elevation lapse rate
temp_correction	True	
pet_method	debruin	Method to compute reference evapotranspiration from De Bruin and Lablans (1998)
setup_constant_pars		
EoverR	0.11	Gash interception model parameter
InfiltCapPath	5	infiltration capacity of the compacted areas
InfiltCapSoil	600	soil infiltration capacity
rootdistpar	-500	controls how roots are linked to the water table

Table A.2: Most relevant tettings parsed to the *HydroMT* model builder in the `*.ini` file.

A

A.2. *Wflow_SBM*

Table A.3 lists the settings used in the *Wflow_SBM* models. These settings are parsed using a `*.toml` file and may vary per model type (e.g. reservoirs, river routing). Specific settings such as the start date, references to filenames, variable mapping, and output settings are not included, as they either vary per model or are trivial and can be found in the *Wflow_SBM* documentation (Deltares, 2022).

***Wflow_SBM* settings**

`type`	sbm	wflow framework model type
`masswasting`	false	lateral snow transport
`snow`	false	vertical snow modeling
`reinit`	false (warm), true (cold)	start with cold or warm state
`reservoirs`	false true	include reservoir modeling
`lakes`	false	include lakes in model
`glacier`	false	include glaciers in model
`river_routing`	kinematic-wave **(Wflow-KW)** local-inertial	river routing scheme
`land_routing`	kinematic-wave	land routing scheme (using "local-inertial" enables 2D-modelling)
`thicknesslayers`	[100, 300, 800,]	specify the number of soil layers and thickness
`min_streamorderriver` `min_streamorder_land`	6 5	minimum stream order to delineate subbasins (for multi-threading computing purposes)
`kin_wave_iteration`	true	solve the kinematic-wave equation iteratively
`kw_river_tstep`	900	fixed sub-timestep for iterations of flow calculations
`kw_land_tstep`	3600	
`floodplain_1d`	false **(Wflow-LI)** true **(Wflow-FP)**	include or exclude 1D floodplain schematization
`inertial_flow_alpha`	0.7	coefficient for model stability
`froude_limit`	false	limit flow to subcritical-critical according to Froude number
`h_thresh`	0.001	water depth threshold

Table A.3: Most relevant settings parsed to the Wflow model in the `*.toml` file.

A.3. *ProMaIDes*

Table A.4 lists the settings used in the *ProMaIDes* models. These settings are parsed using a `*.ilm` file and may vary by model type (PM-1D, PM-2D). Specific settings such

as the start date, references to filenames, output settings, or river-model and floodplain-model information are not included, as they vary per model or are trivial and can be found in the *ProMaIDes* documentation (HS Magdeburg, 2022).

Time settings		
`TSTEP`	3600	output timestep size
`TNOF`	120	number of timesteps
`NOFITS`	120	number of internal (synchronisation) timesteps

Model settings		
`NOFFP`	0 **(PM-1D)** 5 **(PM-2D)**	number of floodplain models
`NOFRV`	1 (hindcast, forecast) 2 (regular)	number of river models

Integration settings		
`MAXNUMSTEPS`	200000	Maximum number of solver steps to reach the next timestep
`MAXSTEPSIZE`	3000	Maximum solver step size
`INISTEPSIZE`	0	Initial step size for the solver

Tolerance settings		
`RTOL`	1e-6	relative tolerance
`ATOL`	1e-5	absolute tolerance

Table A.4: Most relevant settings parsed to the *ProMaIDes* model in the `*.ilm` file.

B

CALIBRATING THE *Wflow_SBM* MODEL

B.1. MODELLING THE RUR RESERVOIR SYSTEM

B.1.1. CALIBRATION APPROACH

As inflow, outflow, and storage data are available for the Rur, Urft, and Olef reservoirs, the calibration process can be performed outside of *Wflow_SBM*. To this end, the algorithm to simulate reservoirs in *Wflow_SBM* is extracted from the Julia source code and translated into a separate Python script[1]. As a result, the reservoir response can be simulated without running an entire *Wflow_SBM* model. It saves computing time and allows the use of WVER inflow data as forcing of the reservoir.

The calibration process is divided into three parts. First, the free room in the operation plan is discretised by simulating the whole system as a linked reservoir system. Second, a constant storage of the Olef reservoir is assumed and optimised, which unlinks the reservoir system. Finally, the performance of the reservoir system is evaluated inside the final *Wflow_SBM* model and compared to WVER observations from 2012 to 2020. This approach is summarised in Figure B.1.

B.1.2. CALIBRATION RESULTS

CALIBRATING FREE OPERATION ROOM Q_1 AND Q_2

The Urft and Rur reservoirs are combined as a single reservoir in *Wflow_SBM* as explained in the Appendix D.2.2 and a volume-discharge relationship has been derived from the Olef-Urft-Rur operation plan, which can be found in the Appendix E.1. This plan shows that the outflow at Heimbach is discretised for low- and high-flow regimes, summarised as Q_{low} and Q_{high} in Figure B.3. In between these regions, the reservoir

[1] This code has been published as a Python package under the name reservoirs_wflow and can be installed via Pip.

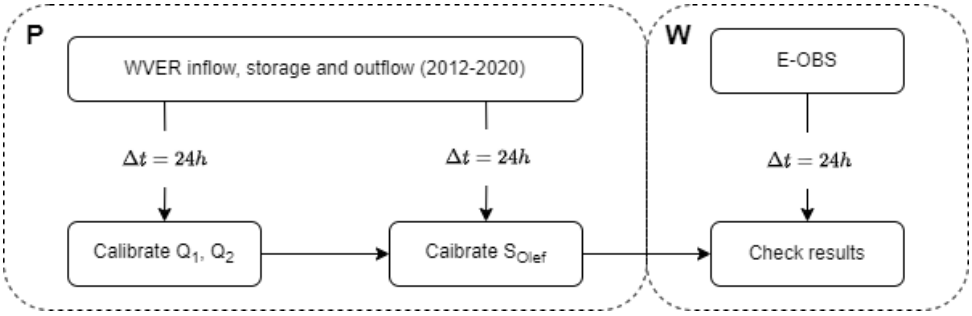

Figure B.1: Approach for calibrating the Rur reservoir system for the *Wflow_SBM* model. **P** indicates that the process takes place in an isolated Python script, and **W** indicates that the *Wflow_SBM* model is used.

operator is free to vary the outflow based, for example, on specific demands from downstream industry.

However, it is difficult to include this variability in a *Wflow_SBM* model driven by a volume-discharge-based approach, especially since the observed average daily outflow shows a large spread centred around 5-6 m^3/s (as shown in Figure B.2). Therefore, the free operating room is divided into a lower and upper section with a discretised outflow, Q_1 and Q_2 respectively, where $Q_2 > Q_1$. The division of these regimes is based on the target reservoir volume indicated with the green line in Figure B.3 and Appendix E.1.

The modelled outflow of the reservoir is compared with the observed outflow to Heimbach, which consists of the sum outflow of the Rur reservoir and the power station outflow. Figure B.4 indicates that lower values for Q_1 and Q_2 result in a more accurate approximation of the exit. These lower flows also result in a lower error for modelled reservoir storage measured by relative bias (Figure B.4). The best results are obtained for $Q_1 = 5$ m^3/s and $Q_2 = 8$ m^3/s. It should be noted that $Q_1 < \max(Q_{low}) = 6$ m^3/s, which seems contradictory. However, the analysis of the frequency of the average daily outflows of the reservoirs (Figure B.2) indicates that outflow below 6 m^3/s occurs often for the Rur reservoir system, and therefore can be applied.

UNLINKING THE RESERVOIRS AND DALIBRATING S_{Olef}

As a next step, a constant volume is assumed for the Olef reservoir, resulting in an unlinked reservoir system. Figure B.5 indicates that assuming low storage at the Olef reservoir results in a higher NSE score for the Urft-Rur outflow, with the best score for $S_{Olef} = 2$ Mm^3. However, observations show that storage values for which $S_{Olef} < 8$ Mm^3 occur rarely, and that the average storage fluctuates around $S_{Olef} = 10$ Mm^3. Therefore, a trade-off has been made and a storage level of $S_{Olef} = 6$ $Mm^3$is chosen.

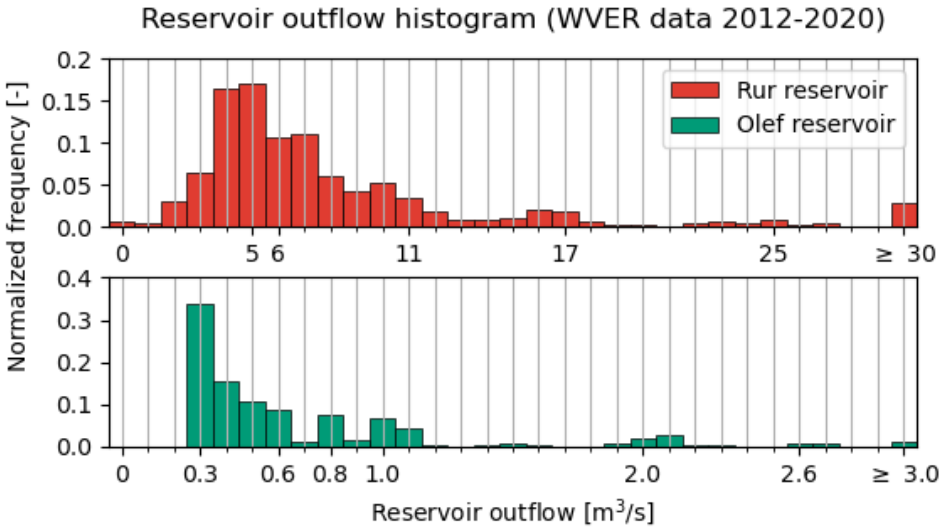

Figure B.2: Relative frequency of daily reservoir outflow.

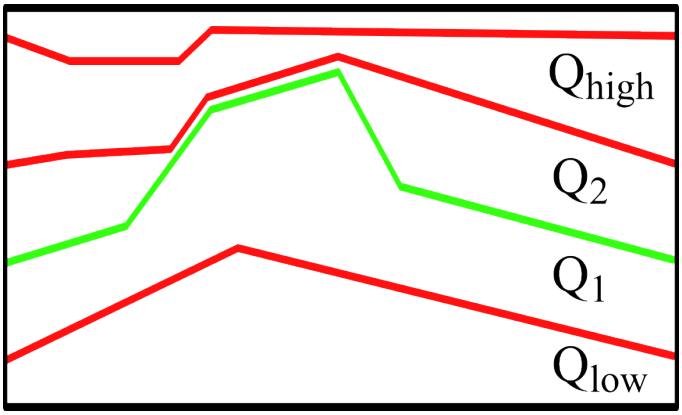

Figure B.3: Schematization of the Olef-Urft-Rur volume-based operation plan. A distinction is made between low-flow and high-flow regime (Q_{low} and Q_{high}), the free operation room (Q_1 and Q_2) and the target volume (green line).

IMPLEMENTATION IN *Wflow_SBM* MODEL

Finally, volume-based operation rules have been implemented in the Wflow-KW model using discretization of the free operation room and constant storage of the Olef reservoir. This results in the volume-based operation plans shown in Figures E.1a and E.1b showing the resulting volume-based operation plans. The performance of the Wflow-KW model is addressed by investigating the NSE scores of stations located downstream of the Olef, Urft, and Rur reservoirs.

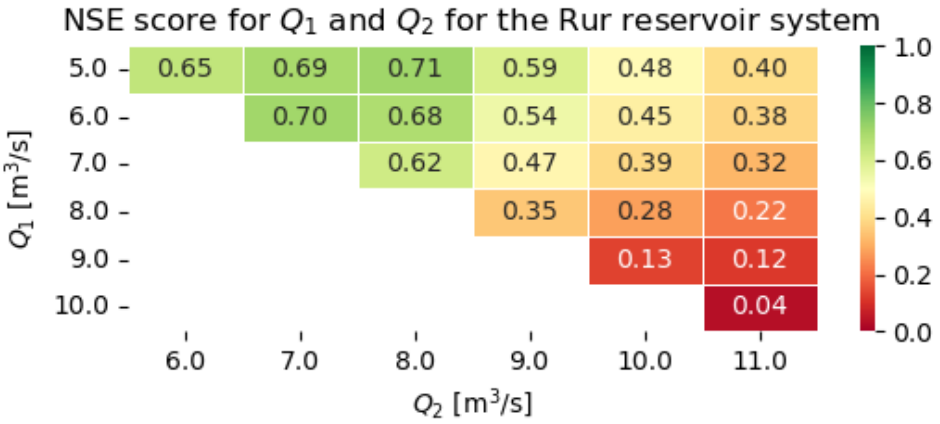

Figure B.4: NSE score for the reservoir outflow during calibration of Q_1 and Q_2.

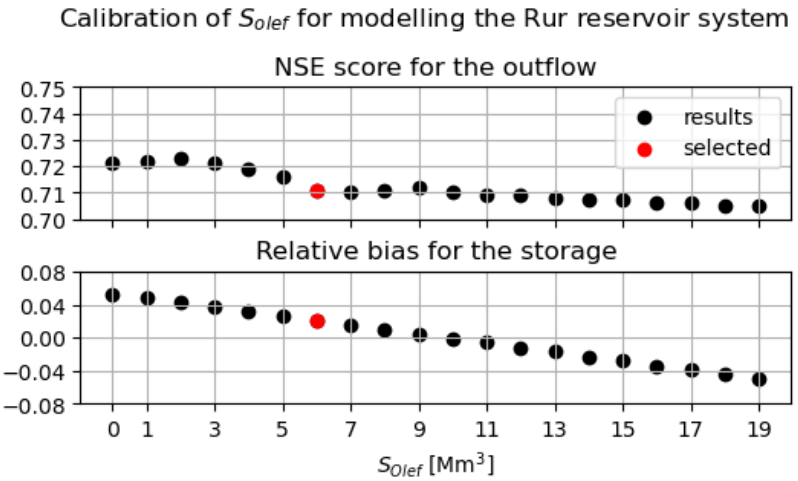

Figure B.5: NSE score and relative bias for the reservoir during calibration of S_{Olef}.

First, a comparison between observed and modelled outflow and storage of the Rur reservoir system and the Olef reservoir shows a strong resemblance, particularly in terms of simulating storage of the reservoir (Figure B.6). Correctly simulating outflow is more difficult, especially for the Rur reservoir system where high peak outflows are underestimated. A possible explanation may be the assumption of S_{Olef} = 6 Mm^{3}which, in high flow conditions, is an underestimation of the volume of the Olef reservoir, resulting in a lower outflow from the Rur reservoir system.

Moreover, the effects of integrating the reservoir system into the *Wflow_SBM* model on the hydrographs at the gauge stations in the Rur catchment are investigated. Generally,

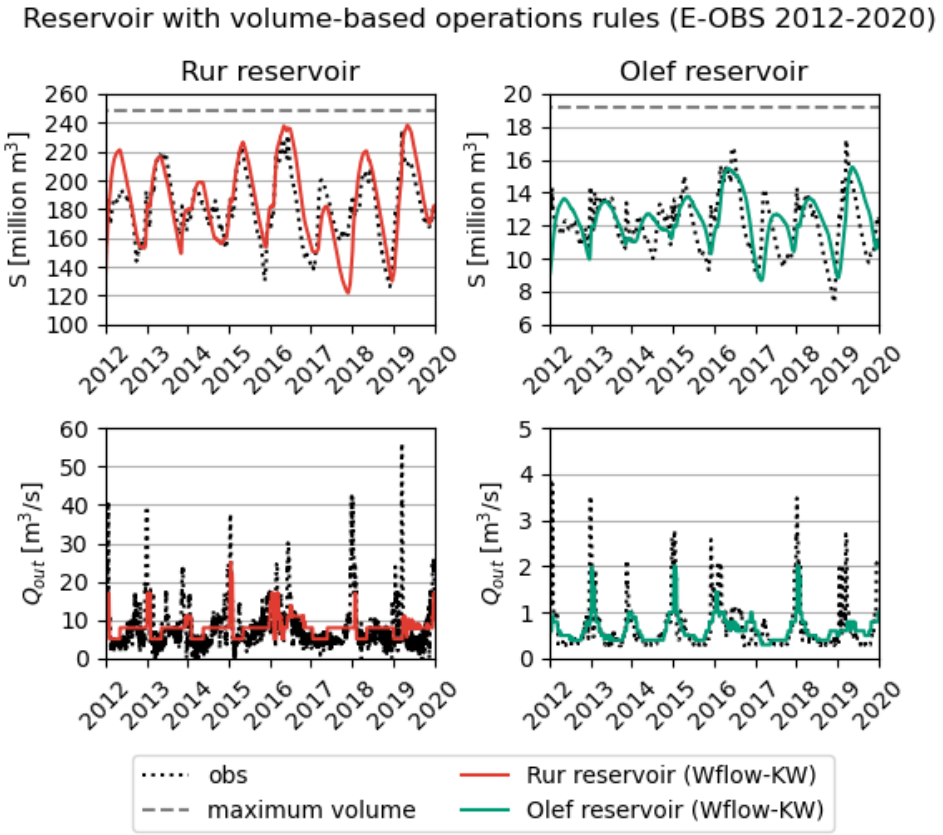

Figure B.6: Simulated and observed reservoir storage and outflow using Wflow-KW.

results improve for the stations located in Rur downstream of the Rur reservoir system (Figure B.7). However, the NSE score decreases at Zerkall 1, which is the gauge station closest to Heimbach where the reservoir outlet is located.

However, the hydrographs at Zerkall 1, Selhausen, and Altenburg 1 (Figure B.8) show that the base flow at these stations is better captured by including reservoirs in the model. The low NSE score may be attributed to the underestimation of the peaks in Zerkall 1. These peaks in the reservoir outflow are driven by the operating rules of a high-flow regime, which is located in the narrow upper band in Figure E.1a. Therefore, a small deviation in the modelled storage may result in a large difference in the outflow. Furthermore, the absence of Heimbach and Obermaubach reservoirs in *Wflow_SBM* can decrease the precision of the results of the *Wflow_SBM* model.

No calibration is needed for the Olef reservoir as its operation plan is fully explicit (see also Appendix E.2). However, performance at the stations downstream of the Olef reservoir does not show significant improvement when implemented in the *Wflow_SBM*

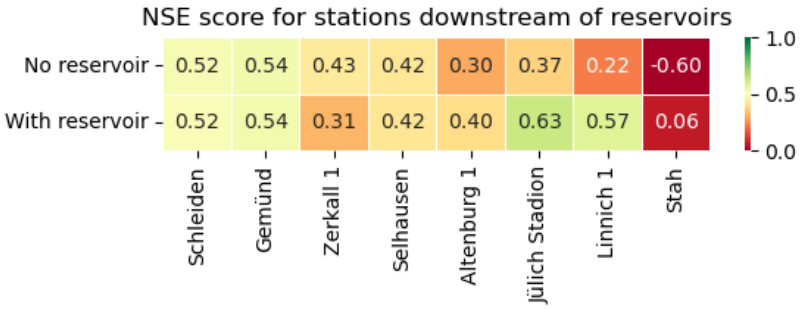

Figure B.7: NSE score for stations downstream of the Rur reservoir system with and without reservoir modelling in Wflow-KW.

model, as confirmed by the hydrographs in Figure B.9.

Similarly, an operation plan is derived for the Wehebach reservoir based on the written operation plan. In this plan, three outflow regimes are defined: low flow (Q = 0.1 /mm-m/s), high flow (Q = 0.2 /mmm/s) and maximum flow (Q = 0.2 /mmm/s). These flow conditions are mainly based on the inflow to the Wehebach reservoir and not strictly on the volume of the reservoir. As a result, it remains difficult to improve the hydrograph at Luchem, located downstream of the Wehebach reservoir (Figure B.10). This is especially challenging as the reservoir and the gauge station are both located near the lignite mine where, in this stage of the calibration process, no leakage has yet been applied (appendix B.3). Further improvement of calibration of the Wehebach reservoir is not considered as the magnitude of the outflow is limited compared to the Olef reservoir and the Rur reservoir system, and no detailed inflow, outflow and storage data was available for the Wehebach reservoir.

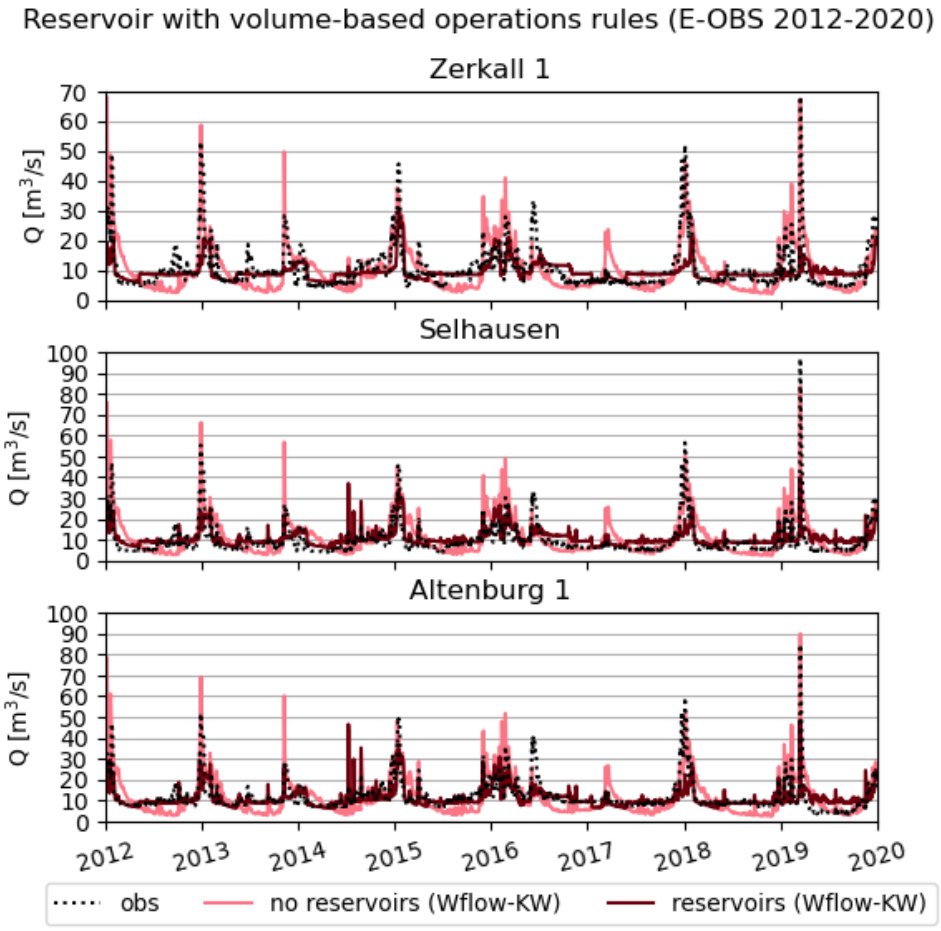

Figure B.8: Hydrographs at gauge stations downstream of Rur reservoir system.

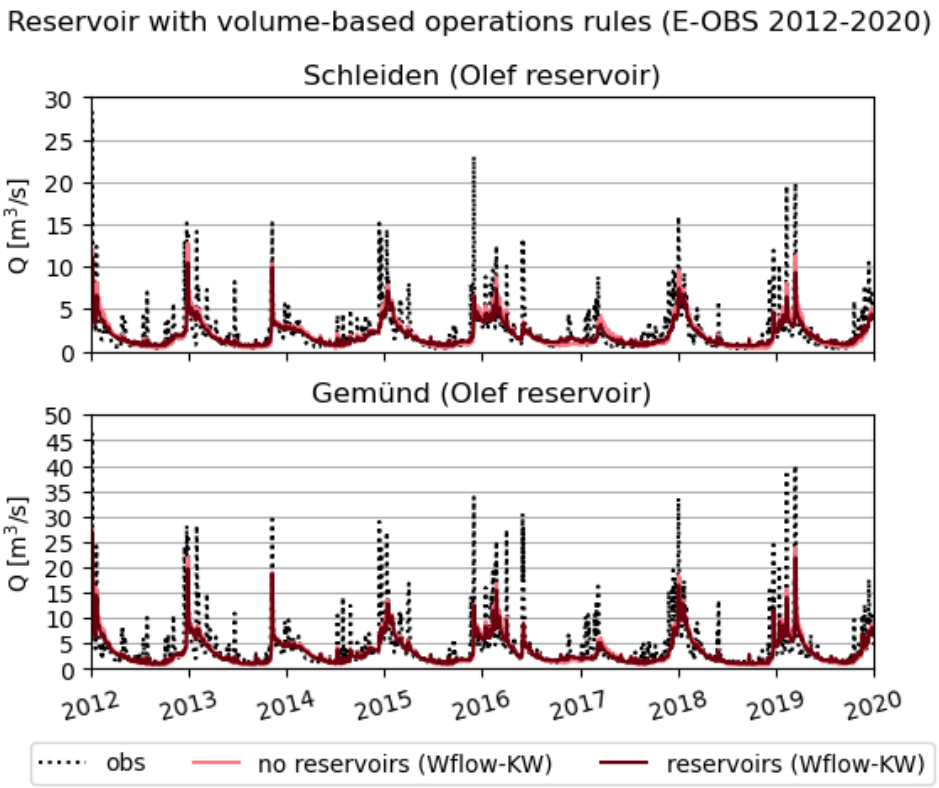

Figure B.9: Hydrographs at gauge stations downstream of Olef reservoir.

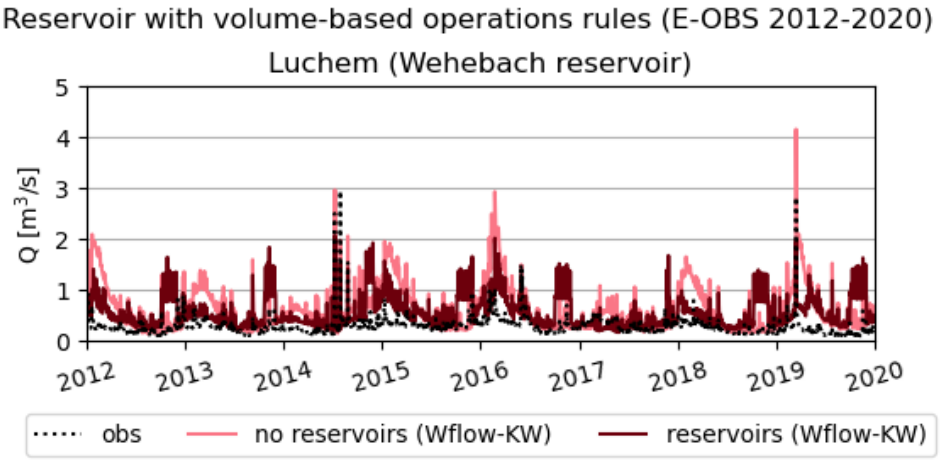

Figure B.10: Hydrographs at gauge station downstream of Wehebach reservoir.

B.2. KSATHORFRAC

B.2.1. VERTICAL AND HORIZONTAL CONDUCTIVITY

Section 3.1.1 describes the geohydrological characteristics of the Rur catchment and how the subsurface is modelled by *Wflow_SBM*. To this end, the BK50 (Geodienst NRW, 2023a) and HÜK250 maps (Geodienst NRW, 2023b) are used to improve the modelling of subsurface flow, which is strongly dependent on the vertical conductivity of the soil, determining how much water infiltrates the soil, and the horizontal conductivity, which governs the subsurface flow itself. To this end, the map `KsatVer` in *Wflow_SBM* is updated using values for saturated vertical conductivity from BK50, and the parameter `ksathorfrac` is calibrated.

B.2.2. CALIBRATION APPROACH

The calibration of the parameter `ksathorfrac` is performed based on the geohydrological characteristics of the catchment, since the parameter describes the ratio of the vertical saturated conductivity of the soil (which is given) and the horizontal saturated conductivity (which is calculated). To this end, the HÜK250 geohydrological map of North Rhine-Westphalia (NRW) (Figure 3.4a) is used to divide the catchment into six zones with expected horizontal hydraulic conductivity similar to that shown in Figure B.11.

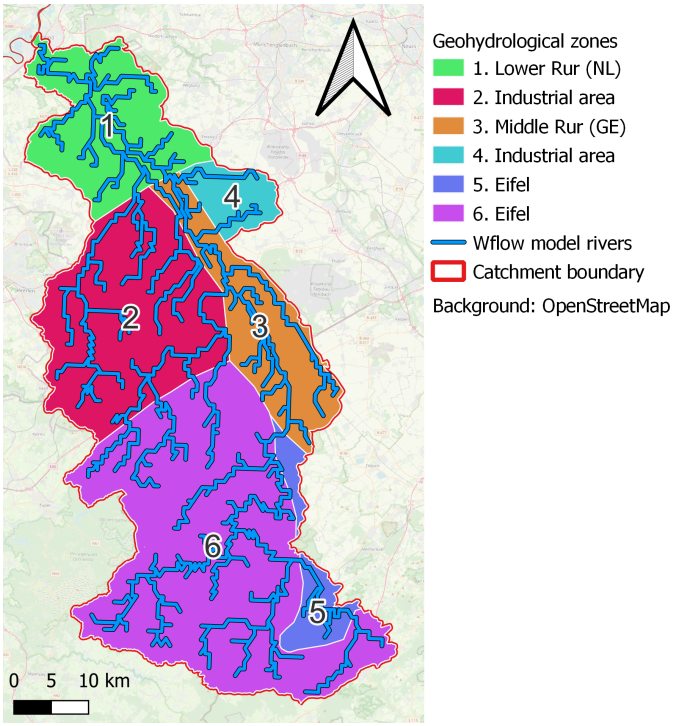

Figure B.11: Regions for the calibration of `ksathorfrac` based on the HÜK250 map.

Calibration begins in the upstream regions of the catchment and continues in the down-

stream direction. Therefore, the calibration is performed first for regions 5 and 6, then for 2 and 4, and finally for 1 and 3. The results are evaluated using the NSE score based on the E-OBS dataset (2012-2020).

B

B.2.3. CALIBRATION RESULTS

The results for regions 5 and 6 are shown in Figure B.12. It is clear that the stations in the Eifel region are all sensitive to variations in the `ksathorfrac` parameter, and that a high value for this parameter is favoured, resulting in a better NSE score. The Eifel streams are relatively steep and small and respond quickly to precipitation. Therefore, the separation between base flow and peak flows is governed by the `ksathorfrac`, as a high horizontal conductivity feeds the base flow which, due to the high steepness, can become significant. The optimal results were obtained with `ksathorfrac` being 500 for region 5 and 1000 for region 6.

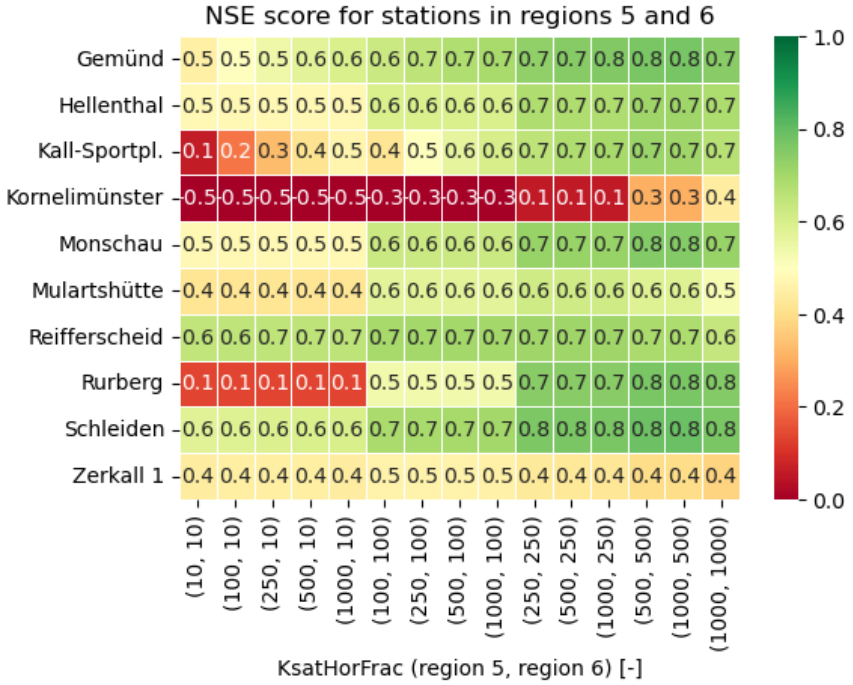

Figure B.12: Calibration result for `ksathorfrac` in regions 5 and 6.

The results of several stations in regions 2 and 4 show very poor NSE scores compared to stations in the other regions, even with three stations with very poor performance left out (figure B.13). These stations at Honsdorf, Luchem, and Welz show very low runoff coefficients (0.05, 0.13 and 0.07 respectively) and *Wflow_SBM* results strongly overestimate the volume of water passing along these stations. Improvements in modelling the flow at these stations using the `MaxLeakage` parameter are described in the Appendix B.3. Furthermore, it is known that the stations in Herzogenrath 1 and 2 are influenced

by flows from the sewage system in Aachen that strongly affect the baseflow at these stations, resulting in a low NSE score.

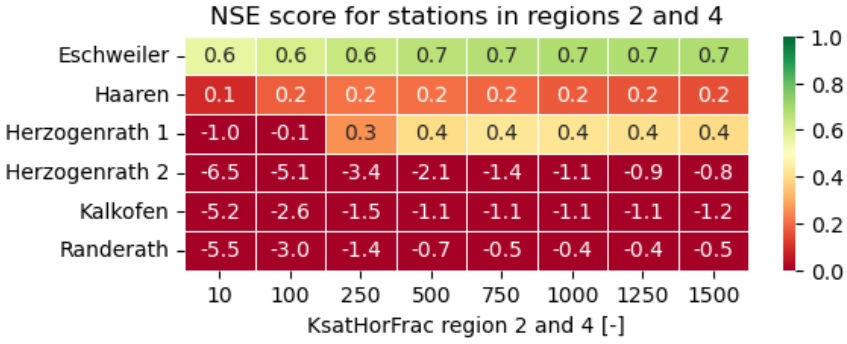

Figure B.13: Calibration result for `ksathorfrac` in regions 2 and 4.

The stations less affected by leakage and sewage water show a distinction in the modelling results, where the downstream stations show a constant performance and the upstream stations show a strong improvement for a larger `ksathorfrac`. Optimal results were found for a value of 1000, which is chosen as the optimal value.

The calibration of the stations in regions 1 and 3 similarly shows an increase in the results with an optimum at `ksathorfrac` = 1000 (figure B.14). Flow at upstream stations (Selhausen and Altenburg 1) is governed by the reservoir outflow and therefore less affected by variations in this parameter, and the effect of varying the parameter increases in the downstream direction.

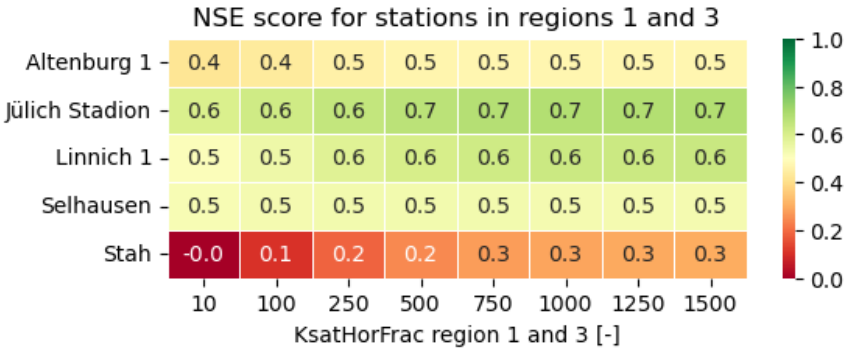

Figure B.14: Calibration result for `ksathorfrac` in regions 1 and 3.

The final results of the calibration of `ksathorfrac` are listed in table B.1 with a comparison to the horizontal conductivity described by Geodienst NRW (2023b).

Region	Description	Horizontal conductivity (Geodienst NRW, 2023b)	ksathorfrac [-]
1	Lower Rur (NL)	medium to high	1000
2	Industrial	high	1000
3	Middle Rur (GE)	medium	1000
4	Industrial	high, strongly variable	1000
5	Eifel	high	500
6	Eifel	low	1000

Table B.1: Overview of the calibration results for the six geohydrological zones in the Rur catchment.

B.3. MAXLEAKAGE

B.3.1. LIGNITE MINING AND RURSCHOLLE MODEL

Sections 2.5.1 and 3.1.3 describe in greater detail how lignite mining can affect the hydrology of the catchment. This section describes the approach and the results of the calibration of this parameter using the results of the Rurscholle groundwater model by Bachmann et al. (2005).

B.3.2. CALIBRATION APPROACH

The leakage from the saturated zone occurs in all cells in the *Wflow_SBM* model as part of the vertical processes. Therefore, it is expected and confirmed that the leakage itself is identical for the Wflow-KW, Wflow-LI, and Wflow-FP models. Similarly to the reservoirs and `ksathorfrac`, the calibration of the parameter `MaxLeakage` is executed using Wflow-KW models. The E-OBS dataset is used during calibration, and the model is run at a daily timestep from 2012 to 2020.

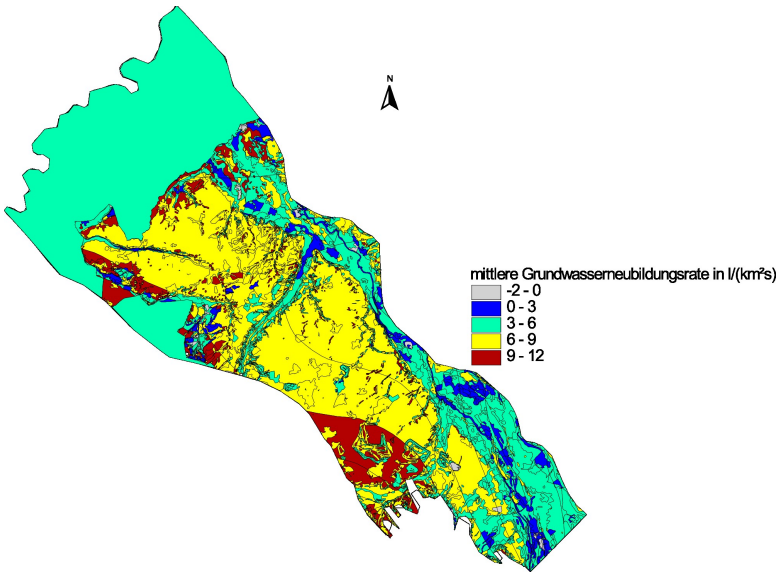

Figure B.15: Average recharge in the Rurscholle model Bachmann et al. (2005).

Several combinations of $L_{max,1}$ and $L_{max,2}$ are tested, where $L_{max,1} \leq L_{max,2}$ as this follows from the recharge distribution derived from the Rurscholle model. In general, the Rurscholle recharge rates vary from 0 to 6 $l/(km^2 s)$ in region 1, and from 6 to 12 $l/(km^2 s)$ in region 2, as shown in Figure B.15. These ranges correspond respectively to 0 to 0.5184 mm/day and 0.5184 to 1.0368 mm/day. Based on these values, combinations for L_{max} are chosen from the set [0.4, 0.6, 0.8, 1.0] mm/day, producing a total of 9 combinations, and the Rurscholle model area is divided into two leakage zones to be applied to the *Wflow_SBM* model (Figure B.16).

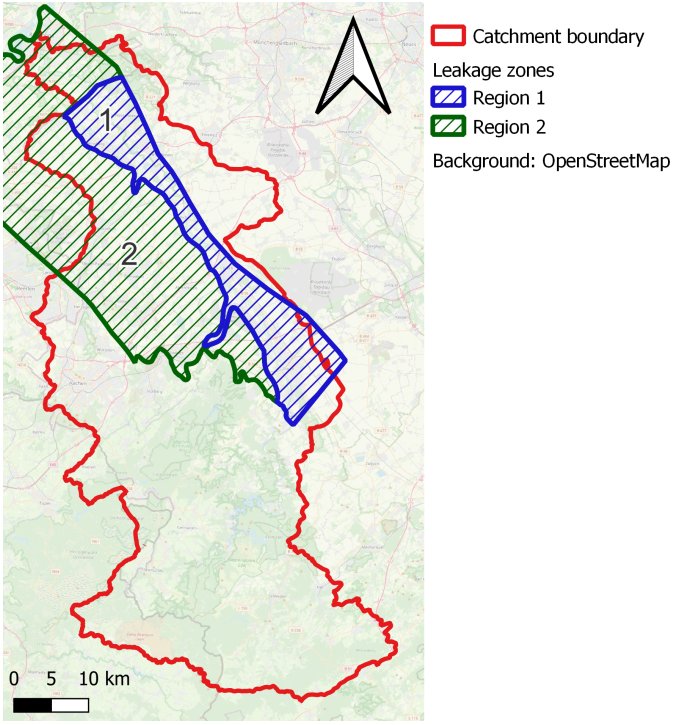

Figure B.16: Regions for the calibration of `ksathorfrac` based on the Rurscholle model.

B.3.3. Calibration results

The NSE scores are calculated for the stations located in the watersheds that overlap the Rurscholle and are shown in figure B.17. Generally, model results improve as leakage increases, especially at stations located on the Wurm (Randerath) or its tributary (Honsdorf). This also improves the score at Stah, as this is the only station downstream of the Wurm and Rur confluence. The NSE score decreases at Altenburg 1 for all combinations of leakage parameters, but it should be noted that the flow at the station is dominated by the outflow of the reservoir, which in itself is difficult to correctly model.

The combinations of $L_{max,1}$ and $L_{max,2}$ and their respective annual leakage are shown in figure B.19. Annual leakage shows variations which may depend on climatological

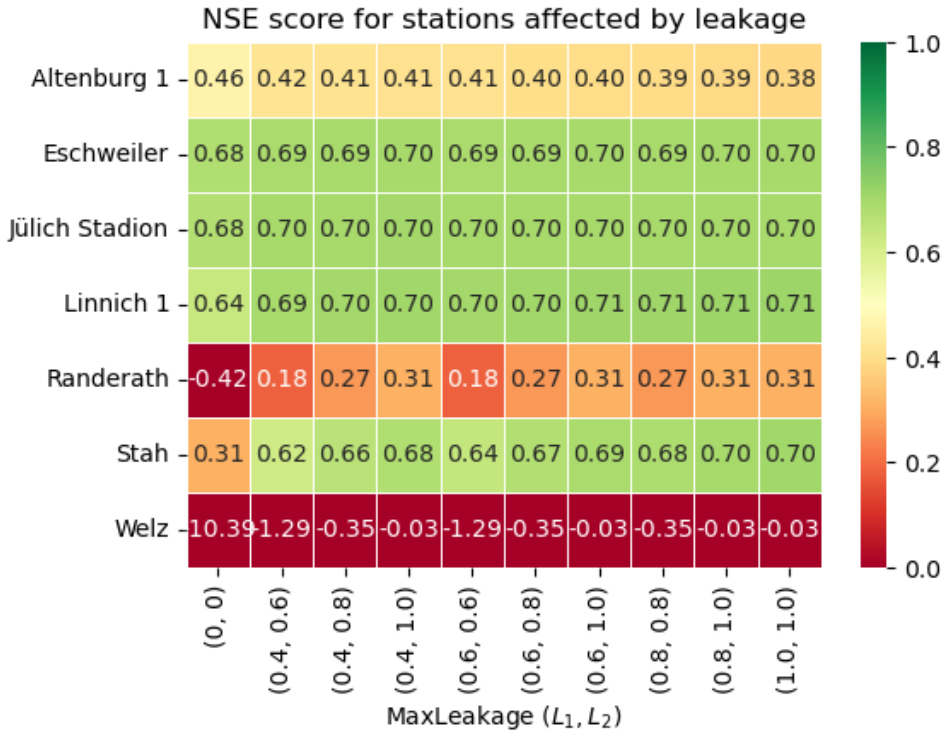

Figure B.17: NSE score for combinations of $L_{max,1}$ and $L_{max,2}$.

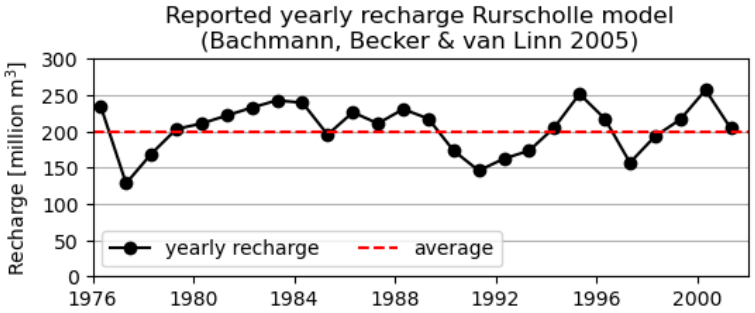

Figure B.18: Reported yearly recharge in Rurscholle by Bachmann et al. (2005).

conditions such as, for example, the soil is less saturated during a dry year, resulting in a lower annual leakage. Overall, combinations of `MaxLeakage` show annual leakages between the margins of the reported Rurscholle recharge at 125 and 250 million m^3/year (figure B.18).

The combination of $L_{max,1} = 0.4$ and $L_{max,2} = 0.8$ mm/day shows significant improve-

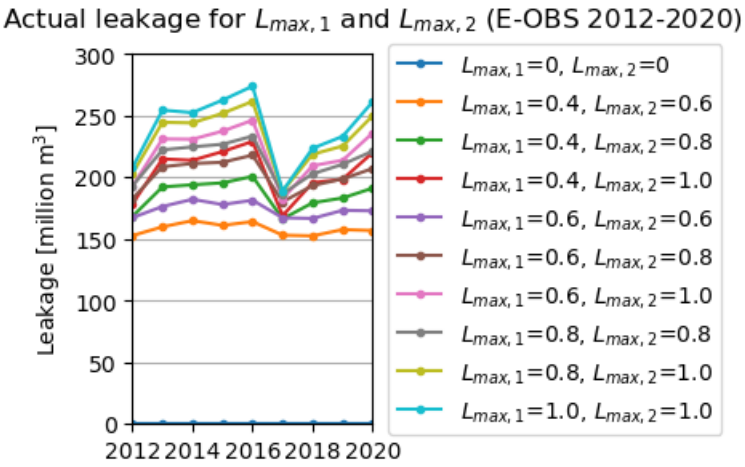

Figure B.19: Yearly total leakage for combinations of $L_{max,1}$ and $L_{max,2}$.

ments in terms of NSE scores compared to results without leakage, and the total leakage is still conservative compared to the reported recharge. Therefore, this combination is chosen as the optimal results for the `MaxLeakage` parameter in the *Wflow_SBM* model.

B.4. BANKFULL DEPTH AND WIDTH

The accuracy of the river routing schemes depends on the availability of data describing the bankfull river depth and width. The river width affects the flow velocities in the river cells, and the bankfull river depth helps model inundation using the local-inertial approach. River width information was found using the GSK3E dataset from LANUV, but no source was found for the bankfull depth. As a result, the bankfull depth was set to an unrealistic high value (10 m) to avoid inundation when using the local-inertial method, as the river flow is forced to stay within the river. However, the bankfull depth and width for the Rur River could be derived using the detailed profiles from the hydrodynamic ProMaIDes model.

As a result, an algorithm was developed that determined the bankfull depth $d_{bankfull}$ based on the height difference between the lowest point in the cross-section and the highest point on the lower side of the main channel. Then the area $A_{bankfull}$ of the profile was determined using a trapezoidal integration method, resulting in a bankfull width $A_{bankfull}/d_{bankfull}$. This results in detailed information on the bankfull width and depth of each profile.

For simple geometries, this approach is straightforward. However, asymmetrical and flat geometries are challenging to map and may result in erroneous values for the cross-sectional area and, consequently, the bankfull depth. Therefore, the definition of the main channel was extended to include the first two points of the embankment to ac-

count for flat and skewed main channel geometries, and a minimum bankfull depth of 0.5 metres was assumed to address unrealistic values, based on varying these values and observing how it improved model results.

For burning the Rur river map values, *HydroMT* is used, which, in turn, uses the rasterise method of `rasterio.features module`. It is important to note that this method uses the 'painter' algorithm, which means that the geometries are handled in order and can thus overwrite each other. Both the kinematic wave and local-inertial river routing schemes in the hydrological model depend on the width of the river cell to determine the flow velocity. The width profiles of the Rur River vary as a result of river meandering, canalisation of the Rur in urban areas and the presence of lakes and floodplains in the river profile, and the grid cells in the hydrological model have a 550 by 1000 metre resolution, while the river profiles from the ProMaIDes model are typically separated by 100 metres. Therefore, arbitrariness in mapping the width to the river cell can influence the flow velocity and the arrival time of the flood wave. A moving average is applied to account for this effect, including the twenty profiles neighbouring points on each side.

The final results are shown in Figures B.20 and B.21. In particular, the bankfull depth and width increase in German areas with wide floodplains, where the cross-sections are discretised wide and deep in the *ProMaIDes* river model.

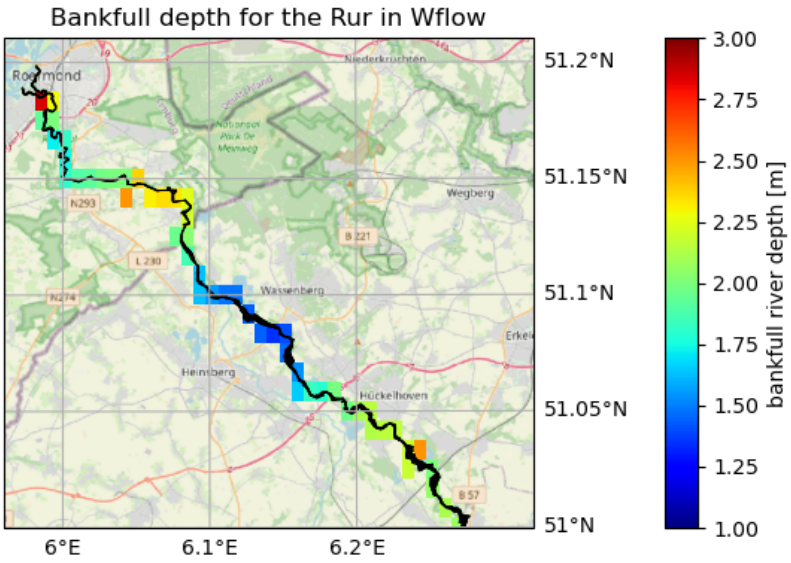

Figure B.20: Bankfull river depth in the *Wflow_SBM* model after including *ProMaIDes* cross-sectional information.

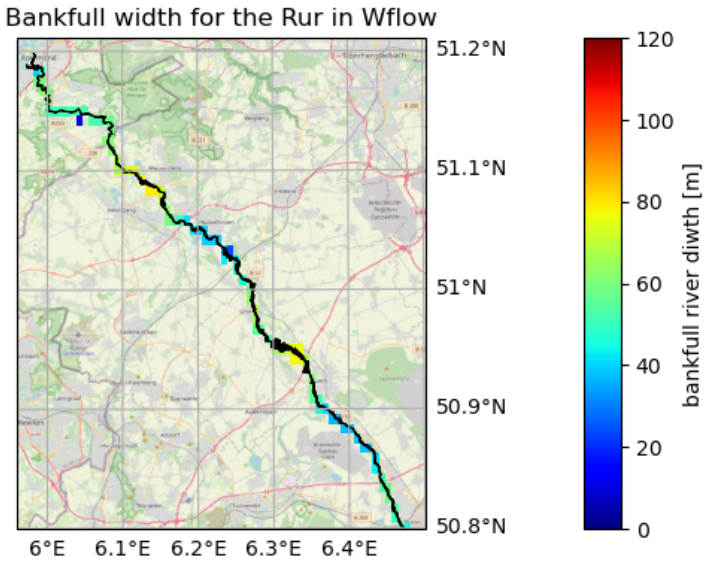

Figure B.21: Bankfull river width in the *Wflow_SBM* model after including *ProMaIDes* cross-sectional information.

C

ADJUSTING THE *ProMaIDes* MODEL

C.1. WATER DEPTHS IN RIVER CROSS-SECTIONS

The downstream boundary condition is given by the water level of the Meuse River. This is necessary because ProMaIDes use the diffusive wave approach, and the flow in the river is assumed to be subcritical. Therefore, excluding the downstream boundary condition would result in an ill-posed problem.

The water level measurements in 'Roermond Boven' were provided by RWS and used to calculate the depth of the downstream water (Rijkswaterstaat, 2022). The water level at this gauge station was applied to the boundary conditions without correcting for the inclination of the water level since the station was only 1.5 km from the Hambeek outlet. An additional check was performed by comparing the ProMaIDes river profiles at these locations with profiles from a *D-HYDRO* model of the Rur used by Deltares and HKV, which confirmed that their position relative to the Meuse was indeed correct.

C.2. HAMBEEK AND RUR IN ROERMOND

The Rur river splits into two upon entering Roermond at the bellow weir (in Dutch: 'Balgstuw') Hoge Bat. It continues its flow through the Hambeek in the south and Rur in the north, both ending in the Meuse River. This final part of the Rur contains two flood gates (Figure C.1) that close for water levels exceeding +19 metres NAP, resulting in the full flow being diverted to the Hambeek (T. Geertsema & Asselman, 2022; Horn & Hurkmans, 2022).

The *ProMaIDes* model contains the bifurcation of the Hambeek and Rur, which is modelled as a diversion channel with a weir. However, the model does not support a straightforward approach to implementing the closing of the flood gates in the Rur, and model results with no adjustment show inundation for relatively low discharges near the city

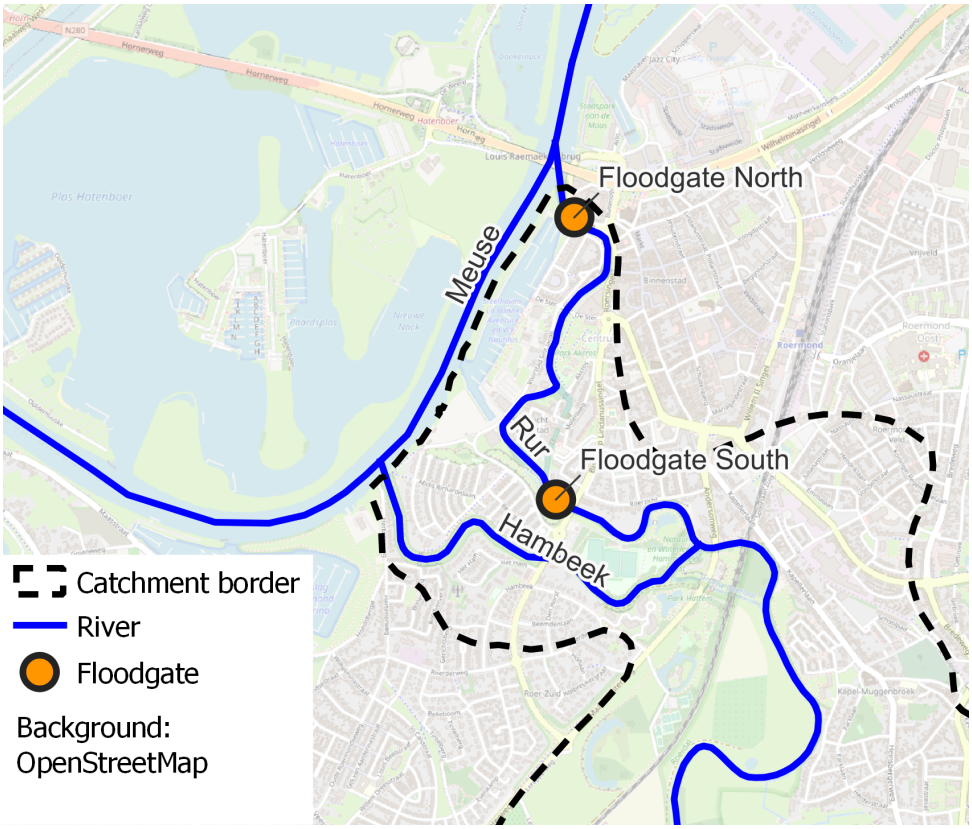

Figure C.1: The Hambeek and Rur rivers with the locations of the flood gates.

centre of Roermond from this part of the Rur. Therefore, an adjustment is made to the *ProMaIDes* model for the forecast of the flood event in which the Rur section downstream of the bifurcation is removed from the model. For lower discharges, the original model for the Rur River, which includes the bifurcation, continues to be used.

C.3. TRIBUTARY INFLOWS

The Rur River model begins at the Obermaubach dam, forming the upstream boundary condition. To this end, the discharge at this point is derived using a hydrological *Wflow_SBM* model. The Obermaubach dam can regulate outflow and is therefore in practise a reservoir. However, the choice was made to simplify the hydrological model by only considering the three largest reservoirs in the catchment (see also Section D.2.2). As a result, flow regulation at the Obermaubach dam is not included in these simulations, and the inflow of the ProMaIDes model will mainly be governed by the outflow of the Rur reservoir upstream of Obermaubach.

In addition, tributaries are included in the model and discretised as point inflows in se-

lected river profiles. These inflows are also computed using a *Wflow_SBM* model. To this end, the *Wflow_SBM* river map (generated using *HydroMT*) is compared with a detailed GSK3E river map of the catchment provided by LANUV (to do: find citation), which allowed the identification of tributaries flowing into the Rur River. The river map generated by *Wflow_SBM* differs from the observed river network for three reasons: 1) it is generated based on a hydrologically conditioned DEM, 2) the *Wflow_SBM* model is limited to $\mathcal{O}$(1km) resolution, and 3) *Wflow_SBM* does not support bifurcations. In total, 17 tributaries are identified and included as a lateral inflow in the *ProMaIDes* model as listed in table C.1

The mapping of the *Wflow_SBM* tributary to the *ProMaIDes* profile is performed mainly based on the location of the confluence, but also considers the deviations from the actual river network and their locations relative to the gauge stations. As a result, inflow locations with strong deviations are manually corrected to ensure that modelled observations at the gauge stations include the correct upstream tributaries. Finally, lateral inflow (e.g. surface runoff or precipitation) and outflow (e.g. infiltration and evaporation) are not included in the *ProMaIDes* model.

An overview of typical values for the simulated discharge at these inflow locations is also given in Table C.1. These values are the result of Wflow-FP simulations using the E-OBS dataset for the period 2010-2022. The results of the Wflow-KW and Wflow-LI models produced similar statistical results with larger maxima. Table C.1 confirms in fact that these are the most important flows of the Rur river. The model with the reduced river network contains only the inflows of the Wurm and Inde tributaries, and the upstream inflow boundary condition at the Obermaubach dam.

				complete network [m^3/s]				reduced network [m^3/s]			
tributary name	**ID**	**lat**	**lon**	Q_{mean}	$Q_{10\%}$	$Q_{\%90}$	Q_{max}	Q_{mean}	$Q_{10\%}$	$Q_{90\%}$	Q_{max}
Baaler Bach	5	51.033	6.252	0.34	0.15	0.6	2.67				
Birgeler Bach	14	50.783	6.469	0.1	0.03	0.24	2.03				
Buschbach	1	51.158	6.085	0.11	0.03	0.2	0.46				
Drover Bach	9	50.742	6.498	0.11	0.03	0.24	1.56				
Ellebach	7	50.917	6.368	0.51	0.16	0.96	6.07				
Hückelhovener Bach	17	51.042	6.235	0.12	0.06	0.22	0.83				
Inde	8	50.892	6.36	3.68	0.98	8.62	36.07	3.08	0.72	9.54	40.20
Kitschbach	2	51.117	6.077	0.1	0.02	0.22	0.94				
Kufferather Bach	15	50.758	6.477	0.04	0.01	0.08	0.46				
Lieker Bach	13	51.093	6.094	0.05	0.01	0.1	0.76				
Malefinkbach	6	50.958	6.302	0.34	0.13	0.64	3.27				
Millicher Bach	16	51.058	6.202	0.1	0.05	0.18	0.7				
Mühlenbach	18	51.067	6.168	0.03	0.01	0.06	0.27				
Obermaubach	10	50.717	6.443	9.11	6.12	11.83	46.92	13.29	6.94	22.92	55.38
Rode Beek	12	51.142	6.093	0.15	0.05	0.28	1.48				
Schaagbach	3	51.1	6.127	0.17	0.02	0.39	1.53				
Schlichbach	11	50.85	6.427	0.2	0.06	0.39	3.52				
Wurm	4	51.092	6.11	3.29	1.19	6.21	49.68	3.73	0.97	6.11	47.95

Table C.1: Tributary inflows included in the *ProMalDes* model. Statistical values are based on E-OBS 2011-2022 precipitation data using a Wflow-FP model with the full river network (UPA = 5 km^2) and the reduced network (UPA = 100 km^2).

D

ADDITIONAL CATCHMENT CHARACTERISTICS

D.1. LANUV GAUGE STATIONS

The data for the observations at the gauge station in the Rur catchment are provided by LANUV via the ELWAS-WEB portal (ELWAS-WEB, 2023). In this thesis, average daily discharges are used from the 1st of October 2011 to the 30th of September 2020. Detailed information on these measurements is given in Table D.1. Furthermore, the hourly water levels for the year 2021 have been provided by LANUV via e-mail. A graphical overview of the gauge stations is provided in Figure D.1.

Furthermore, gauge stations located on the Rur were compared with the cross sections of river profiles available in the *ProMaIDes* model at these locations. Not all cross sections could be matches to their corresponding gauge station as cross-sectional data did not match gauge station's characteristics such as the water level reference point of the station. Only the stations at Stah and Selhausen matched a river profile and the model results matched observations in regular flow conditions generated using the RADCLIM database.

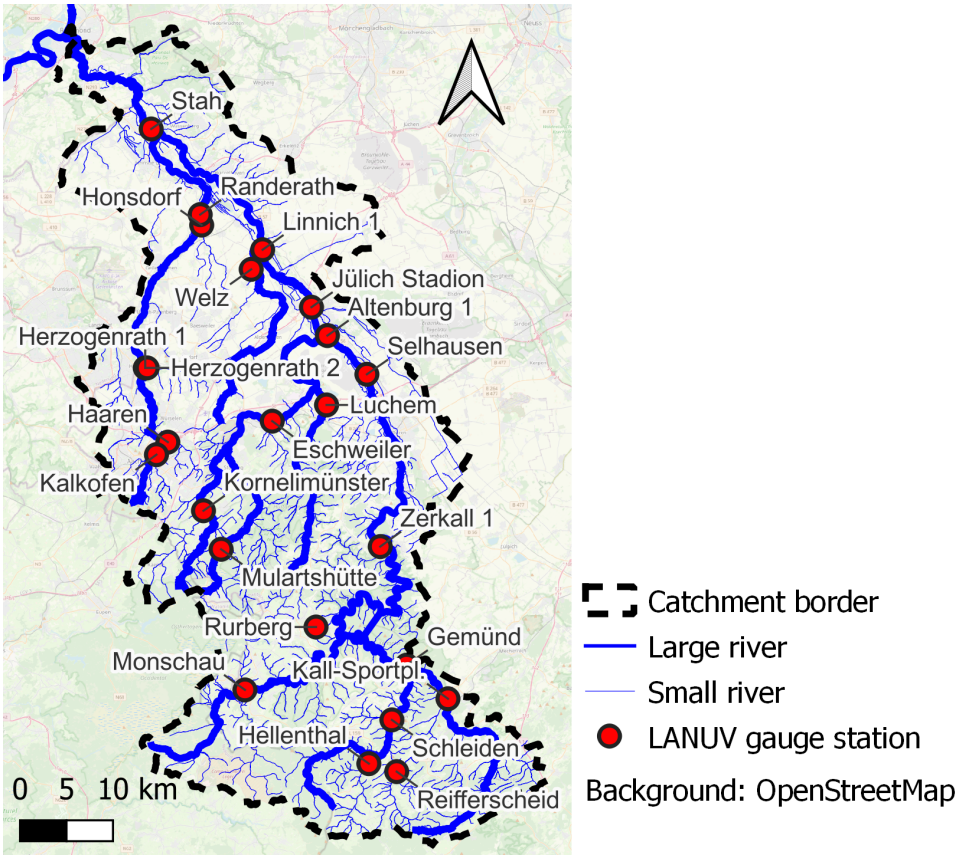

Figure D.1: Map of LANUV gauge stations in the Rur catchment.

stations name	station ID	lat	lon	Q_{mean} [m^3/s]	Q_{10} [m^3/s]	Q_{90} [m^3/s]	Q_{max} [m^3/s]	river basin
Altenburg 1	28239000002	50.897	6.374	11.75	5.27	20.61	84.89	Rur
Eschweiler	28245900004	50.815	6.289	2.26	0.44	5.11	51.13	Inde → Rur
Gemünd	28229000002	50.578	6.491	4.1	1.28	9.26	40.06	Urft → Rur
Haaren	28282000002	50.795	6.129	0.28	0.1	0.51	5.5	Haarbach → Wurm → Rur
Hellenthal	28228490001	50.483	6.433	0.57	0.05	1.53	8.61	Platisbach → Olef → Urft → Rur
Herzogenrath 1	28283000002	50.867	6.095	1.68	0.87	2.95	21.45	Wurm → Rur
Herzogenrath 2	28284000002	50.867	6.098	0.3	0.18	0.5	2.75	Broicher Bach → Wurm → Rur
Honsdorf	28288900002	51.005	6.182	0.08	0.03	0.18	1.83	Beekfließ → Wurm → Rur
Jülich Stadion	28251900002	50.925	6.349	13.26	5.81	27.33	124.16	Rur
Kalkofen	28281000001	50.783	6.112	0.19	0.06	0.36	3.34	Wurm → Rur
Kall-Sportpl.	28227000002	50.545	6.554	0.92	0.16	2.2	13.32	Urft → Rur
Kornelimünster	28243000001	50.728	6.183	0.51	0.06	1.29	14.58	Inde → Rur
Linnich 1	28253300001	50.981	6.275	13.36	5.86	26.4	115.2	Rur
Luchem	28248900003	50.83	6.372	0.28	0.13	0.43	2.94	Wehebach → Inde → Rur
Monschau	28215300002	50.555	6.246	3.24	0.37	8.51	48.7	Rur
Mulartshütte	28244500001	50.691	6.21	0.51	0.09	1.19	14.12	Vichtbach → Inde → Rur
Randerath	28289000002	51.015	6.179	2.68	1.29	4.95	29.24	Wurm → Rur
Reifferscheid	28228690001	50.475	6.475	0.55	0.03	1.38	8.78	Reifferscheider Bach → Olef → Urft → Rur
Rurberg	28231000001	50.615	6.354	0.04	0.0	0.12	0.71	Weidenbach → Rur
Schleiden	28228700001	50.525	6.468	2.24	0.46	5.32	23.03	Olef → Urft → Rur
Selhausen	28239000001	50.86	6.434	9.95	4.78	17.91	97.03	Rur
Stah	28291000001	51.098	6.105	17.17	8.46	31.26	120.8	Rur
Welz	28253490001	50.962	6.257	0.21	0.04	0.43	5.76	Merzbach → Rur
Zerkall 1	28235000001	50.693	6.452	10.36	5.19	18.13	68.34	Rur

Table D.1: LANUV gauge stations located in the Rur catchment. Statistical values are based on 2011-2022 period.

D.2. WVER RESERVOIRS

This section elaborates on the information given in Section 3.1.2. It provides details on the reservoirs located in the Rur catchment and describes how the Rur reservoir system operates.

D.2.1. RESERVOIR CHARACTERISTICS

Table D.2 highlights the main characteristics of the six reservoirs managed by WVER in the Rur catchment. This overview shows that flood protection is an important function of reservoirs and that the flood retention capacity is greatest during the winter period. The locations of these reservoirs are shown in Figure D.2.

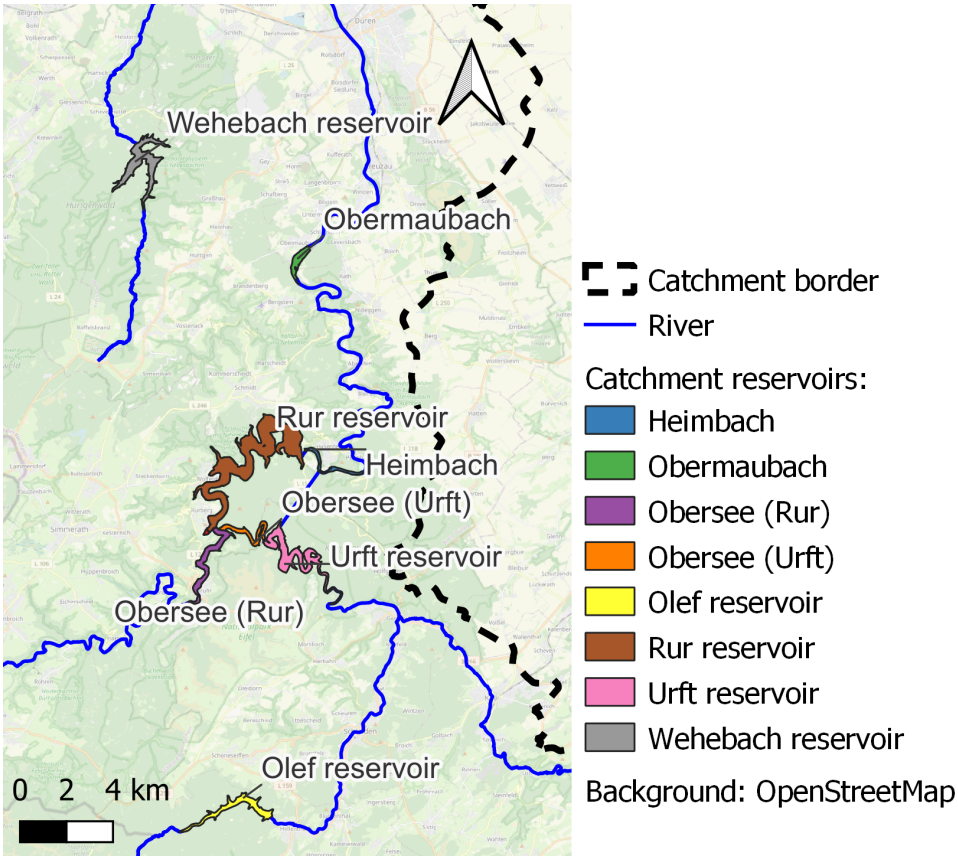

Figure D.2: Map showing the six reservoirs in the Rur catchment and the Obersee.

D.2.2. RUR RESERVOIR SYSTEM

The Rur reservoir system consists of a network of reservoirs and dams that regulate the flow of the Rur, of which the Urft and Rur reservoirs are the largest. Figure D.3 gives an overview of the main features of the reservoir system. The Obersee functions as a forebay (in German: 'Vorsperre') of the Rur reservoir, facilitating easier water quality control. As such, the Obersee is connected to external reservoirs via an underground canal, resulting in an additional outflow (Homann, 2021a).

The main sources of inflow are the Urft and Rur rivers, but smaller streams, such as the Eiserbach and Weidenbach, and overland runoff also contribute to the reservoir inflow. The reservoir system has two objectives related to flow regulation: flood protection by reducing peak outflow to 60 m^3/s at Heimbach, and low-water enrichment by providing a minimum discharge of 5 m^3/s at Obermaubach (Kufeld, 2013; Homann, 2021a) (see also Section E.1).

In addition, the water from the reservoir is used for hydropower and water supply, both for drinking water and for industrial purposes. Hydropower is of minor importance to the reservoir system, but almost all the water released by the Urft reservoir flows through the underground hydropower channel. At Heimbach, a power plant receives water directly from the Urft reservoir, thus surpassing the Rur reservoir. During floods, this connection can prevent the Urft reservoir from overflowing into the Rur reservoir, reaching a maximum discharge of 18 m3/s (Kufeld, 2013; Homann, 2021a). A schematic overview of the Rur reservoir system is given in Figure D.4.

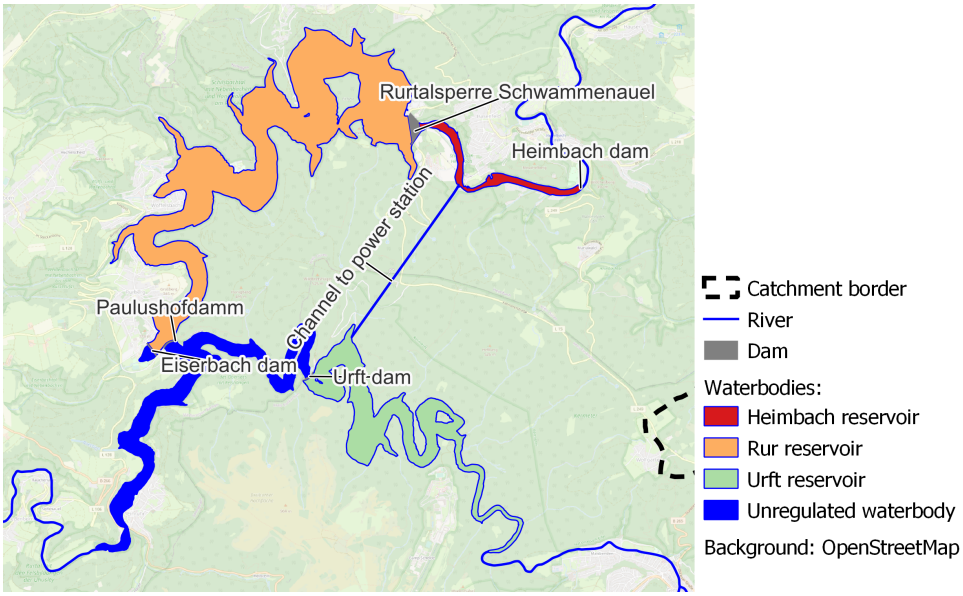

Figure D.3: Map showing the most important features of the Rur reservoir system.

This system is simplified in order to make it compatible with reservoir modelling in

Wflow_SBM. To this end, the Urft and Rur reservoirs have been combined into a single reservoir, and all other reservoirs have been removed, as schematised in Figure D.4. The outflow at Heimbach is determined by the Olef-Urft-Rur operation plan, which is still applicable when the Obersee and Heimbach reservoirs are removed, as they only depend on the storage at the (combined) Urft and Rur reservoirs. However, the flood retention capacity of the Heimach and Obermaubach reservoirs is lost in the model, and the hydrograph at Obermaubach will become a smoother version of the simulated outflow at Heimbach as it is not actively managed. However, the simplification provides sufficient results for the objective of this thesis.

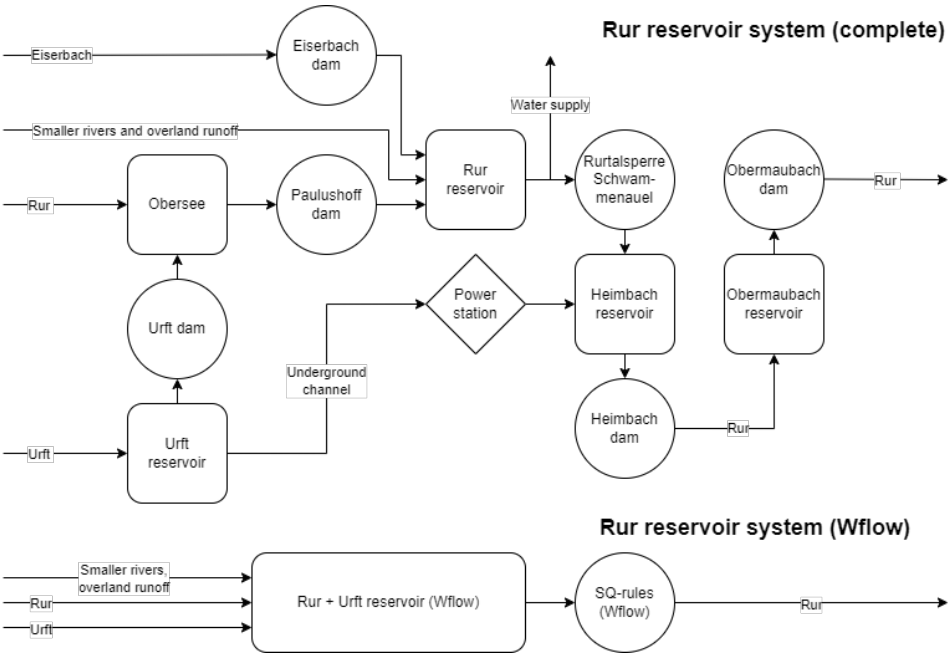

Figure D.4: Schematic overview of the complete Rur reservoir system and the simplified system implemented in *Wflow_SBM*.

name	total capacity [million m^3]	flood retention capacity min - max mil.m^3]	HHQ [m^3/s]	river basin	hydro-power	water supply	water sports
Rur and Obersee	202.6	6 (May-Sept.) - 38 (Dec.-Jan.)	450	Rur	✗	✓	✓
Urft	45.5	3 (May-Sept) - 20 (Dec.-Jan.)	> 275	Urft → Rur	✓	✗	✗
Olef	19.3	1 (May-Sept) - 6 (Dec.-Jan.)	73	Olef → Urft → Rur	✓	✓	✗
Wehebach	25.1	1 (May-Sept.) - 4.5 (Dec.-Jan.)	65	Wehebach → Inde → Rur	✓	✓	✗
Heimbach	1.2	none	550	Rur	✓	✗	✓
Obermaubach	1.7	none	600	Rur	✓	✗	✓

Table D.2: Characteristics of the six reservoirs in the Rur catchment operated by WVER (WVER, 2017a, 2017b, 2017c, 2017d, 2017e, 2017f)

E

RESERVOIR OPERATION PLANS

E.1. OLEF-URFT-RUR RESERVOIRS OPERATION PLAN

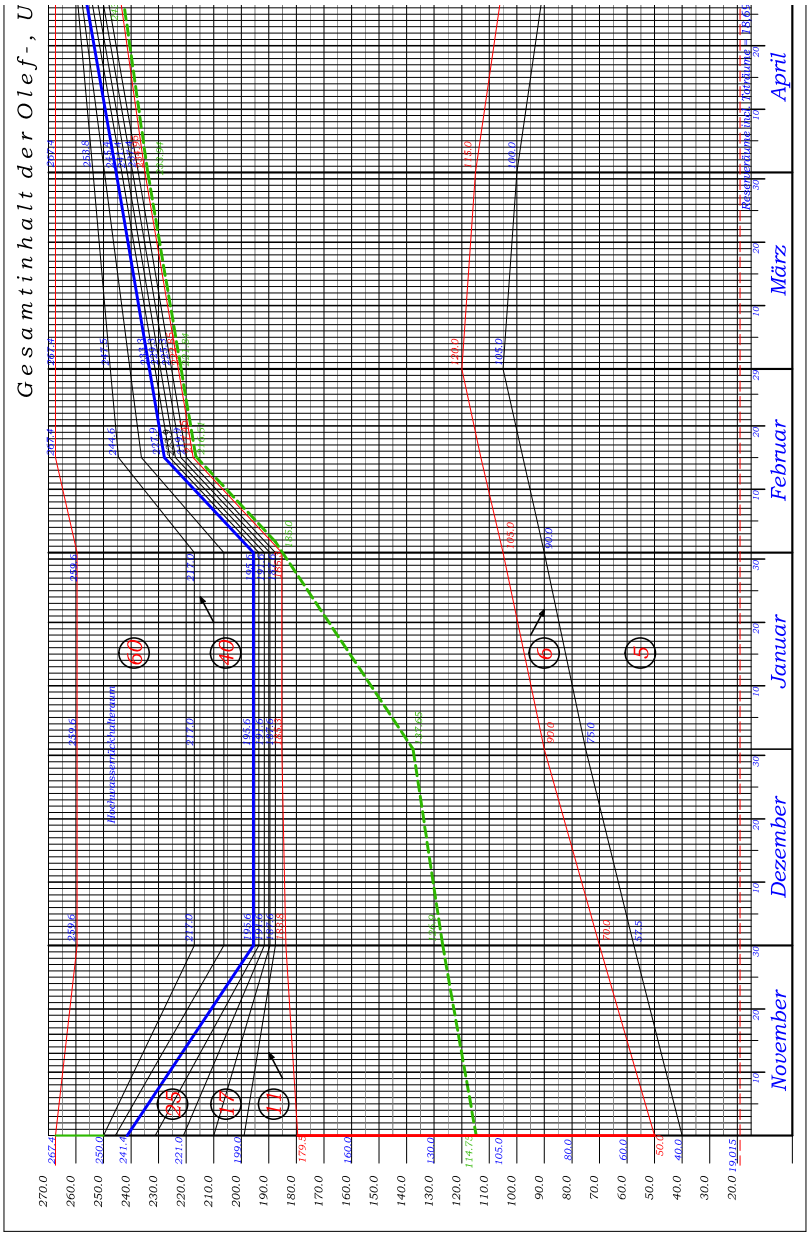

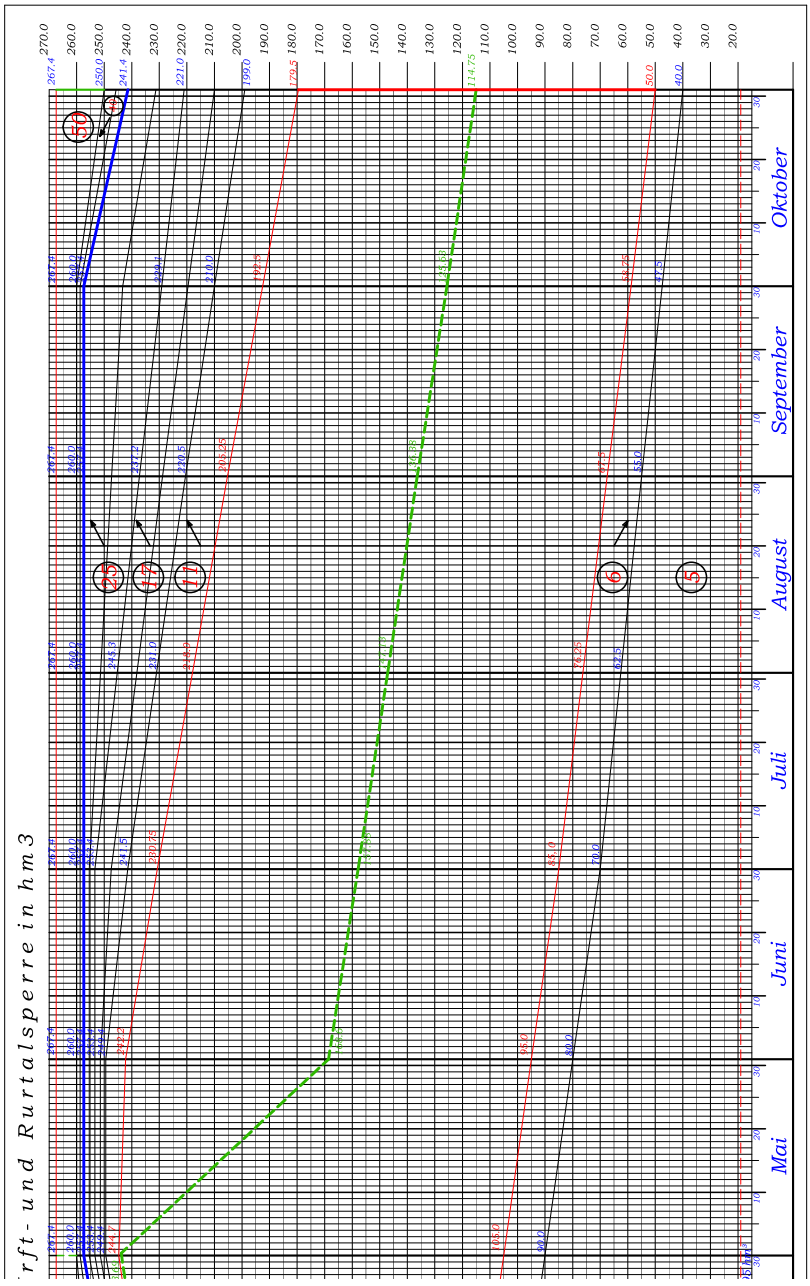

E

E.2. OLEF RESERVOIR OPERATION PLAN

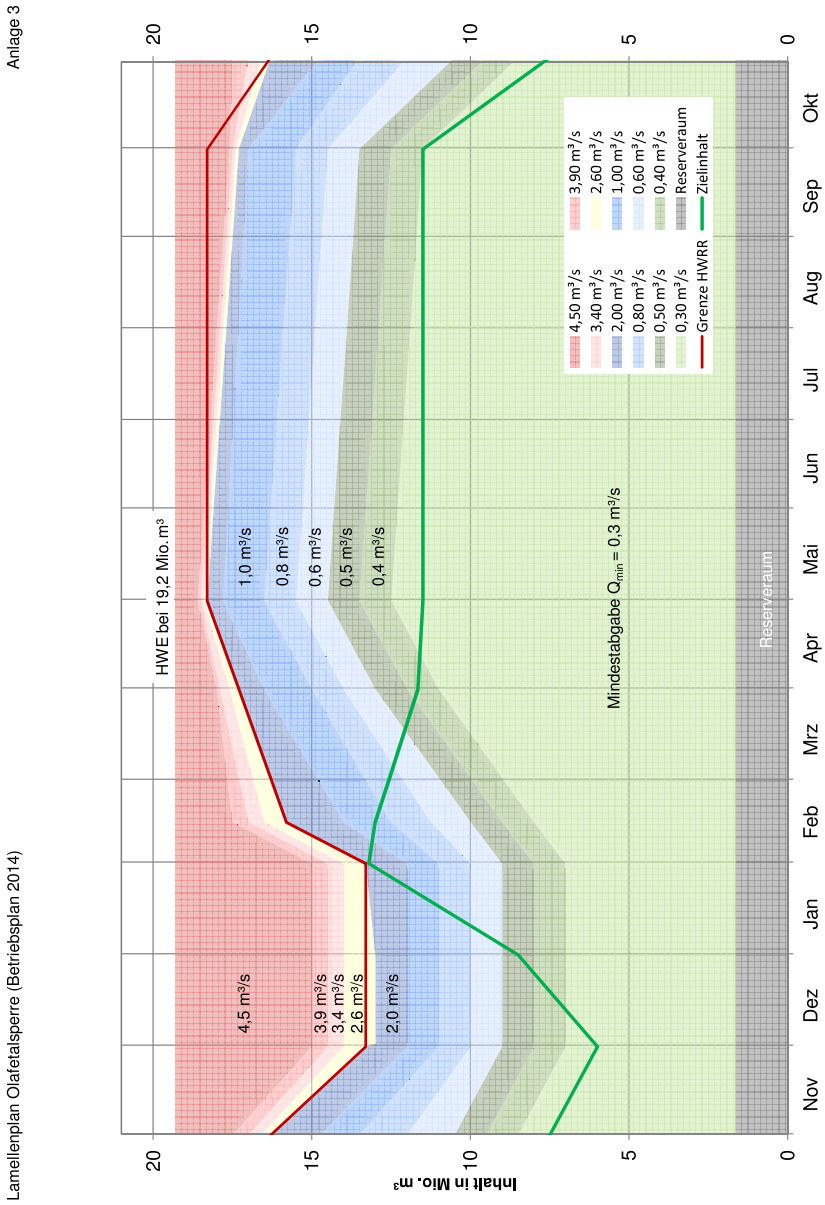

E.3. IMPLEMENTATION OF THE OPERATION PLANS IN *Wflow_SBM*

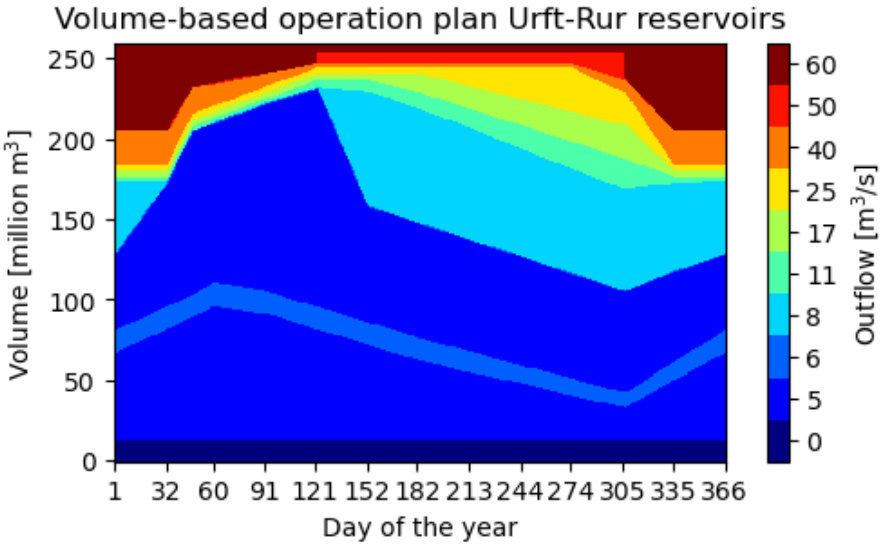

(a)

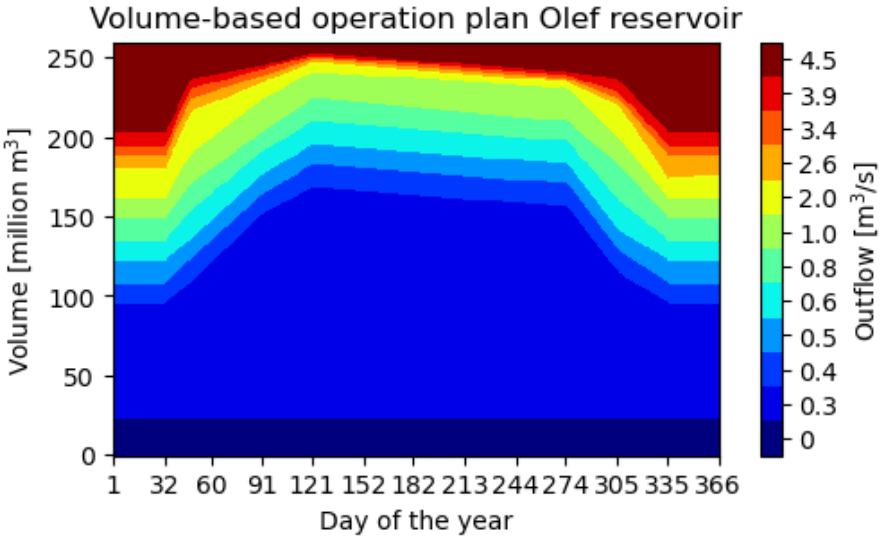

(b)

Figure E.1: Implementation of the volume-based operation plans of the Rur reservoir system and the Olef reservoir in *Wflow_SBM*.

F

ADDITIONAL MAPS

F.1. GEOLOGICAL MAP OF THE RUR CATCHMENT

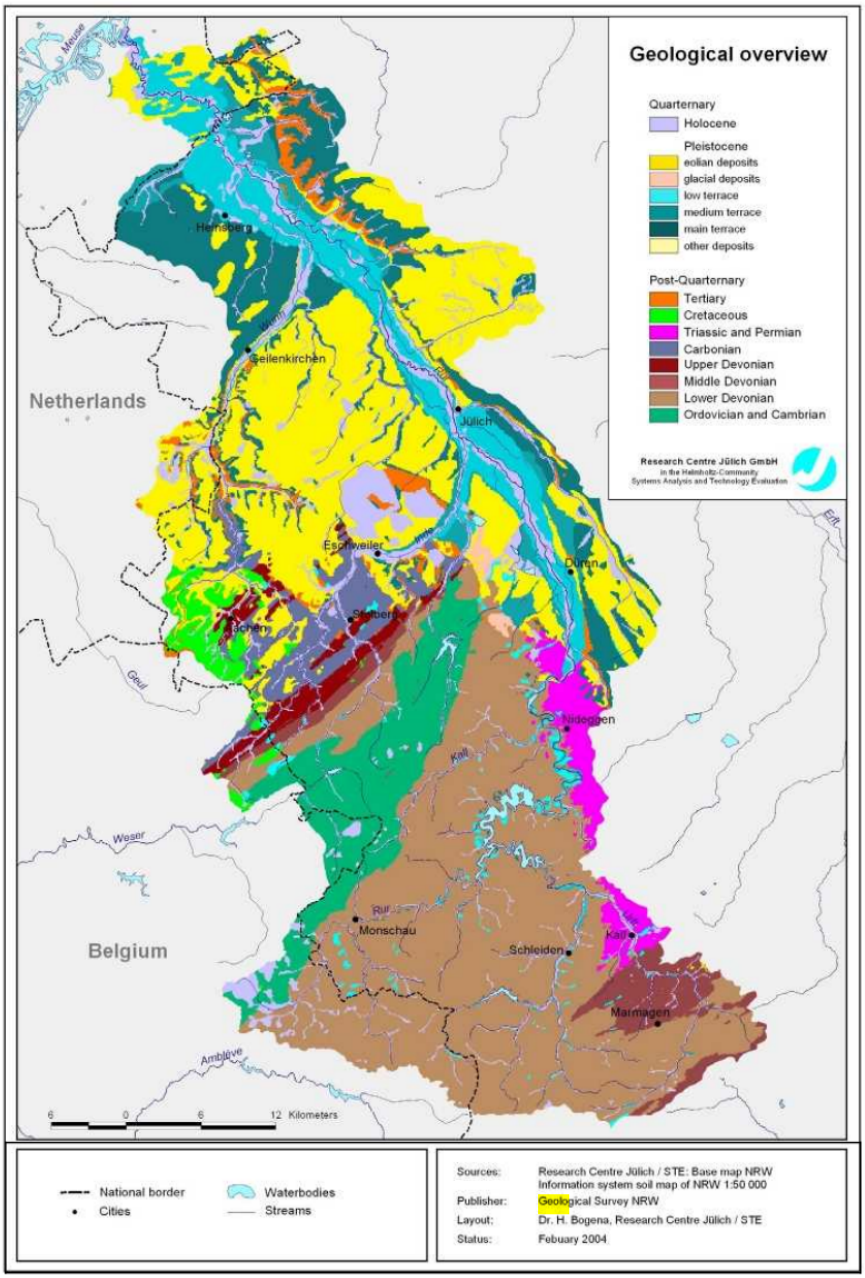

Figure F.1: Geological map of the Rur catchment. Obtained from Bogena, Pütz, et al. (2005).

F.2. INUNDATION MAPS OF THE PM-2D HINDCAST

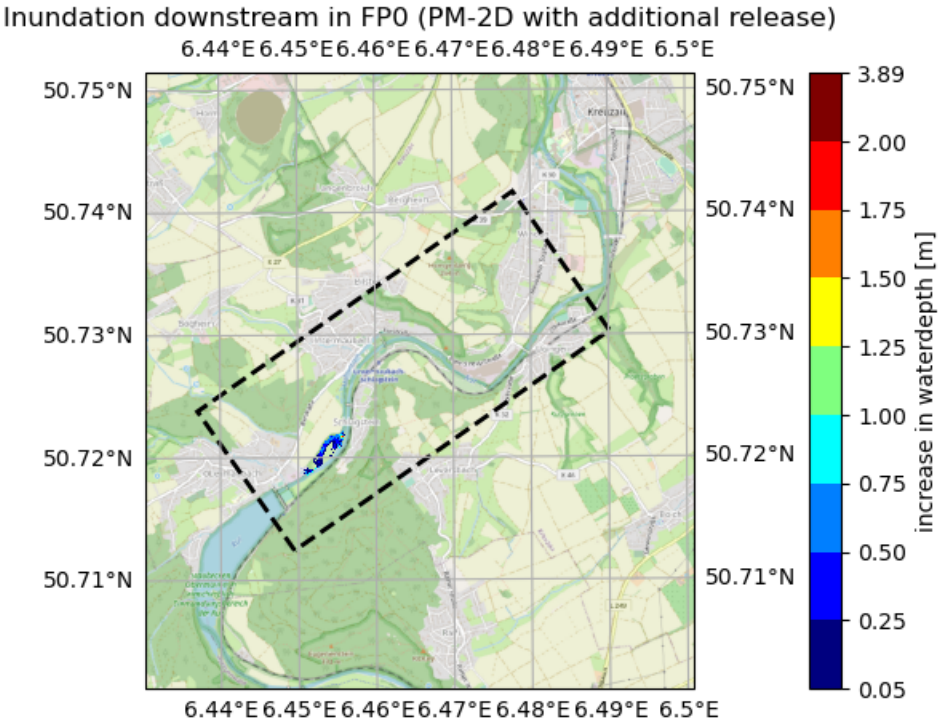

Figure F.2: Inundation map of floodplain grid 0 using the PM-2D model with additional reservoir release and RADFLOOD21.

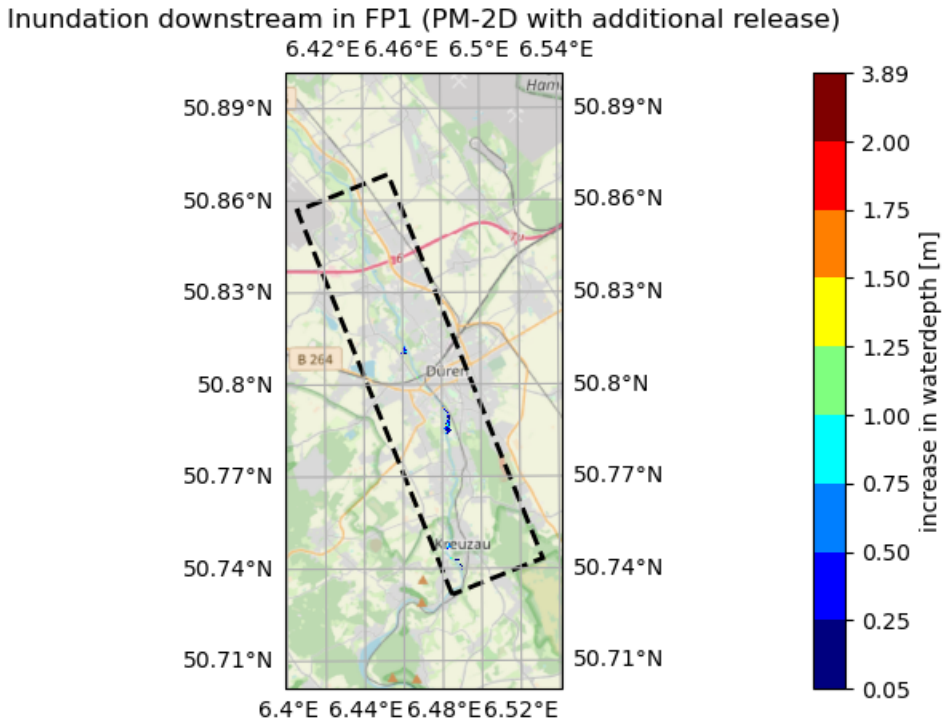

Figure F.3: Inundation map of floodplain grid 1 using the PM-2D model with additional reservoir release and RADFLOOD21.

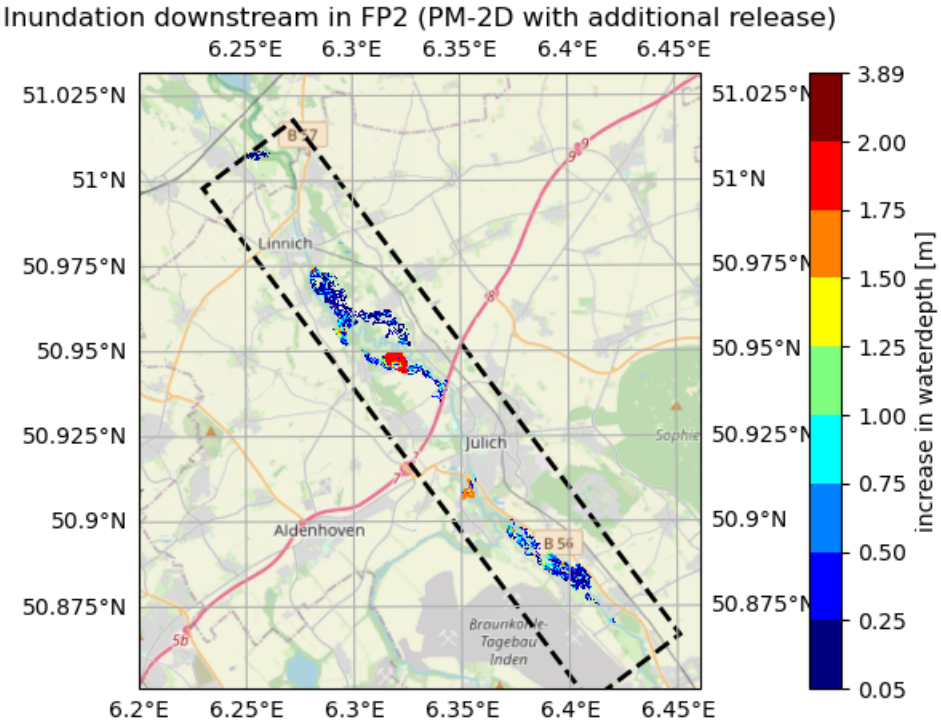

Figure F.4: Inundation map of floodplain grid 2 using the PM-2D model with additional reservoir release and RADFLOOD21.

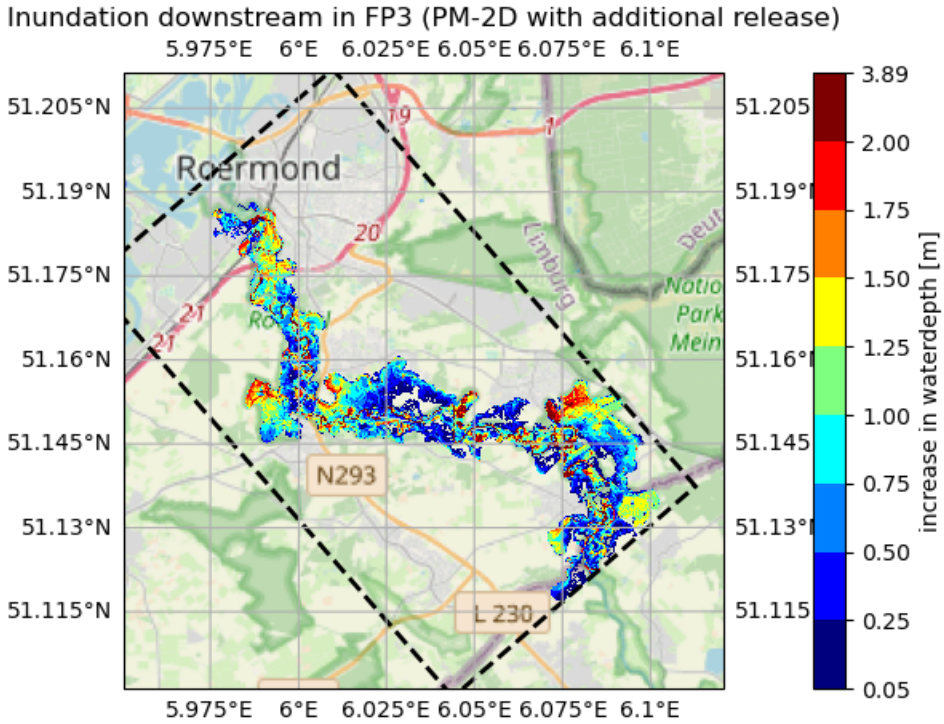

Figure F.5: Inundation map of floodplain grid 3 using the PM-2D model with additional reservoir release and RADFLOOD21.

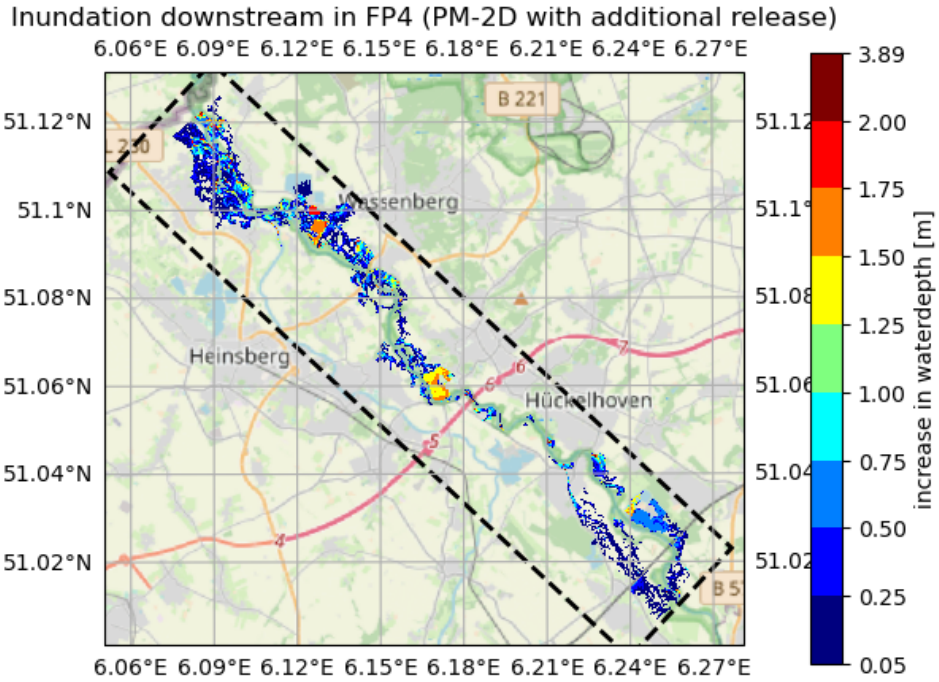

Figure F.6: Inundation map of floodplain grid 4 using the PM-2D model with additional reservoir release and RADFLOOD21.

F

F.3. RUNOFF COEFFICIENT FOR LANUV GAUGE STATIONS

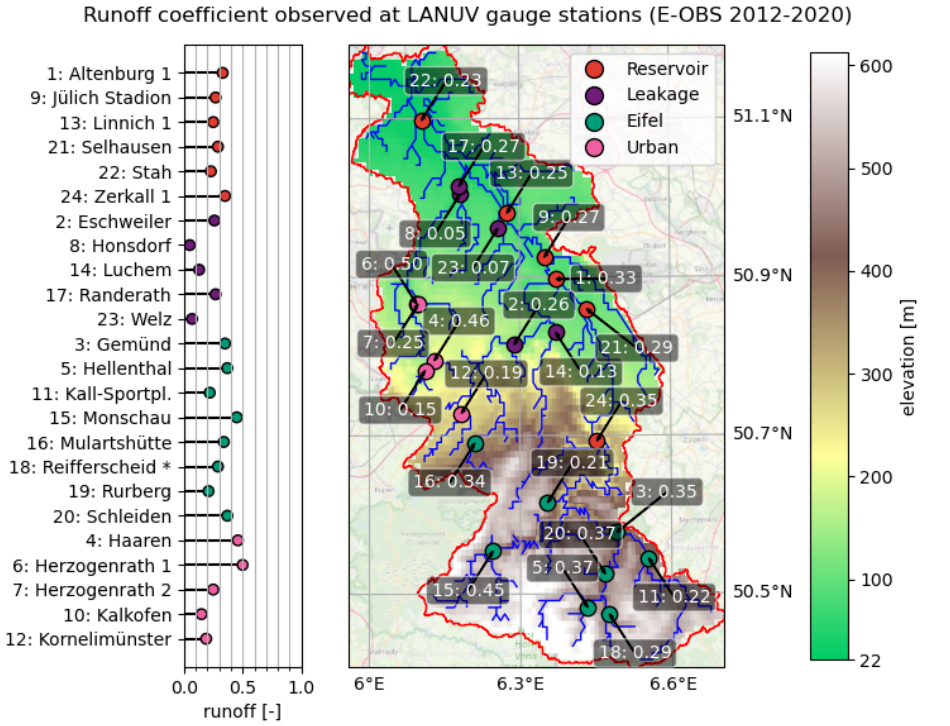

Figure F.7: Runoff coefficients for the LANUV gauge stations in the Rur catchment. Created using E-OBS data for precipitation and LANUV data for discharge.